

**Quasi-particle Breakdown and Heat Transport in a
Homogeneous Strongly-interacting Fermi Gas**

by

Zhenjie Yan

B.S., Tsinghua University (2014)

Submitted to the Department of Physics
in partial fulfillment of the requirements for the degree of
Doctor of Philosophy

at the

MASSACHUSETTS INSTITUTE OF TECHNOLOGY

February 2022

© Massachusetts Institute of Technology 2022. All rights reserved.

Author
Department of Physics
October 29, 2021

Certified by
Martin W. Zwierlein
Thomas A. Frank (1977) Professor of Physics
Thesis Supervisor

Accepted by
Deepto Chakrabarty
Associate Department Head

Quasi-particle Breakdown and Heat Transport in a Homogeneous Strongly-interacting Fermi Gas

by

Zhenjie Yan

Submitted to the Department of Physics
on October 29, 2021, in partial fulfillment of the
requirements for the degree of
Doctor of Philosophy

Abstract

This thesis describes experiments on a homogeneous strongly-interacting Fermi gas, consisting of a spin mixture of ${}^6\text{Li}$ atoms with interactions induced by a Feshbach resonance. The tunability and universality of this atomic gas make it an ideal platform to study many-body physics of interacting Fermi systems. The implementation of a uniform trapping potential enables experiments at constant density, allowing the study of transport, critical phenomena near phase transitions, and novel states of matter predicted in a narrow range of densities.

Radio-frequency (rf) spectroscopy provides a powerful tool for probing single-particle excitations in quantum gases. In particular, we employ it to study the thermal evolution of resonantly interacting spin impurities immersed in a Fermi gas. The rf spectra reveal a dramatic transition from an attractive polaronic Fermi liquid at low temperature to a classical Boltzmann gas above the Fermi temperature. In the polaron regime, the spectral width shows a characteristic T^2 temperature dependence, corresponding to the quasiparticle decay rate in a Fermi liquid. At high temperatures, the spectral width approaches the scattering rate of a classical, unitary Boltzmann gas, which scales as $T^{-1/2}$. In the transition regime, a spectral width on the order of the Fermi energy is observed, indicating the breakdown of the quasiparticle picture of well-defined, long-lived excitations.

I further describe the first direct observation of heat transport in a strongly interacting Fermi gas, using the temperature dependence of the rf spectra as a local thermometer. The superfluid phase transition in our attractive Fermi system separates two different regimes of heat propagation. While heat propagates diffusively in the normal phase, in a superfluid it propagates as a wave, called second sound. The measured speed of second sound yields the superfluid fraction, which quantifies the inertia against phase twists. The damping time scales of second sound and heat diffusion show a minimum diffusivity on the order of the quantum limit \hbar/m for both modes. The diffusivity is observed to feature a peak at the phase transition temperature which is evidence for critical behavior, as seen in liquid ${}^4\text{He}$.

Thesis Supervisor: Martin W. Zwierlein
Title: Thomas A. Frank (1977) Professor of Physics

Acknowledgments

My Ph.D. study at MIT has truly been an incredible journey. Here I want to thank all the individuals who provided guidance and support and made this work possible.

First of all, I would like to express my gratitude to Martin Zwierlein, my research advisor. Not only does he pass down all the valuable knowledge about physics and experiments, but he also inspires me to always find new solutions and explore the unknown. We would always have a brainstorm when a new idea or new question is raised, and these discussions often led to a new research path or better understanding of physics. To me, the most memorable discussion was the one time we had a spontaneous meeting in the CUA hallway with coffee in our hands. Martin suggested many ideas to improve the signal of a second sound, including using a spectroscopic signal as a thermometer. This idea then led to our beautiful observation of heat transport within days.

The results in this thesis would have been impossible without good teamwork. Tarik Yefsah and Julian Struck are two postdocs I worked with when I first joined the group. Though my overlap with Tarik was brief, his guidance allowed me to learn the operation and maintenance of the BEC1 machine in a short time. Together with Julian, we finished our projects on uniform trapping potential, radio-frequency spectroscopy of strongly interacting Fermi gas, and the observation of first sound. His insight into atomic and many-body physics was crucial in shaping many of our projects. His focus on details also helped the team perfect the experiment and data analysis procedure in BEC1. Richard Fletcher joined as our next postdoc, and we mainly collaborated on the search for second sound in BEC1 and the building of Fermi3. I can still vividly remember the late nights when we were trying to debug the machine and find the signal of second sound, and the time we spent winding the magnetic coils for Fermi3 with gloves covered in epoxy. Richard's pleasant and caring personality made our teamwork really enjoyable. Biswaroop Mukherjee and Parth Patel are the other two graduate students in BEC1. We often worked side by side for long hours fixing a vacuum leak or burnt electric cables to keep the machine running.

We were rewarded not only by beautiful scientific results but also by a deep friendship with each other. Airlia Shaffer and Cedric Wilson are the next generation of graduate students. Their brilliance and hard work were what made the Fermi3 experiment possible. Just recently, Eric wolf and Huan Bui joined BEC1, and Ruixiao Yao joined Fermi3 as new team members. I believe they will soon produce some exciting new results.

I am also grateful to all the other members of the Zwierlein group, including Zoe Yan, Yiqi Ni, Alex Chuang, Carsten Robens, Peter Park, Sebastian Will, Huanqian Loh, Elmer Guardado-Sanchez, Mark Ku, Lev Kendrick, Tom Hartke, Botond Oreg, Ningyuan Jia, Matt Nichols, Lawrence Cheuk, Melih Okan, and Hao Zhang. Together we had many stimulating discussions on physics and exchanged many useful lab tricks. Our group social events like beach and hiking trips, paintball, video game night, and so on were all enjoyable and brought everyone together. I really appreciate the supportive and fun group environment created by everyone.

I want to thank my thesis committee members Wolfgang Ketterle and Leonid Levitov for their comments and feedback. I also learned a lot from Wolfgang's AMO lectures. Many of my questions on AMO physics were clarified by his intuitive and concise explanations. Dave Pritchard is my academic advisor, and I am grateful for his advice on science, career, and life. I would also like to thank many physicists outside of our group for their collaboration and valuable suggestions. Zoran Hadzibabic made a significant contribution to the uniform trap project during his sabbatical here. Richard Schmidt provided many helpful discussions about our project of quantum impurity. Christopher Vale collaborated with us on the heat transport project.

Next, I want to thank many friends and colleagues in the CUA and MIT community. Niki Jepsen, Ivana Dimitrova, Jesse Amato-Grill, Timur Rvachov, Hyungmok Son, Juliana Park, Jun-Ru Li, Boris Shteynas, Furkan Top, Alan Jamison, Colin Kennedy, Cody Burton, Zachary Vendeiro, Yi-Xiang Liu, Mo Chen, Calvin Sun, Jasmine Kalia, and Jared Rivera are all very friendly CUA coworkers who lent a helping hand in times of need. Cathy Modica, Sydney Miller, and Al McGurl are MIT staff members who have provided tremendous assistance to my study and research at MIT.

I also want to express my appreciation to Edgerton shop master Mark Belanger, who accompanied me to MIT Medical when I cut myself on a lathe.

Finally, I would like to thank my family. My parents, Hong and Yaping, provided me a pleasant childhood and a good education, and they have given me tremendous support and encouragement in my pursuit of science. Meeting my wife, Yi Xue, at MIT is the best thing in my life. The time we spend together is always filled with love and joy. Her advice and help as a fellow scientist are also invaluable to me.

*To my family, Hong and Yaping,
and the woman I love, Yi*

Contents

1	Introduction	19
1.1	A brief history of strongly interacting Fermi gas experiments	21
1.2	A Uniform trapping potential for Fermi gases	24
1.3	Radio-frequency spectroscopy and quasiparticle breakdown	25
1.4	Thermal transport in a strongly interacting Fermi gas	26
2	Strongly interacting Fermi gases	29
2.1	Quantum statistics	29
2.2	Ideal Fermi gases	30
2.3	Interparticle interactions and Feshbach resonances	33
2.3.1	Quantum scattering theory	34
2.3.2	Pseudo-potential	37
2.3.3	Feshbach resonances	38
2.4	Unitary Fermi gas	41
2.4.1	Scale invariance	41
2.4.2	Universal thermodynamics of unitary Fermi gases	43
2.5	rf spectroscopy of interacting Fermi gases	46
2.5.1	Molecular dissociation spectrum: a simple example	48
2.5.2	Two body contact and the rf tail	49
3	Experimental apparatus and homogeneous Fermi gas	53
3.1	A homogeneous Fermi gas	54
3.1.1	Experimental setup	54

3.1.2	Calibration of the uniform potential	57
3.1.3	Momentum Distribution of an Ideal Fermi gas	58
3.1.4	Rapid Ramp and Pair Condensate in a Uniform Potential. . .	61
3.1.5	The hybrid Potential	62
3.2	Absorption imaging	66
3.3	Phase contrast imaging	71
3.4	Coil systems and magnetic transport for a new quantum gas experiment	76
3.4.1	MOT Chamber Coils	78
3.4.2	Magnetic Transport System	80
3.4.3	Glass Cell Coils	82
4	Resonant quantum impurities in a Fermi gas at finite temperature	85
4.1	Fermi polarons at low temperature	86
4.1.1	Chevy ansatz and variational wavefunction approach	86
4.1.2	Fermi liquid behavior: scattering rate	90
4.1.3	Fermi liquid behavior: equation of state	92
4.2	Classical Boltzmann gas at high temperatures	93
4.2.1	Scattering rate	93
4.2.2	Virial expansion	93
4.3	rf spectroscopy of the quantum impurity	96
4.3.1	Temperature dependence of the quasiparticle energy and lifetime	96
4.3.2	Contact of the spin impurity	99
4.3.3	Rabi oscillation between a Fermi polaron and a free particle .	100
4.4	Thermodynamics of spin-imbalanced Fermi gases	102
4.4.1	Density of dressing clouds	102
4.4.2	Polaronic Fermi gases	104
4.4.3	Equatation of state calibration	105
5	Heat transport in unitary Fermi gases	107
5.1	Superfluid hydrodynamics	108
5.1.1	Two-fluid model	108

5.1.2	Hydrodynamic equations of a superfluid	112
5.1.3	Sound propagation modes in superfluids	116
5.1.4	Response functions	120
5.1.5	Normal fluid hydrodynamics	124
5.2	rf spectroscopy of spin-balanced unitary gases	126
5.3	Second sound in the superfluid phase	129
5.3.1	rf spectroscopic thermometry	130
5.3.2	Creation and observation of the second sound	133
5.3.3	Response functions	136
5.3.4	Speed and diffusivity of the second sound	139
5.4	Thermal diffusion in the normal phase	141
5.4.1	Thermal conductivity measured from thermal diffusion	142
5.4.2	Viscosity measured from thermal and sound diffusivity	143
6	Conclusions and outlooks	145
A	Homogeneous Atomic Fermi Gases	149
B	Boiling a Unitary Fermi Liquid	159
C	Spectral Response and Contact of the Unitary Fermi gas	171
D	Universal sound diffusion in a strongly interacting Fermi gas	181
E	Correlation functions and response functions	199
F	Magnetic coils making	205

List of Figures

2-1	Momentum distribution of an ideal Fermi gas	32
2-2	Universal Thermodynamics of an ideal Fermi gas	34
2-3	A Schematic of Feshbach Resonance	39
2-4	Feshbach Resonances of Ground State ${}^6\text{Li}$	40
2-5	Neutron star and unitary Fermi gas	45
2-6	rf spectroscopy of interacting Fermi gases	48
3-1	Homogeneous Fermi gas	55
3-2	Cylindrical Potential	56
3-3	Endcap Potential	57
3-4	Calibration of the radial trapping potential	58
3-5	Schematic of momentum-space mapping	59
3-6	Momentum distribution of the homogeneous spin-polarized Fermi gas	61
3-7	Rapid ramp and pair condensate in a Homogeneous cloud	62
3-8	Hybrid Potential	63
3-9	Isoenergetic expansion from uniform trap to hybrid trap	65
3-10	Polarization of Imaging beams	66
3-11	Lookup table for absorption imaging	68
3-12	Calibration of absorption images	69
3-13	Saturation of high density imaging	71
3-14	Phase contrast imaging	72
3-15	Equation of state measured with phase contrast imaging	76
3-16	The vacuum chamber of Fermi 3	77

3-17	Magnetic coils of Fermi	3	78
3-18	Calibration of magnetic field gradient	79
3-19	Magnetic Transport	80
3-20	The Feshbach field	83
4-1	Chevy Ansatz: Polaron Energy and contact	89
4-2	Chevy Ansatz: Dispersion and effective mass	90
4-3	Impurity rf spectroscopy	97
4-4	Impurity Contact	100
4-5	Polaron Rabi oscillations	101
4-6	Majority Dressing cloud	103
4-7	Isothermal compressibility of polaronic Fermi gases	104
4-8	Pressure of the spin-imbalanced unitary Fermi gas	106
5-1	Superfluid fraction and speed of second sound from the phonon and pair breaking model	112
5-2	Density-density and heat-density response functions in superfluid and normal phase.	125
5-3	rf spectroscopy of spin-balanced unitary gases	127
5-4	Contact of a spin-balanced unitary Fermi gas	129
5-5	Spectroscopic thermometry	130
5-6	Calibration of the rf thermometer	132
5-7	Creation of second sound and temperature variation	133
5-8	Heat propagation in the unitary Fermi gas	134
5-9	Steady state density and temperature responses	136
5-10	Density and temperature Responses	138
5-11	Thermodynamic quantities extracted from the response function fit	. .	139
5-12	The speed and diffusivity of second sound.	140
5-13	Density evolution during heat transport	142
5-14	Second Sound and thermal diffusivity	143
5-15	Temperature dependence of thermal conductivity and shear viscosity	144

6-1	Schematic of FFLO state	146
6-2	Phase diagram of imbalanced Fermi gas	147
F-1	Coils winding mold	205
F-2	Coils winding method	206
F-3	Casting of the MOT chamber coil set	207
F-4	Casting of the science cell coil set	208
F-5	Coil support structure and transport coils	209

List of Tables

2.1	Properties of Feshbach Reonances	41
2.2	Properties of Unitary Fermi gas	44
3.1	MOT chamber coils	78
3.2	Transport coils	81
3.3	Glass cell coils	83
E.1	Examples of observable quantities and corresponding generalized external forces	200

Chapter 1

Introduction

Interactions and correlations in many-body systems result in the diversity of states of matter observed in our universe. The spectrum of stable bound states of interacting protons and neutrons gives rise to the atomic elements. Atoms and molecules form a gas, liquid, or solid depending on the interparticle interactions. For metals at extremely low temperatures, thanks to the phonon-induced attraction and electron Fermi surface, electrons form a coherent condensate of loose Bardeen–Cooper–Schrieffer (BCS) pairs and become superconducting. However, it has long been a major challenge for the science community to understand the many-body behavior of strongly interacting quantum systems. The dimension of Hilbert space diverges exponentially with the number of particles in the system, making an exact solution of quantum many-body systems almost impossible to achieve, while strong interaction and potential long-range correlation exclude cluster expansion methods. The quantum statistics of fermionic particles, which make up the majority of the mass of the known universe, leads to the so-called sign problem, further complicating the theoretical understanding of many-body Fermi systems. To address these difficulties, Feynman made the proposal of emulating an unknown system using an analog quantum simulator that is easy to control and measure [49]. Quantum simulation allows detailed comparisons between highly controlled experiments with approximate solutions and therefore serves as a crucial benchmark for theory frameworks. It also provides a powerful tool for the search for exotic phases of matter that have not yet been observed in nature.

In recent years, ultracold gases of atoms and molecules have emerged as a versatile quantum simulator [11]. Precisely controlled by lasers and electromagnetic fields, atoms and molecules serve as building blocks for a variety of many-body systems. Interacting systems composed of bosonic [91] and fermionic [92] atomic species have been realized. A wide range of trapping configurations can be used to tackle various physical problems. For example, a bulk gas trapped in a harmonic or uniform potential can be used to simulate the thermodynamics and hydrodynamics of quantum fluids, while atoms loaded into an optical lattice provide an ideal testbed for lattice models such as the famous Fermi Hubbard model [125, 24, 13]. A strong confining potential can also be used to tune the dimensionality of the system. Quantum gas experiments offer excellent control of the interparticle interaction. A magnetic or optical Feshbach resonance [28] can arbitrarily tune the strength of short-range interactions, while long-range interactions can be achieved with Rydberg atoms [117, 9, 65], polar molecules [210, 212, 169], or atoms with a strong magnetic dipole [2, 118, 48]. For the detection of quantum gases, a great number of methods have been demonstrated in experiments. While absorption and phase contrast imaging are used to detect the density and spin distribution in a bulk system, fluorescence imaging can achieve single site resolution in an optical lattice [5]. Spectroscopic techniques, such as radio-frequency (rf) or two-photon Raman spectroscopy, are able to detect the energy-momentum spectrum of the single-particle excitations. The local phase of coherent quantum fluids, which has not been measured in superfluid helium or superconductors, can be mapped out by a matter wave interference measurement [139, 42, 3] in a quantum gas.

Among all the inspiring fields of quantum gas research, this thesis focuses on a strongly interacting Fermi gas composed of ^6Li atoms. A highly tunable contact interaction between different hyperfine states can be induced by a broad magnetic Feshbach resonance. The tunable interaction in the atomic Fermi gas has allowed the observation of a crossover from Bose–Einstein condensation (BEC) of repulsive bound molecules to BCS superfluidity of long-range Cooper pairs [64, 219, 86, 163, 220, 14, 95, 148]. The superfluidity and phase coherence were demonstrated via the

observation of lattices of quantized vortices [218], Josephson oscillations [206], reduced moment of inertia [166], and second sound [184, 75]. At the center of Feshbach resonance, the interaction strength reaches the maximum value quantum mechanics allows, i.e., the unitary limit, where each scattering event results in a phase shift of $\pi/2$. Despite the strong interaction, long-lived quasiparticles called Fermi polarons exist in highly imbalanced spin mixtures [173, 211] at low temperature, thanks to the Pauli blocking in the majority Fermi sea. As the temperature rises to the Fermi temperature, the polaronic quasiparticle breaks down into a classical bare particle [211]. In balanced spin mixtures, the strong interactions lead to a broad single-particle excitation spectrum with a width on the order of Fermi energy E_F , as the quasiparticles are short-lived and their mean-free-path is limited to the interparticle spacing. This also leads to a quantum-limited transport: the kinematic viscosity, spin and thermal diffusivity are all on the order of the quantum limit \hbar/m . The Hamiltonian of a Fermi gas in the unitary limit is scale-invariant and also describes the physics of a wide range of fermionic systems, including nuclear matter and quark-gluon plasma. This connection makes our experiment an important benchmark for any unitary limited fermion system.

1.1 A brief history of strongly interacting Fermi gas experiments

The laser cooling, magnetic and optical trapping techniques developed for bosonic alkali atoms can also be used for the fermionic species. However, evaporative cooling is inapplicable to single-species Fermi gases due to the lack of s-wave interaction between identical fermions. An additional atomic species or a mixture of hyperfine states needs to be introduced to circumvent this issue. In 1999, the first degenerate Fermi gas was realized by B. DeMarco and D. Jin at JILA [39] with a stable mixture of two hyperfine states of ^{40}K in a magnetic trap. Within the next 4 years, degenerate Fermi gases were realized using sympathetic cooling with ^6Li (by W. Ketterle's group

at MIT [68], R. Hulet’s group at Rice [204], and C. Salomon’s group at ENS [176]) and ^{40}K (M. Inguscio’s group in Florence [167]), and optical trapping of a two states mixture of ^6Li (J. Thomas’ group at Duke [62]).

Feshbach resonances provide a powerful tool to induce tunable, strong interactions in degenerate Fermi gases. The initial signal of Feshbach resonance is observed in the change of elastic collision rate [116, 87, 144], inelastic decay rate [40], and emergence of hydrodynamic evolution [143]. An underlying molecular state is present on the repulsive side of the Feshbach resonance, and is accessible through an adiabatic magnetic field sweep across the Feshbach resonance [165, 37, 85, 194]. In contrast to their counterpart in Bose gases, these molecules consisting of fermionic atoms are long-lived near the Feshbach resonance due to Pauli blocking [153], and can form a stable BEC of repulsive molecules [64, 86, 219, 7]. Fermi gases in the strongly interacting regime are also realized in these experiments as the scattering length a , which also corresponds to the molecular size, is comparable to the interparticle distance $1/k_F$. In this regime, the fermion pairing is a many-body effect and will not show a singularity in thermodynamics when the two-body molecule state vanishes at the Feshbach resonance as $|a| \rightarrow \infty$. Indeed, fermion pair condensations at a Feshbach resonance or on the BCS side are also observed shortly after [220, 163]: the fermion pairs created by the many-body effect are projected into molecules by a rapid magnetic field ramp, and a bimodal distribution is observed in the molecular density profile after time-of-flight expansion.

Though the observation of a molecular condensate after the rapid ramp is consistent with predictions assuming superfluidity, it is not direct evidence of superfluid behavior. The first definitive evidence of superfluidity in the strongly interacting Fermi gas was the observation of a lattice of quantized vortices at MIT [218] as a result of an irrotational flow described by the macroscopic wavefunction. A number of other independent observations of superfluidity were made in the following years. The observation of second sound [184], which is a wave-like entropy propagation mode, confirms the two-fluid hydrodynamics in a strongly interacting Fermi gas: the superfluid and normal components are distinct hydrodynamic fluids and

can oscillate in- or out-of-phase with each other. Josephson oscillations observed in 3D [206] and 2D [121] Fermi gases demonstrated the phase coherence of the macroscopic superfluid wavefunction and that the supercurrent flow is proportional to the phase difference. Other observations of superfluid behavior in strongly interacting Fermi gases include reduced moment of inertia [166], drop of flow resistance [189], observation of solitons in the order parameter [213, 100], and critical velocity for energy dissipation [128, 38, 185].

Measurements of the density profile in a calibrated trapping potential provide the equation of state and phase diagram of the gas in the BEC-BCS crossover. Spin-imbalanced Fermi gases, which emulate fermionic systems under a strong magnetic field, show a phase transition in the density profile [222, 180, 147, 182]: a near spin-balanced superfluid core is formed in the center of the trap, and a spin-polarized normal fluid is present in the outer wings. A Clogston–Chandrasekhar limit of maximum spin polarization for superfluidity is observed [182] and qualitatively consistent with the vanishing vortex lattice in imbalanced systems [222]. The in-situ density profile $n(\mu - V(r), T, a)$ is a direct representation of the equation of state of the strongly interacting Fermi gas [101, 134, 80, 138, 137] and can be used to determine the universal value of all thermodynamic quantities in the unitary limit [73]. The experimentally measured equation of state provides a crucial benchmark for theoretical studies on the properties of strongly interacting fermion systems.

Spectroscopic methods allow measurements of the excitation spectrum of the strongly interacting Fermi gas. Radio-frequency spectroscopy [67, 164, 26, 179, 177, 172] probes the single-particle excitations, by transferring the interacting atoms into a weakly-interacting state or vice versa. A double-peak spectrum measured in [26] was originally considered as evidence of the fermionic pairing gap, but it was later understood as the combined effect of mean-field shift and trap averaging. Later experiments at MIT measured the superfluid gap with rf spectroscopy on a slightly imbalanced spin mixture [172]. rf spectroscopy of atomic impurities immersed in a majority Fermi sea reveals the formation of polaronic quasiparticles [173, 96, 97, 170]. The very weak final state interaction in ^{40}K allows momentum-resolved rf spectroscopy [192].

This technique yields the spectral function $A(\mathbf{k}, \omega)$ and has been used to explore the pseudogap behavior in a strongly interacting Fermi gas [56]. Two-photon Bragg spectroscopy is another powerful tool to probe both single-particle [103, 79, 208] and collective excitations [78, 102], and yields the dynamic structure factor $S(\mathbf{k}, \omega)$.

Beyond the equilibrium properties, the transport properties have also been studied experimentally. The measurements of kinematic viscosity [20] and spin diffusion [187, 188, 6, 98] reveal a quantum-limited diffusivity \hbar/m . A series of experiments on particle and spin transport between two terminals connected by a mesoscopic channel [18, 17, 189] or quantum point contact [99, 84, 108] enable direct comparison with the results in solid-state systems.

1.2 A Uniform trapping potential for Fermi gases

A major shortcoming of the previous Fermi gas experiments is the inhomogeneous trapping potential. In a system with spatially varying density, a large region of the phase diagram is traversed. This prevents a precise measurement of the system at a single point in the phase diagram, for example, the rf response or speed of sound at a given T/T_F . The spatial variation in density also hinders the potential observation of supersolid FFLO state [161, 106, 55], as it is predicted to exist only in a narrow regime in the phase diagram. The lack of translational symmetry also poses a fundamental problem for studies of physics beyond local density approximation, such as measuring the correlation length.

This thesis describes Fermi gas experiments in a uniform trapping potential [131]. Similar to the experimental setup used for Bose gases [58], we tailor blue-detuned laser lights as potential barriers to confine the atoms. Trapped in the dark region of the optical potential, the atoms encounter no light and therefore experience a uniform potential. The experimental realization of the uniform potential will be discussed in Ch. 3. The homogeneous Fermi gas provides an ideal platform for spectroscopic measurements, as the constant Fermi energy E_F , spin polarization n_\downarrow/n_\uparrow , and reduced temperature T/T_F avoid spectral broadening. The translational symmetry of the sys-

tem allows for the observation of dynamical processes with a well-defined wavevector \mathbf{k} , making the system suitable for measuring the speeds of sound or diffusivities in dissipative transport.

1.3 Radio-frequency spectroscopy and quasiparticle breakdown

The fate of quasiparticles in the strongly interacting Fermi gas is of great interest. The thermodynamic and transport properties of many-body systems are closely tied to the energy, and lifetime of the quasiparticle spectrum. Intuitively, the strong interactions at unitarity imply a short mean-free path on the order of the interparticle distance, and thus quasiparticles are likely to be short-lived, with their energy width comparable to the Fermi energy. However, this picture can also be complicated by the spin imbalance and protection against collisions provided by Pauli blocking. rf spectroscopy measures the momentum integrated spectral function, providing a powerful tool for studying the properties of the quasiparticles. The peak position and width of the spectra reflect the energy and decay rate of the quasiparticles. Note the decay rate discussed here should be viewed as the rate of momentum relaxation in a transport measurement [19]. The high-frequency tails of the rf spectra yield the short-range correlation quantified by the contact [15, 175, 8], which also governs the tail of the momentum distribution and the change in energy with scattering length [198, 197].

The temperature dependence of the rf spectra for the unitary Fermi gas is discussed in this thesis. Ch. 4 details our study on a highly spin imbalanced system. We observe a drastic transition from polaronic Fermi liquid at low temperatures to a classical Boltzmann gas, signaled by a quasiparticle breakdown at a temperature close to T_F . We then turn our attention to a spin balanced system in Ch. 5. While the system shares the same Boltzmann gas behavior at high temperature, the spectral width remains on the order of Fermi energy at the lowest temperature we can reach, agreeing with the short-lived quasiparticle picture. More importantly, the knowledge about

the temperature dependence of the rf response can be used as a local thermometer, allowing direct local observation of heat transport in a quantum gas for the first time.

1.4 Thermal transport in a strongly interacting Fermi gas

Thermal transport offers powerful insights into the underlying mechanisms of entropy propagation in any material. In many conventional materials, transport processes involving heat, charge, or spin are directly associated with the motion of free quasiparticles. For strongly correlated systems such as unitary Fermi gases, the notion of well-defined quasiparticles may no longer be valid, and the existence of a superfluid phase further complicates the transport phenomenon. It remains an open question whether there is a common relaxation rate for heat, density, and spin transport. Interestingly, the strong interaction also brings simplicity to the transport problem. The diffusivity for dissipation may be estimated by the mean free path l and the velocity v of the heat carriers: $D \simeq lv$. Strong interaction yields a mean free path on the order of the interparticle distance, and the velocity takes on the Heisenberg-limited value \hbar/ml . This leads to a universal quantum limit \hbar/m for transport processes in strongly interacting systems.

With the rf thermometer, we are able to observe heat transport across the superfluid transition point. Ch. 5 presents the observation of an exotic wave-like entropy propagation called "second sound" in the superfluid phase, as well as the heat diffusion in the normal phase. On both sides of the superfluid phase transition, the measured second sound / thermal diffusivities have a minimum value close to the quantum limit \hbar/m , which is also found for damping of first sound, kinematic viscosity, and spin diffusivity in a unitary Fermi gas. However, the diffusivity of heat transport has unique non-monotonic temperature dependence and displays a peak at the phase transition temperature. The observed diffusivity peak at T_c is in qualitative agreement with the $D_2 \sim |T - T_c|^{-1/3}$ critical behavior indicated by the 3D XY

universality class. This is the first time a critical phenomenon is observed close to the transition temperature in a transport coefficient for quantum gases.

Chapter 2

Strongly interacting Fermi gases

In this chapter, I present the theoretical background for our strongly interacting Fermi gas experiments. I highlight the unique quantum statistics of fermionic systems, which lead to the properties of non-interacting Fermi gases. Next, I turn to the interaction and introduce the powerful tool of Feshbach resonance for tuning the scattering length. The system reaches the scale-invariant unitary limit at the center of the Feshbach resonance, where its thermodynamics functions have a universal form. This allows a direct comparison with other strongly interacting systems with vastly different length scales, such as neutron stars or nuclear matters. Finally, the physics of rf spectroscopy in an interacting system will be discussed.

2.1 Quantum statistics

Quantum mechanics indicates microscopic particles of the same kind are indistinguishable. This concept of identical particles brings an extra constraint on a many-body wavefunction: after swapping two particles, the wavefunction must represent the same quantum state. Let us consider a swapping operator \hat{P}_{ij} that will switch the position of the i th and j th particle in a wavefunction of N identical particles $\psi(q_1, \dots, q_N)$:

$$\hat{P}_{ij}\psi(\dots, q_i, \dots, q_j, \dots) = \psi(\dots, q_j, \dots, q_i, \dots). \quad (2.1)$$

The indistinguishability of particles requires $\hat{P}_{ij}\psi = C\psi$, with C being a constant with a norm of 1. Exchanging the two particles once more naturally leads to the original wavefunction $\psi = \hat{P}_{ij}\hat{P}_{ij}\psi = C^2\psi$. Therefore the only possible value for the exchange factor C is 1 and -1 . Particles with exchange factor $C = 1$ are bosons which follow Bose-Einstein statistics, and particles with exchange factor $C = -1$ are fermions which follow Fermi-Dirac statistics. According to spin-statistics theorem [150], the spins of bosons are integer while the spins of fermions are half-integer (with a unit of Planck constant \hbar). The antisymmetric wavefunction for a fermionic system directly leads to the Pauli exclusion principle. Assuming two fermions in the same quantum state labeled by a generalized coordinate q_0 , swapping these two fermions yields $\psi(\dots, q_0, \dots, q_0, \dots) = -\psi(\dots, q_0, \dots, q_0, \dots) = 0$. Thus no two identical fermions are allowed to occupy the same quantum state.

The quantum statistics of a compound particle will be determined by the number of its fermionic constituents, as swapping two compound particles would be equivalent to swapping all the constituents. A particle consisting of an odd number of fermions is also a fermion while a particle consisting of an even number of fermions is a boson. An example of this change in quantum statistics is two fermions forming a tightly bound bosonic molecule, which will be discussed later in this chapter.

2.2 Ideal Fermi gases

An ideal Fermi gas is an ensemble of many non-interacting identical fermions. The energy state occupation number $f(k)$ in the ideal Fermi gas follows the Fermi-Dirac distribution:

$$f(k) = \frac{1}{e^{(E_k - \mu)/k_B T} + 1}, \quad (2.2)$$

here E_k are energy eigenvalues of single-particle states, and μ is the chemical potential of the system. For a non-relativistic particle with mass m in free space, the energy dispersion is $E(k) = \frac{\hbar k^2}{2m}$. As the Pauli exclusion principle forbids two fermions

occupying the same state, we have $f(k) \leq 1$. In the low-temperature limit $T \rightarrow 0$, all energy states below the chemical potential have unity occupation number, while all the energy states above chemical potential are empty, as shown in fig.2-1(a). The surface in the phase space with an energy equal to the chemical potential is called the Fermi surface. In free space, the Fermi surface is a sphere and its radius is called the Fermi wavevector k_F . The density per spin state at zero temperature can be calculated by merely counting the energy states within the Fermi surface, $n = \int_{k < k_F} \frac{d^3k}{(2\pi)^3} = \frac{k_F^3}{6\pi^2}$. The Fermi wavevector is thus defined as $k_F \equiv (6\pi^2 n)^{1/3}$, and the Fermi energy E_F is the particle energy at $k = k_F$: $E_F \equiv \frac{\hbar^2 k_F^2}{2m}$. For a zero temperature ideal Fermi gas, the chemical potential μ equals the Fermi energy E_F . A Fermi temperature defined as $k_B T_F \equiv E_F$ sets the criteria for Fermi degeneracy: only at $T \ll T_F$ a sharp Fermi surface can be observed. When the temperature is raised close to T_F , the Fermi surface is smeared by thermal excitations and the occupation numbers at low k states are no longer unity. Although the Fermi surface is not sharp at finite temperature or in interacting systems, the Fermi wavevector k_F , energy E_F , and temperature T_F are still relevant scales for quantum effects in many-body systems.

The notion of a sharp Fermi surface is valid globally for homogeneous systems or only locally for inhomogeneous systems. For a zero temperature Fermi gas in a 3D harmonic trap, the Thomas-Fermi approximation can be applied when the center Fermi energy E_{F0} is much larger than the energy spacing of the trap, $E_{F0} \gg \hbar\omega_{x,y,z}$. Within this approximation, the local Fermi energy $E_F(\mathbf{r})$ and density $n(\mathbf{r})$ are $E_F(\mathbf{r}) = E_{F0} - V(\mathbf{r})$ and $n(\mathbf{r}) = \frac{(2m/\hbar^2)^{3/2}(E_{F0}-V(\mathbf{r}))^{3/2}}{6\pi^2}$. The Thomas-Fermi volume is the spatial volume with a non-zero density, and it can be expressed in terms of E_{F0} or total particle number N : $V_{TF} = \frac{4}{3}\pi \left(\frac{E_{F0}}{m\omega_0^2/2}\right)^{3/2} = \frac{4}{3}(6N)^{1/2} \left(\frac{2\hbar}{m\omega_0}\right)^{3/2}$. The varying Fermi energy in a trap will smear the global momentum distribution even at zero temperature, as shown by the red dashed curves in fig.2-1.

The thermodynamic quantities of the ideal Fermi gas can be acquired using the state occupation number in eq.2.2. For example, the number density n and energy

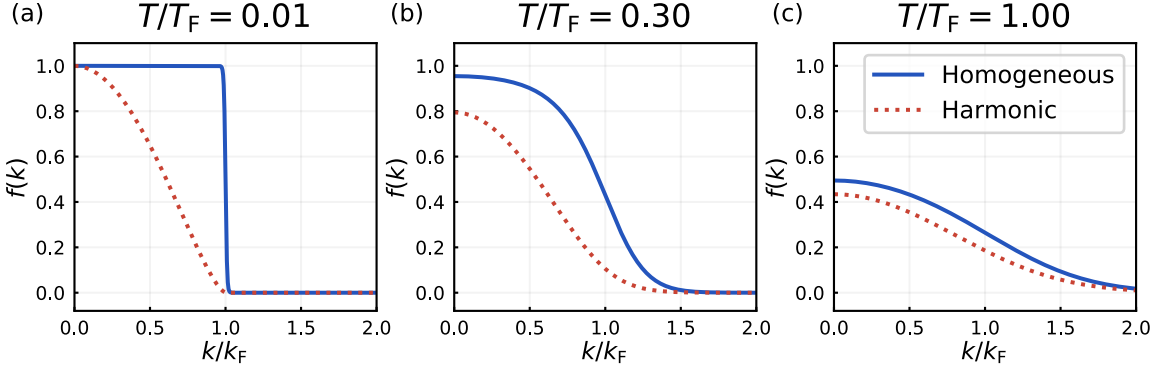


Figure 2-1: Trap averaged momentum distribution of an ideal Fermi gas. The reduced temperature at the center of trap is $T/T_F = 0.01$ (a), 0.30 (b), 1.00 (c), and the corresponding $\mu/k_B = 100$ (a), 3.05 (b), -0.0215 (c). The blue solid curve and the red dashed curve are the trap averaged momentum distribution in a uniform and harmonic trap, respectively. The effective volume used for the harmonic trap is the Thomas-Fermi volume at zero temperature $V_{TF} = \frac{4}{3}(6N)^{1/2}(\frac{2\hbar}{m\omega_0})^{3/2}$.

density ϵ of the system are:

$$n(\mu, T) = \int f(k) \frac{d^3k}{(2\pi)^3} = -\lambda_T^{-3} \text{Li}_{3/2}(-e^{\frac{\mu}{k_B T}}), \quad (2.3)$$

$$\epsilon(\mu, T) = \int E(k) f(k) \frac{d^3k}{(2\pi)^3} = -\frac{k_B T}{\lambda_T^3} \text{Li}_{5/2}(-e^{\frac{\mu}{k_B T}}), \quad (2.4)$$

where $\lambda_T = \sqrt{\frac{2\pi\hbar^2}{mk_B T}}$ is the thermal de Broglie wavelength and Li_s is the polylogarithm function of order s . The quantity $e^{\frac{\mu}{k_B T}} \equiv z$ is the fugacity. The compressibility κ can be calculated using $\kappa = \frac{1}{n^2} \frac{\partial n}{\partial \mu} \Big|_T$.

$$\kappa(\mu, T) = \frac{\lambda_T^3}{k_B T} \frac{-\text{Li}_{1/2}(-e^{\frac{\mu}{k_B T}})}{[-\text{Li}_{3/2}(-e^{\frac{\mu}{k_B T}})]^2} \quad (2.5)$$

From Eq. (2.3), we can get the reduced temperature T/T_F as a function of fugacity

$$\frac{T}{T_F}(z) = \frac{4\pi}{[-6\pi^2 \text{Li}_{3/2}(-z)]^{2/3}}. \quad (2.6)$$

The ideal Fermi gas is a scale invariant system due to a lack of interaction term in the Hamiltonian. A spatial dialation $x \rightarrow \lambda x$ results in a rescaling of Hamiltonian

$H \rightarrow H/\lambda^2$, and the space-time formulation of the Schrodinger equation is invariant under $x \rightarrow \lambda x$ and $t \rightarrow \lambda^2 t$. The only two length scales for the system are the inter-particle distance $l \sim 1/k_F$ and the thermal de Broglie wavelength λ_T . With a dimensional rescaling, all the thermodynamic quantities can be expressed as a universal function of the ratio between the two length scale $\lambda_T k_F$, or more commonly as a function of $T/T_F \sim (k_F \lambda_T)^{-2}$ or fugacity z . The universal form of the chemical potential μ , energy density ϵ , and compressibility κ is shown in fig.2-2. Each quantity is normalized by its value at zero temperature, with $\mu(0) = E_F$, $\epsilon_0 = \frac{3}{5}nE_F$, and $\kappa_0 = \frac{3}{2nE_F}$. The analytical forms of these unitless thermodynamic quantities as a function of z are

$$\frac{\mu}{E_F} = \frac{4\pi \ln z}{[-6\pi^2 \text{Li}_{3/2}(-z)]^{2/3}}, \quad (2.7)$$

$$\frac{\epsilon}{\epsilon_0} = \frac{-10\pi \text{Li}_{5/2}(-z)}{(6\pi^2)^{5/3} [-\text{Li}_{3/2}(-z)]^{2/3}}, \quad (2.8)$$

$$\frac{\kappa}{\kappa_0} = \frac{-(6\pi^2)^{2/3} \text{Li}_{1/2}(-z)}{6\pi [-\text{Li}_{3/2}(-z)]^{1/3}}. \quad (2.9)$$

Their dependence on T/T_F can be calculated numerically using Eq. (2.6). Another useful thermodynamic relation for non-relativistic systems resulted from scale invariance is that pressure $p = \frac{2}{3}\epsilon$ is always proportional to the energy density ϵ . Although the scale invariance seems a trivial conclusion for the ideal Fermi gas, I will later show it is also the case for the unitary Fermi gas, and they share the same form of universal thermodynamic functions.

2.3 Interparticle interactions and Feshbach resonances

Interactions play a leading role in exotic quantum states of fermionic matter from high-temperature superconductivity [109] to fractional quantum hall effect [193]. In this section, I discuss interparticle interactions under the framework of two-body scattering. The interaction Hamiltonian can be expressed as a generalized pseudo-potential characterized by the s-wave scattering length. In our experiment, magnetic

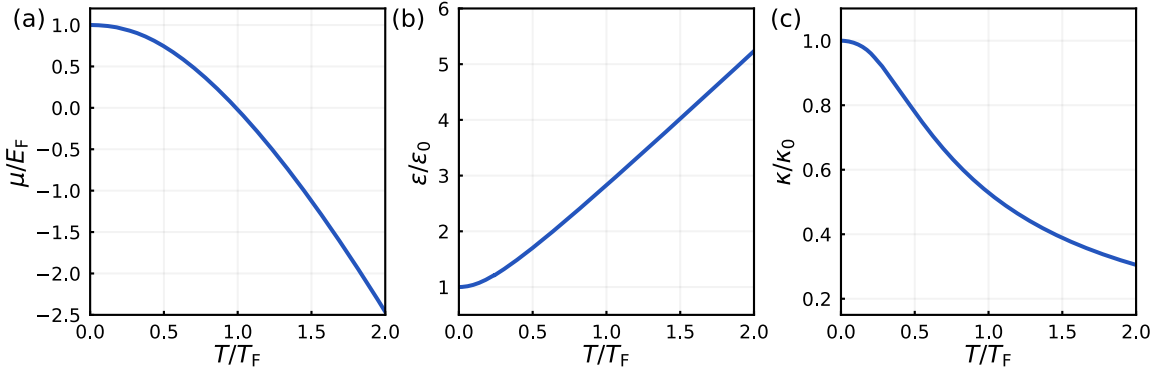


Figure 2-2: Universal Thermodynamics of an ideal Fermi gas. (a) Chemical potential, (b) energy, and (c) compressibility of an ideal Fermi gas.)

Feshbach resonances are used to continuously tune the scattering length, allowing the exploration of Fermi systems at various interaction strengths, especially the strongly interacting unitary regime.

2.3.1 Quantum scattering theory

Microscopically, the interactions in a quantum gas can be described by the interatomic potential $V(r)$. Generally, the atoms experience a strong 'hard-core' repulsion at a distance of a few Bohr radii a_0 due to the Coulomb force between the two electron clouds. At larger distance, the atoms interact with the van der Waals potential $V(r) \simeq -\frac{C_6}{r^6}$. The range of the van der Waals potential is $r_0 \simeq (\frac{mC_6}{\hbar^2})^{1/4} \simeq 2$ nm for ${}^6\text{Li}$, which is much smaller than both the interparticle distance $l \sim 1$ μm or the typical thermal de Broglie wavelengths λ_T (in a degenerate gas $T \lesssim T_F$, $\lambda_T \gtrsim l$). As a result, the detailed shape of the interatomic potential is barely experienced by atoms. The interaction effect can be characterized by the phase shifts and scattering lengths of the two-body scattering events.

The Schrodinger equation for a two particle scattering problem is:

$$\left(-\frac{\hbar^2}{2\mu} \nabla^2 + V(r) \right) \psi(\mathbf{r}) = E \psi(\mathbf{r}). \quad (2.10)$$

Here $\mu = \frac{m_1 m_2}{m_1 + m_2}$ is the reduced mass in the center-of-mass frame. $E = \hbar^2 k^2 / (2\mu)$

is the total energy of the two-body system, and $\hbar k$ is the relative momentum of the two particles far away from the potential center. The asymptote of the scattering wavefunction $\psi(r \rightarrow \infty)$ consists of the incident planer wave $e^{i\mathbf{k} \cdot \mathbf{r}}$ and the scattering part $f(\mathbf{k}', \mathbf{k}) \frac{e^{ikr}}{r}$:

$$\psi(\mathbf{r}) \stackrel{r \rightarrow \infty}{=} e^{i\mathbf{k} \cdot \mathbf{r}} + f(\mathbf{k}', \mathbf{k}) \frac{e^{ikr}}{r}, \quad (2.11)$$

where $f(\mathbf{k}', \mathbf{k})$ is the scattering amplitude into the final state with wavevector $\mathbf{k}' = \frac{\mathbf{r}}{|r|} |k|$. This asymptotic wavefunction obeys Eq.2.10 under the far-field limit $r \rightarrow \infty$ and $V(r) \rightarrow 0$. The scattering amplitude quantifies differential scattering cross section:

$$\frac{d\sigma}{d\Omega} = |f(\mathbf{k}', \mathbf{k})|^2. \quad (2.12)$$

Under an isotropic potential, the scattering wavefunction has a rotational symmetry along the incident direction \mathbf{k} , and the scattering amplitude $f(\mathbf{k}', \mathbf{k})$ is a function of the initial wavenumber k and angle θ between \mathbf{k} and \mathbf{k}' : $f(\theta, k) \equiv f(\mathbf{k}', \mathbf{k})$.

In the quantum scattering problem, the angular momentum of the system is conserved and quantized. The scattering wavefunction can be expanded as a sum of partial waves with fixed total angular momentum $l\hbar$ (in a spherical coordinate system with z-axis aligned with incident \mathbf{k}):

$$\psi(\mathbf{r}) = \sum_{l=0}^{\infty} R_l(kr) Y_{l0}(\theta), \quad (2.13)$$

where Y_{l0} are the spherical harmonics with total momentum $l\hbar$ and $R_l(kr)$ are the corresponding radial wavefunctions. Since the incident beam is a plane wave, the projection of angular momentum along the incident axis is always zero. The eigenvalue equation for $R_l(kr)$ is:

$$\left[-\frac{\hbar^2}{2\mu} \left(\frac{1}{r} \frac{\partial}{\partial r^2} r \right) + l(l+1) \frac{\hbar^2}{2\mu r^2} + V(r) - \frac{\hbar^2 k^2}{2\mu} \right] R_l(r) = 0. \quad (2.14)$$

In the far-field limit, the general solution for Eq.2.14 is:

$$R_l(r) \xrightarrow{r \rightarrow \infty} \frac{B_l}{kr} \sin(kr - \frac{l\pi}{2} + \delta_l), \quad (2.15)$$

where B_l is the expansion coefficient and δ_l is the phase shift of the partial wave. For non-interacting particles, the phase shift δ_l is zero. The spherical harmonic expansion of a plane wave is $e^{ikz} = \sum_l \sqrt{4\pi(2l+1)} i^l \cdot j_l(kr) Y_{l0}(\theta)$, where $j_l(kr)$ are the spherical Bessel functions with asymptotic form $j_l(kr) \simeq \frac{1}{kr} \sin(kr - l\pi/2)$ in the far-field limit. Substituting the Y_{l0} expansion of the plane wave and $R_l(r)$ with their far-field approximation in Eq.2.11 and 2.13 yields the scattering amplitude of each partial wave:

$$f(\theta, k) = \sum_{l=0}^{\infty} f_l(k) P_l(\cos \theta) = \sum_{l=0}^{\infty} \frac{2l+1}{k(\cot \delta_l - i)} P_l(\cos \theta), \quad (2.16)$$

here $P_l(\cos \theta) = \sqrt{\frac{4\pi}{(2l+1)}} Y_{l0}(\theta)$ are the Legendre polynomials. The scattering amplitude of each partial wave is determined by its phase shift δ_l .

When $l > 0$, the scattering particles experience a centrifugal barrier potential $l(l+1)\frac{\hbar^2}{2\mu r^2}$ (see Eq.2.14). For ${}^6\text{Li}$ atoms in the p-wave scattering channel, the barrier potential at the interaction range $r_0 \simeq 2\text{nm}$ is $40 \text{ mK} \cdot k_B$. The centrifugal barrier is much higher than the Fermi energy or temperature we can achieve in an optical trap, which are both on the order of $1 \mu\text{K} \cdot k_B$, or even the Doppler limit for laser cooling at $140 \mu\text{K} \cdot k_B$ for ${}^6\text{Li}$. As a result, atom pairs with non-zero angular momentum are blocked from the short range interaction by the centrifugal barrier in our experiments, while the inter-atomic scattering is dominated by the s-wave channel.

The s-wave scattering amplitude is isotropic and only a function of k :

$$f_s(k) = \frac{1}{k \cot \delta_s - ik}. \quad (2.17)$$

In the zero-momentum limit, $k \cot \delta_s$ provides the definition of the scattering length: $\lim_{k \rightarrow 0} k \cot \delta_s = -1/a$. With a finite k , time-reversal symmetry requires that $k \cot \delta_s$ is an even function of k . The low momenta expansion of $k \cot \delta_s$ is $k \cot \delta_s = -\frac{1}{a} + \frac{r_{\text{eff}} k^2}{2}$, which also defines the effective range r_{eff} of the interaction potential. Numerical [35,

123, 36] and analytical [57, 50] calculations for van der Waals potential have shown r_{eff} is on the same order of r_0 . The scattering amplitude can be expressed by a and r_{eff} :

$$f(k) = \frac{1}{-\frac{1}{a} - ik + \frac{r_{\text{eff}}k^2}{2}}. \quad (2.18)$$

In our experiments, the de Broglie wavelength of the atoms is much larger than the interaction range, thus we have $k \ll 1/r_{\text{eff}}$ and $\frac{r_{\text{eff}}k^2}{2} \ll k$. In the limit $|1/a| \gg k$ or $k|a| \ll 1$, the scattering amplitude $f \simeq -a$ is k independent. In the limit $|1/a| \ll k$ or $k|a| \gg 1$, the scattering amplitude is $f \simeq \frac{i}{k}$ and the scattering cross section is $\sigma = \frac{4\pi}{k^2}$. This is the so-called unitary limit when the scattering length diverges.

Quantum statistics also play an important role for the scattering problem. The full scattering wavefunction can be divided into the spatial and the spin wavefunction: $\Psi = \psi(\mathbf{r}) \otimes \chi(s_1, s_2)$. Swapping the two particles will invert the spatial part of the two-body wavefunction: $\psi(\mathbf{r}) \rightarrow \psi(-\mathbf{r})$. The spatial wavefunctions with even l are symmetric under spatial inversion $\psi(\mathbf{r}) = \psi(-\mathbf{r})$, while the spatial wavefunctions with odd l are antisymmetric $\psi(\mathbf{r}) = -\psi(-\mathbf{r})$. Therefore, two identical fermions can not undergo s-wave scattering. A spin polarized Fermi gas is thus a pristine example of non-interacting Fermi gas: quantum statistics forbid s-wave scattering, and the energy of the particles are not high enough to overcome the centrifugal barrier. When the two scattering atoms are in different internal states, which can be labeled as two pseudo-spin states $|\uparrow\rangle$ and $|\downarrow\rangle$. The s-wave scattering is allowed for both fermions and bosons. For fermions it requires the singlet spin state $\chi(s_1, s_2) = (|\uparrow_1\rangle|\downarrow_2\rangle - |\downarrow_1\rangle|\uparrow_2\rangle)/\sqrt{2}$, while for bosons it requires the triplet state $\chi(s_1, s_2) = (|\uparrow_1\rangle|\downarrow_2\rangle + |\downarrow_1\rangle|\uparrow_2\rangle)/\sqrt{2}$.

2.3.2 Pseudo-potential

Since the scattering process can be characterized by the s-wave scattering length a , a generalized short range pseudo-potential can be used to replace the complicated interatomic potential to simplify the many-body Hamiltonian. The new pesudo-potential needs to preserve the two-body scattering amplitude $f(k) \simeq \frac{1}{-1/a - ik}$. A delta function

$g\delta(\mathbf{r})$ [92] can be used as a generalized pesudo-potential, with

$$\frac{1}{g} = \frac{m}{4\pi\hbar^2 a} - \frac{m}{\hbar^2} \int \frac{d^3 q}{(2\pi)^3} \frac{1}{q^2}. \quad (2.19)$$

Though the summation over momentum states in the second term of $1/g$ diverges, a high momentum cut-off at $q_c = 1/R$ can be applied to suppress the divergence. A cut-off length close to the effective range $R = \frac{4}{\pi}r_{\text{eff}}$ will conserve the low-momenta expansion of $1/f = -\frac{1}{a} - ik + \frac{r_{\text{eff}}k^2}{2}$. When calculating physical quantities in a quantum gas, we will find the cut-off value irrelevant to the final results, as the corresponding momentum scale $1/R$ is much higher than all the other momentum scales in the system. In Sec. 4.1.1, we will calculate the energy of a spin impurity immersed in a majority Fermi gas using the delta pseudo-potential, and we will realize that the divergence in Eq. (2.19) will be canceled by a summation over possible final states after scattering. For a two-state mixture of fermions, the delta interaction potential can be rewritten in a second quantized form as

$$\hat{V}_{\text{int}} = \frac{g}{V} \sum_{\mathbf{k}, \mathbf{k}', \mathbf{q}} a_{\mathbf{k}+\mathbf{q}, \uparrow}^\dagger a_{\mathbf{k}'-\mathbf{q}, \downarrow}^\dagger a_{\mathbf{k}, \uparrow} a_{\mathbf{k}', \downarrow}, \quad (2.20)$$

where V is the quantization volume.

Another choice for the pseudo-potential is [81]:

$$V_{\text{int}}(\mathbf{r})\psi(\mathbf{r}) = g\delta(\mathbf{r}) \frac{\partial}{\partial r}(r\psi(\mathbf{r})). \quad (2.21)$$

This potential leads to a scattering amplitude of $f(k) = \frac{1}{-1/a - ik}$ with $g = \frac{4\pi\hbar^2 a}{m}$.

2.3.3 Feshbach resonances

Feshbach resonances provide a powerful tool to control the scattering length of a system, allowing the access of the unitary interaction regime where $k_F|a| \rightarrow \infty$. A schematic of the physics of Feshbach resonances is illustrated in Fig.2-3(a). When the two scattering atoms approach each other, they are in the open channel with an

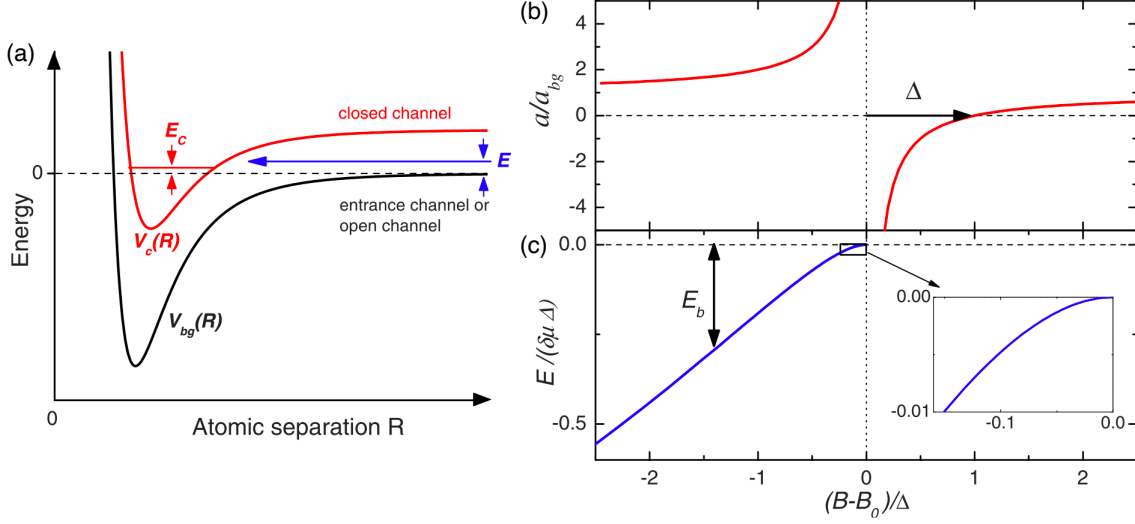


Figure 2-3: Schematic of a Feshbach resonance. (a) Scattering particles in the open channel are coupled with a bound state in a closed channel. A magnetic field can be used to tune the relative energy between the two channels. (b) The scattering length diverges at the Feshbach resonance where the bound state energy is close to zero. (c) Energy of the Feshbach molecule state, where $\delta\mu$ is the difference in magnetic moments between the two scattering channels. The inset shows the binding energy scale as $E_b \sim (B - B_0)^2 \sim a^{-2}$ in the universal regime where a is very large. This figure is taken from Ref. [28].

energy E only slightly above zero. A closed scattering channel with an asymptotic potential energy larger than E can exist for atoms in different internal states. Though energy conservation forbids incident atoms from scattering into the closed channel in the far field, the hyperfine interaction couples the two channels at short range. The Feshbach resonance arises when the energy of a bound state in the closed channel is tuned close to zero, resulting in a greatly altered scattering length. When the total magnetic momentum in the two channels are different, a magnetic field \mathbf{B} can be used to shift the relative energy of the bound state E_c close to zero, this scenario is called a *magnetic Feshbach resonance*. The scattering length a near the resonance is:

$$a(B) = a_{bg} \left(1 - \frac{\Delta B}{B - B_0}\right), \quad (2.22)$$

where B_0 is the center of resonance, ΔB the width of resonance, and a_{bg} the background scattering length [Fig.2-3(b)]. A bound molecule state emerges on one side of the Feshbach resonance where $a > 0$ [Fig.2-3(c)]. Close to the resonance with

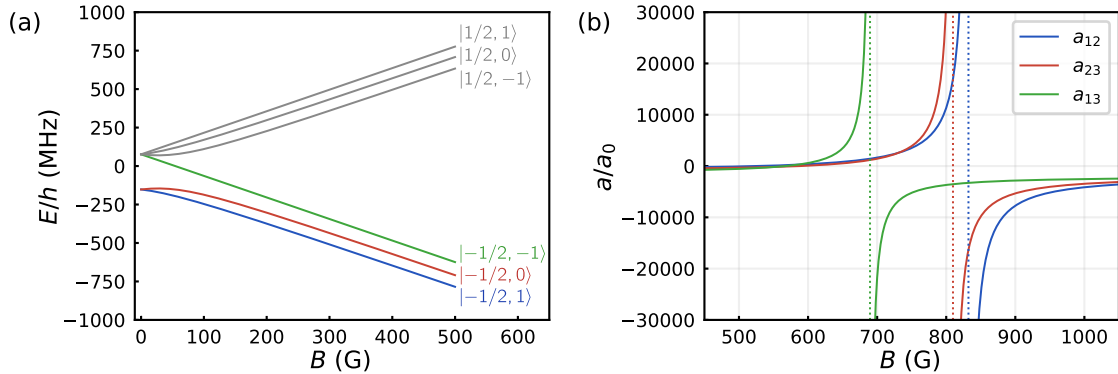


Figure 2-4: Feshbach resonances of ${}^6\text{Li}$ in the ground state manifold. (a) The energy levels of ground state ${}^6\text{Li}$, labeled by $|m_S, m_I\rangle$. (b) S-wave scattering length between the three lowest energy states. A very narrow resonance in a_{12} at 543 G is omitted in this plot.

$|B - B_0| \ll \Delta$, the molecular energy is $E_m = \frac{\hbar^2}{ma^2}$, and the radius of molecule is a .

The spatial wavefunction of a Feshbach molecule is:

$$\phi_m(\mathbf{r}) = \sqrt{\frac{1}{2\pi a}} \frac{e^{-r/a}}{r}. \quad (2.23)$$

The results in Eq. (2.22) and (2.23) can be derived by considering two coupled spherical well potentials [27, 28].

Three broad Feshbach resonances exist for each pair of the three lowest hyperfine states in ${}^6\text{Li}$, which are labeled as state $|1\rangle$, $|2\rangle$, and $|3\rangle$ in the order of increasing energy. In a magnetic field $B \gtrsim 200$ G, the coupling between the electron spin and the external field is larger than the hyperfine splitting, so the energy eigenstates can be labeled with the projection of electron and nuclear spin $|m_S, m_I\rangle$ [Fig. 2-4(a)]. The three lowest states all have electron spin antialigned with the magnetic field. The open channel is thus in the electron spin triplet state, while the closed channel is in the singlet state. The landscape of Feshbach resonances between the three lowest energy states is shown in Fig. 2-4(b), the exact positions of resonances are measured via precision molecular dissociation spectroscopy in Ref [216]. The choice of state mixture in our experiment is relevant for radio-frequency spectroscopy experiments, where an atom is transferred from a strongly interacting mixture to a third state.

States	B_0 (G)	Δ (G)	a_{bg} (a_0)	Final State interaction
$ 1\rangle + 2\rangle$	832.18	-262.3	-1582	$a_{23} = -16305 a_0$ $a_{13} = -3271 a_0$
$ 2\rangle + 3\rangle$	809.76	-200.2	-1642	$a_{13} = 16986 a_0$ $a_{13} = -3532 a_0$
$ 1\rangle + 3\rangle$	689.68	-166.6	-1770	$a_{12} = 1417 a_0$ $a_{23} = 1170 a_0$

Table 2.1: Properties of Feshbach Reonances measured in Ref. [216].

A low final state interaction is desirable to highlight the signal from the interaction in the initial state and to avoid three-body losses after rf transfer. The final state interaction at each resonance is listed in Tab. 2.1. The (1,3) mixture appears to be the best choice for rf spectroscopy experiments as it features small final state interaction and allows both $1 \rightarrow 2$ and $3 \rightarrow 2$ transition with a single photon.

2.4 Unitary Fermi gas

At the Feshbach resonance, the scattering length diverges and the absolute value of the scattering amplitude reaches its maximum $|f(k)| = \frac{1}{k^2}$. This is the so called unitary limit where scattering becomes as strong as quantum mechanics allows. The two-body scattering cross section is $\sigma = \frac{4\pi}{k^2}$ under this limit. In a unitary Fermi gas, the characteristic momentum scale is $k_F \sim n^{1/3}$ and proportional to the inverse interparticle distance. The mean free path $\bar{l} = 1/n\sigma \sim n^{-1/3}$ is then on the order of one interparticle distance. This strongly interacting system is often referred to as a "perfect fluid". A unitary gas is a scale invariant system. as a result all its physical properties can be expressed with universal functions of the reduced temperature T/T_F or chemical potential $\mu/k_B T$.

2.4.1 Scale invariance

With a diverging scattering length, there is no longer a relevant length scale to describe the interaction of the system. To demonstrate the scale invariance of the many-

body Hamiltonian [22], we can start with the interaction Hamiltonian in Eq.2.21. The eigenvalue equation for the many-body state is:

$$\left[-\frac{\hbar^2}{2m} \sum_i \nabla_{\mathbf{r}_i}^2 + \sum_{i,j} g\delta(\mathbf{r}_{ij}) \frac{\partial}{\partial \mathbf{r}_{\mathbf{r}_j}} r_{rj} \right] \psi = E\psi, \quad (2.24)$$

where $\mathbf{r}_{ij} \equiv \mathbf{r}_i - \mathbf{r}_j$ is the relative position between two particles, and $g = \frac{4\pi\hbar^2 a}{m}$ the coupling constant. In the short range limit $r_{ij} \rightarrow 0$ for any particle pair (i, j) , the delta interaction must be canceled out by the kinetic energy to ensure a finite total energy. This boundary condition leads to two possibilities: (1) $\lim_{r_{ij} \rightarrow 0} \psi(\mathbf{r}_{ij}, \dots) = O(r_{ij})$, so the interaction term is zero; or (2) $\lim_{r_{ij} \rightarrow 0} \psi(\mathbf{r}_{ij}, \dots) = \frac{1}{r_{ij}} - \frac{1}{a}$, so the delta function in the interaction term will be canceled out using $\nabla^2(1/r) = -4\pi\delta(r)$. The general form of the wavefunction fulfilling these two condition is

$$\psi(\mathbf{r}_1, \dots, \mathbf{r}_N) = A_{i,j}(\mathbf{R}_{i,j}; \{\mathbf{r}_k, k \neq i \text{ or } j\}) \left(\frac{1}{r_{ij}} - \frac{1}{a} \right) + O(r_{ij}), \quad (2.25)$$

here $\mathbf{R}_{i,j}$ is the center of mass coordination of the pair (i, j) . This is the so called Wigner-Bethe-Peierls contact boundary condition. The short range interaction is exactly canceled by kinetic energy of the relative motion of pair (i, j) :

$$\left[-\frac{\hbar^2}{m} \nabla_{\mathbf{r}_{ij}}^2 + g\delta(\mathbf{r}_{ij}) \frac{\partial}{\partial \mathbf{r}_{\mathbf{r}_j}} r_{rj} \right] A_{i,j}(\mathbf{R}_{i,j}; \{\mathbf{r}_k, k \neq i \text{ or } j\}) \left(\frac{1}{r_{ij}} - \frac{1}{a} \right) = 0. \quad (2.26)$$

After fixing the short range wavefunction in Eq. (2.25), the left hand side of Eq. 2.24 can be simplified to the "principle part" of the kinetic energy, that is the kinetic energy operator only acting on the non-singular part of the wavefunction. The eigenvalue equation becomes

$$-\frac{\hbar^2}{2m} \sum_i \nabla_{\mathbf{r}_i}^2 \psi = E\psi \quad (\text{at } r_{ij} > 0), \text{ or} \quad (2.27)$$

$$-\frac{\hbar^2}{2m} \sum_i \nabla_{\mathbf{r}_i}^2 \psi + \sum_{i,j} \left[\frac{\hbar^2}{m} \nabla_{\mathbf{r}_{ij}}^2 A_{i,j}(\mathbf{R}_{i,j}; \{\mathbf{r}_k, k \neq i \text{ or } j\}) \left(\frac{1}{r_{ij}} - \frac{1}{a} \right) \right] = E\psi. \quad (2.28)$$

With a rescaling of coordinate $\mathbf{r} \rightarrow \lambda\mathbf{r}$, the transformed wavefunction is

$$\psi_\lambda(\mathbf{r}_1, \dots, \mathbf{r}_N) = \frac{1}{\lambda^{3/2}} \psi(\mathbf{r}_1/\lambda, \dots, \mathbf{r}_N/\lambda). \quad (2.29)$$

At the unitary limit $a \rightarrow \infty$, the transformed wavefunction will still fulfill the boundary condition in Eq. 2.25, as well as the eigenvalue equation in Eq. 2.28 with a transform in energy $E_\lambda \rightarrow E/\lambda^2$. Thus, the Schrodiner equation describing a unitary gas is invariant under the transformation $\{\mathbf{r} \rightarrow \lambda\mathbf{r}, H \rightarrow H/\lambda^2\}$ or $\{\mathbf{r} \rightarrow \lambda\mathbf{r}, t \rightarrow \lambda^2t\}$. This is the same case as ideal Fermi gas. With a finite value of a , the Hamiltonian is no longer scale invariant. However, the transformed wavefunction will still be the solution of the Hamiltonian with a rescaled scattering length $H(a) \rightarrow H(\lambda a)/\lambda^2$.

2.4.2 Universal thermodynamics of unitary Fermi gases

Thanks to the scale invariance, the thermodynamics of unitary Fermi gases can be described by a universal function that is unitless¹. At zero temperature, the only length scale is the interparticle distance $n^{-1/3}$. The energy of the system scales as $E \sim n^{2/3}$, while both the energy density ϵ and pressure P scale as $n^{5/3}$. The compressibility $\kappa = \frac{1}{n} \frac{\partial n}{\partial P}$ scale as $\kappa \sim n^{-5/3}$. The property of the ground state unitary Fermi gas thus can be determined by a single number, such as the ratio between its chemical potential and energy. This quantity is the so called Bertsch factor ξ [60], which is also relevant to the ground state energy of nuclear matter or the dilute crest of neutron star. Its value has been measured at MIT to be $\xi = 0.37(1)$ [101]. A list of thermodynamic quantities at $T = 0$ for both unitary and ideal Fermi gas is shown in Tab. 2.2.

For a unitary system at finite temperature, the overall shape of the energy spectrum and state occupation does not change with a spatial rescaling. As a result, the total entropy of the system is invariant. For a closed microcanonical ensemble, the temperature of the system is defined as the derivative of energy with respect to

¹This is of course only valid when the interparticle spacing is still much larger than the effective interaction range.

	Unitary	Ideal
Chemical potential	$\mu = \xi E_F$	$\mu = E_F$
Energy	$E = \xi \cdot \frac{3}{5} N E_F$	$E = \frac{3}{5} N E_F$
Energy density	$\epsilon = \xi \cdot \frac{3}{5} n E_F$	$\epsilon = \frac{3}{5} n E_F$
Pressure	$P = \xi \cdot \frac{2}{5} n E_F$	$P = \frac{2}{5} n E_F$
Compressibility	$\kappa = \frac{3}{2\xi} \frac{1}{n E_F}$	$\kappa = \frac{3}{2} \frac{1}{n E_F}$

Table 2.2: Properties of Unitary Fermi gas and ideal Fermi gas at $T = 0$

entropy $T = \frac{\partial E}{\partial S}$, and shares the same scaling factor with the energy $T \sim E \sim n^{2/3}$. Thus unitless quantities like reduced temperature $\frac{T}{T_F}$ or chemical potential $\frac{\mu}{k_B T}$ are scale invariant, and can serve as the independent variable for the equation of state. These variables quantifies ratio between the two remaining length scales in the system: the interparticle distance and the de Broglie wave length. For a spin balanced system, the thermodynamic quantities such as energy density ϵ , chemical potential μ , or specific heat C_V can all be expressed with a universal function and respective normalizing factors:

$$\epsilon = \tilde{\epsilon} \left(\frac{T}{T_F} \right) \cdot \frac{3}{5} n E_F, \quad (2.30)$$

$$\mu = \tilde{\mu} \left(\frac{T}{T_F} \right) \cdot E_F, \quad (2.31)$$

$$C_V = \tilde{C}_V \left(\frac{T}{T_F} \right) \cdot N k_B. \quad (2.32)$$

A very useful relation for pressure P and energy density ϵ in the unitary Fermi gas is $P = \frac{2}{3}\epsilon$, which is identical to the case in ideal Fermi gases. This relation is independent of the spin polarization. In order to prove this, we can assume the universal pressure $\tilde{P}(\tilde{\mu}_\uparrow, \tilde{\mu}_\downarrow)$ as a function of chemical potentials of the two spin states, with $\tilde{\mu}_\sigma = \frac{\mu_\sigma}{k_B T}$. Instead of interparticle distance, we use the de Broglie wave length $\lambda_T = \sqrt{\frac{2\pi\hbar^2}{mk_B T}}$ as the normalization factor:

$$P = \frac{\mu_\uparrow + \mu_\downarrow}{\lambda_T^3} \cdot \tilde{P}\left(\frac{\mu_\uparrow}{k_B T}, \frac{\mu_\downarrow}{k_B T}\right). \quad (2.33)$$

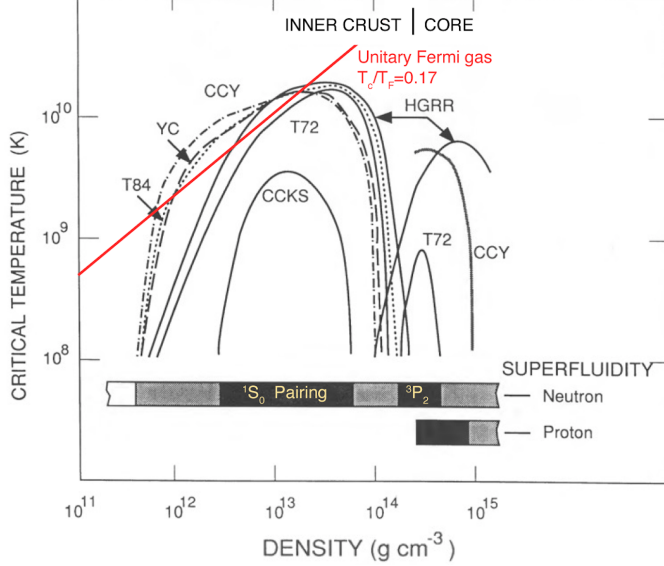


Figure 2-5: The critical temperature for neutron matter in a neutron star predicted by various theoretical methods. The superfluid phase arises from s-wave pairing in the crust of neutron star and p-wave pairing in the core. In the s-wave pairing regime, the critical temperature is quantitatively consistent with the measured $T_c = 0.17(1)T_F$ (the red line) in unitary Fermi gases [101]. The critical temperature for neutron star is taken from Ref. [45].

The density of each spin state can be acquired from $n_\sigma = \frac{\partial P}{\partial \mu_\sigma} \Big|_T$, while the entropy density s is $\frac{\partial P}{\partial T} \Big|_\mu$:

$$n_\sigma = \frac{1}{\lambda_T^3} \cdot \tilde{P}\left(\frac{\mu_\uparrow}{k_B T}, \frac{\mu_\downarrow}{k_B T}\right) + \frac{\mu_\uparrow + \mu_\downarrow}{\lambda_T^3} \cdot \frac{\partial}{\partial \tilde{\mu}_\sigma} \tilde{P}\left(\frac{\mu_\uparrow}{k_B T}, \frac{\mu_\downarrow}{k_B T}\right) \frac{1}{k_B} \quad (2.34)$$

$$s = \frac{3(\mu_\uparrow + \mu_\downarrow)}{T \lambda_T^3} \cdot \tilde{P}\left(\frac{\mu_\uparrow}{k_B T}, \frac{\mu_\downarrow}{k_B T}\right) - \frac{\mu_\uparrow + \mu_\downarrow}{\lambda_T^3} \left[\frac{\mu_\uparrow}{k_B T^2} \frac{\partial}{\partial \tilde{\mu}_\uparrow} \tilde{P}\left(\frac{\mu_\uparrow}{k_B T}, \frac{\mu_\downarrow}{k_B T}\right) + \frac{\mu_\downarrow}{k_B T^2} \frac{\partial}{\partial \tilde{\mu}_\downarrow} \tilde{P}\left(\frac{\mu_\uparrow}{k_B T}, \frac{\mu_\downarrow}{k_B T}\right) \right] \quad (2.35)$$

The energy density of system can be calculated using the density of Gibbs free energy $G/V = \mu_\uparrow n_\uparrow + \mu_\downarrow n_\downarrow$:

$$\begin{aligned} \epsilon &= \mu_\uparrow n_\uparrow + \mu_\downarrow n_\downarrow + Ts - P \\ &= \frac{3}{2} \frac{\mu_\uparrow + \mu_\downarrow}{\lambda_T^3} \cdot \tilde{P}\left(\frac{\mu_\uparrow}{k_B T}, \frac{\mu_\downarrow}{k_B T}\right). \end{aligned} \quad (2.36)$$

Comparing Eq. 2.33 and 2.36, we get $P = \frac{2}{3}\epsilon$.

The universality of the unitary Fermi gas means that the experimental result of ultracold gases can be directly compared with other strongly correlated systems. An interesting example is the dilute neutron matter in the crust of neutron stars. At a density of about $\rho \sim 10^{13} \text{ g/cm}^{-3}$, the neutron-neutron interaction is dominated by s-wave scattering with a scattering length of $a = 19 \mu\text{m}$ much larger than the interparticle distance of $\sim 1 \mu\text{m}$. The near-unitary neutron matter thus has thermodynamic properties similar to those of unitary Fermi gases, such as the superfluid critical temperature as shown in Fig. 2-5, though having a density difference of 25 orders of magnitude. Therefore quantum gas experiments provide an accessible benchmark for many-body theories on strongly interacting fermions with vastly different length scales including neutron stars, nuclei, and quark-gluon plasma.

2.5 rf spectroscopy of interacting Fermi gases

rf spectroscopy provides a powerful tool to probe the single particle excitations in the strongly interacting Fermi gas, as illustrated in Fig. 2-6. Thanks to the hyperfine structure in the ground state atoms, the interacting pseudo-spin states can be transferred to a non- or weakly- interacting state with a single rf photon (or vice versa). This is impossible in a condensed matter system due to the lack of degrees of freedom in the internal states of electrons. The rf spectroscopy that sends atoms out-of or into the interacting states are called *ejection* or *injection* spectroscopy, respectively. In this thesis I focus on the ejection spectroscopy.

For a cosinusoidal oscillating magnetic field $\mathbf{B}(t) = \mathbf{B}_0 \cos(\omega t)$, the quantum operator of the rf coupling \hat{V}_{rf} between state i and state j can be expressed as:

$$\hat{V}_{\text{rf}}(\omega) = \hbar \Omega_R \int d^3r [\psi_j^\dagger(\mathbf{r}) \psi_i(\mathbf{r}) + \psi_i^\dagger(\mathbf{r}) \psi_j(\mathbf{r})] \cos(\omega t), \quad (2.37)$$

here $\Omega_R = \langle j | \mathbf{B}_0 | i \rangle$ is the Rabi frequency, and $\psi_{i,j}(\mathbf{r})$ is the annihilation operator of state i, j . In our experiment, an rf frequency of 80 MHz is used to transferred the atoms in or out of the strongly interacting state. Because both the rf wavelength

(~ 4 m) and the size of the antenna (~ 10 cm) are much larger than the size of the atomic cloud (~ 0.1 mm), the Rabi frequency can be considered spatially uniform and the rf transfer will not alter the momentum of atoms. Therefore, the creation and annihilation operators can also be expressed in momentum space. Since the rf frequency is much higher than any other frequency (energy) scale in the probed system, such as detuning or Fermi energy, the rotating wave approximation can be applied. Assuming the energy of state j is higher than that of state i , the coupling Hamiltonian is:

$$\hat{V}_{\text{rf}}(\omega) = \frac{\hbar\Omega_{\text{R}}}{2} \sum_k \left[c_{\mathbf{k},j}^\dagger c_{\mathbf{k},i} e^{-i\omega t} + c_{\mathbf{k},i}^\dagger c_{\mathbf{k},j} e^{i\omega t} \right]. \quad (2.38)$$

For a single atom initially in $|i\rangle$ at $t = 0$ under a resonant rf coupling, the probability that the atom is in the final state at time t is $\frac{1-\cos(\Omega_R t)}{2}$.

In the co-rotating frame of the rf field, the coupling Hamiltonian is time independent:

$$\hat{V}_{\text{rf}} = \frac{\hbar\Omega_{\text{R}}}{2} \sum_k [c_{\mathbf{k},j}^\dagger c_{\mathbf{k},i} + c_{\mathbf{k},i}^\dagger c_{\mathbf{k},j}]. \quad (2.39)$$

The rf transfer rate $\Gamma(\omega) = N_f/T_{\text{pulse}}$ of particle leaving the initial many-body state $|\psi_{MB}\rangle$ and arriving in the final energy eigenstate $|f\rangle$, can be calculated by Fermi's golden rule:

$$\Gamma(\omega) = \frac{2\pi}{\hbar} \sum_f |\langle f | \hat{V}_{\text{rf}} | \psi_{MB} \rangle|^2 \delta(\hbar\omega - E_f + E_i), \quad (2.40)$$

where E_f and E_i are the energies of the final and initial state. Under this definition, the total atom number arriving in the final state after a pulse with duration t is $\Gamma(\omega)t$ (assuming transferred atom number is still negligible compared to the total number). The integral of the rf spectrum yields the total atom number in the initial state $|i\rangle$:

$$\begin{aligned} \int_{-\infty}^{\infty} \Gamma(\omega) d\omega &= \int_{-\infty}^{\infty} \frac{2\pi}{\hbar} \sum_f |\langle f | \hat{V}_{\text{rf}} | \psi_{MB} \rangle|^2 \delta(\hbar\omega - E_f + E_i) d\omega \\ &= \frac{\pi\Omega_{\text{R}}^2}{2} N_i. \end{aligned} \quad (2.41)$$

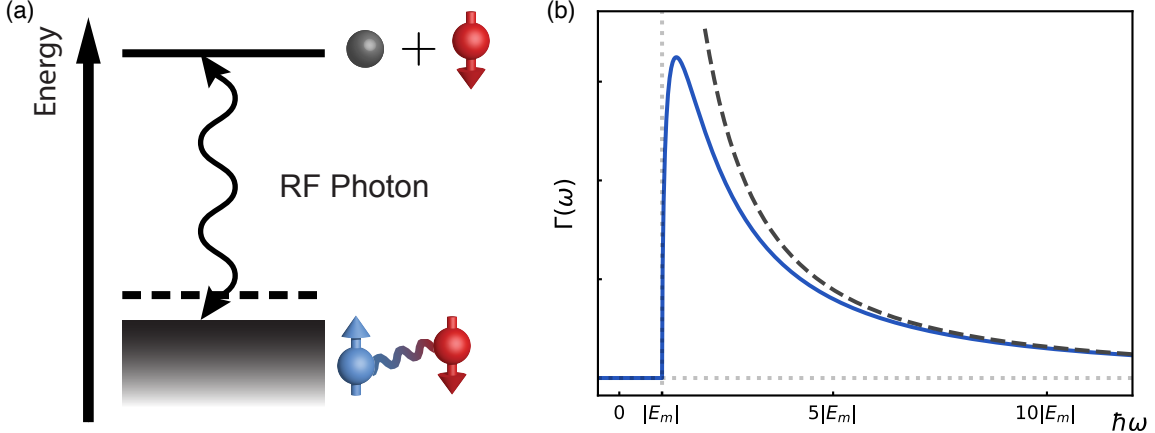


Figure 2-6: (a) A schematic of rf spectroscopy. An rf photon converts one of the initial interacting spin states (blue and red spins) to a non-interacting state (grey). (b) Molecular dissociation spectrum (blue solid line), calculated using Eq. 2.43. The black dashed line is the $\omega^{-3/2}$ contact wing at high detuning.

Note when the initial many-body state is a two state mixture, for example the mixture of state $|1\rangle$ and $|3\rangle$, and the rf pulse couples $|1\rangle$ and final state $|2\rangle$, $N_i = N_1$ is the total atom number in the coupled spin state $|1\rangle$.

2.5.1 Molecular dissociation spectrum: a simple example

A simple yet crucial application for the rf spectroscopy is the single molecular dissociation spectrum. This experiment provides the initial evidence of stable molecules on the BEC side [165] of the crossover, and the onset of the spectra provides a precision measurement of the molecular binding state as well as the exact position of the Feshbach resonance [216]. In the universal regime, we can assume a molecule wavefunction $\phi_m(r) = \sqrt{\frac{1}{2\pi a}} e^{-r/a}/r$. Here $\mathbf{r} = \mathbf{r}_1 - \mathbf{r}_2$ is the relative position of the two constituents, a is the scattering length, and the wavefunction is defined in the center of mass frame. The wavefunction of the molecule in the momentum space would be:

$$\phi_m(\mathbf{k}) = \langle \mathbf{k} | \phi_m \rangle = \int d\mathbf{r}^3 \frac{1}{\sqrt{V}} e^{-i\mathbf{k}\cdot\mathbf{r}} \frac{1}{\sqrt{2\pi a}} e^{-r/a}/r = \frac{2}{(1 + a^2 k^2)} \sqrt{\frac{2\pi a^3}{V}}, \quad (2.42)$$

where \mathbf{k} is the relative momentum and V is the quantization volume. We assume a bound to free transition is driven with an rf pulse, the two atoms composing the

molecule is initially at state $|1\rangle$ and state $|3\rangle$, the rf pulse couples state 1 and 2. We also assume there is no final state interaction, so also no bound state in the final state. The energy of the initial molecule is $E_m = -\frac{\hbar}{ma^2}$, while the total energy of the remnants is $E_f = \frac{\hbar^2 k^2}{m}$ (the reduced mass in center of mass frame is $m/2$). Fermi's golden rule gives the rf transfer rate:

$$\begin{aligned}\Gamma(\omega) &= \frac{2\pi}{\hbar} \sum_k |\langle \mathbf{k}, 2 | \hat{V}_{\text{rf}} | \phi_{m,13} \rangle|^2 \delta\left(\hbar\omega - \frac{\hbar^2 k^2}{m} - \frac{\hbar}{ma^2}\right) \\ &= \hbar \Omega_R^2 \left(\frac{\hbar^2}{ma^2} \right)^{1/2} \frac{\sqrt{\hbar\omega - |E_m|}}{(\hbar\omega)^2},\end{aligned}\quad (2.43)$$

where ω is the frequency detuning from the bare atomic transition frequency. The shape of a molecular dissociation spectrum is shown in Fig. 2-6. The molecular binding energy sets the onset of the rf spectrum. The sum rule we get from the single molecule dissociation spectrum is:

$$\int_{-\infty}^{+\infty} \Gamma(\omega) d\omega = \int_0^{+\infty} \hbar \Omega_R^2 E_B^{1/2} \frac{\sqrt{\hbar\omega - |E_m|}}{(\hbar\omega)^2} d\omega = \frac{\pi \Omega_R^2}{2}. \quad (2.44)$$

This result is consistent with Eq.2.41 at the single particle limit $N_1 = 1$.

2.5.2 Two body contact and the rf tail

In Sec. 2.4.1, it is shown that the many-body wavefunction takes the form of $\psi(\mathbf{r}_{ij}) \sim \left(\frac{1}{r_{ij}} - \frac{1}{a}\right)$ when two particles are in close proximity. A Fourier transform of this short range interaction leads to a wavefunction in momentum space $\psi(\mathbf{k}) \sim k^{-2}$, and momentum distribution $n(k) \sim k^{-4}$ in large momentum limit. A quantity called the *contact* C is used to characterize the weight of this high momentum tail:

$$C \equiv \lim_{k \rightarrow \infty} n_\sigma(k) k^4. \quad (2.45)$$

Here $n_\sigma(k)$ is defined under a given volume, for one spin component in the system. The atom number of one spin species σ in momentum range $[k, k + dk]$ would be $4\pi k^2 n(k) dk / (2\pi)^3$. The total number of fermions (of both spin states) with momenta

larger than K ($K \gg k_F$) in a balanced two-spin system will be $N_{k>K} = \frac{C}{\pi^2 K}$. A simple example of this k power law is the momentum distribution of a single Feshbach molecule shown in Eqn. 2.42. In the large k limit, the momentum distribution of a single molecule is $\lim_{k \rightarrow \infty} n(k) = \frac{8\pi}{a} k^{-4}$, and the contact is $C_m = \frac{8\pi}{a}$.

The contact is a central quantity in a set of universal relations, linking microscopic momentum distribution to pair correlation functions and thermodynamics [197, 198], which apply to all many-body systems with contact interactions. The pair correlation function at short distance is governed by the local contact density $c(\mathbf{r}_0)$:

$$\langle \rho_\uparrow(\mathbf{r}_0 - \mathbf{r}/2) \rho_\downarrow(\mathbf{r}_0 + \mathbf{r}/2) \rangle = \frac{c(\mathbf{r}_0)}{16\pi^2} \left(\frac{1}{r^2} - \frac{2}{ar} \right) + O(r^0), \quad (2.46)$$

where $\rho_\sigma(\mathbf{r}) = \psi_\sigma^\dagger(\mathbf{r}) \psi_\sigma(\mathbf{r})$. For a homogeneous system, we have $c(\mathbf{r}) = C/V$. In thermodynamics, the contact C is the conjugate variable of the inverse of scattering length a^{-1} , and it governs the change of total energy under an adiabatic ramp of scattering length:

$$C = \frac{4\pi m}{\hbar^2} \left. \frac{\partial E}{\partial(a^{-1})} \right|_{S,N,V}. \quad (2.47)$$

This relation is also called adiabatic sweep theorem [198].

The contact of an interacting Fermi gas can be measured by rf spectroscopy [8, 160, 154, 175, 15, 191, 221]. To excite an atom in a high momentum state $k \gg k_F$, the energy cost would be $E_f - E_i = 2\epsilon_k$, where $\epsilon_k = \frac{\hbar^2 k^2}{2m}$ [221]. We again assume the bare energy difference $\hbar\omega_{12}$ has been subtract from ω , and there is no final state

interaction. The high-frequency wing of the rf spectrum is²:

$$\begin{aligned}
\lim_{\omega \rightarrow \infty} \Gamma(\omega) &= \frac{2\pi}{\hbar} \sum_k |\langle k | \hat{V}_{\text{rf}} | \psi_{MB} \rangle|^2 \delta(\hbar\omega - 2\epsilon_k) \\
&= \frac{2\pi}{\hbar} \left(\frac{\hbar\Omega_R}{2} \right)^2 \sum_k |\langle k | c_{\mathbf{k},2}^\dagger c_{\mathbf{k},1} | \psi_{MB} \rangle|^2 \delta(\hbar\omega - 2\epsilon_k) \\
&= \frac{\pi\hbar\Omega_R^2}{2} \int \frac{dk^3}{(2\pi)^3} \frac{C}{k^4} \delta(\hbar\omega - \frac{\hbar^2 k^2}{m}) \\
&= \frac{\Omega_R^2}{8\pi} \sqrt{\frac{\hbar}{m}} \frac{C}{\omega^{3/2}}.
\end{aligned} \tag{2.48}$$

Therefore, the contact can be measured by the weight of the $\omega^{-3/2}$ wing. The high-frequency tail of the molecular dissociation spectrum in Eqn. 2.43 is consistent with Eqn. 2.48 with a contact of $C = \frac{8\pi}{a}$. With the presence of a final state interaction a_f between the final state $|2\rangle$ and the unaffected state $|3\rangle$, a correction to the Eq. (2.48) is needed [15]:

$$\lim_{\omega \rightarrow \infty} \Gamma(\omega) = \frac{\Omega_R^2}{8\pi} \sqrt{\frac{\hbar}{m}} \frac{(1 - \frac{a_f}{a})^2}{\omega^{3/2}(1 + m\omega a_f^2/\hbar)} C. \tag{2.49}$$

With an rf detuning larger than the final state energy scale $\frac{\hbar^2}{ma_f^2}$, the power law of the high-frequency tail becomes $\Gamma \sim \omega^{-5/2}$.

²This expression was given in Ref. [15], however we found there is a missing factor of 2 later.

Chapter 3

Experimental apparatus and homogeneous Fermi gas

The geometry of trapping potential plays an important role in quantum gas experiments. In a 3D harmonic trap, reconstructing the local density from line-of-sight integrated density profiles typically increases noise, and the trapping potential strongly modifies the modes of collective excitations. The variation of local density and hence reduced temperature T/T_F and interaction $1/k_F a$ hinders the observation of exotic phases that are predicted to occur in a narrow range of parameters, such as the FFLO state [106, 161, 55], and measurement of physical properties at a single point in the phase diagram. In this chapter, I describe the uniform trapping potential used in our experiment to address these problems. In a homogeneous Fermi gas, we measure the temperature dependence of rf spectroscopy at unitarity. The translational symmetry of the system allows the study of collective excitations, such as first and second sound, with a well defined wavevector k . In addition, a hybrid potential that is uniform in two dimensions and harmonic in the third brings the advantages of both homogeneous and spatially varying potential. Without a need for reconstruction, we can directly image the local density of the cloud at a varying chemical potential. This technique allows us to calibrate the equation of state of a unitary Fermi gas and measure the temperature or total energy. Experimental methods used to image the homogeneous atomic clouds are also discussed in this chapter. Similar to our

experiment, a uniform trapping potential [58] had already been used for thermodynamic [174], hydrodynamic [139], and coherence measurements [29, 140] in a Bose gas by Z. Hadzibabic at Cambridge and J. Dalibard at ENS. H. Moritz at University of Hamburg later realized a homogeneous 2D Fermi gas [83] with strong interaction, and was able to measure the Josephson oscillation [122], excitation spectrum [12, 10], and critical velocity [186] in a 2D superfluid.

A new experimental apparatus for ultracold Bose-Fermi mixture was built during my Ph.D. studies. The new apparatus aims to study rotating quantum gases in tunable dimensionality with a sub-micron optical resolution. To achieve better optical access, we perform all scientific experiments in a glass cell attached to the main chamber, where the atoms are captured and cooled by a magneto-optical trap (MOT). At the end of this chapter, I detail the magnetic transport system that moves the atoms from the MOT chamber to the glass cell and the magnetic coil system at both sites.

3.1 A homogeneous Fermi gas

In this section, I present the experimental method used to create and calibrate a homogeneous Fermi gas. The signature Fermi-Dirac distribution is observed in a nearly spin-polarized system, while a pair condensate is observed in a spin-balanced system. A hybrid potential, which is harmonic in one dimension and uniform in the other two, provides a versatile platform for thermodynamic measurements.

3.1.1 Experimental setup

The uniform trapping potential consists of repulsive boundaries which are created by blue-detuned laser light, as shown in Fig. 3-1. The laser wavelength is 532 nm. A ring-shaped beam provides the radial confinement while two light sheets act as end caps to seal the two ends. Absorption imaging along the axial and radial direction shows a uniform line-of-sight-integrated density profile.

The optical setup for the radial trapping potential is illustrated in Fig. 3-2. A

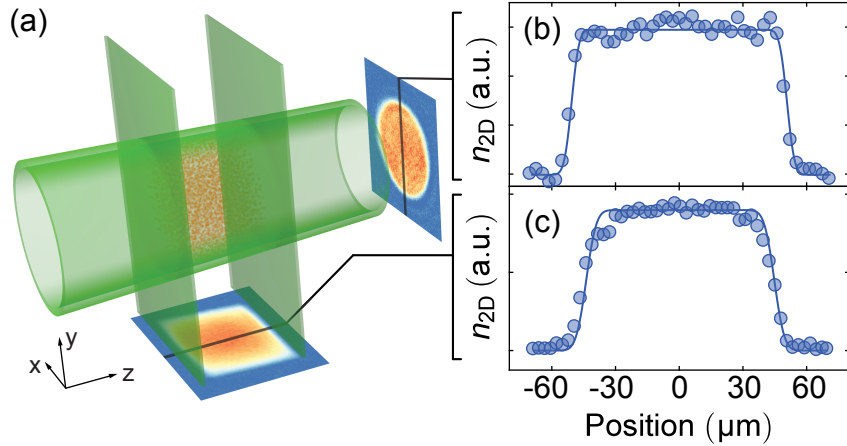


Figure 3-1: (a) Schematic of a cylindrical uniform potential and column-integrated density profiles along axial and radial direction. (b)-(c) Cut through the radial (b) and axial density profile (c).

collimated gaussian beam propagates through an axicon and a microscope objective, generating a hollow cylindrical beam in the Fourier plane. The maximum beam power used here is $\sim 1 \text{ W}$, corresponding to a trap depth of $\sim 2\mu\text{K}$. The axicon we used is conical-shaped prism with an α angle of 0.5° . The axicon creates a Bessel beam in the near field, which is Fourier transformed into a gaussian ring by a microscopy objective¹. A reflective silver mask with a radius of $60 \mu\text{m}$ is used to clean up the interference pattern inside the ring. Though silver has a high reflectivity of $\gtrsim 95\%$, the mask need to be aligned with low laser power to prevent thermal damage. The shadow of the mask is then projected onto the atoms with an 1:1 imaging system. A small variation of cylinder radius is unavoidable when using a single axicon [59]. An 80/20 beam splitter (not shown in the figure) diverts 20% of the input light to a photodiode as the signal for intensity stabilization. The whole axicon-objective-mask setup is mounted on a 3-axis translation stage with piezo actuators for easy alignment, while the mask is mounted on a secondary 3-axis translation stage for independent adjustment. For the initial alignment, the ring shape beam is projected onto the atoms without the mask, and we tune the focusing of the setup to have a circular cloud with a radius matching the silver mask. We then put in the mask and

¹Both the axicon and the objective were bought from Thorlabs, and the part number is ax2505-A and MH-10X-532.

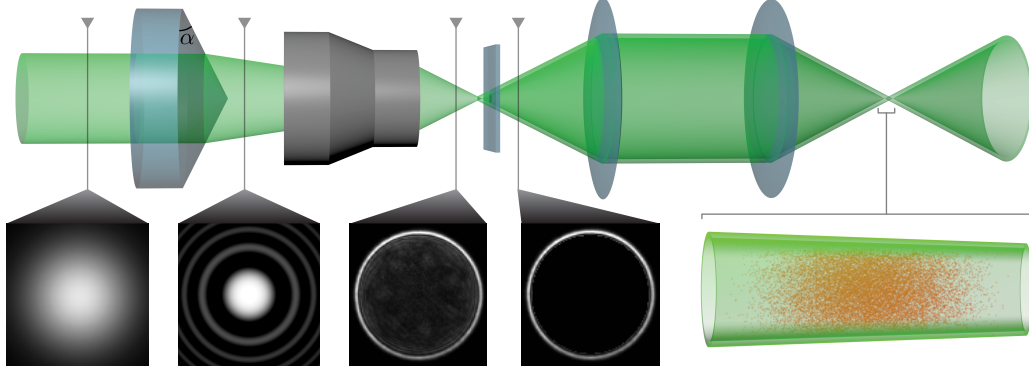


Figure 3-2: Optical setup for cylindrical trap. From left to right: A gaussian beam propagates through an axicon resulting in a Bessel beam in the near field. Subsequently the Bessel beam is focused through a microscope objective. In the focal plane, the resulting intensity pattern is a gaussian ring with interference pattern inside. A circular reflective mask is used to block residual light in the center of the ring. Finally the mask is projected through an 1:1 imaging system onto the atoms, creating the cylindrical trapping potential for the atoms.

adjust its position to achieve the sharpest box edge in the images of atoms.

The schematics of the optical setup for the endcap beams is shown in Fig. 3-3. The laser light used for the endcaps is 160 MHz detuned from the radial trapping light to avoid interference patterns. Two gaussian beams with $500 \mu\text{m}$ beam waists and orthogonal polarizations are combined on a polarizing beam splitter with a spatial offset. A cylindrical lens focuses the beam waist along one axis down to $67 \mu\text{m}$ at its focal point. A long rectangular mask creates two sharp edges in the endcap beams and the image of the mask is projected to the atom through a 3:1 imaging system. The endcap beams are combined with the radial imaging beam on a dichroic beam combiner. The position of the endcap beams can be moved independently by adjusting the pointing of the fiber collimator or collectively using a mirror between the cylindrical lens and mask controlled by piezo actuators (not shown in the figure). The rectangular mask is mounted on a 3-axis translation stage for positioning and focusing.

The magnetic moments of the three lowest states of ${}^6\text{Li}$ differ by less than 0.2% at a magnetic field of $B \geq 500\text{G}$. Therefore, a magnetic gradient can be used to compensate the gravity of a spin mixture. In our experiment, the gravitational po-

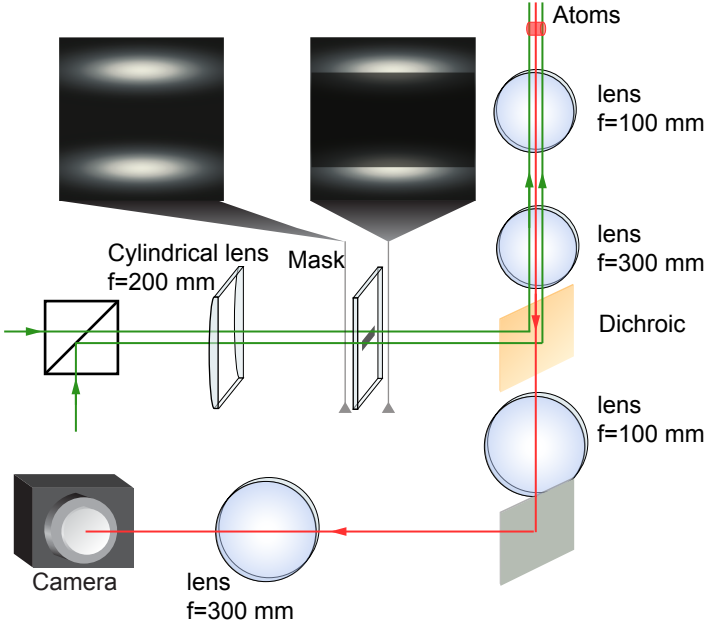


Figure 3-3: Schematics of the optical setup for the endcap beams and imaging beam along the radial direction. The shadow of the rectangular mask is imaged onto the atom with a 3:1 demagnification, while the image of atoms is captured by the camera with a 1:9 magnification.

tential points towards the $-y$ direction shown in Fig. 3-1. The position of the uniform potential is set on the flank of a magnetic saddle potential, where the local magnetic gradient cancels the gravity². The residual magnetic potential is a weak trapping potential of ~ 23.5 Hz along the axial direction and an anti trapping potential of ~ 16.5 Hz in the radial direction. The radial anti-trapping potential is compensated by an attractive 1064 nm beam with a waist of $\sim 100\mu\text{m}$. The residual axial trapping potential is less than 5% of the Fermi energy.

3.1.2 Calibration of the uniform potential

To characterize the steepness of the trap walls, we measure the dependence of the radial extent R of the cloud on the Fermi energy of the system, in a spin-balanced unitary gas with a low temperature of $T \leq 0.1T_F$. Under an ideal uniform potential, the cloud size is independent of the Fermi energy. The radius of the gas is determined

²Due to this setup, we need to move the position of the cloud when we change the current in the Feshbach or curvature coils, since both coils make a contribution to the local magnetic curvature.

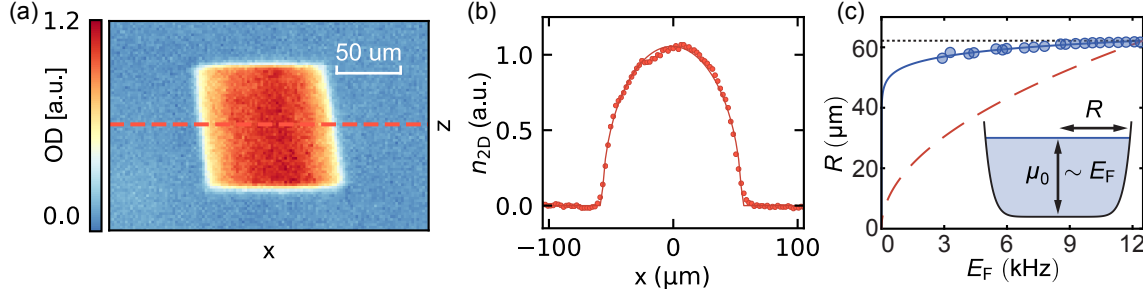


Figure 3-4: (a) Absorption image of the atomic cloud along the radial direction. (b) The column density profile along the radial direction, labeled by the red dashed line in (a). The solid line indicate a fit with Eq. 3.1. (c) Radius of the cloud as a function of the Fermi energy. The blue solid line corresponds to a power law potential $V(r) \sim r^{16}$, while the red dashed line corresponds to a harmonic trap.

by fitting the column integrated density profile with a half-circle function:

$$n_{2D}(x) = \bar{n}_{2D} \sqrt{R^2 - x^2}, \quad (3.1)$$

as illustrated in Fig. 3-4. We found less than 10% variation in the radius of the cloud when changing the Fermi energy by a factor of 4. A power law potential can be used to model the radial trapping potential $U(r) = \alpha r^m$. For an infinite square well potential $m \rightarrow \infty$, while a trivial harmonic trapping potential has $m = 2$. Close to zero temperature, the cloud has a well defined Thomas-Fermi radius R where trapping potential equals the chemical potential at the trap center:

$$\mu_0 = \xi E_F = \alpha R^m, \quad (3.2)$$

where ξ is the Bertsch parameter [60, 11]. Fitting the measured radius $R(E_F)$ with Eq. 3.2 gives $m = 16 \pm 2$. A similar calibration on the length of the box results in a power-law for the axial trapping potential with $m = 15 \pm 3$.

3.1.3 Momentum Distribution of an Ideal Fermi gas

The formation of a sharp Fermi surface at low temperature is a signature of a weakly interacting Fermi gas. The uniform box potential is an ideal platform for measuring

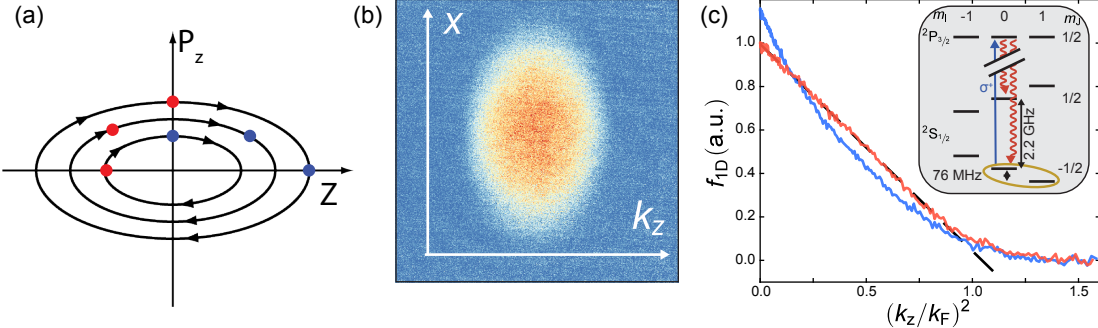


Figure 3-5: Schematics of momentum-space mapping. (a) Phase space trajectory of particles in a harmonic trapping potential. The position of particle at quarter period corresponds to the initial momentum: $z(T/4) = p_z(0)/(m\omega_z)$. (b) Image of the majority cloud after a quarter period expansion in the z -direction harmonic potential. (c) Effect of the minority atoms on the expansion of the majority cloud. The blue (red) curve is the measured 1D momentum distribution with (without) optical pumping of the minority atoms. The inset shows the state diagram of the optical pumping scheme. The yellow ellipse marks the two strongly interacting spin states, and the minority is in state $|2\rangle$. A σ^+ light (blue line) is used to optically pump the spin minority into state $|5\rangle$. The spontaneous decay is shown with red curly lines.

the global momentum distribution, while previously the Fermi surface could only be observed by cropping the center region in a harmonic trap [41]. We prepare a highly spin-imbalanced gas with $n_\downarrow/n_\uparrow < 0.05$, where the momentum distribution of the spin majority resembles that of an ideal Fermi gas [209]. The majority state is prepared in $|\uparrow\rangle = |1\rangle$, while the minority state is prepared in $|\downarrow\rangle = |2\rangle$. At a magnetic field of $B = 832$ G, a unitary interaction between the two spin states ensures fast thermalization. A momentum-space mapping technique [207, 205, 133, 183] is used to convert the initial momentum distribution into a density distribution, as illustrated in Fig. 3-5. We release the homogeneous cloud into the residual axial harmonic trapping potential whose frequency is $\omega = 2\pi \times 23.9$ Hz. A quarter period free evolution in the harmonic potential maps the initial momentum onto the position:

$$z(T/4) = \frac{p_z(0)}{m\omega_z} = \frac{\hbar k_z(0)}{m\omega_z}. \quad (3.3)$$

Before the expansion, the spin minority is optically pumped into the weakly interacting state $|5\rangle = |m_S = 1/2, m_I = 0\rangle$ with a 5 μ s laser pulse to eliminate the interac-

tions between the spin states. It only takes on average 1.5 photons to pump an atom into state $|5\rangle$. As shown in Fig. 3-5(c), the integrated 1D density profile along the axial direction $n_{1D}(z) = \iint dx dy n(x, y, z)$ reflects the 1D momentum distribution $f_{1D}(k_z) = \iint \frac{dk_x dk_y}{(2\pi)^2} f(k_x, k_y, k_z)$:

$$\begin{aligned} f_{1D}(k_z) \cdot V \frac{dk}{2\pi} &= n_{1D}(z) \cdot dz, \\ f_{1D}(k_z) &= \frac{2\pi\hbar}{m\omega V} n_{1D}(z), \end{aligned} \quad (3.4)$$

where V is the box volume and $dz = \hbar dk / (m\omega)$. For an isotropic momentum distribution $f(\mathbf{k}) = f(|\mathbf{k}|)$, the 1D momentum distribution takes the form:

$$\begin{aligned} f_{1D}(k_z) &= \iint \frac{dk_x dk_y}{(2\pi)^2} f(\sqrt{k_x^2 + k_y^2 + k_z^2}) \\ &= \int_0^\infty \frac{k_\perp dk_\perp}{2\pi} f(\sqrt{k_\perp^2 + k_z^2}) \\ &= \int_0^\infty \frac{dk_\perp^2}{4\pi} f(\sqrt{k_\perp^2 + k_z^2}) \\ &= \int_{k_z^2}^\infty \frac{dk^2}{4\pi} f(k), \end{aligned} \quad (3.5)$$

where variable substitution $k_\perp = \sqrt{k_x^2 + k_y^2}$, and $k^2 = k_\perp^2 + k_z^2$ are used. Therefore, the 3D momentum distribution $f(k)$ can be reconstructed from $f_{1D}(k_z)$ by derivative:

$$f(k) = -4\pi \frac{df_{1D}(k_z)}{dk_z^2}. \quad (3.6)$$

The measured 3D momentum distribution is shown in Fig. 3-6. We observe the formation of a Fermi surface in the k -space with decreasing temperature. At the lowest temperature T/T_F , determined by a Fermi-Dirac fit, the measured momentum state occupation at $k = 0$ is $f(k = 0) = 1.04(15)$, where the error is dominated by the systematic uncertainties in the box volume and the atom number calibration. This is the direct consequence of Pauli blocking and confirms saturation at one fermion per momentum state.

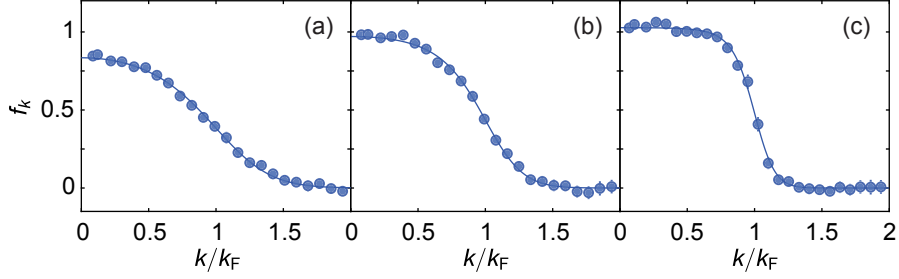


Figure 3-6: Momentum distribution of the homogeneous spin-polarized Fermi gas. A fit to Fermi-Dirac distribution (blue solid line) give (a) $T/T_{\text{F}} = 0.49(2)$, (b) $T/T_{\text{F}} = 0.32(1)$, (c) $T/T_{\text{F}} = 0.16(1)$, with the Fermi wavevector (a) $k_{\text{F}} = 2.8 \mu\text{m}$, (a) $k_{\text{F}} = 3.3 \mu\text{m}$, and (c) $k_{\text{F}} = 3.7 \mu\text{m}$.

3.1.4 Rapid Ramp and Pair Condensate in a Uniform Potential.

A rapid ramp procedure [220, 163] during time-of-flight expansion can be used to probe the pair condensate, which is evidence for superfluidity, as shown in Fig. 3-7(a). While a superfluid is initially prepared in the strongly interacting regime, a rapid magnetic field ramp to the weakly-interacting BEC side B_{mol} adiabatically converts the correlated pairs into tightly-bound molecules. The initial ramp down takes less than 0.1 ms, much shorter than the many-body state dynamics. Since the tightly-bound molecules cannot be directly imaged, the magnetic field is ramped back to a value B_{img} close to the Feshbach resonance before imaging. A bimodal density distribution will be evidence for condensation of correlated pairs before the rapid ramp.

For a uniformly trapped unitary Fermi gas, forced evaporative cooling is highly effective and can produce a fermionic superfluid. We observe the emergence of pair condensation in a spin-balanced Fermi gas through a rapid ramp procedure, as shown in Fig. 3-7(b)-(d). The pair condensate carries zero momentum and will not expand during time-of-flight expansion. As a result, the in-trap homogeneity is reflected in a flat top profile of the condensate [see Fig. 3-7(g)].

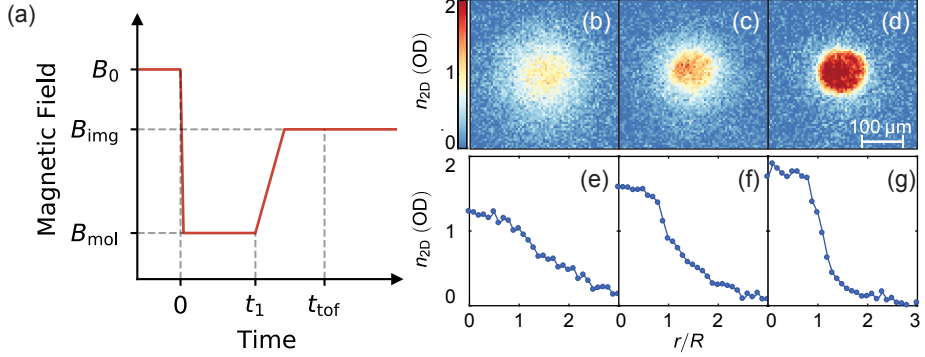


Figure 3-7: Rapid ramp and pair condensate in a Homogeneous cloud. (a) Schematics of the rapid ramp procedure during time-of-flight. The system was initially prepared at unitarity with a bias magnetic field B_0 . The magnetic field is rapidly ramped to B_{mol} and then ramped back to B_{img} at t_1 . The total time-of-flight before imaging is t_{tof} . (b)-(d) Absorption images from the axial direction after rapid ramp. The temperature of the gas is lowered (left to right) by evaporation in the uniform trap. (e)-(g) Radial density cuts through the images in the top row. Here R is the radius of the uniform trap. The data shown in (b)-(g) was taken with a spin balanced 1-2 mixture initially prepared at $B_0 = 832$ G, and the rapid ramp parameters are $B_{\text{mol}} = 390$ G, $B_{\text{img}} = 760$ G, $t_1 = 5$ ms, and $t_{\text{tof}} = 10$ ms.

3.1.5 The hybrid Potential

While a uniform potential allows an easier measurement of local density, a spatially-varying potential gives access to a large region of the phase diagram in a single experimental run. To harness the advantages of both potentials, we introduce a hybrid geometry that combines the radially uniform cylinder trap with an axially harmonic magnetic trap along the z -direction, as illustrated in Fig. 3-8(a). A single image along the radial direction will reveal the potential dependence of density $n(U)$, making it an ideal platform for thermodynamic study. Fitting the density profile $n(U)$ to the known equation of state will provide the temperature and chemical potential of the cloud. Alternatively, the pressure P and compressibility κ can be acquired by the integral and derivative of density n over potential V [101], respectively:

$$P(U) = \int_U^\infty n(U') dU' \quad (3.7)$$

$$\kappa(U) = -\frac{1}{n^2} \frac{dn(U)}{dU}. \quad (3.8)$$

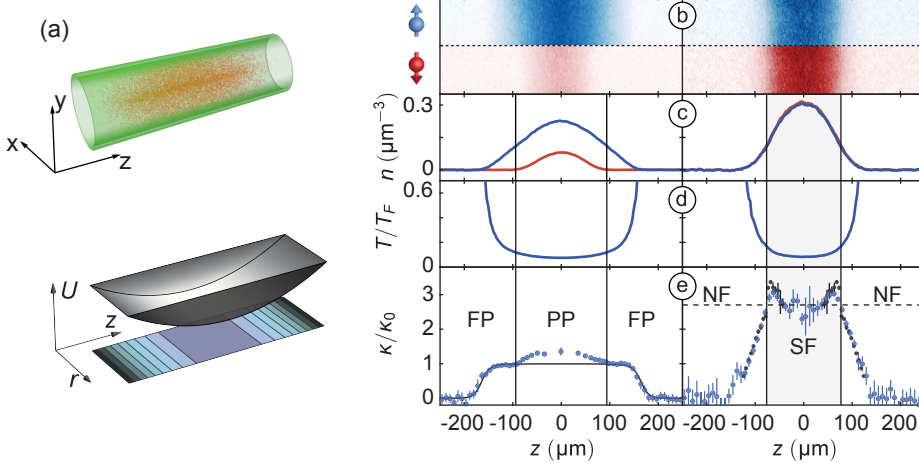


Figure 3-8: Unitary Fermi gases in the hybrid trap. (a) Schematic and potential of the trap. The cloud is imaged along an equipotential direction (x -axis). Left panels of (b)-(e) show a spin-imbalanced gas above the Clogston-Chandrasekhar limit, whereas the right side corresponds to a spin-balanced gas. The data is averaged over 6 images. (b) Local density for both spin components, obtained by dividing the column density by the column length. (c) Average density for each $x - y$ equipotential slice. The blue (red) line shows the spin-up (-down) component. (d) Spatially resolved temperature of the gas. The blue shaded region represents the error in the temperature determination. (e) Compressibility of the gas. The solid line in the left panel is the compressibility for an ideal Fermi gas. The crossover from fully polarized (FP) region to partially polarized (PP) region is accompanied by an increase in $\tilde{\kappa}$. The yellow squares in the right panel correspond to a precision measurement of the balanced unitary equation of state in harmonic trap [101]. The peaks in the compressibility signal the phase transition from normal (N) to superfluid (SF). The horizontal dashed line shows the zero-temperature equation of state $\kappa/\kappa_0 = 1/\xi$. The data shown in (b)-(d) is an average of 6 images per spin state.

As a benchmark for the hybrid trap, we perform a thermodynamic study of a strongly spin-imbalanced and a spin-balanced unitary gas, as shown in Fig. 3-8(b)-(e). The temperature is obtained by fitting the low density wings to the known equations of state of the non-interacting and spin-balanced unitary Fermi gas respectively. The compressibility κ is normalized by the compressibility of the non-interacting Fermi gas at zero temperature $\kappa_0 = \frac{3}{2} \frac{1}{nE_F}$. The normalized isothermal compressibility can be simplified to: $\tilde{\kappa} = \frac{\kappa}{\kappa_0} = - \left. \frac{\partial E_F}{\partial U} \right|_T$.

The strongly spin-imbalanced cloud features two distinct regions in the trap. The center of the cloud is a partially polarized region in which $(n_\uparrow - n_\downarrow)/(n_\uparrow + n_\downarrow) > 0.64$, well above the Clogston-Chandrasekhar limit of superfluidity [222, 23, 32, 182].

Surrounding the center is a fully polarized region, where the compressibility is seen to saturate: the real space consequence of the Pauli blocking in momentum space demonstrated in Fig. 3-6. The majority spin component in the partially polarized region is affected by the presence of the minority spin component. We measure the compressibility $\tilde{\kappa}_\uparrow = -\frac{\partial E_{F\uparrow}}{\partial U}$ in the partially polarized region, and observe an increase compared to the fully polarized gas. This is expected as the minority atoms in the center of the trap attract majority atoms and form polarons, and will be discussed in detail in Ch. 4.

In the spin-balanced case, κ/κ_0 is significantly larger than for the ideal Fermi gas due to strong interactions. The two prominent peaks in the reduced compressibility signal the superfluid transition at the two boundary surfaces between the superfluid core and the surrounding normal fluid. Near the center of the trap, the reduced compressibility agrees with the $T = 0$ equation of state $\kappa/\kappa_0 = 1/\xi = 2.65(4)$, where ξ is the Bertsch parameter. The shaded region in the right column of Fig. 3-8 shows the superfluid part of the gas, where the temperature is below the critical temperature for superfluidity $T_c = 0.17 T_F$ [101].

An isoenergetic expansion from the 3D uniform trap to the hybrid trap provide a measurement for the total energy, as illustrated in Fig. 3-9. For the expansion the two endcaps of the cylindrical trap are instantaneously removed and therefore no work is performed on the atoms. Subsequently the gas expands isoenergetically along the axial direction. Note that the underlying harmonic potential along the axial direction is always present, even for the experiments in the uniform trap. However, the potential variation due to the harmonic potential is only a few percent of the Fermi energy. After the removal of the endcaps, we wait for 2 s to equilibrate the gas. The total energy of the gas in the hybrid cylindrical trap can be determined from the *in situ* density profiles using a one-dimensional version of the virial theorem.

The total energy of the system is given by sum of the internal and potential energy

$$E = \int d^3r (\epsilon(r) + n(r) U(r)). \quad (3.9)$$

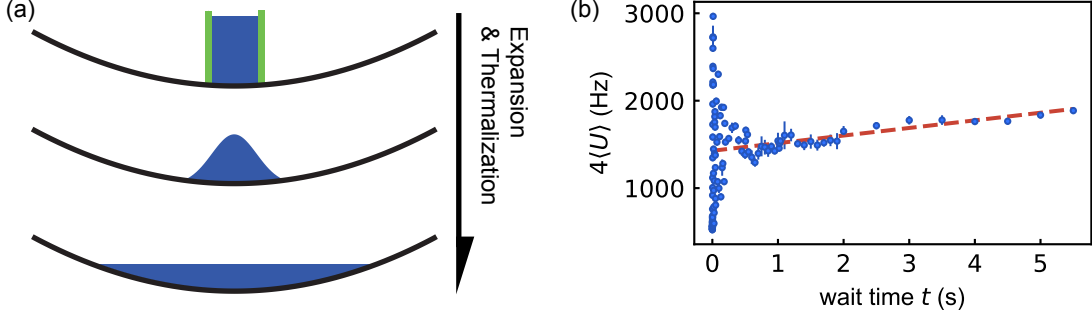


Figure 3-9: (a) Isoenergetic expansion from the uniform trap to hybrid trap. (b) Time evolution of the average potential energy. The red dashed line is a linear fit of the heating rate in the hybrid trap after 1 s waiting.

Since the hybrid trap is uniform along the radial direction, we can express Eq. (3.9) with the cylindrical cross-section A_{cyl} as

$$E = A_{\text{cyl}} \int dz (\epsilon(z) + n(z) U(z)). \quad (3.10)$$

For the unitary Fermi gas the internal energy is directly related to the pressure $\epsilon(z) = 3/2 P(z)$ [73]. Combined with a partial integration of the first term in Eq. (3.10) this leads to

$$E = -\frac{3}{2} A_{\text{cyl}} \int z \frac{\partial P(z)}{\partial z} dz + A_{\text{cyl}} \int n(z) U(z) dz. \quad (3.11)$$

For a cloud in thermal equilibrium, temperature is constant across the trap. From the Gibbs-Duhem equation at constant temperature $dP = n d\mu$, and the local density approximation $d\mu = -dU$, we obtain the one-dimensional virial theorem

$$\begin{aligned} E &= \frac{3}{2} A_{\text{cyl}} \int z n(z) \frac{\partial U(z)}{\partial z} dz + A_{\text{cyl}} \int n(z) U(z) dz \\ &= 2 A_{\text{cyl}} m \omega_z^2 \int n(z) z^2 dz \\ &= 4 \langle U \rangle N. \end{aligned} \quad (3.12)$$

In the second step of Eq. (3.12) we have used the expression for the harmonic potential $U(z) = m \omega_z^2 z^2 / 2$. The total energy per particle is 4 times the average potential energy: $E/N = 4 \langle U \rangle$. This conclusion is valid for any scale-invariant system, such as unitary Fermi gas or ideal Fermi gas. The time evolution of $\langle U \rangle$ after the expansion

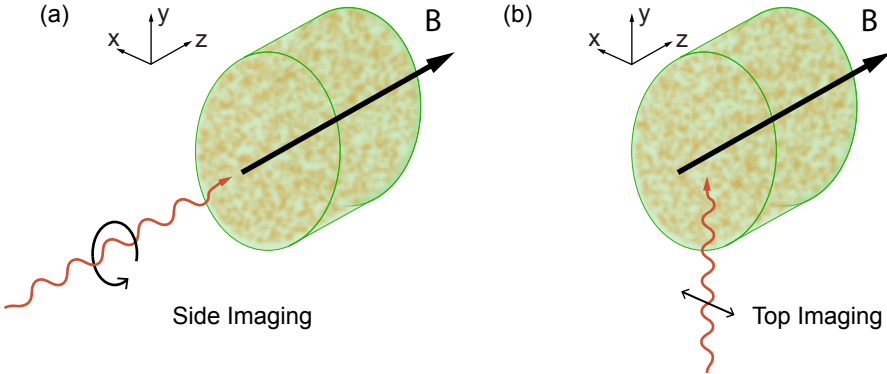


Figure 3-10: Polarization of the side (a) and top (b) imaging beam. The black arrow labels the direction of magnetic field and quantization axis.

is shown in Fig. 3-9(b). The dynamics in the hybrid potential is damped out after 1 s. A weak heating effect is observed after reaching thermal equilibrium. A linear fit of the data with $t > 1$ s gives a heating rate of $\frac{d(E/N)}{dt} = 85(10)$ Hz/s, and the $t = 0$ extrapolation gives the initial energy. Experimentally, we find the heating rate is independent of atom number.

3.2 Absorption imaging

Absorption imaging is the most straightforward method to probe the density profile of the atomic cloud. A resonant laser light is shone upon the atoms, and the absorption shadow is imaged on a camera. Two images taken with and without atoms are used to calculate the local absorption rate, thus the local column density. For the ${}^6\text{Li}$ atoms in the 3 lowest energy states $|1, 2, 3\rangle = |m_J = -1/2, m_I = 1, 0, -1\rangle$ under a bias magnetic field, the imaging light is on resonance with the σ^- transition with $\Delta m_J = -1$ and $\Delta m_I = 0$ to ensure the cycling transition, which means when the atoms sent to the excited state by the imaging light can only decay into its original state. In our experiment, we take the images of the atomic cloud from two different axes: along the axial direction of the cylinder trap (side imaging) or along one of the radial direction (top imaging), as illustrated in Fig. 3-10. The quantization axis is along the axial direction. A left-handed circular polarization is used for the side imaging beam, while the top imaging beam has an electric field perpendicular to

both the propagation and quantization axis. Though the top imaging beam has a linear polarization with a frequency resonant with σ^- transition, the imaging light can still be 100% absorbed by the atomic cloud, since the polarization of a photon propagating along the y-axis cannot be decomposed into the basis of $\left\{ \frac{|\hat{x}\rangle+i|\hat{y}\rangle}{\sqrt{2}}, \frac{|\hat{x}\rangle-i|\hat{y}\rangle}{\sqrt{2}} \right\}$; here $|\hat{x}\rangle$ ($|\hat{y}\rangle$) denotes a polarization state with electric field align with the x (y) axis. Experimentally, we found that the maximum absorption rate for the top imaging is above 99%, and the residual transmission can be mostly attributed to the spontaneous emission collected by the imaging system.

The scattering rate of an optical cycling transition is [31]:

$$R(\delta, I) = \frac{\Gamma}{2} \frac{I/I_{\text{sat}}}{1 + (2\delta/\Gamma)^2 + I/I_{\text{sat}}}, \quad (3.13)$$

where Γ is the spontaneous decay rate, δ the laser detuning, and I_{sat} the saturation intensity. The scattering cross section is $\sigma = \frac{R\hbar\omega}{I}$:

$$\sigma(\delta, I) = \frac{\hbar\omega\Gamma}{2I_{\text{sat}}} \frac{1}{1 + (2\delta/\Gamma)^2 + I/I_{\text{sat}}}. \quad (3.14)$$

For the side imaging beam, the saturation intensity takes the form of $I_{\text{sat}} = \frac{2\pi^2}{3} \frac{hc}{\lambda^3} \Gamma = 2.54 \text{ mW/cm}^2$, and the resonant scattering cross section in the low-intensity limit $I \rightarrow 0$ is $\sigma_0 = \frac{3\lambda^2}{2\pi} = 0.215 \mu\text{m}^2$. For the top imaging beam, due to the coupling matrix element being reduced by a factor of $\frac{1}{\sqrt{2}}$, its saturation intensity is twice that of side imaging beam while the resonant cross section is halved. Assuming a light beam propagating along the z axis, the intensity evolution in a absorptive medium is:

$$-\frac{dI}{dz} = n(z)\sigma(\delta, I)I(z). \quad (3.15)$$

For resonant light, the scattering cross section takes the form $\sigma(I) = \frac{\sigma_0}{1+I/I_{\text{sat}}}$, and the analytical solution for Eq. (3.15) is:

$$\int n(z) dz = \frac{1}{\sigma_0} \left(\ln \frac{I_i}{I_f} + \frac{I_i - I_f}{I_{\text{sat}}} \right), \quad (3.16)$$

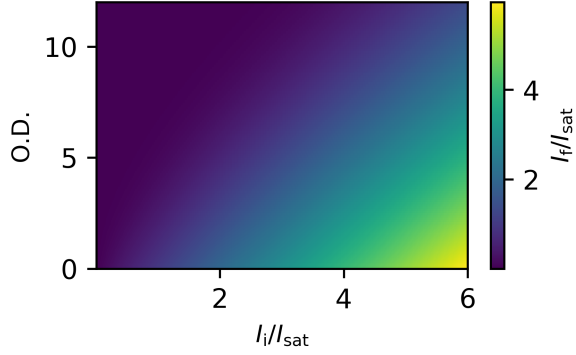


Figure 3-11: The numerical simulated lookup table for a $10 \mu\text{s}$ absorption imaging. For a given resonant incident light with intensity I_i and atomic optical density $OD = n_{2D}\sigma_0$, the outgoing beam intensity I_f is calculated.

where $\int n(z) dz = n_{2D}$ is the line-of-sight integrated column density, and I_i (I_f) is the beam intensity before (after) it goes through the atomic cloud. With a low intensity $I_i \ll I_{\text{sat}}$, Eq. (3.16) can be simplified to: $n_{2D} = \frac{1}{\sigma_0} \ln \frac{I_i}{I_f}$, also known as the Beer-Lambert law.

Unfortunately, the light mass of lithium atoms leads to a significant recoil-induced Doppler shift during imaging. With each photon scattered causing a Doppler shift of 0.17 MHz , it only takes 33 photons to detune the atom by one natural linewidth Γ . For our experiment, a typical imaging intensity is $I \simeq I_{\text{sat}}$ at an exposure time of $10 \mu\text{s}$, corresponding to ~ 90 scatterings. In order to account for the Doppler and saturation effects, we numerically solve two coupled differential equations for the local, time-dependent saturation parameter $s(z, t) = I(z, t)/I_{\text{sat}}$ and atom velocity $v(z, t)$:

$$\frac{\partial s}{\partial z} = -n\sigma_0 \frac{s}{1 + s + (2kv/\Gamma)^2}. \quad (3.17a)$$

$$\frac{\partial v}{\partial t} = \frac{\hbar k \Gamma}{2m} \frac{s}{1 + s + (2kv/\Gamma)^2}. \quad (3.17b)$$

Here, σ_0 , k , m and Γ are the bare scattering cross-section, photon wave vector, atomic mass and natural linewidth. Experimentally, we used the simulated result as a lookup table (see Fig 3-11) to determine the local column density with the measured intensity I_i and I_f with and without the atoms, respectively.

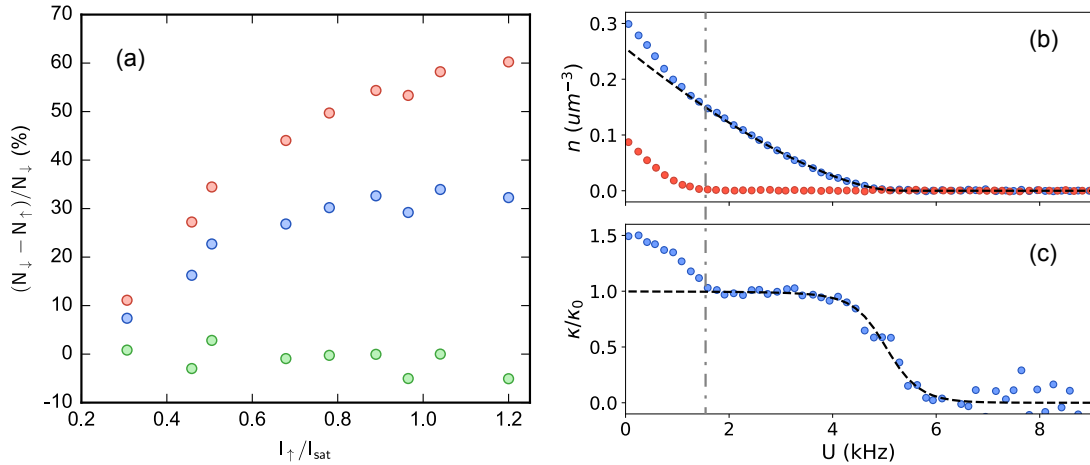


Figure 3-12: Calibration of absorption images. (a) Apparent atom count in a spin balanced atom cloud. The spin up component (N_\uparrow) is measured at different imaging intensities ($I \uparrow$), while a reference atom count (N_\downarrow) is obtained at a fixed imaging intensity ($I \downarrow = 0.23 I_{\text{sat}}$). Red circles, blue squares, and green triangles are obtained using Beer-Lambert, saturated Beer-Lambert (Eq. (3.16)), and Doppler Beer-Lambert, respectively. (b)-(c) Density calibration using the spin-imbalanced Fermi gas in the hybrid potential. (b) Majority (minority) density profiles in blue (red) data points. The dashed black line is a fit to the equation of state of the ideal Fermi gas for the fully spin-polarized regime (labeled with the dot-dashed line). The fitted temperature is $T = 0.05 T_{F\uparrow}$, where $T_{F\uparrow}$ is the majority Fermi temperature at the center of the trap. (c) A saturated normalized isothermal compressibility κ/κ_0 is observed in the majority component in the fully polarized regime.

To benchmark the absorption image, we measure the apparent atom numbers at various image intensities in a spin-balanced cloud, as shown in Fig. 3-12(a). Since the evaporative cooling process predominately removes the majority spin state, a deep evaporative cooling ensures an equal spin population. Images of the two spin states are taken subsequently with a fast CMOS camera. The first image is taken with a fixed saturation intensity of $s_{\downarrow} = 0.23$ and serves as the density reference. The second absorption image for the other spin component, with a variable s_{\uparrow} , is obtained $15 \mu\text{s}$ after the first image. The atom number acquired from the lookup table including both the saturation and Doppler effect is independent of the imaging intensity, while the atom number calculated with Eq. (3.16) shows an atom number deviation when the imaging intensity is high. We used the density profile of a spin polarized Fermi gas in a hybrid trap to calibrate the absolute value of atomic density, as illustrated in Fig. 3-12(b) and (c). The presence of minority atoms allows a sufficient cooling and thermalization of the majority cloud. In the fully polarized regime, the majority cloud is an ideal Fermi gas, whose normalized compressibility $\kappa/\kappa_0 = -dE_F/dU$ saturates to 1 at low temperature. The ideal Fermi gas equation of state $n(\mu, T)$ and an overall scaling factor f is used to fit the measured density $n_m(U)$ in the fully polarized regime:

$$n_m(U) = n(\mu - U, T)/f. \quad (3.18)$$

In an ideal world with perfect calibration of image pixel size, imaging beam polarization and atomic scattering cross section, we will have $f = 1$. However, experimentally we typically get $f \simeq 1.5$. The data shown in Fig. 3-12 is the corrected density profile $n(U) = f \cdot n_m(U)$, and its corresponding compressibility.

Our calibration on atom density works well at density $n \lesssim 0.3 \mu\text{m}^{-3}$. However, a saturation effect is observed at higher density, as shown in Fig. 3-13. While the absorption images after a 5 ms time-of-flight yield a good measurement of the total atom number, the measured atom number is reduced in the in-situ image. This is possibly due to reabsorption of spontaneously emitted photons by other atoms, resulting in a larger probability for atoms to be in the excited state. The saturation

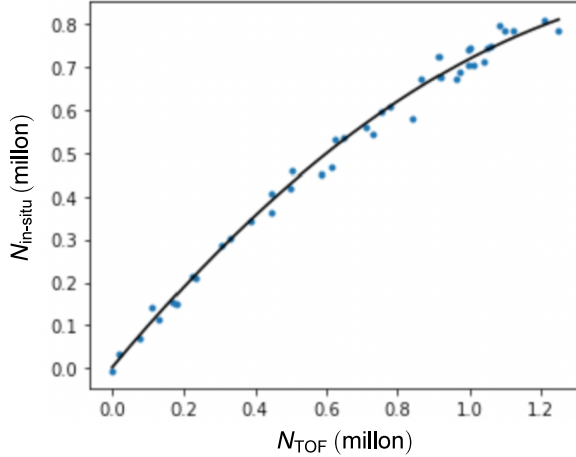


Figure 3-13: Saturation of high density imaging. For a homogeneous cloud with various densities, the total atom number is measured in situ ($N_{\text{in-situ}}$) or after an time-of-flight (N_{TOF}). The black solid curve is a fit with the function $y = x + a_2x^2$, with $a_2 = -0.29(1)$. The volume of the uniform trap is $1.06 \times 10^6 \mu\text{m}^3$.

of the apparent in situ density n_{app} can be well fitted by a quadratic function $n_{\text{app}} = n + a_2n^2$. This effect plays an important role when a small density variation is measured, as a rescaling factor $\frac{\partial n}{\partial n_{\text{app}}} \simeq 1.8$ needs to be applied for a cloud with a Fermi energy of 10 kHz.

3.3 Phase contrast imaging

To address the saturation effect in absorption imaging, we adopt a phase contrast imaging technique [91, 92]. For imaging light with a frequency detuning much larger than the atomic natural linewidth $\delta \gg \Gamma$, photon scattering is significantly reduced, and the off-resonant light instead experiences a phase shift. Interference between the imaging beam and a reference beam yields the spatial phase pattern, hence the atomic density profile.

In our experiment, a phase contrast imaging is applied for the top imaging axis, as shown in Fig. 3-14. The imaging beam is typically detuned by 20-80 MHz from the resonant σ^- cycling transition. At the 1-3 Feshbach resonance $B = 690$ G, the laser detuning from the π transition is 1.3 G, therefore a beam with \hat{z} polarization gets negligible phase shift and can be used as the reference beam. A half-wave plate

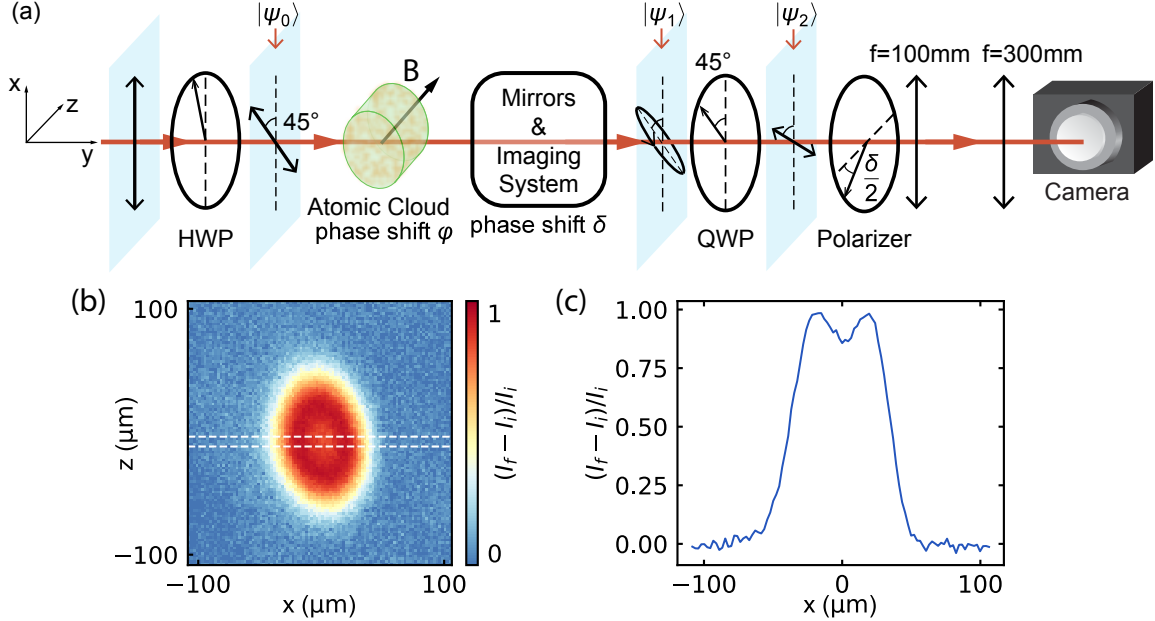


Figure 3-14: Phase contrast imaging. (a) A schematic of the phase contrast imaging setup. The polarization of the imaging beam is rotated 45° by a half-wave plate (HWP), and has a 45° angle with the quantization axis. After experiencing a differential phase shift ϕ between \hat{x} and \hat{z} axis from the the atomic cloud and the δ from the optical elements in the imaging path, the beam polarization becomes elliptical. A quarter-wave plate (QWP) converts the elliptical polarization back to a rotated linear polarization. A polarizer is used to detect the polarization rotation angle contributed by the atoms, and the interference pattern on the polarizer will be imaged on the camera. The polarization state at various location is labeled as $|\psi_0\rangle$, $|\psi_1\rangle$, and $|\psi_2\rangle$. Phase shift signal of an atomic cloud is shown in (b), and its horizontal cut in (c). The signal here is intensity difference between images taken with (I_f) and without (I_i) atoms. The central dip indicates a phase shift larger than $\pi/4$. The image shown in (b) and (c) is taken with a 20 MHz detuning.

is used to rotate the beam polarization to a 45° angle state $|\psi_0\rangle$ to both x- and z-axes:

$$|\psi_0\rangle = \frac{|\hat{x}\rangle - |\hat{z}\rangle}{\sqrt{2}}. \quad (3.19)$$

The imaging beam with polarization $|\hat{x}\rangle$ acquires a phase shift ϕ from the atomic cloud. Since the s and p axes of all the optical elements are aligned with the \hat{x} and \hat{z} , their effect on the imaging light is also a differential phase shift δ on the $|\hat{x}\rangle$ polarized beam. The phase shift turns the beam polarization into an elliptical one $|\psi_1\rangle$:

$$|\psi_1\rangle = \frac{e^{i(\phi+\delta)} |\hat{x}\rangle - |\hat{z}\rangle}{\sqrt{2}}. \quad (3.20)$$

A quarter-wave plate with its fast axis aligned with the initial 45° polarization direction is able to convert the polarization to $|\psi_2\rangle$:

$$|\psi_2\rangle = \frac{e^{i\frac{\phi+\delta}{2}}}{\sqrt{2}} \left[\cos\left(\frac{\pi+\delta}{2} + \pi/4\right) |\hat{x}\rangle - \sin\left(\frac{\pi+\delta}{2} + \pi/4\right) |\hat{z}\rangle \right], \quad (3.21)$$

which is a linear polarization with an angle of $\frac{\pi+\delta}{2} + \pi/4$ from the x-axis. The polarization rotation caused by the atoms is read out by a polarizer positioned at an $\pi/4 + \delta/2$ angle from the x-axis, which cause an interference between the phase shifted and reference polarization components. The dependence of the transmission rate P_t on the phase shift ϕ is:

$$P_t(\phi) = \frac{1 - \sin \phi}{2}. \quad (3.22)$$

The 45° angle between the polarizer transmission axis and the imaging beam polarization without an atomic phase shift yields maximum sensitivity on a small phase rotation.

Our phase contrast imaging scheme requires accurate control of the beam polarization. In order to achieve this, we mount the half-wave plate, the quarter-wave plate, and the polarizer on precision rotation mounts with 5 arcmin resolution³. To generate the initial 45° polarization, a polarized beam splitter cube is placed at the position of the QWP, and we tune the angle of the HWP to achieve power balance between the transmission and reflection port. The angle of the initial polarization can be checked by the maximum absorption rate when σ^- resonant imaging light is sent through a dense atomic cloud. Experimentally, we found the maximum absorption rate is 49.2%. We then adjust the orientation of the QWP and the polarizer without atoms. The angle of the QWP is set by maximizing the extinction ratio on the polarizer, then the angle of polarizer is set to allow 50% of maximum transmission power through. The QWP and polarizer are installed close to each other without any optical elements in-between to preserve the polarization information. The polarizer

³We use a Thorlabs PRM1 mount

is put at a imaging plane of the system, so the interference pattern yields the density distribution and is directly imaged by the camera. A demonstration of the phase contrast imaging is shown in Fig.3-14(b) and (c) with a 20 MHz detuned imaging beam. Here a dense atomic cloud is prepared in two crossed optical dipole traps along the z- and y-axes, and the signal is the relative transmission rate on the polarizer. The high column density of the cloud allows the observation of a signal dip in the center of the trap, which indicates the phase shift ϕ exceeds $\pi/4$.

To quantitatively acquire the local density from phase contrast imaging, we use the expression of phase shift ϕ and absorption A for a beam going through an atomic cloud with column density n_{2D} :

$$\phi(n_{2D}, \delta, I) = -n_{2D}\sigma_0 \frac{\delta/\Gamma}{4\delta^2/\Gamma^2 + (I/I_{sat}) + 1}, \quad (3.23a)$$

$$A(n_{2D}, \delta, I) = \frac{n_{2D}\sigma_0}{2} \frac{1}{4\delta^2/\Gamma^2 + (I/I_{sat}) + 1}. \quad (3.23b)$$

The complex electric field of the outgoing laser beam is $\tilde{E} = \tilde{E}_0 e^{-A+i\phi}$, where \tilde{E}_0 is the initial amplitude. When keeping the light absorption in consideration, the transmission rate on the polarizer becomes:

$$P_t(\phi, A) = \frac{e^{-2A} + 1}{4} - \frac{e^{-A} \sin \phi}{2}. \quad (3.24)$$

Experimentally, the transmission rate is measured by the captured image intensity with (I_f) and without (I_i) atoms: $P_t = I_f/(2I_i)$. The factor of 2 comes from the fact that only 50% of light goes through the polarizer without atoms.

We used the phase contrast imaging technique to probe a 1-3 mixture at Feshbach resonance $B = 690$ G; the two atomic states are labeled as $|\uparrow\rangle = |1\rangle$, and $|\downarrow\rangle = |3\rangle$. Two consecutive images (labeled as image a and b) with different frequencies are used to probe the atomic density. The phase shift ($\phi_{a,b}$) and absorption ($A_{a,b}$) of

each imaging beam is contributed by both atomic species:

$$\phi_{a,b} = \phi(n_{2D\uparrow}, \delta_{a,b;\uparrow}, I_{i;a,b}) + \phi(n_{2D\downarrow}, \delta_{a,b;\downarrow}, I_{i;a,b}), \quad (3.25a)$$

$$A_{a,b} = A(n_{2D\uparrow}, \delta_{a,b;\uparrow}, I_{i;a,b}) + A(n_{2D\downarrow}, \delta_{a,b;\downarrow}, I_{i;a,b}), \quad (3.25b)$$

where $n_{2D\uparrow,\downarrow}$ is the column density of the two spin states, and $\delta_{a,b;\uparrow,\downarrow}$ is the detuning of each imaging beam from the resonance of each spin states. The density of each spin state can be obtained by solving non-linear equations involving the transmission rate of the two imaging beams:

$$\frac{I_{f,a}}{2I_{i,a}} = \frac{e^{-2A_a} + 1}{4} - \frac{e^{-A_a} \sin \phi_a}{2}, \quad (3.26a)$$

$$\frac{I_{f,b}}{2I_{i,b}} = \frac{e^{-2A_b} + 1}{4} - \frac{e^{-A_b} \sin \phi_b}{2}, \quad (3.26b)$$

where the phase shift $\phi_{a,b}$ and absorption $A_{a,b}$ takes the form in Eq. (3.25) and (3.23). For a spin-polarized or a spin-balanced system, one density variable can be dropped and the density can be determined with a single image. A polarized Fermi gas is used to calibrate the absolute atom density, similar to the process shown in Sec. 3.2. A rescaling factor of $f = 1.03(9)$ is acquired by fitting the density profile with Eq. (3.18), indicating a near-perfect estimation of atom number using phase contrast imaging technique. Thus the phase contrast imaging can be used as a calibration method for density change measured with absorption imaging.

Phase contrast imaging provides an ideal method for measuring small density variations on top of a background density. Using this technique, we measure the compressibility of a homogeneous unitary gas $\kappa = -\frac{1}{n^2} \frac{dn}{dU} \Big|_T$ by imaging the axial density variation $\Delta n(z)$ under a linear gradient potential $U(z) = g \cdot z$. The typical density per spin state used in this experiment is $n \simeq 0.9 \text{ um}^{-3}$. With a finite density variation, the in situ superfluid transition point can be observed as a sudden change of slope in the density profile [see Fig. 3-15(a)]. The measured compressibility at center of the trap is shown in Fig. 3-15(b), with a normalizing factor $\kappa_0 = \frac{3}{2nE_F}$. The new result obtained by phase contrast imaging is consistent with the previous result

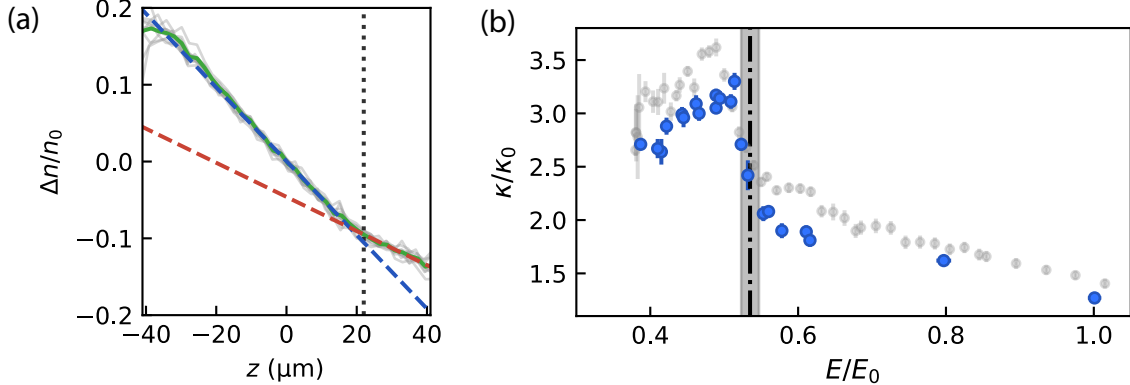


Figure 3-15: Equation of state measured with the phase contrast imaging technique. (a) local density variation Δn under a linear gradient of $12.74 \text{ h}\cdot\text{Hz}/\mu\text{m}$. The blue and red dashed line represent density slope below and above superfluid transition point (vertical dotted line). The gray curves are results from individual images, while the green curve is the averaged profile using 12 images with the gradient potential and 6 background images without. (b) Measured compressibility κ/κ_0 with phase contrast imaging at a density of $n \simeq 0.9 \text{ um}^{-3}$ per spin state (blue circles) at various energies E/E_0 , compared with previous results measured at $n \lesssim 0.3 \text{ um}^{-3}$ (gray dots) [101]. The energy in the uniform trap is measured by an isoenergetic expansion into the hybrid trap.

measured in a low density cloud $n \lesssim 0.3 \text{ um}^{-3}$ using absorption imaging [101].

3.4 Coil systems and magnetic transport for a new quantum gas experiment

A new experimental apparatus, named Fermi3, was built as an upgraded version of the old BEC1 experiment. The most significant improvement is the usage of a glass cell, which provide excellent optical access for controlling and probing the atoms. With the help of a high numerical-aperture (NA) objective at the glass cell, we are able to achieve imaging resolution on the order of $\sim 1 \mu\text{m}$ [52]. Fig. 3-16 shows the 3D model of the main vacuum system of Fermi3. The atomic beam going through the Zeeman slower is laser-cooled and trapped in the magneto-optical trap (MOT), and subsequently transferred to the glass cell for further cooling and experiments. A magnetic transport technique [63], which generates a moving magnetic trap by controlling the current in a series of coils, is used to move the atoms from the MOT

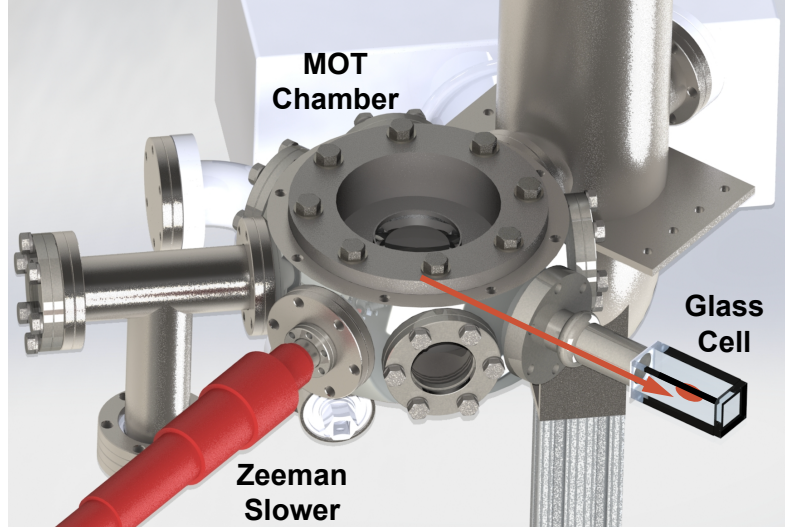


Figure 3-16: 3D model of the vacuum chamber of the Fermi 3 experiment. The atomic cloud is initially trapped in a magneto-optical trap (MOT) in the MOT chamber. The atom cloud is then transferred to the glass cell with a magnetic transport system.

chamber to the glass cell. In this section, I detail the magnetic coil system used to trap, transport, and induce Feshbach resonances on the atoms.

The complete set of magnetic coils is outlined in Fig. 3-17. All coils here have a cylindrical geometry. For a circular coil of radius R and current I perpendicular to the z-axis and centered at origin, the magnetic field expressed in a cylindrical coordinate system is [171]:

$$B_\rho = \frac{\mu_0 I}{2\pi} \frac{z}{\rho\sqrt{(R+\rho)^2 + z^2}} \cdot \left[-K(k^2) + E(k^2) \frac{R^2 + \rho^2 + z^2}{(R-\rho)^2 + z^2} \right], \quad (3.27a)$$

$$B_z = \frac{\mu_0 I}{2\pi} \frac{1}{\sqrt{(R+\rho)^2 + z^2}} \cdot \left[K(k^2) + E(k^2) \frac{R^2 - \rho^2 - z^2}{(R-\rho)^2 + \rho^2} \right], \quad (3.27b)$$

where K and E are the complete elliptic integral of the first and second kind, $k = \sqrt{\frac{4R\rho}{(R+r)^2 + z^2}}$. A numerical integral of infinitesimal current loops yields magnetic field generated by a cylindrical coil, and we assume a uniform current density $j = NI/S_A$, where N is the winding number of the coil and S_A is the coil cross-sectional area. Two different copper wires are used for the coils: a solid flat wire with a cross-section area of $2.90 \text{ mm} \times 1.37 \text{ mm}$ is used for magnetic coils with a transient current (such as transport coils), while a hollow core square wire with an outer side length of 3.6 mm

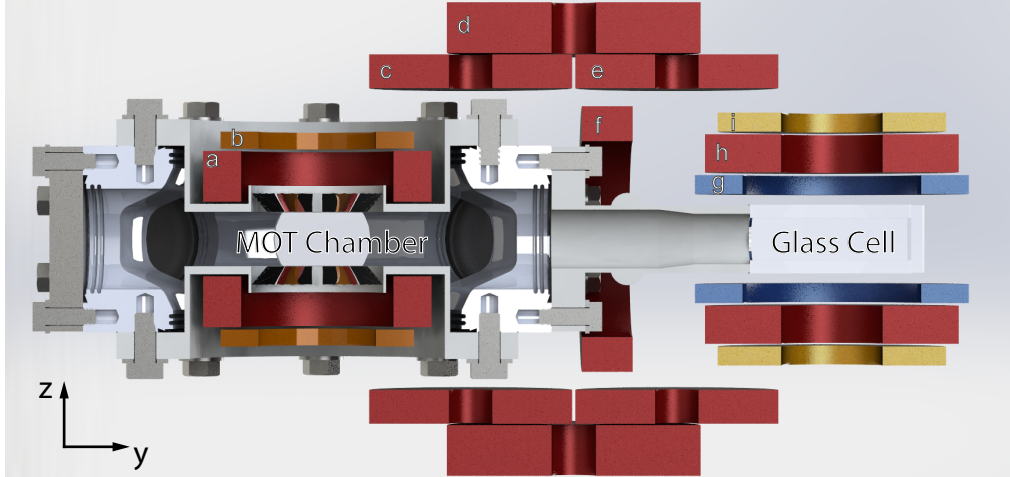


Figure 3-17: A cross section view of the coils of the Fermi 3 apparatus. Each coil (pair) is label with a letter: (a) MOT coils, (b) MOT bias coils, (c) Transport 1 coils, (d) Transport 2 coils, (e) Transport 3 coils, (f) "Push & Pull" coil, (g) Feshbach coils, (h) quadrupole coils, and (i) curvature coils. The coils in red color are used during magnetic transport. The mounting structure is not shown in the figure.

Coil	Wire	Axial Gradient g (G/cm/A)	Axial Bias b (G/A)
MOT	hollow square	1.27	3.57
MOT bias	flat	1.49	2.99

Table 3.1: Properties of MOT chamber coils. The axial gradient (bias) value corresponding to the anti-Helmholtz (Helmholtz) configuration.

is used for coils with persistent high current (such as MOT and Feshbach coils)⁴. A detailed description of the manufacturing of the coils can be found in Appendix. F.

3.4.1 MOT Chamber Coils

The properties of coils at the MOT chamber are shown in Tab. 3.1. The magnetic field for both laser cooling and magnetic trapping is generated by the MOT coils in an anti-Helmholtz configuration. Under such a configuration, the magnetic field at

⁴The dimension of wire mentioned here includes the insulation layer and the estimated epoxy thickness after coil winding. The flat wire is an AWG 12 wire compressed into a rectangular shape, with a copper cross-section of $0.05064'' \times 0.10128''$. The hollow copper core of the square wire have a outer side length of $1/8''$ and a square hole with a length of $1/16''$.

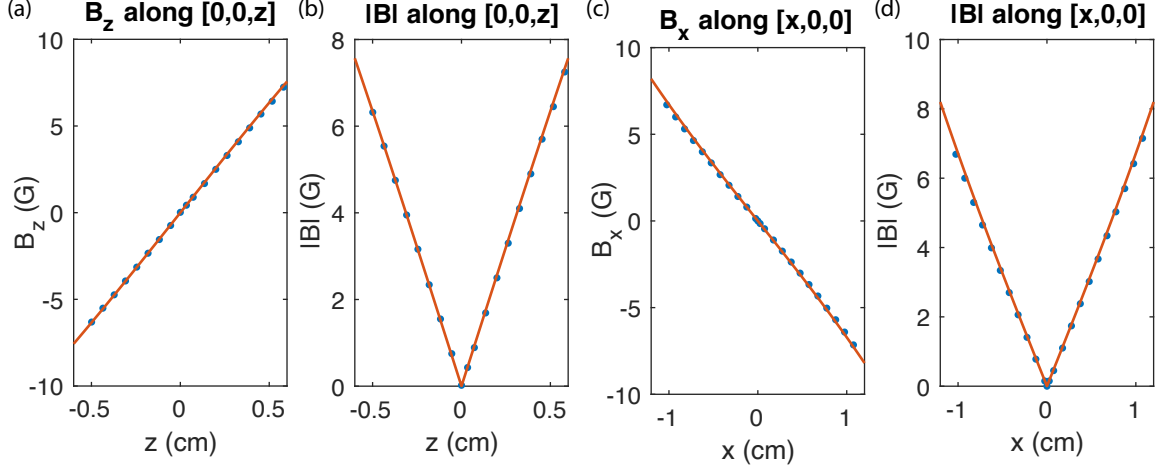


Figure 3-18: Calibrating the magnetic field gradient of MOT coils. (a)-(b) The magnetic field B_z (a) and its amplitude (b) along the axial z -axis. (c)-(d) The magnetic field B_x (a) and its amplitude (b) along the radial x -axis. The blue circles are measured by a hall probe, while the orange line is the calculated magnetic field.

the center of the coil pair takes the quadrupole form:

$$\mathbf{B} = Gz\hat{\mathbf{e}}_z - \frac{Gx}{2}\hat{\mathbf{e}}_x - \frac{Gy}{2}\hat{\mathbf{e}}_y, \quad (3.28)$$

where $\hat{\mathbf{e}}_i$ is the unit vector along i axis. A calibration of the MOT coils is shown in Fig. 3-18. During the MOT loading, the magnetic field away from the trap center will bring the cooling light closer to resonance, creating an effective restoring force. The quadrupole magnetic field then serves as the magnetic trap for atoms in the low field seeking state. Since the atomic spin state stays the same when an atom moves adiabatically in the magnetic field, the magnetic dipole energy only depends on the magnitude of the B field

$$U(\mathbf{r}) = g_F\mu_B M_F B(\mathbf{r}). \quad (3.29)$$

Therefore, the quadrupole magnetic field provides a V-shape trapping potential for an atomic state with $g_F M_F > 0$. In our experiment, we trap the Na atoms in $|F = 2, M_F = 2\rangle$ and the Li atoms in $|3/2, 3/2\rangle$ state. To prepare the atoms in these states, we generate a 5 G bias magnetic field using the MOT bias coils and apply optical pumping with σ^+ pumping and repumping light.

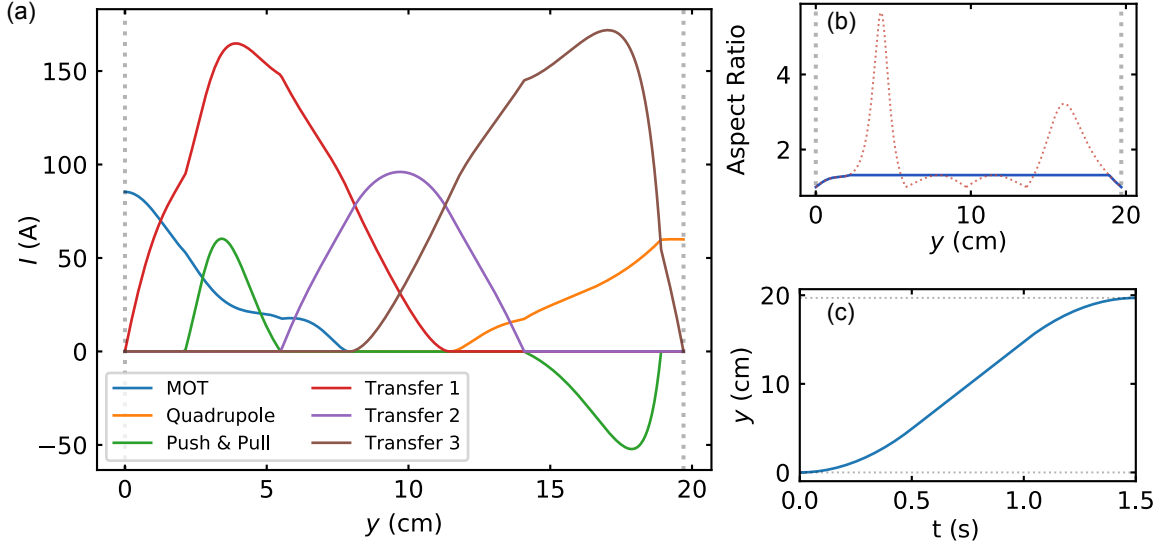


Figure 3-19: The magnetic transport scheme. (a) The current profile of the magnetic transport. The vertical dashed lines indicates the starting and ending point. (b) Aspect ratio of the magnetic trap as a function of y position, with 2 (red dotted line) or 3 pairs (blue solid line) of coils simultaneously. (c) The trajectory $y(t)$ of the magnetic trap center used in the experiment.

3.4.2 Magnetic Transport System

After the atoms are trapped at the MOT chamber, we use a magnetic transport system to move the atoms into the glass cell. The position and properties of the coils used for transport are listed in Tab. 3.2. By subsequently ramping up and then down the magnetic coils along the path, we can smoothly move the center of magnetic trap. Due to the inversion symmetry along x and z direction, the magnetic field close to the y axis has the general form:

$$\mathbf{B}(\mathbf{x}, \mathbf{y}, \mathbf{z}) \simeq G_z z \hat{\mathbf{e}}_z + G_x x \hat{\mathbf{e}}_x + (G_y y + B_0) \hat{\mathbf{e}}_y. \quad (3.30)$$

The center position of the magnetic trap is located at the zero point of the magnetic field $B_0 = 0$. The divergence of the magnetic field is zero, $\nabla \cdot \mathbf{B} = 0$, hence $G_x + G_y + G_z = 0$. The magnetic gradients G_i quantify the steepness of the trapping potential along each axis i . We can define the aspect ratio of the trap as $A \equiv G_x/G_y$, and the

Coil	Wire	y-position (cm)	Axial Gradient g (G/cm/A)
MOT	hollow square	0	1.27
Transfer 1	flat	5.8	0.80
Transfer 2	flat	9.7	1.00
Transfer 3	flat	13.6	0.80
Quadrupole	hollow square	19.7	1.84
Push & Pull	flat	11.2	N/A

Table 3.2: Position and properties of transport coils. The axial gradient is calculated at the center of each pair of coils.

magnetic gradients can be rewritten as:

$$(G_x, G_y, G_z) = G_z \cdot \left(-\frac{A}{1+A}, -\frac{1}{1+A}, 1 \right). \quad (3.31)$$

A simple solution for the magnetic transport will be using the nearest two sets of coils to generate a magnetic trap at any given position and achieve a z-gradient of G_{z0} . The current equation for nearest coil pairs i, j to create a trap centered at y_0 is:

$$b_z^i(y_0)I_i + b_z^j(y_0)I_j = 0, \quad (3.32a)$$

$$g_z^i(y_0)I_i + g_z^j(y_0)I_j = G_{z0}. \quad (3.32b)$$

Here $b_z^i(y_0)$ and $g_z^i(y_0)$ is the magnetic field and gradient generated by coil pair i at position y_0 per unit current. However, this procedure creates a strong modulation of the aspect ratio of the trap [Fig. 3-19(b)], and will lead to heating during transport. A third pair of coils k can be added to put an constraint on the aspect ratio of the potential:

$$b_z^i(y_0)I_i + b_z^j(y_0)I_j + b_z^k(y_0)I_k = 0, \quad (3.33a)$$

$$g_z^i(y_0)I_i + g_z^j(y_0)I_j + g_z^k(y_0)I_k = G_{z0}, \quad (3.33b)$$

$$g_x^i(y_0)I_i + g_x^j(y_0)I_j + g_x^k(y_0)I_k = -\frac{A}{1+A} G_{z0}. \quad (3.33c)$$

We set the the maximum global aspect ratio to be the same as the maximum two-pair aspect ratio between transfer 1 and 2 or transfer 2 and 3 in order to avoid changing the sign of the current in one of these coils. The switching point for coil pairs is where the global aspect ratio intersects the 2-pair aspect ratio. During the very beginning and end of the transport, only 2 coil pairs are running when the atoms are moved out of (into) the initial (final) symmetric potential. In our experiment, we use a magnetic field gradient of $G_z = 110 \text{ G/cm}$ and 1.5 s transfer time. During the transfer, the atoms experience a 0.5 s acceleration, then a 0.5 s motion with constant velocity, and finally a 0.5 s deceleration. The rate of acceleration and deceleration is 39.4 cm/s^2 . The current profile during the transport is shown in Fig.3-19(a), and the space-time trajectory of the trap center is shown Fig.3-19(b). For a laser cooled Na cloud at $350 \mu\text{K}$, we found more than 80% of atoms can be transferred with a temperature increase of less than $50 \mu\text{K}$.

3.4.3 Glass Cell Coils

The parameters of the coils around the glass cell are shown in Tab. 3.3. After the magnetic transport, atoms are trapped by the quadrupole coils, which are able to generate a strong magnetic gradient, thus tight confinement for the atoms. With a 15 V , 400 A power supply⁵, the quadrupole coils can reach a maximum axial gradient of $> 400 \text{ G/cm}$.

The Feshbach coils and curvature coils are connected in the Helmholtz configuration. The Feshbach coils are designed to have zero magnetic field curvature, so they will generate a uniform bias field up to z^4 order. In contrast, the curvature coils will produce a significant magnetic curvature, while they generate a relatively small bias field. The strongly interacting ${}^6\text{Li}$ states $|1\rangle$, $|2\rangle$, and $|3\rangle$ are all high field seekers with almost identical magnetic moment at a large magnetic field. By independently tuning the Feshbach and curvature current, we are able to tune the bias field to induce a certain interaction, as well as generate an axial trapping potential, as illustrated in Fig. 3-20.

⁵Here we are limited by the available voltage

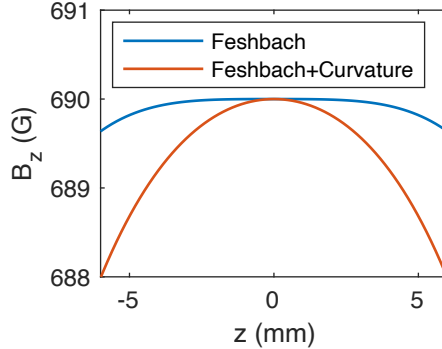


Figure 3-20: The high magnetic field $B = 690$ G generated by the Feshbach and curvature coils. The blue line is the B field generated by Feshbach coils alone at $I = 322$ A, while the red line shows a combined field by the Feshbach coils at $I = 340$ A and curvature coils at $I = 50$ A. The magnetic field curvature of the red line corresponds to a harmonic trapping frequency of 20.5 Hz for the ${}^6\text{Li}$ atoms.

Coil	Wire	Axial Gradient g (G/cm/A)	Axial Bias b (G/A)	Axial Curvature c (G/cm 2 /A)
Feshbach	hollow square	0.60	2.15	< 0.004
Quadrupole	hollow square	1.84	4.47	0.75
Curvature	hollow square	0.34	0.76	0.18

Table 3.3: Properties of glass cell coils. The axial gradient is measured in an anti-Helmholtz configuration, while the bias and curvature is measured in a Helmholtz configuration.

Chapter 4

Resonant quantum impurities in a Fermi gas at finite temperature

In this chapter I discuss a seemingly simple scenario of strongly interacting system: resonantly interacting impurities immersed in a majority Fermi gas. Despite the simplicity, the system shows a rich phase diagram. At low temperature, due to the pauli blocking of the majority Fermi sea, the impurity is only allowed to interact with majority atoms close to the Fermi surface. This leads to the formation of a well-defined quasiparticle [25, 115, 33, 158, 173, 135, 211], called Fermi polaron, even in the strongly interacting regime. An ensemble of these Fermi polarons behaves like a Fermi liquid: a weakly interacting Fermi gas of dressed quasiparticles with a distinct effective mass. As the temperature increases, the softened Fermi surface leads to more scattering and an reduced lifetime for the Fermi polarons [19]. Above the Fermi temperature $T > T_F$, the quasiparticle and Fermi liquid picture will break down and both majority and minority states will act like classical scatters with a cross-section $\sigma \sim 1/T$ [44]. In our recent experiment [211], we were able to observe how a polaronic Fermi liquid evolves into a classical Boltzmann gas.

The rf spectroscopy on an homogeneous Fermi gas is an ideal tool to study the thermal evolution of the strongly interacting impurities. While the rf spectroscopy provides the quasiparticle energy, lifetime, and two-body correlation in the polaronic Fermi liquid or classical Boltzmann gas, the uniform trap ensures a global spectral

measurement on a single T/T_F and minority concentration. Our spectroscopy measurement reveals a drastic transition between the Fermi liquid and classical gas at a temperature $T \simeq T_F$. In the transitional regime, the spectral width attains its maximum on the scale of the Fermi energy, indicating the breakdown of a quasiparticle description. In addition, density measurements in a harmonic trap directly reveal the majority dressing cloud surrounding the minority spins and yield the compressibility along with the effective mass of Fermi polarons.

4.1 Fermi polarons at low temperature

In this section, I will briefly introduce the theory of Fermi polarons. On unitarity, a trial wavefunction proposed by F. Chevy in Ref [25] models the Fermi polaron as a bare impurity particle dressed by a continuum of single particle-hole excitations close to the majority Fermi surface. This model successfully predicted the energy, effective mass, quasiparticle residue, and two-body contact, at $T = 0$. The zero-temperature equation of state of an polaronic gas is predicted to take a Fermi liquid form [115, 129]. This was confirmed in subsequent experiments [181, 135, 138]. The collisional decay rate of Fermi polarons at finite temperature also takes the Fermi liquid form $\Gamma \sim T^2$ [19].

4.1.1 Chevy ansatz and variational wavefunction approach

As I have discussed in Ch.2.3.2, the Hamiltonian describing a spin mixture with equal mass and short range interaction can be expressed as:

$$H = \sum_{\mathbf{k},\sigma} \epsilon_k \hat{a}_{k,\sigma}^\dagger \hat{a}_{k,\sigma} + \frac{g}{V} \sum_{\mathbf{k},\mathbf{k}',\mathbf{q}} a_{\mathbf{k}+\mathbf{q},\uparrow}^\dagger a_{\mathbf{k}'-\mathbf{q},\downarrow}^\dagger a_{\mathbf{k},\uparrow} a_{\mathbf{k}',\downarrow}, \quad (4.1)$$

where g is the pseudo-potential strength shown in Eq.(2.19), $\epsilon_k = \frac{\hbar^2 k^2}{2m}$, and $\hat{a}_{k,\sigma}$ is the annihilation operator of a species σ with momentum \mathbf{k} . When a spin minority (spin \downarrow) interacts with a majority Fermi gas (spin \uparrow), the ground state wavefunction

can be well approximated by the famous Chevy ansatz [25]:

$$|\psi\rangle = \phi_0 \hat{a}_{0\downarrow}^\dagger |\text{FS}_\uparrow\rangle + \sum_{\mathbf{k}, \mathbf{q}} \phi_{\mathbf{k}, \mathbf{q}} \hat{a}_{\mathbf{q}-\mathbf{k}\downarrow}^\dagger \hat{a}_{\mathbf{k}\uparrow}^\dagger \hat{a}_{\mathbf{q}\uparrow} |\text{FS}_\uparrow\rangle. \quad (4.2)$$

Here $|\text{FS}_\uparrow\rangle$ is an ideal majority Fermi sea. The first term in the wavefunction represents the non-interacting ground state, and the prefactor $\phi_0 = \sqrt{Z}$ quantifies the quasiparticle residue Z . The second term corresponds to the perturbed Fermi sea with a majority atom excited from momentum \mathbf{q} below Fermi surface to momentum k above Fermi surface plus a recoiled impurity. The energy of this state respect to the non-interacting ground state is:

$$\begin{aligned} \langle \Delta \hat{H} \rangle &= \sum_{\mathbf{k}, \mathbf{q}} |\phi_{\mathbf{k}, \mathbf{q}}|^2 (\epsilon_{\mathbf{q}-\mathbf{k}} + \epsilon_{\mathbf{k}} - \epsilon_{\mathbf{q}}) + \\ &\quad \frac{g}{V} \left[\sum_{\mathbf{q}} |\phi_0|^2 + \sum_{\mathbf{q}, \mathbf{k}, \mathbf{k}'} \phi_{\mathbf{k}', \mathbf{q}}^* \phi_{\mathbf{k}, \mathbf{q}} + \sum_{\mathbf{k}, \mathbf{q}, \mathbf{q}'} \phi_{\mathbf{k}, \mathbf{q}'}^* \phi_{\mathbf{k}, \mathbf{q}} + \sum_{\mathbf{k}, \mathbf{q}} (\phi_0^* \phi_{\phi_{\mathbf{k}, \mathbf{q}}} + \phi_{\phi_{\mathbf{k}, \mathbf{q}}}^* \phi_0) \right]. \end{aligned} \quad (4.3)$$

The sum over \mathbf{k} (\mathbf{k}') and \mathbf{q} (\mathbf{q}') are limited to $k > k_F$ and $q < k_F$. This covention will be kept in this section. At large momentum limit $k \ll k_F$, the wavefunction is governed by short range contact (Sec. 2.5.2) and scales as $\phi_{\mathbf{k}, \mathbf{q}} \sim 1/k^2$. The term $\sum_{\mathbf{k}, \mathbf{q}, \mathbf{q}'} \phi_{\mathbf{k}, \mathbf{q}'}^* \phi_{\mathbf{k}, \mathbf{q}} \sim \frac{1}{k_F}$ can be omitted in the calculation, since it is convergent while other terms either diverges or scale as k_F^3 . We will show that the diverging terms in Eq.(4.3) will be cancelled by the diverging g in Eq.(2.19).

To find the ground state of the system, we need to minimize the energy in Eq.(4.3) while conserving the normalization of the wavefunction:

$$\langle \psi | \psi \rangle = |\phi_0|^2 + \sum_{\mathbf{k}, \mathbf{q}} |\phi_{\mathbf{k}, \mathbf{q}}|^2 = 1. \quad (4.4)$$

Therefore, the ground state energy E and wavefunction $|\psi\rangle$ can be solved by finding the stationary point of the Lagrange multiplier $\mathcal{L} = \langle \Delta H \rangle - E(\langle \psi | \psi \rangle - 1)$. The

stationary point condition $\partial\mathcal{L}/\partial\phi_{\mathbf{k},\mathbf{q}}^* = 0$ and $\partial\mathcal{L}/\partial\phi_0^* = 0$ yields:

$$\phi_{\mathbf{k},\mathbf{q}}(\epsilon_{\mathbf{q}-\mathbf{k}} + \epsilon_{\mathbf{k}} - \epsilon_{\mathbf{q}}) + \frac{g}{V} \left(\sum_{\mathbf{k}'} \phi_{\mathbf{k}',\mathbf{q}} + \phi_0 \right) = E\phi_{\mathbf{k},\mathbf{q}}, \quad (4.5)$$

$$\frac{g}{V} \left(\sum_{\mathbf{q}} \phi_0 + \sum_{\mathbf{k},\mathbf{q}} \phi_{\mathbf{k},\mathbf{q}} \right) = E\phi_0. \quad (4.6)$$

An auxiliary function $\chi(\mathbf{q}) = \phi_0 + \sum_{\mathbf{k}} \phi_{\mathbf{k},\mathbf{q}}$ can be used to solve these equations. The previous equations can be written as:

$$\phi_{\mathbf{k},\mathbf{q}}(\epsilon_{\mathbf{q}-\mathbf{k}} + \epsilon_{\mathbf{k}} - \epsilon_{\mathbf{q}}) + \frac{g}{V} \chi(\mathbf{q}) = E\phi_{\mathbf{k},\mathbf{q}}, \quad (4.7)$$

$$\frac{g}{V} \sum_{\mathbf{q}} \chi(\mathbf{q}) = E\phi_0. \quad (4.8)$$

From Eq.(4.7), we get $\phi_{\mathbf{k},\mathbf{q}} = \frac{g}{V} \frac{\chi(\mathbf{q})}{E - (\epsilon_{\mathbf{k}} + \epsilon_{\mathbf{q}-\mathbf{k}} - \epsilon_{\mathbf{q}})}$, and this can be put back into the definition of $\chi(\mathbf{q})$ to give:

$$\chi(q) = \phi_0 \left[1 - \frac{g}{V} \sum_{\mathbf{k}} \frac{1}{E - (\epsilon_{\mathbf{k}} + \epsilon_{\mathbf{k}-\mathbf{q}} - \epsilon_{\mathbf{q}})} \right]^{-1}. \quad (4.9)$$

The self-consistent equation for energy E can be acquired by substituting $\chi(q)$ in Eq. (4.8) with Eq. (4.9):

$$\begin{aligned} E &= \sum_{\mathbf{q}} \frac{1}{\frac{V}{g} - \sum_{\mathbf{k}} \frac{1}{E - (\epsilon_{\mathbf{k}} + \epsilon_{\mathbf{k}-\mathbf{q}} - \epsilon_{\mathbf{q}})}}, \\ &= \sum_{\mathbf{q}} \frac{1}{\frac{mV}{4\pi\hbar^2a} - \sum_{\mathbf{q}'} \frac{1}{2\epsilon_{\mathbf{q}}} + \sum_{\mathbf{k}} \left[\frac{1}{(\epsilon_{\mathbf{k}} + \epsilon_{\mathbf{k}-\mathbf{q}} - \epsilon_{\mathbf{q}}) - E} - \frac{1}{2\epsilon_{\mathbf{k}}} \right]}. \end{aligned} \quad (4.10)$$

We can carry out the azimuthal integral and use the normalized energy $\tilde{E} = E/E_F$ and momentum $\tilde{k} = k/k_F$ in the final expression:

$$\tilde{E} = \int_0^1 d\tilde{q} \frac{2\tilde{q}^2}{\frac{\pi}{2k_F a} - 1 + \int_1^\infty d\tilde{k} \left[\frac{\tilde{k}}{2\tilde{q}} \ln \frac{2\tilde{k}^2 + 2\tilde{k}\tilde{q} - \tilde{E}}{2\tilde{k}^2 - 2\tilde{k}\tilde{q} - \tilde{E}} - 1 \right]}. \quad (4.11)$$

The energy of a Fermi polaron solved from Eq. (4.11) is shown in Fig. 4-1(a). At unitarity, the variational method gives a polaron energy $E_\downarrow = -0.607E_F$, which

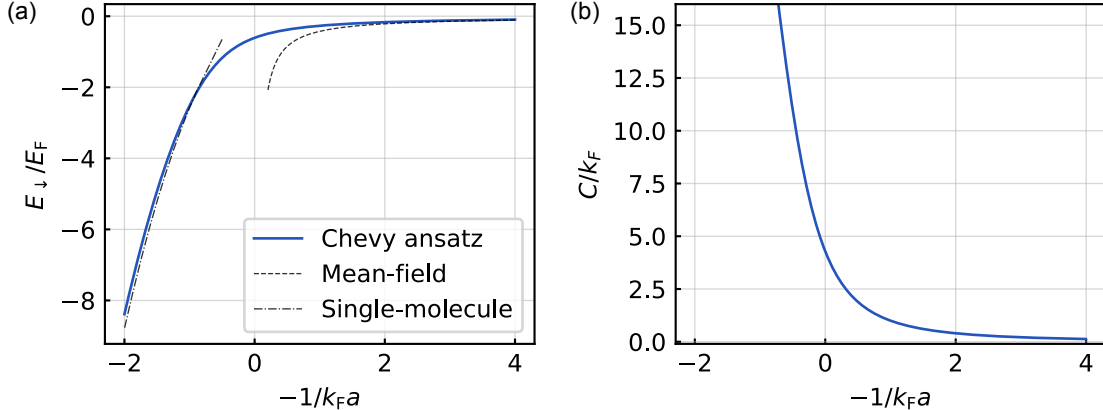


Figure 4-1: Energy (a) and contact (b) of a Fermi polaron acquired by a variational method. The dashed line corresponds to the attractive mean field energy $E_{\downarrow} = \frac{4\pi\hbar^2 a n_{\uparrow}}{m}$, while the dot-dashed line indicates the approximated energy of a molecule embedded in a Fermi sea (see eq. (4.12)).

agrees remarkably well with the value $E_{\downarrow} = -0.615E_F$ given by a bold diagrammatic Monte-Carlo calculation [157] $E_{\downarrow} = -0.615E_F$ and our experimental result $E_{\downarrow} = -0.60(5)E_F$. On the BEC side $a > 0$, the polaron energy intersects the energy of a molecule embedded in an interacting Fermi gas with $N-1$ particles at $(k_F a)^{-1} = 0.92$. This indicates a quantum phase transition from a polaron to a molecule state. The molecular state energy shown here is calculated in its BEC limit $a \rightarrow 0^+$:

$$E_m = -\frac{\hbar}{ma^2} - E_F + \frac{4\pi\hbar^2 a}{m} n_{\uparrow} + O(a^2), \quad (4.12)$$

while a detailed variational calculation on the "molaron" state energy [159] provides more accurate results in the universal regime and predicts a transition point at $(k_F a)^{-1} = 0.84$. This polaron to molecule phase transition have been observed in the rf spectroscopy of an imbalanced spin mixture [173], where the molecules show an overlapping rf spectrum between the minority and majority and the polarons have a distinct peak in the minority spectrum.

The contact C of a Fermi polaron can be calculated using the adiabatic sweep theorem Eq. (2.47), as shown in Fig. 4-1(b). In the Fermi polaron problem ¹, the

¹Note this is true for all the 2-spin Fermi mixture with s wave interaction

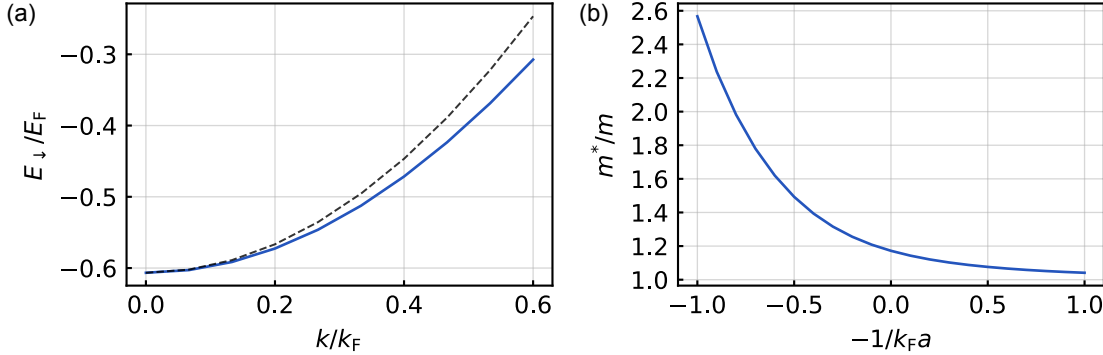


Figure 4-2: The energy dispersion (a) and effective mass (b) from the variational method. The blue solid line in (a) is calculated at unitarity, while the black dashed line is the dispersion of a bare particle, shifted by the zero momentum polaron energy. The effective mass is fitted with the energy dispersion $E_{\downarrow}(k)$ at $k < 0.05k_F$.

contact also quantifies the high momentum tail in both spin states:

$$n_{\downarrow}(\mathbf{k}) = n_{\uparrow}(\mathbf{k}) = \sum_{|\mathbf{q}| < k_F} |\phi_{\mathbf{q}, \mathbf{k}}|^2 = \frac{C}{k^4} \quad (k \gg k_F). \quad (4.13)$$

At unitarity, the variational method gives a polaron contact $C/k_F = 4.28$, which is consistent with our experiment result in Sec. 4.3.2.

The energy of a polaron with finite momentum \mathbf{p} can also be calculated using a modified trial wavefunction:

$$|\psi_{\mathbf{p}}\rangle = \phi_0 \hat{a}_{\mathbf{p}\downarrow}^\dagger |FS\rangle + \sum_{\mathbf{k}, \mathbf{q}} \phi_{\mathbf{k}, \mathbf{q}} \hat{a}_{\mathbf{p}+\mathbf{q}-\mathbf{k}\downarrow}^\dagger \hat{a}_{\mathbf{k}\uparrow}^\dagger \hat{a}_{\mathbf{q}\uparrow} |FS\rangle, \quad (4.14)$$

and the same variational method described in Eq. (4.7)-(4.10). Fig. 4-2 shows the effective mass m^* acquired by fitting the polaron dispersion $E_{\downarrow}(k)$ with $E_{\downarrow}(k) = \frac{\hbar^2 k^2}{2m^*}$. The effective mass at unitarity is $m^*/m = 1.17$.

4.1.2 Fermi liquid behavior: scattering rate

Landau's Fermi liquid theory provides a quasiparticle description for unordered interacting fermion systems at low temperatures. The interaction effect is manifested as the renormalized values for the dynamic properties of stable quasiparticles, such as effective mass or energy, while the quasiparticles are only weakly interacting with each

other. Fermi gases with highly imbalanced spin populations have been identified as Fermi liquid at low temperature, with dressed Fermi polarons acting as quasiparticles.

The stability of quasiparticles is a consequence of the restricted phase space for collisions due to Pauli blocking. As temperature increases, the accessible phase space increases, leading to a shortened lifetime for the Fermi polarons. In ref. [19], the decay rate of Fermi polarons is calculated under the framework of momentum relaxation. We can assume the minority gas have a mean velocity \mathbf{v} relative to the majority gas, the momentum density is $\mathbf{P}_\downarrow = n_\downarrow m^* \mathbf{v}$. The momentum relaxation time τ_P is defined as

$$\frac{d\mathbf{P}_\downarrow}{dt} = -\frac{\mathbf{P}_\downarrow}{\tau_P}. \quad (4.15)$$

The rate of change of the momentum of polarons can be calculated from a momentum independent interaction U and the phase space density of the two spin species:

$$\begin{aligned} \frac{d\mathbf{P}_\downarrow}{dt} = & -2\pi \frac{|U|^2}{V^3} \sum_{\mathbf{p}, \mathbf{p}', \mathbf{q}} \mathbf{p} [n_{\mathbf{p}\downarrow} n_{\mathbf{p}'\uparrow} (1 - n_{\mathbf{p}-\mathbf{q}\downarrow}) (1 - n_{\mathbf{p}'+\mathbf{q}\downarrow}) \\ & - n_{\mathbf{p}-\mathbf{q}\downarrow} n_{\mathbf{p}'+\mathbf{q}\uparrow} (1 - n_{\mathbf{p}\downarrow}) (1 - n_{\mathbf{p}'\downarrow})] \times \delta(\epsilon_{\mathbf{p}\downarrow} + \epsilon_{\mathbf{p}'\uparrow} - \epsilon_{\mathbf{p}-\mathbf{q}\downarrow} - \epsilon_{\mathbf{p}'+\mathbf{q}\uparrow}). \end{aligned} \quad (4.16)$$

Here n_\uparrow and n_\downarrow are both Fermi-Dirac momentum distribution, and $n_{\mathbf{k}\downarrow} = [1 + e^{\beta(h^2 k^2 / 2m^* - \hbar \mathbf{k} \cdot \mathbf{v} - \mu_\downarrow)}]^{-1}$ incorporates the effective mass and velocity shift. We also assume the scattering amplitude takes the form $U = \frac{\partial \mu_\downarrow}{\partial n_\uparrow} = \frac{2\pi^2}{mk_{F\uparrow}} \gamma$, $\gamma = E_\downarrow / E_{F\uparrow} = 0.61$ for unitarity.

The analytical form of the decay rate can be derived from Eq. (4.16) under two limits: $T \ll T_{F\downarrow} \ll T_{F\uparrow}$ or $T_{F\downarrow} \ll T \ll T_{F\uparrow}$. With a degenerate polaron gas $T \ll T_{F\downarrow} \ll T_{F\uparrow}$, the decay rate takes the form:

$$\frac{1}{\tau_P} = \frac{2\pi^3}{9} \frac{E_{F\uparrow}}{\hbar} |\gamma|^2 \frac{m^*}{m} \left(\frac{T}{T_{F\uparrow}} \right)^2 = 6.89 \times \frac{E_{F\uparrow}}{\hbar} |\gamma|^2 \frac{m^*}{m} \left(\frac{T}{T_{F\uparrow}} \right)^2, \quad (4.17)$$

while the decay rate in a non-degenerate polaron gas ($T_{F\downarrow} \ll T \ll T_{F\uparrow}$) is:

$$\frac{1}{\tau_P} = \frac{\pi^3 + 6\pi\zeta(3)}{9} \frac{E_{F\uparrow}}{\hbar} |\gamma|^2 \frac{m^*}{m} \left(\frac{T}{T_{F\uparrow}} \right)^2 = 5.96 \times \frac{E_{F\uparrow}}{\hbar} |\gamma|^2 \frac{m^*}{m} \left(\frac{T}{T_{F\uparrow}} \right)^2. \quad (4.18)$$

In both limits, the polaron decay rate scale as T^2 , which is a signature for the Fermi liquid behavior, and the two expressions only differ by a small numerical factor. The result from Eq. 4.18 is consistent with the measured spectral widths of Fermi polarons at finite temperature $T < 0.7 T_{F\uparrow}$ (see Sec. 4.3.1).

4.1.3 Fermi liquid behavior: equation of state

ENS experiment on the equation of state of a spin-imbalanced unitary gas [135, 138] shows the zero-temperature pressure can be well fitted by a Fermi liquid grand-canonical equation of state close to unitarity:

$$P(\mu_\uparrow, \mu_\downarrow) = P_0(\mu_\uparrow, m) + P_0(\mu_\downarrow - A\mu_\uparrow, m^*), \quad (4.19)$$

where $P_0(\mu, m) = \frac{1}{15\pi^2} \left(\frac{2m}{\hbar^2}\right)^{3/2} \mu^{5/2}$ is the pressure of an ideal Fermi gas, and A is the normalized single polaron energy: $E_\downarrow = AE_{F\uparrow}$. While Eq. (4.19) describes a mixture of ideal Fermi gas of majority cloud and polaron, a density coupling occurs due to the effective potential $A\mu_\uparrow$ experienced by polarons [115]. The density of each spin state is $n_\sigma = \frac{\partial P}{\partial \mu_\sigma}$:

$$n_\downarrow = n_0(\mu_\downarrow - A\mu_\uparrow, m^*), \quad (4.20)$$

$$n_\uparrow = n_0(\mu_\uparrow, m) - An_0(\mu_\downarrow - A\mu_\uparrow, m^*), \quad (4.21)$$

where $n_0(\mu, m) = \frac{1}{6\pi^2} \left(\frac{2m}{\hbar^2}\right)^{3/2} \mu^{3/2}$ is the density of an ideal Fermi gas. The density profile of the minority cloud reflects that of a polaronic ideal gas. A density increase is coupled to the presence of spin impurity $\delta n_\uparrow = -An_\downarrow$. In Sec. 4.4, we will show the experiment observation of the majority dressing cloud, and the equation of state Eq. 4.19 can be extended to finite temperature as long as the majority cloud is still degenerate $T \ll T_{F\uparrow}$.

4.2 Classical Boltzmann gas at high temperatures

4.2.1 Scattering rate

At high temperatures $T \gg T_{F\uparrow}$, stable quasiparticles can no longer exist due to the softened Fermi surface. As the characteristic momentum scale is the thermal momentum $p_T = \sqrt{2\pi mk_B T}$, the unitary scattering amplitude $f(k) \simeq \frac{i\hbar}{p_T}$ is suppressed as $f(k) \sim T^{-1/2}$. The scattering cross-section $\sigma = 4\pi|f|^2$ scales as $\sigma \sim T^{-1}$, and the classical relaxation rate is $\Gamma \simeq n\sigma v \sim T^{-1/2}$. A detailed T-matrix calculation in ref. [44] yields a vanishing real on-shell self-energy while its imaginary part corresponding to the particle relaxation rate Γ is:

$$\hbar\Gamma_\downarrow(\mathbf{p}) = \Sigma_\downarrow(\mathbf{p}, \epsilon_p - \mu) = \frac{8E_{F\uparrow}}{3\pi} \frac{\text{erf}(\sqrt{\pi}p/p_T)}{p/p_F}, \quad (4.22)$$

where erf is the error function. At low momenta $p \ll p_T$, the relaxation rate is momentum independent and indeed scale as $\Gamma \sim T^{-1/2}$:

$$\hbar\Gamma_\downarrow(\mathbf{p} \rightarrow 0) = \frac{16}{3\pi^{3/2}} E_{F\uparrow} \sqrt{\frac{T_{F\uparrow}}{T}}. \quad (4.23)$$

The mean relaxation rate can be acquired with an average over the thermal ensemble:

$$\langle \Gamma_\downarrow \rangle = \frac{8\sqrt{2}E_{F\uparrow}}{3\pi^{3/2}\hbar} \sqrt{\frac{T_{F\downarrow}}{T}}. \quad (4.24)$$

4.2.2 Virial expansion

The thermodynamics of a spin-imbalanced Fermi gas at high temperatures can be described with a Virial expansion [113]. The grand potential $\Omega \equiv -PV$ can be expanded in powers of fugacity $z_\sigma = \exp(-\mu_\sigma/k_B T)$, where $\sigma = \uparrow$ or \downarrow labels the spin state. Since the backbone of any interacting Fermi system is Fermi-Dirac statistics, we can organize Ω into two parts, one is that of a non-interacting Fermi gas, the other

is from the interaction effect:

$$\Omega(z_\uparrow, z_\downarrow, T) = \Omega^{(1)}(z_\uparrow, T) + \Omega^{(1)}(z_\downarrow, T) - k_B T Q_1 \left(\sum_{n=2}^{\infty} \sum_{k=0}^n z_\uparrow^{n-k} z_\downarrow^k \Delta b_{n,k} \right), \quad (4.25)$$

where $\Omega^{(1)}$ is the grand potential of a polarized non-interacting Fermi gas, $\Delta b_{n,k}$ are the Virial coefficients corresponding to interactions, and $Q_1 = \text{Tr}[\exp(-\hat{H}/k_B T)]$ is the single particle partition function. The symmetry between spin configurations requires $\Delta b_{n,k} = \Delta b_{n,n-k}$. By setting $z_\uparrow = z_\downarrow$, we get $\sum_{k=0}^n \Delta b_{n,k} = \Delta b_n$, where Δb_n are the Virial coefficients for a spin balanced system. Because there are no interactions in a spin polarized system, $\Delta b_{n,0} = \Delta b_{n,n} = 0$. Therefore, a third order Virial expansion for a spin-imbalanced system is

$$\Omega(z_\uparrow, z_\downarrow, T) = \Omega^{(1)}(z_\uparrow, T) + \Omega^{(1)}(z_\downarrow, T) - k_B T Q_1 \left(z_\uparrow z_\downarrow \Delta b_2 + \frac{z_\uparrow^2 z_\downarrow + z_\uparrow z_\downarrow^2}{2} \Delta b_3 \right). \quad (4.26)$$

In a homogeneous system, $Q_1 = 2V/\lambda^3$. The factor of 2 come from the 2 spin components. The single component grand potential is:

$$\Omega(z, T) = -V \frac{k_B T}{\lambda^3} \frac{2}{\sqrt{\pi}} \int_0^\infty t^{1/2} \ln(1 + ze^{-t}) dt, \quad (4.27)$$

where V is the volume and $\lambda = \left(\frac{2\pi\hbar}{mk_B T}\right)^{1/2}$ is the thermal de Broglie wavelength. At unitarity, the second order Virial coefficient can be solved exactly while the third order Virial coefficient is numerically calculated in Ref.[114]:

$$\Delta b_2 = 1/\sqrt{2}, \quad (4.28)$$

$$\Delta b_3 \simeq -0.355. \quad (4.29)$$

The density profile of the system can be acquired using the Gibbs-Duhem equation

$$n_\sigma = \frac{\partial P}{\partial \mu_\sigma} \Big|_T,$$

$$n_\uparrow(z_\uparrow, z_\downarrow, T) = n_0(z_\uparrow, T) + \lambda^3 [2z_\uparrow z_\downarrow \Delta b_2 + (2z_\uparrow^2 z_\downarrow + z_\downarrow^2 z_\uparrow) \Delta b_3], \quad (4.30)$$

$$n_\downarrow(z_\uparrow, z_\downarrow, T) = n_0(z_\downarrow, T) + \lambda^3 [2z_\uparrow z_\downarrow \Delta b_2 + (z_\uparrow^2 z_\downarrow + 2z_\downarrow^2 z_\uparrow) \Delta b_3], \quad (4.31)$$

where $n_0(z, T) = -\text{Li}_{3/2}(-z)\lambda^{-3}$ is the density of a spin-polarized ideal Fermi gas (see Sec. 2.2). In our experiment, we use Eq. (4.30) and (4.31) to fit high temperature density profiles in a hybrid trap, in order to determine the chemical potentials and temperature of the system.

The Virial expansion for the s-wave contact C can be acquired using Tan's adiabatic sweep theorem in the grand-canonical ensemble [197, 198, 112],

$$\left. \frac{\partial \Omega}{\partial(-a^{-1})} \right|_{\mu, T} = \frac{\hbar^2}{4\pi m} C. \quad (4.32)$$

The contact for a spin imbalanced system takes the form

$$C = \frac{4\pi m k_B T \lambda}{\hbar^2} Q_1 \left[z_\uparrow z_\downarrow c_2 + \frac{z_\uparrow^2 z_\downarrow + z_\uparrow z_\downarrow^2}{2} c_3 + O(z^3) \right], \quad (4.33)$$

where $c_n = \partial \Delta b_n / \partial (\lambda/a)$ are the contact Virial coefficients. Ref. [112] gives the values of the second and third order contact coefficients at unitarity

$$c_2 = 1/\pi, \quad (4.34)$$

$$c_3 \simeq -0.141. \quad (4.35)$$

A non-degenerate Fermi gas is insensitive to the spin degree of freedom, in contrast to the a low temperature Fermi gas, which will experience a phase transition from a polaronic Fermi liquid to a superfluid when the spin-imbalance is reduced. Hence the scattering rate and the Virial expansion for density and contact discussed above are valid for spin balanced systems as well.

4.3 rf spectroscopy of the quantum impurity

We measured the internal properties of the resonant impurities via radio frequency (rf) spectroscopy [173, 96, 97, 170] on a homogeneous Fermi gas [131, 83]. At low temperatures the peak position and width of the rf spectra reflect polaron energy and decay rate. Note that the decay rate of a quasiparticle can be viewed as the rate of momentum relaxation in a transport measurement (see Set. 4.1.2 and Ref. [19]). The wings of the rf spectra yield information about the short-range correlations and the contact [198, 8, 160, 175, 15], controlling the change in the polaron energy with interaction strength. With a strong resonant rf drive, we are able to observe a coherent Rabi oscillation between Fermi polarons and bare particles, whose Rabi frequency Ω provide a measurement on the quasiparticle residue Z .

For the spectroscopic studies we employ rf *ejection* spectroscopy, where the many body state is first prepared and then probed by transferring a small fraction of one spin component into a weakly or non-interacting final state. The three energetically lowest hyperfine states of ${}^6\text{Li}$ (labelled $|1\rangle$, $|2\rangle$, $|3\rangle$) are utilized to create and probe the strongly interacting spin mixture. The minority (impurity) and majority components are prepared in $|\downarrow\rangle = |1\rangle$ and $|\uparrow\rangle = |3\rangle$ and transferred via the rf drive into the final state $|f\rangle = |2\rangle$ [177]. All measurements have been performed at a magnetic field of 690 G, where the interactions between minority and majority atoms are unitarity limited. Final state interactions are weakly repulsive with $k_{F\uparrow}a_{\uparrow f} \lesssim 0.2$ ($a_{\uparrow f} = 62$ nm). The impurity concentration (minority to majority density ratio n_\downarrow/n_\uparrow) used for spectroscopic studies is controlled at 10(3)%.

4.3.1 Temperature dependence of the quasiparticle energy and lifetime

The rf response is linked to the probability that a hole of energy E and momentum \mathbf{p} is excited by ejecting a particle from the many-body state, as described by the occupied spectral function $\mathcal{A}_{-\downarrow}(\mathbf{p}, E)$ [173, 124, 202, 217]. Detecting a free particle of momentum \mathbf{p} after rf transfer implies a momentum \mathbf{p} and energy $E_{\mathbf{p}} = \mathbf{p}^2/2m -$

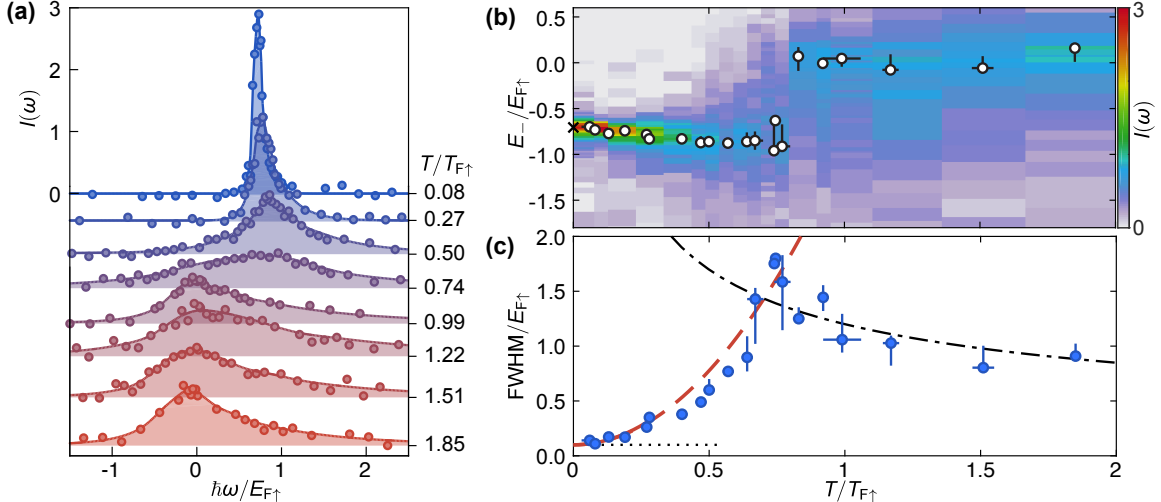


Figure 4-3: (a) Thermal evolution of the minority rf spectra. The impurity concentration is $n_\downarrow/n_\uparrow = 0.10 \pm 0.03$, the Rabi frequency $\Omega_R = 2\pi \cdot 0.5$ kHz and the pulse duration $T_{\text{Pulse}} = 1$ ms. (b) 2D plot of the minority spectra with maxima highlighted by white points. To reflect the energy of the initial many-body state, the spectra are shown with the inverse frequency $E_-/E_{F\uparrow}$, where $E_- = -\hbar\omega$. The cross corresponds to the theoretical zero temperature result for the polaron energy, including a correction for final state interactions [25, 115, 33, 158, 124]. (c) FWHM of the rf spectra. Dotted line: Fourier resolution limit; dashed red line: single-polaron decay rate $\Gamma/E_{F\uparrow} = 2.71(T/T_{F\uparrow})^2$ [19], offset by the Fourier limit; dash-dotted black line: FWHM of the rf spectrum in the high-temperature limit $\Gamma/E_{F\uparrow} = 1.2\sqrt{T_{F\uparrow}/T}$ [44, 195], reflecting the scattering rate in the classical, unitary Boltzmann gas. This figure is taken from Ref. [211].

$\mu_\downarrow - \hbar\omega$ of the leftover hole, where μ_\downarrow is the minority chemical potential and $\hbar\omega$ the energy of the rf photon with respect to the non-interacting transition. The number of transferred minority atoms $N_f(\omega)$ is proportional to the momentum integral of the occupied spectral function $\mathcal{A}_{-\downarrow}(\mathbf{p}, E_p)$. Fermi liquids feature a spectral function that is sharply peaked around $\epsilon_0 + \mathbf{p}^2/2m^* - \mu_\downarrow$, with the effective mass m^* and dressed energy ϵ_0 of the quasiparticles. The width of the peak is determined by the quasiparticle decay rate $\Gamma(p, T)$. For low temperatures and impurity concentrations only low-momentum states are populated and the peak position of the rf spectrum corresponds to the polaron binding energy [173].

Fig. 4-3(a) shows the evolution with temperature of the rf spectra. Here, we have

defined the normalized transfer:

$$I(\omega) = \frac{N_f(\omega)}{N_\downarrow} \frac{E_{F\uparrow}}{\hbar\Omega_R^2 T_{\text{Pulse}}}, \quad (4.36)$$

with the number of particles in the final (initial) state N_f (N_\downarrow), the pulse duration T_{Pulse} and the single particle Rabi frequency Ω_R . The term $\Omega_R^2 T_{\text{Pulse}}$ originates from the linear response to the rf pulse. The factor $E_{F\uparrow}/\hbar$ in I is owed to the scale invariance of the unitary Fermi gas, which implies that its spectral features, such as the peak position, amplitude and width directly scale with the Fermi energy [221, 217]. The normalized transfer only depends on the dimensionless parameters $T/T_{F\uparrow}$, n_\downarrow/n_\uparrow and $\hbar\omega/E_{F\uparrow}$, except for small corrections due to final state interactions and Fourier broadening that break the scale invariance of the system. The energy of the gas is measured by an isoenergetic release from the uniform to a harmonic trap (see Sec. 3.1.5). From the energy we obtain the temperature via the equation of state (see Sec. 4.4.3).

In the deeply degenerate limit ($T/T_{F\uparrow} < 0.1$) we observe a sharply defined resonance [Fig. 1(a)] signaling the stable, long-lived Fermi polaron [173]. Its width, defined by the full width at half maximum (FWHM), is limited by the Fourier resolution. From the position of the spectral peak at low temperature [Fig. 1(b)] and correction for weak final state interactions $E_f = \frac{4\pi\hbar^2 a_{\uparrow f}}{m} n_\uparrow$, we obtain a zero temperature polaron binding energy $A \equiv \epsilon_0/E_{F\uparrow} = -0.60 \pm 0.05$, with a linear extrapolation of the peak positions below $T/T_{F\uparrow} = 0.3$.

With increasing temperature the spectral peak initially shifts to higher frequencies and broadens significantly [Fig. 4-3(b) and (c)]. A rise in the polaron binding energy with temperature is expected given the increased scattering phase space of the majority spins, and is found theoretically [196, 132]. However, note that the position of the maximum at finite temperature and impurity concentration is influenced by the density of states, the difference in the effective mass between initial and final state [170] and the thermal population of momentum states. At a temperature near $T/T_{F\uparrow} \approx 0.75$ a sharp jump in the position of the global maximum to

$\omega \approx 0$ is observed [Fig. 4-3(a) and (b)] [196]. In this regime, the width of the spectra reaches its maximum, on the order of the Fermi energy [Fig. 4-3(c)]. Beyond this temperature, the position of the maximum remains constant at $\omega \approx 0$, as expected theoretically [44, 195]. It reflects a merging of attractive and repulsive branches, that are symmetric about zero on resonance [74], as the temperature exceeds their splitting.

The spectral function of a Fermi liquid is a single Lorentzian peak with a width given by the decay rate of the quasiparticles [155]. The width of the rf spectra is dominated by this decay rate at low temperatures. We observe a quadratic scaling of the width at low temperatures, a hallmark of Fermi liquid theory, in agreement with Eq. (4.18) [see Fig. 4-3(c)]. In the quantum critical regime around $T \approx T_{F\uparrow}$, the lifetime of the polarons drops below the Fermi time ($\hbar/E_{F\uparrow}$), signaling a breakdown of quasiparticles [141, 43, 53]. The decrease in width at temperatures beyond the Fermi temperature is expected for a classical Boltzmann gas with unitarity limited interactions. The thermal scattering rate in the dilute impurity limit is given by $\Gamma_{\text{th}} = n_{\uparrow}\sigma_{\text{th}}v_{\text{th}} \sim 1/\sqrt{T}$, with the thermal velocity $v_{\text{th}} \sim \sqrt{T}$, and the unitarity limited scattering cross section $\sigma_{\text{th}} \sim \lambda^2 \sim 1/T$.

4.3.2 Contact of the spin impurity

Apart from energies and lifetimes, rf spectra also yield the strength of short-range correlations, quantified by contact C (see Sec. 2.5.2). As the contact is a measure of pair correlations, the tails of the rf spectrum of the minority and majority components are identical [Fig 4-4(a)]. For unitary-limited interactions in the initial state, the normalized transfer rate in the high frequency limit is given by [15]

$$I(\omega) \underset{\omega \rightarrow \infty}{=} \frac{C}{2N_{\downarrow}k_{F\uparrow}} \frac{1}{2\sqrt{2}\pi(1 + \hbar\omega/E_b)} \left(\frac{E_{F\uparrow}}{\hbar\omega} \right)^{3/2}, \quad (4.37)$$

where $E_b = \hbar^2/ma_{\text{rf}}^2 \approx h \cdot 433$ kHz. The inset of Fig. 4-4(a) shows the corresponding fit of the tails with Eq. (4.37), leaving only the contact as a free parameter.

The temperature dependence of the contact displays a non-monotonic behaviour

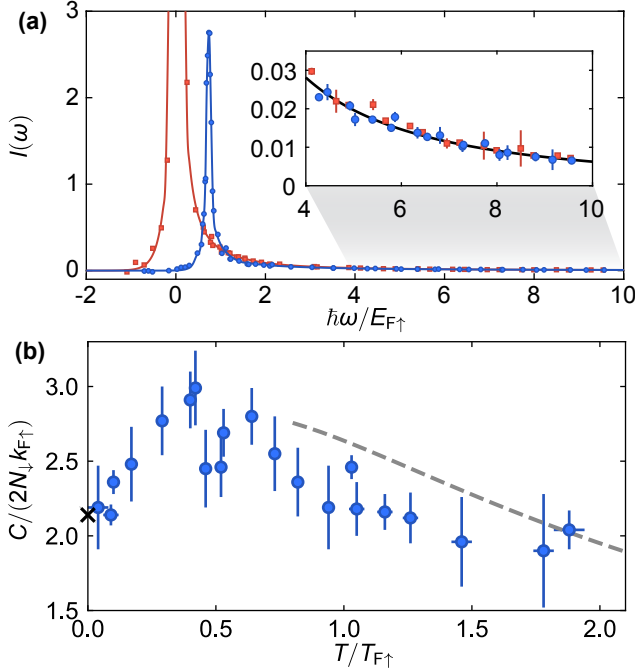


Figure 4-4: Contact of the spin-imbalanced Fermi gas. (a) Typical rf spectra of the spin minority (blue circles) and majority (red squares). The impurity concentration is 10%. The inset shows the high frequency tails of the minority and majority spectra together with a fit of Eq. (4.37). (b) Contact as a function of temperature, obtained by measuring the transferred fraction of atoms as a function of rf pulse duration for frequencies $\hbar\omega/E_{F\uparrow} > 5.5$ and use of Eq. (4.37). The gray dashed line shows the third order viral expansion [113] and the cross the result from the Chevy ansatz (see Sec. 4.1.1). This figure is taken from Ref. [211].

with a maximum located around $T \approx 0.4 T_{F\uparrow}$ [Fig. 4-4(b)]. The observed initial rise in temperature is partially expected from the increase in scattering phase space and has latter be confirmed by theoretical calculation using finite-temperature variational method [111]. In the high-temperature limit, the contact is proportional to the scattering cross section and vanishes as $1/T$.

4.3.3 Rabi oscillation between a Fermi polaron and a free particle

While the high-frequency wing of the rf spectra measures short-range correlations, the weight of the coherent polaron peak measures the quasiparticle residue Z , which is the extended wave function overlap between Fermi polarons and free particles [124].

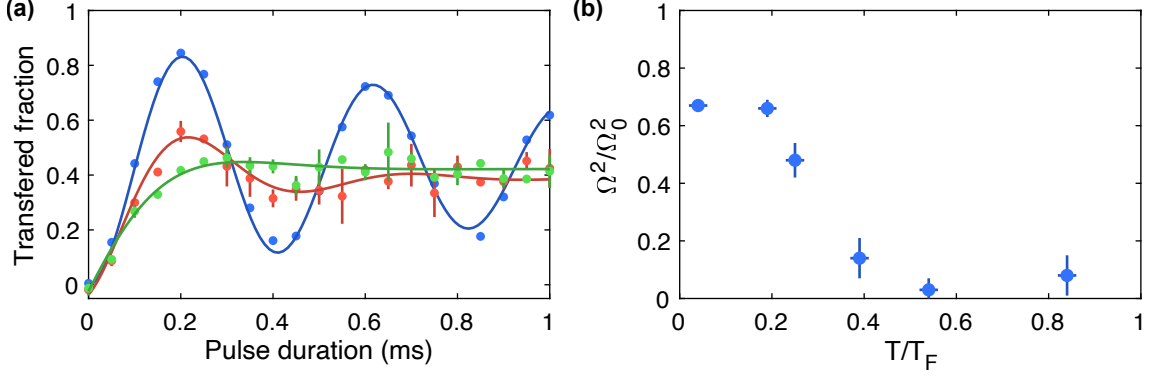


Figure 4-5: Polaron Rabi oscillations. (a) The fraction of impurities transferred to the final state under an rf drive with a Rabi frequency of 2.9 kHz. The driving frequency is set by the spectral peak positions shown in Fig 4-3(b). The temperature of the system is $T/T_{F\uparrow} = 0.04$ (blue), 0.25 (red), and 0.39 (green), and the impurity concentration is $n_\downarrow/n_\uparrow = 0.10(3)$. Solid lines are the damped sinusoidal fits used to extract Ω . (b) Ω/Ω_0 for the impurity measured at various temperature.

We measure the weight of coherent polaron peak by driving Rabi oscillations on the polaron-to-free transition [96, 170], as shown in Fig. 4-5(a). A Fermi polaron, whose wave function has the form in Eq. (4.14), can be coherently driven into a non-interacting state $\hat{a}_{\mathbf{p},f}^\dagger |\text{FS}_\uparrow\rangle$, where $\hat{a}_{\mathbf{p},f}^\dagger$ is the creation operator of a final state atom with momentum \mathbf{p} . The polaron rabi frequency Ω under the rf driving $\hat{V}_{\text{rf}} = \frac{\hbar\Omega_0}{2} \sum_k [\hat{a}_{\mathbf{k},f}^\dagger \hat{a}_{\mathbf{k},\downarrow} + \hat{a}_{\mathbf{k},\downarrow}^\dagger \hat{a}_{\mathbf{k},f}]$ is

$$\begin{aligned} \frac{\hbar\Omega}{2} &= \langle \text{FS}_\uparrow | \hat{a}_{\mathbf{p},f} \hat{V}_{\text{rf}} \left(\phi_0 \hat{a}_{\mathbf{p}\downarrow}^\dagger |\text{FS}_\uparrow\rangle + \sum_{\mathbf{k},\mathbf{q}} \phi_{\mathbf{k},\mathbf{q}} \hat{a}_{\mathbf{p}+\mathbf{q}-\mathbf{k}\downarrow}^\dagger \hat{a}_{\mathbf{k}\uparrow}^\dagger \hat{a}_{\mathbf{q}\uparrow} |\text{FS}_\uparrow\rangle \right) \right) \\ &= \phi_0 \frac{\hbar\Omega_0}{2}, \end{aligned} \quad (4.38)$$

where Ω_0 is the bare atomic Rabi frequency. Therefore $\Omega^2/\Omega_0^2 = \phi_0^2 = Z$.

The measured polaron Rabi frequency at various temperature is shown in Fig. 4-5(b). At low temperatures $T < 0.2 T_{F\uparrow}$, we observe a constant residue $Z = 0.68(2)$, which is consistent with result from injection spectroscopy in Ref. [170] and close to the theoretical prediction by the variational method [25] $Z = 0.78$. At higher temperatures the quasiparticle residue drops rapidly, which is consistent with the quasiparticle breakdown observed in the width and peak shift of the rf spectra.

4.4 Thermodynamics of spin-imbalanced Fermi gases

While rf spectroscopy measures the internal properties of the spin impurities, the thermodynamic properties of the polaron gas are directly obtained from the *in situ* density profile in a hybrid trapping potential (see Sec. 3.1.5). By comparing the density of majority cloud with that of an ideal Fermi gas, we measure the number of atoms in the majority dressing cloud of a polaron. The compressibility of the polaronic Fermi gas at low temperature yields the effective mass of Fermi polarons. The pressure measurement in the hybrid trap provides the equation of state needed for temperature determination.

4.4.1 Density of dressing clouds

The polaron is an extended object with pair correlations extending out over distances beyond the majority interparticle spacing [203]. We thus set out to probe the entire cloud of excess majority atoms surrounding the impurity spin of density

$$\Delta n_{\uparrow} = n_{\uparrow}(\mu_{\uparrow}, \mu_{\downarrow}, T) - n_0(\mu_{\uparrow}, T) \quad (4.39)$$

by *in situ* density measurements [Fig. 4-6 (a)]. Here, $n_{\uparrow}(\mu_{\uparrow}, \mu_{\downarrow}, T)$ is the actual, measured density of the interacting majority component and $n_0(\mu_{\uparrow}, T)$ corresponds to the density of a non-interacting gas with the same temperature and majority chemical potential. Under the local density approximation the knowledge of $n_{\uparrow,\downarrow}(U)$ can be used to extract a variety of thermodynamic quantities [134, 138, 101]. The majority chemical potential and temperature are obtained from the low-fugacity wings of the gas. In the case of a partially spin polarized wing at high temperatures we use the third order virial expansion [113], whereas for a fully spin polarized wing at low temperatures we use the ideal equation of state. For the lowest temperatures the excess majority density per minority atom is $\Delta n_{\uparrow}/n_{\downarrow} = 0.63(5)$ [Fig. 4-6(b)]. For increasing temperature the excess density drops until it reaches the value predicted by the virial expansion for the density. $\Delta n_{\uparrow}/n_{\downarrow}$ displays no dependency on the minority

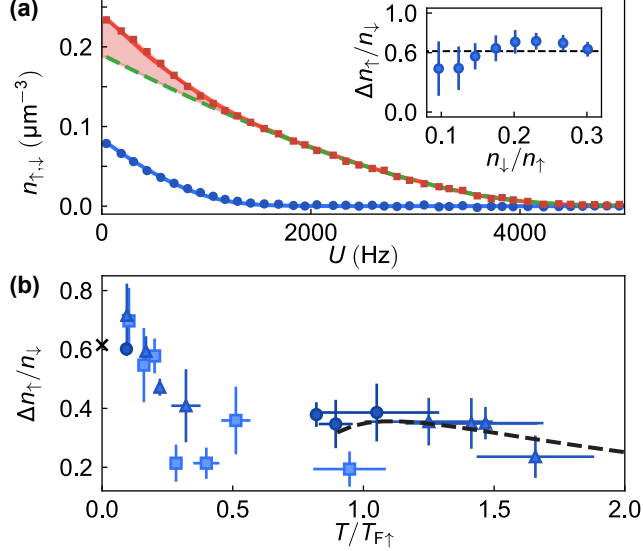


Figure 4-6: Observation of the majority excess cloud. (a) Density profiles in a harmonically varying external potential U . Blue (red) data points indicate the profiles of the minority (majority) spin component. The reduced temperature of the gas is $T/T_{F\uparrow} = 0.07$ in the trap center ($U = 0$). The green dashed line represents the equation of state of the ideal Fermi gas, the red (blue) solid line is the Fermi liquid ansatz (Eq. (4.41)) for the majority (minority) component. The red shaded area displays the excess majority density Δn_{\uparrow} . Inset: Dependence of the excess majority to minority ratio on the impurity concentration. (b) Temperature dependence of the majority excess cloud. Data points show the excess majority density Δn_{\uparrow} for an impurity concentration of $n_{\downarrow}/n_{\uparrow} = 0.1$ (squares), $n_{\downarrow}/n_{\uparrow} = 0.2$ (triangles) and $n_{\downarrow}/n_{\uparrow} = 0.3$ (circles). The cross indicates the low-temperature prediction of the Fermi liquid ansatz $\Delta n_{\uparrow}/n_{\downarrow} = -A = 0.615$ [158] and the dashed line the third order virial expansion. This figure is taken from Ref. [211].

concentration within our error up to $n_{\downarrow}/n_{\uparrow} = 0.3$.

To elucidate the origin of the excess density from thermodynamics, we extend the ENS Fermi liquid pressure ansatz [135, 138] discussed in Sec. 4.1.2 to finite temperature:

$$P(\mu_{\uparrow}, \mu_{\downarrow}, T) = P_0(\mu_{\uparrow}, T, m) + P_0(\mu_{\downarrow} - A\mu_{\uparrow}, T, m^*). \quad (4.40)$$

Here, $P_0(\mu, T, m)$ is the pressure of the non-interacting Fermi gas with mass m (see Sec. 2.2). This ansatz describes the total pressure of the system as the sum of the partial pressure of the non-interacting majority component and the partial pressure of an ensemble of polarons with an effective chemical potential of $\mu_{\downarrow} - A\mu_{\uparrow}$ and an effective mass m^* . It contains weak interactions among the polarons that amount to

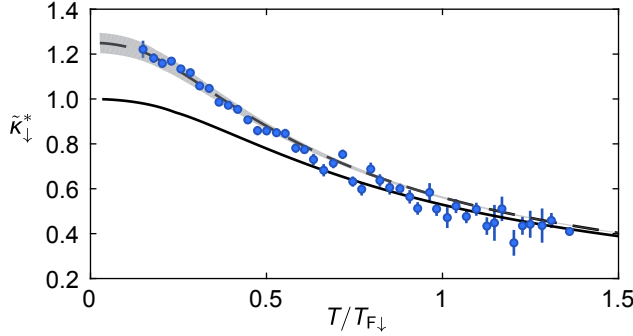


Figure 4-7: Isothermal minority compressibility. The solid line is the Fermi liquid ansatz for $m^*/m = 1$, while the dashed line corresponds to a fit with an effective mass of $m^*/m = 1.25(5)$ assuming $A = -0.615$ [158]. The grey shaded area represents the standard deviation of the fit. For the entire range of temperatures displayed the majority component is degenerate ($T/T_{F\uparrow} < 0.2$). This figure is taken from Ref. [211].

a few percent of the total energy of the system [129]. From this pressure ansatz the density can be calculated with the Gibbs-Duhem equation at constant temperature and scattering length ($dP = n_\uparrow d\mu_\uparrow + n_\downarrow d\mu_\downarrow$):

$$\begin{aligned} n_\uparrow(\mu_\uparrow, \mu_\downarrow, T) &= n_0(\mu_\uparrow, T) - An_\downarrow(\mu_\uparrow, \mu_\downarrow, T), \\ n_\downarrow(\mu_\uparrow, \mu_\downarrow, T) &= (m^*/m)^{\frac{3}{2}} n_0(\mu_\downarrow - A\mu_\uparrow, T), \end{aligned} \quad (4.41)$$

where $n_0(\mu, T) \equiv \partial P_0 / \partial \mu$ is the density of the non-interacting gas. Each minority is accumulating on average $|A| = 0.6$ excess majority atoms over the non-interacting limit, in agreement with our measured value [Fig. 4-6(b)].

4.4.2 Polaronic Fermi gases

Since the Fermi liquid ansatz describes the thermodynamics accurately in the low temperature regime $T/T_{F\uparrow} < 0.2$, we now focus on this temperature regime and utilize the ansatz to determine the effective mass of the polarons from a measurement of the minority compressibility. In analogy to the total compressibility of the gas the normalized isothermal minority compressibility is defined as $\tilde{\kappa}_\downarrow \equiv -dE_{F\downarrow}/dU_{\text{eff}}$ [101]. Here, $U_{\text{eff}} = (1 - A)U$ is the effective potential of the minority component generated by the interaction with the majority component [115, 136]. Using Eq. (4.41) for the

minority density one finds

$$\tilde{\kappa}_\downarrow(T/T_{F\downarrow}) = \frac{m^*}{m} \frac{\kappa_0(T, T_{F\downarrow} \cdot m^*/m)}{\kappa_0(0, T_{F\downarrow} \cdot m^*/m)}, \quad (4.42)$$

where $\kappa_0(T, T_{F\downarrow})$ is the compressibility of the non-interacting Fermi gas at given temperature and density (Fermi temperature). Fig. 4-7 shows the measured isothermal compressibility of the minority component. A fit of Eq. (4.42) fixing $A = -0.615$ [158] results in an effective mass of $m^*/m = 1.25(5)$, which is in agreement with results obtained from diagrammatic Monte Carlo [158], a variational ansatz [33] and previous low-temperature experiments [136, 134, 138]. The saturation of the minority compressibility at low temperatures signals the formation of a degenerate Fermi sea of polarons.

4.4.3 Equatation of state calbration

An isoenergetic expansion into the hybrid trap is used to measure the total energy of a homogeneous unitary gas (see Sec. 3.1.5). The conversion of the total energy into the corresponding temperature requires knowledge of the finite-temperature equation of state of the system. For this purpose, we measure the finite temperature pressure of the spin-imbalanced unitary Fermi gas. As mentioned in Sec. 2.4.1, at unitarity pressure P and energy density ϵ are directly related through $\epsilon = 3/2 P$. From the equation for hydrostatic equilibrium and the local density approximation follows for the pressure $P(U) = \int_U^\infty n(U)dU$ [101] [Fig. 4-8(b)]. The impurity concentration is varying in this non-uniform trapping potential [Fig. 4-8(c)]. To fill the three-dimensional parameter space $P(n, n_\downarrow/n_\uparrow, T)$, we measure density profiles for varying initial evaporation parameters. The temperature is obtained from third order virial expansion fits [113] to the low-fugacity tails of the gas or fits with the equation of state of the non-interacting Fermi gas, in case of spin-polarized tails.

Figure 4-8(d) shows the equation of state at a fixed impurity concentration of $n_\downarrow/n_\uparrow = 0.1$. For the unitary Fermi gas, the normalized pressure and energy are identical: $P/P_{0\uparrow} = E/E_{0\uparrow}$, with the ground state energy $E_{0\uparrow} = 3/5 N_\uparrow E_{F\uparrow}$ and pres-

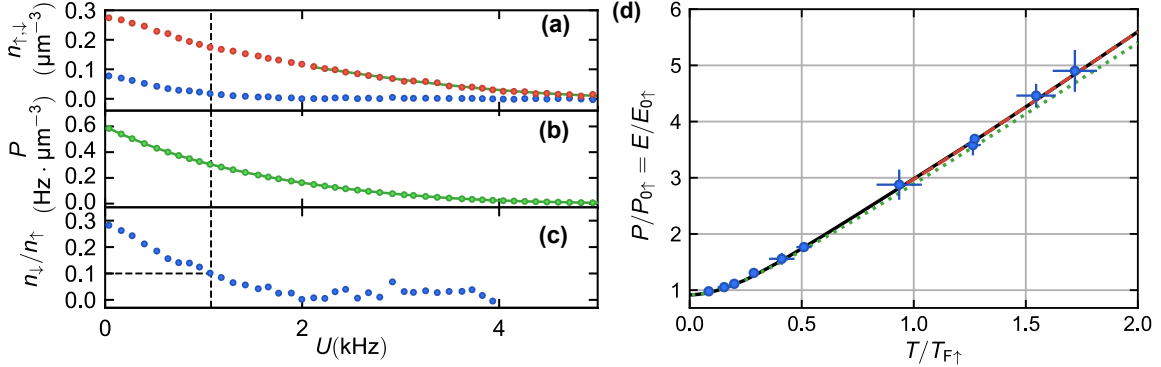


Figure 4-8: Pressure of the spin-imbalanced unitary Fermi gas. (a) An example of *in situ* density profiles of the majority (red) and minority (blue) component in the hybrid trap. The temperature of $T = 31 \pm 2$ nK is determined from a fit of the spin-polarized tail of the majority component with the equation of state of the non-interacting Fermi gas (green solid line). The majority Fermi energy in the center of the trap ($U = 0$) is $E_{F\uparrow}/\hbar = 5.4 \pm 0.2$ kHz. (b) The local pressure of the gas, obtained from integrating the density profiles. (c) The local minority concentration. The relevant values for a minority concentration of $n_{\downarrow}/n_{\uparrow} = 0.1$ are indicated with the dashed line. (d) The equation of state of the gas at fixed impurity concentration of $n_{\downarrow}/n_{\uparrow} = 0.1$. Our measurement is compared with the Fermi liquid ansatz (green dotted line) and 3rd order Virial expansion (red dashed line). An interpolation function (black solid line) is used to connect the Fermi liquid ansatz and Virial expansion. This figure is taken from Ref. [211].

sure $P_{0\uparrow} = 2/5 n_{\uparrow} E_{F\uparrow}$ of the majority atoms. At low temperatures, the normalized pressure is in agreement with the Fermi liquid pressure ansatz [Eq. (4.40)], while at higher temperatures it is in agreement with the virial expansion. Note the difference between the two curve is small, since the pressure of an highly spin-imbalanced Fermi gas is dominated by the kinetic energy of the majority gas, which can be approximated as an ideal Fermi gas. We use an interpolation function that connects the high and low temperature regime to be able to determine the temperature for arbitrary pressure (energy) values [Fig. 4-8(d)].

Chapter 5

Heat transport in unitary Fermi gases

This chapter presents the observation of heat transport in spin-balanced, unitary Fermi gases. In the superfluid phase, the evolution of the unitary gas is governed by the two-fluid hydrodynamics [104, 93, 77, 105]. The superfluid and the normal components form distinct, coupled hydrodynamic fluids and can oscillate in- or out-of-phase with each other, like two coupled pendula. The heat transport in this regime takes the form of an entropy wave called second sound [104, 151], with counter-flowing superfluid and normal components. We can contrast it with the first sound which is the in-phase oscillation between the superfluid and normal components and is similar to the common density wave observed in ordinary materials. A detailed study on the dispersion and dissipation of first sound is attached in Appendix D. Above the transition temperature T_c , the superfluid component vanishes, and the heat propagates diffusively, with a time scale set by thermal conductivity and specific heat.

Using the temperature dependent radio-frequency spectrum as a thermometer [211, 130], we are able to directly measure the local temperature variations at low temperatures $T \leq 0.25T_F$. This novel thermometry method allows independent measurements of the heat and density response functions under external perturbations, which contains complete information about the system. For higher temperatures $T > 0.25T_F$, heat diffusion processes can be indirectly observed using the density-temperature coupling. In addition, the translational symmetry in a homogeneous gas enables the

observations of sound and heat diffusion modes with a well-defined wavevector \mathbf{k} .

5.1 Superfluid hydrodynamics

In this section, I outline the theoretical framework of two-fluid hydrodynamics of a superfluid. The hydrodynamics of a normal fluid can be described under the same framework by setting the superfluid density to zero.

5.1.1 Two-fluid model

The two-fluid model is proposed by Tisza [201] and Landau [104] to explain the hydrodynamics in a superfluid ^4He liquid (also called helium-II). Its principle translates to many other superfluid matters, including the unitary Fermi gas. Experiments on the viscosity of helium-II had found seemingly contradictory results. On the one hand, the superfluid can flow through a thin capillary or fine porous material with an arbitrarily small inner diameter, suggesting the absence of viscosity. On the other hand, a rotating propeller in the superfluid is able to drive the rotation of another paddle wheel. This effect suggests the superfluid is still viscous. The two-fluid model solved this paradox by assuming there are two fluid components in a superfluid. The first one is the superfluid component which is non-viscous and can flow freely through a thin capillary, corresponding to the coherent macroscopic wavefunction of the bosons or fermion pairs. The second one is the normal component which has non-zero viscosity and carries all the thermal excitations. The two-fluid model provides satisfactory explanations on a series of phenomena in superfluids. The famous fountain effect originates from the superfluid component trying to fill the "superfluid vacuum" caused by heating. The emerging non-rotating superfluid components when temperature is cooled below T_c yields a reduction in the moment of inertia [72, 166]. The emergence of second sound, as we are going to discuss in detail in Sec. 5.3, is a counter-oscillation between superfluid and normal components.

The motion of the superfluid and normal part can be described by two velocity fields \mathbf{v}_s and \mathbf{v}_n , and their corresponding density ρ_s and ρ_n . The sum of the two

densities is the total density of the system

$$\rho = \rho_n + \rho_s. \quad (5.1)$$

Thus, the momentum density \mathbf{j} of the system can be divided into two parts:

$$\mathbf{j} = \rho_s \mathbf{v}_s + \rho_n \mathbf{v}_n. \quad (5.2)$$

The superfluid velocity \mathbf{v}_s is a result of phase gradient in the macroscopic wavefunction $\mathbf{v}_s = \frac{\hbar}{m} \nabla \Phi$, therefore it is a non-rotating field $\nabla \times \mathbf{v}_s = 0$. Conceptually, the normal part of the superfluid is an ensemble of all the thermal excitations in the superfluid. The mass of the normal fluid corresponds to the inertia of these excitations. If we assume the thermal excitations are well-defined quasiparticles, their energy distribution is

$$n(E) = (e^{E/k_B T} \pm 1)^{-1}, \quad (5.3)$$

where the \pm sign is determined by the quantum statistics of the quasiparticle (see Sec. 2.1). We consider a quasiparticle with a momentum \mathbf{p} and energy $\mathcal{E}(\mathbf{p})$ in a frame moving with the superfluid component at \mathbf{v}_s , its energy is $E = \mathcal{E}(\mathbf{p}) + \mathbf{p} \cdot \mathbf{v}_s$ in the rest frame, and $E = \mathcal{E}(\mathbf{p}) + \mathbf{p} \cdot (\mathbf{v}_s - \mathbf{v}_n)$ in the frame moving with the normal velocity \mathbf{v}_n . In the reference frame moving at \mathbf{v}_s , the momentum density is

$$\mathbf{j}_0 = \mathbf{j} - \rho \mathbf{v}_s = \rho_n (\mathbf{v}_n - \mathbf{v}_s). \quad (5.4)$$

This relative momentum is solely contributed by the thermal excitations which follow the energy distribution Eq. (5.3) [93]

$$\rho_n (\mathbf{v}_n - \mathbf{v}_s) = \int \mathbf{p} n(\mathcal{E}(\mathbf{p}) + \mathbf{p} \cdot (\mathbf{v}_s - \mathbf{v}_n)) \frac{d^3 p}{h^3}. \quad (5.5)$$

Note that the Doppler effect skews the momentum distribution on the right-hand side of Eq. (5.5), resulting in more particles with momentum aligned with $\mathbf{v}_n - \mathbf{v}_s$. By setting the velocity displacement $(\mathbf{v}_n - \mathbf{v}_s)$ to be infinitesimally small, density of the

normal component ρ_n can be solved at thermal equilibrium using Eq. (5.5). For an isotropic energy dispersion $\mathcal{E}(p)$, Eq. 5.5 can be simplified into

$$\begin{aligned}\rho_n(v_n - v_s) &= \int_0^\infty \frac{dp}{h^3} \int_0^\pi d\theta 2\pi p^2 \sin \theta p \cos \theta n(\mathcal{E}(p) + p(v_n - v_s) \cos \theta) \\ &= \int_0^\infty \frac{dp}{h^3} \frac{4\pi p^4}{3} \frac{\partial n(\mathcal{E}(p))}{\partial \mathcal{E}} (v_n - v_s),\end{aligned}\quad (5.6)$$

$$\rho_n = \int_0^\infty \frac{4\pi p^4}{3} \frac{\partial n(\mathcal{E}(p))}{\partial \mathcal{E}} \frac{dp}{h^3}. \quad (5.7)$$

The normal component density ρ_n increases when more thermal excitations are created by a rising temperature. At the superfluid to normal fluid transition temperature T_c , the normal component density ρ_n equals total density ρ , and the superfluid density ρ_s goes to zero.

Next, I will demonstrate a mean-field calculation for the normal fluid density in unitary Fermi gases using a model including phonon and pair-breaking excitations. The bosonic phonons have a linear energy dispersion relation

$$\mathcal{E}_{\text{ph}}(\mathbf{p}) = p c_1. \quad (5.8)$$

At low temperatures, the speed of first sound $c_1 = v_F \sqrt{\xi/3}$ is determined by the Bertsch parameter ξ [101, 216]. The pair-breaking excitations are fermionic quasiparticles with a minimum energy gap Δ close to Fermi surface. Hence, we model the pair-breaking excitations with energy dispersion

$$\mathcal{E}_{\text{pb}}(\mathbf{p}) = \frac{(p - p_F)^2}{2M} + \Delta, \quad (5.9)$$

where M is the effective mass of quasiparticles close to Fermi surface. The momentum distribution of the phonons obeys Bose-Einstein distribution. Though the gapped pair-breaking excitations are spin-1/2 fermions, its momentum distribution can be approximated with a classical distribution at low temperature $k_B T \ll \Delta$.

$$n_{\text{ph}}(\mathbf{p}) = \frac{1}{e^{\mathcal{E}_{\text{ph}}(\mathbf{p})/k_B T} - 1} \quad (5.10)$$

$$n_{\text{pb}}(\mathbf{p}) = \frac{1}{e^{\mathcal{E}_{\text{pb}}(\mathbf{p})/k_{\text{B}}T} + 1} \approx e^{-\mathcal{E}_{\text{pb}}(\mathbf{p})/k_{\text{B}}T} \quad (5.11)$$

The contribution to energy per particle by phonon and pair-breaking excitations can be calculated using

$$\Delta\epsilon = \int \mathcal{E}(\mathbf{p}) n(\mathbf{p}) \frac{d^3\mathbf{p}}{h^3}. \quad (5.12)$$

The energy contributions of the phonons $\Delta\epsilon_{\text{ph}}$ and broken pairs $\Delta\epsilon_{\text{pb}}$ are

$$\frac{\Delta\epsilon_{\text{ph}}}{\epsilon_0} = \frac{\pi^4}{48} \frac{(T/T_F)^4}{(\xi/3)^{3/2}}, \quad (5.13)$$

$$\frac{\Delta\epsilon_{\text{pb}}}{\epsilon_0} = 5\sqrt{\pi} e^{-\Delta/k_{\text{B}}T} \sqrt{\frac{M}{m} \frac{T}{T_F}} \left(\frac{\Delta}{E_F} + \frac{T}{2T_F} + \frac{1}{2} \frac{T\Delta M}{T_F E_F m} + \frac{3}{4} \frac{T^2 M}{T_F^2 m} \right), \quad (5.14)$$

where $\epsilon_0 = \frac{3}{5}nE_F$ is the energy density of an ideal Fermi gas (see Sec 2.4.2). The total energy density ϵ of the unitary Fermi gas under this model is

$$\frac{\epsilon}{\epsilon_0} = \xi + \frac{\Delta\epsilon_{\text{ph}}}{\epsilon_0} + \frac{\Delta\epsilon_{\text{pb}}}{\epsilon_0}. \quad (5.15)$$

Fitting the measured equation of state of unitary Fermi gas [101] in the superfluid phase $T < T_c$ with Eq. 5.15 yields a superfluid gap $\Delta/E_F = 0.49(2)$, effective mass $M/m = 1.45(0.22)$, and Bertsch parameter $\xi = 0.363(2)$.

From Eq. 5.7, we can calculate the contribution to the normal fluid density from phonons $\rho_{n,\text{ph}}$ and broken pairs $\rho_{n,\text{pb}}$

$$\rho_{n,\text{ph}}/\rho = \frac{\pi^4}{120} \frac{(T/T_F)^4}{(\epsilon/3\epsilon_0)^{5/2}}, \quad (5.16)$$

$$\rho_{n,\text{pb}}/\rho = 2\sqrt{\pi} e^{-\Delta/k_{\text{B}}T} \sqrt{\frac{MT_F}{mT}}. \quad (5.17)$$

The total normal component density of the system is $\rho_n = \rho_{n,\text{ph}} + \rho_{n,\text{pb}}$. The phase transition point is where the normal component density equals total density. The superfluid component density is $\rho_s = \rho - \rho_n$. Fig. 5-1A shows the superfluid fraction calculated using this model. In Sec. 5.1.3 and 5.3.4, we are going to show that the speed of second sound calculated from this "phonon+pair-breaking" model reaches a

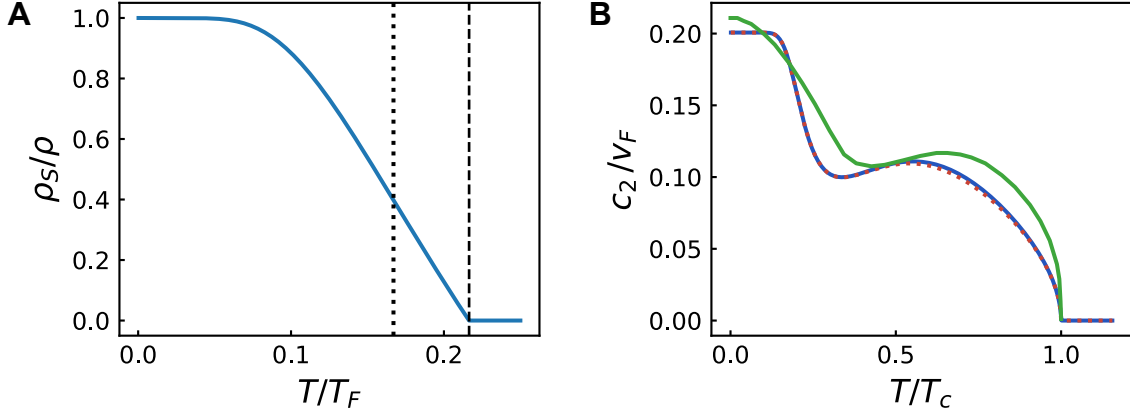


Figure 5-1: (A) The superfluid fraction calculated from the phonon + pair breaking model. This model indicates a phase transition point at $T_c/T_F = 0.216$ (vertical dashed line), while the experimental result [101] is $T_c/T_F = 0.167$. (B) The uncoupled c_{20} (blue solid curve) and coupled c_2 (red dashed line) speed of second sound calculated from the model. This result shows a qualitative agreement with the speed of second sound calculated from the theory of Nozières and Schmitt-Rink [200] (green solid line).

qualitative agreement with a more sophisticated Nozières and Schmitt-Rink (NSR) calculation [200] and our experimental results. Note that in this model we have not considered the temperature dependence of the pairing gap, the finite lifetime of pair-breaking excitations, and the effect of quantum fluctuations [199]. These facts provide a possible explanation on the discrepancy between the calculated critical temperature at $T_c = 0.216 T_F$ and experimental result $T_c = 0.167(13) T_F$ [101].

5.1.2 Hydrodynamic equations of a superfluid

At wavelengths much longer than the mean free path and frequencies much lower than the single-particle relaxation rates, the motion of a superfluid can be described by the hydrodynamic equations. In these equations, we assume thermal equilibrium is achieved locally but not globally. For any system, the hydrodynamic equations governing the density ρ , momentum density \mathbf{j} , and energy density ϵ follows from the

conservation of total mass, momentum, and energy:

$$\frac{\partial \rho}{\partial t} + \nabla \cdot \mathbf{j} = 0, \quad (5.18a)$$

$$\frac{\partial j_i}{\partial t} + \frac{\partial}{\partial r_k} (\Pi_{ik} + \tau_{ik}) = 0, \quad (5.18b)$$

$$\frac{\partial \epsilon}{\partial t} + \nabla \cdot (\mathbf{Q} + \mathbf{Q}') = 0. \quad (5.18c)$$

Here Π_{ik} and \mathbf{Q} are the conservative momentum flux tensor and energy flux, while τ_{ik} and \mathbf{Q}' denotes the dissipative part of momentum and energy flux. For a superfluid, another equation for the evolution of \mathbf{v}_s is needed. Since \mathbf{v}_s is irrotational, its driving force can be expressed as gradient of a scalar field

$$\frac{\partial \mathbf{v}_s}{\partial t} + \nabla \left(\frac{1}{2} v_s^2 + \phi + h \right) = 0, \quad (5.19)$$

where we denote ϕ and h as the conservative and dissipative part of the scalar field.

In Ref. [93], Khalatnikov used Galilean invariance to derive the conservative part of evolution terms Π_{ik} , \mathbf{Q} , and ϕ , while the requirement that entropy can only increase fully specifies the general form of dissipative terms. Here I will give a brief summary of Khalatnikov's results. First, we will consider a frame K_0 that is moving at the superfluid velocity \mathbf{v}_f . The momentum density j_0 in frame K_0 is

$$\mathbf{j}_0 = \mathbf{j} - \rho \mathbf{v}_s = \rho_n (\mathbf{v}_n - \mathbf{v}_s). \quad (5.20)$$

The relative velocity $\mathbf{v}_{rel} = \mathbf{v}_n - \mathbf{v}_s$ between the two components in the lab frame can be acquired by $\mathbf{v}_{rel} = \partial \epsilon_0 / \partial \mathbf{j}_0$, which is a Galilean invariant.

The conservative momentum flux tensor can be written as

$$\Pi_{ik} = \rho (v_{si} v_{sk} + v_{si} j_{0k} + v_{nk} j_{0i}) + p \delta_{ik}, \quad (5.21)$$

where p is the pressure. By thermodynamic definition, pressure p is the derivative of total energy with respect to volume, at constant particle number, entropy and

momentum of relative motion

$$p = \frac{\partial(\epsilon_0 V)}{\partial V} = -\epsilon_0 + Ts + \mu n + [(\mathbf{v}_n - \mathbf{v}_s) \cdot \mathbf{j}_0]. \quad (5.22)$$

Under the assumption that the system is experiencing only small perturbation from the equilibrium, all the quadratic terms in velocities can be neglected, and $\Pi_{ik} = \delta_{ik} p$, where p is independent of local velocity. This assumption is called linearized hydrodynamics. Next, the conservative energy flux Q takes the form

$$\mathbf{Q} = \left(\frac{\mu}{m} + \frac{v_s^2}{2} \right) (\mathbf{j}_0 + \rho \mathbf{v}_s) + ST \mathbf{v}_n + \mathbf{v}_n (\mathbf{n}_n \cdot \mathbf{j}_0), \quad (5.23)$$

where S is the entropy density. Lastly, the conservative driving potential ϕ for the superfluid velocity is the chemical potential μ of the superfluid

$$\phi = \mu/m. \quad (5.24)$$

The law of energy conservation can be converted into an equation describing the flow of entropy. The change in local entropy density S is connected to local energy density ϵ by

$$\frac{\partial \epsilon}{\partial t} = \left(\frac{v_s^2}{2} + \frac{\mu}{m} \right) \dot{\rho} + \dot{\mathbf{v}}_s \cdot \mathbf{j} + \mathbf{v}_n \cdot \dot{\mathbf{j}}_0 + T \dot{S} \quad (5.25)$$

Combining Eq. (5.25) with Eq. (5.18b), (5.18c), and (5.19), we can obtain the rate of increase of entropy

$$T \left(\frac{\partial S}{\partial t} + \nabla(S \mathbf{v}_n + \frac{\mathbf{q}}{T}) \right) = -h \nabla(j - \rho \mathbf{v}_n) - \tau_{ik} \frac{\partial v_{ni}}{\partial r_k} - \frac{1}{T} \mathbf{q} \cdot \nabla T, \quad (5.26)$$

and the expression for the additional dissipative energy flux

$$\mathbf{Q}' = \mathbf{q} + h(\mathbf{j} - \rho \mathbf{v}_n) + (\boldsymbol{\tau} \cdot \mathbf{v}_n). \quad (5.27)$$

Here q is an unknown energy flux related to the gradient of temperature. Assuming

the spatial derivatives of physical quantities are small, then to the first order the dissipative quantities τ , h , \mathbf{q} should be linear functions of these derivatives. From the requirement of entropy increasing, the dissipative function must be a positive definite quadratic form in these derivatives. The general form of the dissipative terms are:

$$\begin{aligned}\tau_{ik} = & -\eta \left(\frac{\partial v_{ni}}{\partial r_k} + \frac{\partial v_{nk}}{\partial r_i} - \frac{2}{3} \frac{\partial v_{nl}}{\partial r_l} \delta_{ik} \right) \\ & - \delta_{ik} [\zeta_1 \nabla \cdot (\mathbf{j} - \rho \mathbf{v}_n) + \zeta_2 \nabla \cdot \mathbf{v}_n],\end{aligned}\quad (5.28)$$

$$h = -\zeta_3 \nabla \cdot (\mathbf{j} - \rho \mathbf{v}_n) - \zeta_4 \nabla \cdot \mathbf{v}_n,\quad (5.29)$$

$$\mathbf{q} = -\kappa \nabla T,\quad (5.30)$$

If we compare the above dissipative quantities with those of a normal fluid [105] by setting $\rho_s = 0$, we can conclude that η and ζ_2 are the shear and bulk viscosity, respectively, and κ is the thermal conductivity. On the contrary, ζ_1 , ζ_3 , and ζ_4 are unique to the superfluid, and they are related to the interconversion of normal and superfluid currents. In addition, the Onsager symmetry of the transport coefficients gives an additional constraint of $\zeta_1 = \zeta_4$ [145].

The final hydrodynamic equations are then

$$\frac{\partial \rho}{\partial t} + \nabla \cdot \mathbf{j} = 0,\quad (5.31a)$$

$$\begin{aligned}\frac{\partial j_i}{\partial t} + \frac{\partial \Pi_{ik}}{\partial r_k} = & \frac{\partial}{\partial r_k} \left\{ \eta \left(\frac{\partial v_{ni}}{\partial r_k} + \frac{\partial v_{nk}}{\partial r_i} - \frac{2}{3} \frac{\partial v_{nl}}{\partial r_l} \delta_{ik} \right) \right. \\ & \left. + \delta_{ik} [\zeta_1 \nabla \cdot (\mathbf{j} - \rho \mathbf{v}_n) + \zeta_2 \nabla \cdot \mathbf{v}_n] \right\},\end{aligned}\quad (5.31b)$$

$$\frac{\partial \mathbf{v}_s}{\partial t} + \nabla \left(\frac{\mu}{m} + \frac{v_s^2}{2} \right) = \nabla [\zeta_3 \nabla \cdot (\mathbf{j} - \rho \mathbf{v}_n) + \zeta_4 \nabla \cdot \mathbf{v}_n],\quad (5.31c)$$

$$\frac{\partial S}{\partial t} + \nabla \cdot \left(S \mathbf{v}_n + \frac{\mathbf{q}}{T} \right) = \frac{R}{T}.\quad (5.31d)$$

Here the dissipative function R is equal to

$$R = \zeta_2(\nabla \cdot \mathbf{v}_n)^2 + \zeta_3 \cdot (\nabla \cdot (\mathbf{j} - \rho \mathbf{v}_n))^2 + 2\zeta_1(\nabla \cdot \mathbf{v}_n)\nabla \cdot (\mathbf{j} - \rho \mathbf{v}_n) + \frac{1}{2}\eta \left(\frac{\partial v_{ni}}{\partial r_k} + \frac{\partial v_{nk}}{\partial r_i} - \frac{2}{3}\delta_{ik}\frac{\partial v_{nl}}{\partial r_l} \right)^2 + \kappa \frac{(\nabla T)^2}{T}, \quad (5.32)$$

$$\frac{1}{2}\eta \left(\frac{\partial v_{ni}}{\partial r_k} + \frac{\partial v_{nk}}{\partial r_i} - \frac{2}{3}\delta_{ik}\frac{\partial v_{nl}}{\partial r_l} \right)^2 + \kappa \frac{(\nabla T)^2}{T}, \quad (5.33)$$

and must be positive, thus ζ_1 , ζ_2 , and ζ_3 must fullfil the inequality:

$$\zeta_1^2 \leq \zeta_2 \zeta_3. \quad (5.34)$$

The dissipation coefficients can be further simplified in the unitary Fermi gases. Due to scale invariance of the system (see Sec. 2.4.1), an isotropic expansion according to a velocity profile $\mathbf{v} \propto \mathbf{r}$ will not increase entropy. Thus the bulk viscosity ζ_2 must vanish. Using Eq. (5.34), we can conclude $\zeta_1 = \zeta_4 = 0$ as well.

5.1.3 Sound propagation modes in superfluids

In order to understand the sound propagation modes in a superfluid, we can look into the solution of Eq. (5.31) without the dissipative terms and using the linearized hydrodynamic approximation

$$\frac{\partial \rho}{\partial t} + \nabla \cdot \mathbf{j} = 0, \quad (5.35a)$$

$$\frac{\partial \mathbf{j}}{\partial t} + \nabla p = 0, \quad (5.35b)$$

$$\frac{\partial(ns)}{\partial t} + ns\nabla \cdot \mathbf{v}_n = 0, \quad (5.35c)$$

$$\frac{\partial \mathbf{v}_s}{\partial t} + \frac{1}{m}\nabla \mu = 0. \quad (5.35d)$$

Note here s is entropy per particle, and n is the particle number density. To solve the hydrodynamic equations, we can write the local variation of any physical quantity

(ΔA) in the Fourier space

$$\Delta A(r, t) = \int \tilde{A}(\mathbf{k}, \omega) e^{i\mathbf{k}\cdot\mathbf{r}-i\omega t} \frac{d^3\mathbf{k}}{(2\pi)^3} \frac{d\omega}{2\pi}. \quad (5.36)$$

The mass conservation Eq. (5.35a) in the Fourier space gives the connection between momentum and density

$$\mathbf{k} \cdot \tilde{\mathbf{j}} = \omega \tilde{\rho}. \quad (5.37)$$

Using Eq. (5.37), the momentum conservation Eq. (5.35b) can be rewritten as

$$\left(-\frac{\omega^2}{k^2} + \frac{\partial p}{\partial \rho} \Big|_s \right) \tilde{\rho} + \frac{\partial p}{\partial s} \Big|_\rho \tilde{s} = 0. \quad (5.38)$$

Note here $\frac{\partial p}{\partial \rho} \Big|_\sigma = c_{10}^{-2}$ corresponds to the speed of first sound in a normal material.

Next, the entropy propagation equation Eq. (5.35c) yields

$$-i\omega \rho \tilde{\sigma} - i\omega \frac{s}{m} \frac{\rho_s}{\rho_n} \tilde{\rho} - i\rho \frac{s}{m} \frac{\rho_s}{\rho_n} \mathbf{k} \cdot \tilde{\mathbf{v}}_s = 0 \quad (5.39)$$

Under the linearized hydrodynamic approximation, ρ , σ , ρ_s , and ρ_n in Eq. (5.39) can be set to their in-equilibrium value. The value of $\mathbf{k} \cdot \tilde{\mathbf{v}}_s$ can be acquired from the Fourier form of Eq. (5.35d)

$$\mathbf{k} \cdot \tilde{\mathbf{v}}_s = \frac{k^2}{m\omega} \left(\frac{\partial \mu}{\partial \rho} \Big|_s \tilde{\rho} + \frac{\partial \mu}{\partial s} \Big|_\rho \tilde{s} \right) \quad (5.40)$$

Combining Eq. (5.39) and (5.40) we get

$$\left(-\frac{\omega^2}{k^2} + \frac{\rho}{m} \frac{\partial \mu}{\partial \rho} \Big|_s \right) \frac{\rho_s}{\rho_n} s \tilde{\rho} + \left(\frac{\omega^2}{k^2} + \frac{s}{m} \frac{\rho_s}{\rho_n} \frac{\partial \mu}{\partial s} \Big|_\rho \right) \rho \tilde{s} = 0 \quad (5.41)$$

Eq. (5.38) and Eq. 5.41 provides the linear 2×2 equations of the free superfluid hydrodynamics in the basis of local density and entropy variation. We can denote $c \equiv \frac{\omega}{k}$ as the speed of sound. A non-zero solution requires the determinant to be zero

$$c^4 - \left[c_{10}^2 + s \frac{\rho_s}{\rho_n} \left(\frac{1}{\rho} \frac{\partial p}{\partial s} \Big|_\rho - \frac{1}{m} \frac{\partial \mu}{\partial s} \Big|_\rho \right) \right] c^2 + \frac{\rho_s}{\rho_n} \frac{s}{m} \left(\frac{\partial p}{\partial s} \Big|_\rho \frac{\partial \mu}{\partial \rho} \Big|_s - c_{10}^2 \frac{\partial \mu}{\partial s} \Big|_\rho \right) = 0. \quad (5.42)$$

The partial derivatives of μ can be carried out using the Gibbs-Duhem equation $d\mu = -s dT + \frac{m}{\rho} dp$ and chain rule

$$\frac{\partial \mu}{\partial \rho} \Big|_s = -s \frac{\partial T}{\partial \rho} \Big|_s + \frac{m}{\rho} \frac{\partial p}{\partial \rho} \Big|_s, \quad (5.43a)$$

$$\frac{\partial \mu}{\partial s} \Big|_\rho = -s \frac{\partial T}{\partial s} \Big|_\rho + \frac{m}{\rho} \frac{\partial p}{\partial s} \Big|_\rho, \quad (5.43b)$$

allowing the simplification of Eq. (5.42) to

$$c^4 - \left[c_{10}^2 + \frac{s^2}{m} \frac{\rho_s}{\rho_n} \frac{\partial T}{\partial s} \Big|_\rho \right] c^2 + c_{10}^2 \frac{s^2}{m} \frac{\rho_s}{\rho_n} \frac{\partial T}{\partial s} \Big|_p = 0. \quad (5.44)$$

We can denote $c_{20}^2 = \frac{s^2}{m} \frac{\rho_s}{\rho_n} \frac{\partial T}{\partial s} \Big|_p$, the two solutions of Eq. (5.44) therefore satisfy the following coupled equations:

$$c_1^2 + c_2^2 = c_{10}^2 + \gamma c_{20}^2, \quad (5.45a)$$

$$c_1 c_2 = c_{10} c_{20}, \quad (5.45b)$$

where $\gamma = (\frac{\partial s}{\partial T})_p / (\frac{\partial s}{\partial T})_\rho$ is the isoentropic expansion coefficient. For an incompressible system $\gamma = 1$, c_{10} and c_{20} are the speed of the first and second sound, respectively. In this scenario, the first sound is purely a density (pressure) wave with $\mathbf{v}_n = \mathbf{v}_s$ while the second sound is purely an entropy (temperature) wave, with $\rho_s \mathbf{v}_s + \rho_n \mathbf{v}_n = 0$. For a compressible fluid with $x \equiv c_{20}^2/c_{10}^2 \ll 1$, c_{10} and c_{20} are still good approximations for the speed of two sound modes, whose value can be expressed in a series expansion of x [76]

$$c_1^2 = c_{10}^2 [1 + (\gamma - 1)x + (\gamma - 1)x^2 + ...], \quad (5.46a)$$

$$c_2^2 = c_{20}^2 [1 - (\gamma - 1)x + ...], \quad (5.46b)$$

or their exact solutions:

$$c_1 = \left(\sqrt{c_{10}^2 + 2c_{10}c_{20} + \gamma c_{20}^2} + \sqrt{c_{10}^2 - 2c_{10}c_{20} + \gamma c_{20}^2} \right) / 2, \quad (5.47a)$$

$$c_2 = \left(\sqrt{c_{10}^2 + 2c_{10}c_{20} + \gamma c_{20}^2} - \sqrt{c_{10}^2 - 2c_{10}c_{20} + \gamma c_{20}^2} \right) / 2. \quad (5.47b)$$

When the superfluid fraction reaches zero above the transition temperature, the second sound mode will vanish. In Sec. 5.1.5, we will show the second sound mode actually degenerates into the thermal diffusion mode in the normal phase.

Using the "phonon+pair-breaking" model described in Sec. 5.1.1, we are able to calculate superfluid fraction ρ_s/ρ_n and speed of sound c_2 or c_{20} (Fig. 5-1B). The difference between the coupled and uncoupled speed of second sound is negligible. The temperature dependence of the speed of second sound has a 2-step shape. In the upper step ($T \lesssim 0.3T_c$), the second sound is a density wave of phonon cloud and the speed of second sound takes the value $c_2 = c_1/\sqrt{3}$. The weak phonon-phonon interaction leads to a long phonon mean free path and high diffusivity for the second sound [214, 152] in this regime. The strong attenuation of second sound in this regime makes it hard to probe. In the lower step ($T \gtrsim 0.3T_c$), the density of normal fluid component is dominated by pair-breaking excitations. These single-particle excitations have a fast decay rate on the order of E_F/\hbar . This leads to a quantum-limited diffusivity, $D_2 \sim \hbar/m$, for the second sound. Remarkably, our simple model agrees with the NSR model qualitatively [199, 200]. An important difference between the two methods are the critical behavior close to T_c . While the method in Ref. [199, 200] assumes $\rho_s \sim (T - T_c)^{2/3}$ according to the exact solution of the 3D XY universality class, our mean field model gives $\rho_s \sim (T - T_c)$.

For a quantitative understanding of the sound propagation modes in the superfluid, including the dissipative effects, we will discuss the superfluid hydrodynamics in the framework of response functions under an external perturbation in the following subsection.

5.1.4 Response functions

In a linearized hydrodynamic system, the response of the system to an external perturbation can be expressed in terms of frequency ω and wavevector \mathbf{k} dependent response functions $\chi(\mathbf{k}, \omega)$. These response functions directly corresponds to the correlation functions in the equilibrium state [89, 77], and a more detailed discussion about this connection can be find in Appendix. E. The response of a quantity A_i under the drive of a generalized external force a_j , corresponding to a generalized coordinate A_j , can be described with the response function $\chi_{i,j}$

$$\tilde{A}_i(\mathbf{k}, \omega) = \chi_{i,j}(\mathbf{k}, \omega) \tilde{a}_j(\mathbf{k}, \omega), \quad (5.48)$$

$$\frac{1}{i\hbar} \eta(t - t') \langle [A_i(\mathbf{r}, t), A_j(\mathbf{r}', t')] \rangle = \int \frac{d\omega}{2\pi} \int \frac{d^3k}{(2\pi)^3} \chi_{i,j}(\mathbf{k}, \omega) e^{i\mathbf{k}\cdot(\mathbf{r}-\mathbf{r}') - i\omega(t-t')} . \quad (5.49)$$

Here $\eta(t)$ is a step function with $\eta(t < 0) = 0$ and $\eta(t \geq 0) = 1$, $\langle \rangle$ denotes an average over the thermal ensemble, and $[A_i, A_j] = A_i A_j - A_j A_i$ is the quantum commutator. In this subsection I will demonstrate how to acquire the general form of the density-density χ_{nn} and heat-density χ_{qn} response functions for a unitary Fermi gas using the hydrodynamic equations.

First, we can define the heat density q as

$$q(\mathbf{r}, t) = \epsilon(\mathbf{r}, t) - \frac{\epsilon + p}{n} n(\mathbf{r}, t). \quad (5.50)$$

Note the $\frac{\epsilon+p}{n}$ term on the right-hand side of Eq. (5.50) is the value at thermal equilibrium. Though the absolute value of q does not have a well-defined physical meaning, its deviation from equilibrium corresponds to the change of entropy per particle s

$$dq = d\epsilon - \frac{\epsilon + p}{n} dn = nT ds. \quad (5.51)$$

Under the scope of linearized hydrodynamics, we can drop terms quadratic in velocity or local density and temperature variation. Therefore the local entropy increase term $\frac{R}{T}$ on the right-hand side of Eq. (5.31d) can be neglected, and total entropy is

conserved. Using Eq. (5.31d), we can get the hydrodynamic equation for the evolution of q

$$\frac{\partial q}{\partial t} + Ts \frac{\partial n}{\partial t} + nTs(\nabla \cdot \mathbf{v}_n) - \kappa \nabla^2 T = 0. \quad (5.52)$$

The external potential V yields a force per unit volume on the fluid $f = -n\nabla V$, the momentum conservation equation can be written as

$$\frac{\partial j_i}{\partial t} + \nabla^2 p - \eta \left[\nabla^2 \mathbf{v}_n + \frac{1}{3} \nabla (\nabla \cdot \mathbf{v}_n) \right] = -n\nabla V. \quad (5.53)$$

Note here we have already applied linearized hydrodynamics approximation to drop the quadratic terms, and used $\zeta_1 = \zeta_2 = \zeta_4 = 0$ for unitary Fermi gas. Besides, the external potential will also shift the chemical potential, thus generates an additional drive to the superfluid velocity

$$\frac{\partial \mathbf{v}_s}{\partial t} + \frac{1}{m} \nabla [\mu + V - \zeta_3 \rho_s \nabla \cdot (\mathbf{v}_s - \mathbf{v}_n)] = 0. \quad (5.54)$$

Combining Eq. (5.52)-(5.54) with the mass conservation Eq. 5.35a, we have the full linearized hydrodynamic equations.

To solve the hydrodynamic equations, we again applied the Fourier transform like we did in Sec. 5.1.3. For the velocity fields \mathbf{v}_n , \mathbf{v}_s and momentum density \mathbf{j} , we only keep the part that is aligned with \mathbf{k} , i.e. the longitudinal modes¹. The variation of local chemical potential $d\mu$ and pressure dp can be rewritten in terms of density dn and heat dq using the thermodynamic relations. The value of the Fourier component of momentum density \tilde{j} , normal and superfluid velocities \tilde{v}_n and \tilde{v}_s can be expressed with density \tilde{n} and heat \tilde{q} using Eq. (5.35a) and (5.52)

$$\tilde{j}(k, \omega) = \frac{m\omega}{k} \tilde{n}(k, \omega), \quad (5.55)$$

$$\tilde{v}_n(k, \omega) = \left(\frac{\omega}{kn} + \frac{i\kappa k \frac{\partial T}{\partial n}|_s}{nTs} \right) \tilde{n}(k, \omega) + \left(\frac{\omega}{knTs} + \frac{i\kappa k \frac{\partial T}{\partial s}|_n}{n^2 T^2 s} \right) \tilde{q}(k, \omega), \quad (5.56)$$

¹The only transverse mode in the system corresponds to a decay of laminar flow, which is not relevant to the experiment I will present in this chapter.

$$\tilde{v}_s = -\frac{\rho_n}{\rho_s} \tilde{v}_n + \frac{\tilde{j}}{\rho_s}. \quad (5.57)$$

Finally, we can convert the full hydrodynamic equations into a 2×2 equations with \tilde{n} and \tilde{q} as unknown variables:

$$\begin{aligned} & \left[-i\omega^2 + ik^2 c_{10}^2 + D_\eta k^2 \omega + i(\gamma - 1) D_\eta k^2 D_T k^2 \frac{\rho c_{10}^2}{s} \frac{\partial s}{\partial p} \Big|_n \right] \tilde{n}(k, \omega) \\ & + \left[i \frac{k^2}{\rho T} \frac{\partial p}{\partial s} \Big|_n + \frac{D_\eta k^2 \omega}{Ts} + i \frac{\gamma D_\eta k^2 D_T k^2}{Ts} \right] \tilde{q}(k, \omega) = \frac{-ik^2 n}{m} \tilde{V}(k, \omega), \end{aligned} \quad (5.58a)$$

$$\begin{aligned} & \left[-i\omega^2 \frac{\rho_s}{\rho_n} Ts - (\gamma - 1) \rho c_{10}^2 \frac{\partial s}{\partial p} \Big|_n T D_T k^2 \omega + ik^2 c_{10}^2 \frac{\rho_s}{\rho_n} Ts - ik^2 \frac{n T s^2 \rho_s}{m \rho_n} \frac{\partial T}{\partial n} \Big|_s \right. \\ & \left. - D_\zeta k^2 D_T k^2 (\gamma - 1) \rho c_{10}^2 T \frac{\rho_s}{\rho_n} \frac{\partial s}{\partial p} \Big|_n \right] \tilde{n}(k, \omega) + \left[i\omega^2 - \gamma \omega D_T k^2 + \frac{ik^2 \rho_s}{mn \rho_n} \left(s \frac{\partial p}{\partial s} \Big|_n - \frac{ns^2 T}{c_V} \right) \right. \\ & \left. - \frac{\rho_s}{\rho_n} D_\zeta k^2 \omega - i\gamma \frac{\rho_s}{\rho_n} D_\zeta k^2 D_T k^2 \right] \tilde{q}(k, \omega) = \frac{-ik^2 n T \sigma}{m} \frac{\rho_s}{\rho_n} \tilde{V}(k, \omega). \end{aligned} \quad (5.58b)$$

Here we have substituted thermal conductivity κ , shear viscosity η , and bulk viscosity ζ_3 with their corresponding diffusivities $D_T = \frac{\kappa}{nc_p}$, $D_\eta = \frac{4\eta}{3\rho}$, and $D_\zeta = \zeta_3 \rho$. c_V and c_p are specific heat per particle at constant density and pressure, respectively. The solutions of $\tilde{n}(k, \omega)$ and $\tilde{q}(k, \omega)$ are linear functions of $\tilde{V}(k, \omega)$, with response functions as the prefactors.

$$\tilde{n}(k, \omega) = -\chi_{n,n}(k, \omega) \cdot \tilde{V}(k, \omega), \quad (5.59a)$$

$$\tilde{q}(k, \omega) = -\chi_{q,n}(k, \omega) \cdot \tilde{V}(k, \omega). \quad (5.59b)$$

The general form of $\chi_{n,n}$ and $\chi_{q,n}$ can be acquired by solving Eq. (5.58)

$$\chi_{n,n}(k, \omega) = \frac{k^2 n}{m} \frac{\gamma k^2 c_{20}^2 + \gamma \frac{\rho_s}{\rho_n} D_T (D_\zeta + D_\eta) k^4 - i[\gamma D_T k^2 + \frac{\rho_s}{\rho_n} (D_\zeta + D_\eta) k^2] \omega - \omega^2}{\det \mathcal{M}}, \quad (5.60a)$$

$$\chi_{q,n}(k, \omega) = n T k^2 \frac{-\alpha_p c_{10}^2 c_{20}^2 k^2 - (D_\eta + D_\zeta) D_T k^4 \frac{\rho_s}{\rho_n} c_{10}^2 \alpha_p + i(\frac{\rho_s}{\rho_n} D_\eta k^2 \omega + \sqrt{(\gamma - 1) \frac{\rho_s}{\rho_n} \frac{c_{10}}{c_{20}} D_T k^2 \omega}) \frac{s}{m}}{\det \mathcal{M}}. \quad (5.60b)$$

Here $\alpha_p = -\frac{1}{n} \frac{\partial n}{\partial T} \Big|_p$ is the thermal expansivity, and \mathcal{M} is the 2×2 matrix corresponding to the homogeneous part of Eq. (5.58). The determinant of \mathcal{M} is

$$\begin{aligned} \det \mathcal{M} = & \omega^4 + i\omega^3 k^2 [(1 + \frac{\rho_s}{\rho_n}) D_\eta + \frac{\rho_s}{\rho_n} D_\zeta + \gamma D_T] \\ & - \omega^2 [(c_{10}^2 + \gamma c_{20}^2) k^2 + \frac{\rho_s}{\rho_n} (\gamma D_T D_\zeta + \gamma D_T D_\eta + D_\zeta D_\eta) k^4 + \gamma D_T D_\eta k^4] \\ & - ik^4 \omega [c_{10}^2 D_T + c_{10}^2 \frac{\rho_s}{\rho_n} D_\zeta + (c_{10}^2 \frac{\rho_s}{\rho_n} + c_{20}^2 (1 - 2a)\gamma) D_\eta + \gamma \frac{\rho_s}{\rho_n} D_\eta D_\zeta D_T k^2] \\ & + k^4 c_{10}^2 c_{20}^2 + \frac{\rho_s}{\rho_n} c_{10}^2 k^6 (D_\eta D_T + D_\zeta D_T), \end{aligned} \quad (5.61)$$

$$\text{where } a \equiv \frac{1}{ns} \frac{\partial p}{\partial T} \Big|_n = \left[\frac{(\gamma-1)c_{10}^2 \rho_s}{\gamma^2 c_{20}^2 \rho_n} \right]^{1/2}.$$

When the dissipative terms D_T , D_η , and D_ζ are small, we can drop the terms in higher orders of Dk^2 , and simplify the response functions into:

$$\chi_{n,n}(\mathbf{k}, \omega) = \frac{nk^2}{m} \frac{-\omega^2 + \gamma c_{20}^2 k^2 - i\Gamma_{n,n} k^2 \omega}{(\omega^2 - c_1^2 k^2 + iD_1 k^2 \omega)(\omega^2 - c_2^2 k^2 + iD_2 k^2 \omega)}, \quad (5.62a)$$

$$\chi_{q,n}(\mathbf{k}, \omega) = nTk^2 \frac{-\alpha_p c_1^2 c_2^2 k^2 + i\Gamma_{q,n} k^2 \omega}{(\omega^2 - c_1^2 k^2 + iD_1 k^2 \omega)(\omega^2 - c_2^2 k^2 + iD_2 k^2 \omega)}. \quad (5.62b)$$

All the response functions share the same denominator, and the poles of the response functions are at frequencies $\omega_{i,\pm} = \pm\sqrt{c_i^2 k^2 - (D_i k^2/2)^2} - iD_i k^2/2$. Speeds of 1st and 2nd sound c_1 and c_2 follow coupled equations in Eq. (5.45). D_1 and D_2 are sound diffusivities for 1st and 2nd sound, and their values are:

$$D_1 = \frac{c_1^2 (\frac{\rho_s}{\rho_n} + 1) - c_{10}^2 \frac{\rho_s}{\rho_n} + (2a - 1)c_{20}^2 \gamma}{c_1^2 - c_2^2} D_\eta + \frac{\gamma c_1^2 - c_{10}^2}{c_1^2 - c_2^2} D_T + \frac{(c_1^2 - c_{10}^2) \frac{\rho_s}{\rho_n}}{c_1^2 - c_2^2} D_\zeta, \quad (5.63)$$

$$D_2 = \frac{c_{10}^2 \frac{\rho_s}{\rho_n} - c_2^2 \frac{\rho_s}{\rho_n} - (2a - 1)c_{20}^2 \gamma}{c_1^2 - c_2^2} D_\eta + \frac{c_{10}^2 - \gamma c_2^2}{c_1^2 - c_2^2} D_T + \frac{(c_{10}^2 - c_2^2) \frac{\rho_s}{\rho_n}}{c_1^2 - c_2^2} D_\zeta. \quad (5.64)$$

$\Gamma_{n,n}$ and $\Gamma_{q,n}$ controls the asymmetry of the first and second sound peak:

$$\Gamma_{n,n} = \gamma D_T + \frac{\rho_s}{\rho_n} (D_\zeta + D_\eta), \quad (5.65)$$

$$\Gamma_{q,n} = \left(\frac{\rho_s}{\rho_n} D_\eta + \sqrt{(\gamma - 1) \frac{\rho_s}{\rho_n} \frac{c_{10}}{c_{20}}} D_T \right) \frac{s}{m}. \quad (5.66)$$

Fig. 5-2 illustrates the absorptive (imaginary) part of the density-density $\text{Im}\chi_{n,n}$ and heat-density $\text{Im}\chi_{q,n}$ response functions. For a superfluid, the main feature in $\text{Im}\chi_{n,n}(\mathbf{k}, \omega)$ corresponds to the first sound, while the main feature in $\text{Im}\chi_{q,n}(\mathbf{k}, \omega)$ corresponds to the second sound.

In addition, the free evolution of the hydrodynamic functions can also be expressed with the response functions, as demonstrated by Kadanoff and Martin in Ref. [89]. The general form of the time evolution of any physical quantities A is

$$\Delta A(\mathbf{k}, t) = \int_{-\infty}^{+\infty} \sum_{i,\pm} \left[\frac{A_{i,\pm}}{z - \omega_{i,\pm}(\mathbf{k})} e^{-izt} \right] dz. \quad (5.67)$$

Here $\omega_{i,\pm}(\mathbf{k})$ are the poles of the response functions at a given wave vector \mathbf{k} , and $A_{i,\pm}$ are determined by the initial condition and the residue of the pole. After carrying out the inverse Fourier transform in Eq. 5.67, we found the free evolution solution is exactly the same as a superposition of two damped harmonic oscillators with frequencies $c_1 k$ and $c_2 k$, and damping rates $D_1 k^2$ and $D_2 k^2$. The general free-evolution solution of second sound and heat diffusion is:

$$\Delta A(\mathbf{k}, t) = \begin{cases} A_0 e^{-D_2 k^2 t/2} \cos(\sqrt{c_2^2 k^2 - (D_2 k^2/2)^2} t + \phi), & \text{if } c_2 k > D_2 k^2/2 \\ A_+ e^{-(D_2 k^2/2 + \sqrt{(D_2 k^2/2)^2 - c_2^2 k^2})t} \\ + A_- e^{-(D_2 k^2/2 - \sqrt{(D_2 k^2/2)^2 - c_2^2 k^2})t}, & \text{if } 0 < c_2 k < D_2 k^2/2 \\ A_0 e^{-D_2 k^2 t}. & \text{if } c_2 k = 0 \end{cases} \quad (5.68)$$

5.1.5 Normal fluid hydrodynamics

The hydrodynamic equations and response functions we used for a superfluid can also be applied to a normal fluid by simply setting $\rho_s=0$. In this scenario, \mathbf{v}_n alone will describe the motion of fluid and \mathbf{v}_s can be dropped from hydrodynamic equations. With $c_{20} = c_2 = 0$, the speed of first sound $c_1 = c_{10}$ will no longer be modified by the

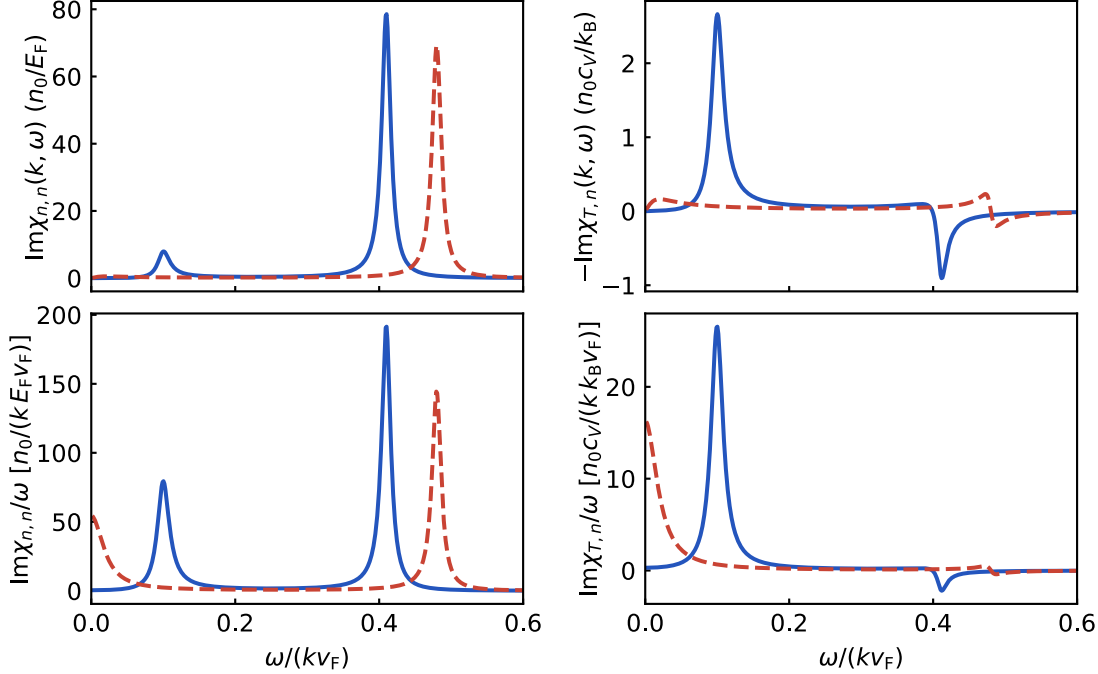


Figure 5-2: Absorptive density-density $\text{Im}\chi_{n,n}$ and heat-density $\text{Im}\chi_{q,n}$ response functions in the superfluid (blue solid line) and the normal phase (red dashed line). For the superfluid response functions, we used $c_1/v_F = 0.41$, $c_2/v_F = 0.10$, $D_1 = 1.5 \hbar/m$, $D_2 = 2 \hbar/m$, $\gamma = 1.5$, $\alpha_T k_B T/c_V = 0.5$, $\Gamma_{nn} = 3 \hbar/m$, $\Gamma_{qn} = 0.25 \hbar c_V/m^2$. For the normal phase response functions, we used $c_1/v_F = 0.48$, $c_2/v_F = 0.0$, $D_1 = 1.5 \hbar/m$, $D_2 = 2 \hbar/m$, $\gamma = 1.2$, $\alpha_T k_B T/c_V = 0.5$, $\Gamma_{nn} = 3 \hbar/m$, $\Gamma_{qn} = 0.25 \hbar c_V/m^2$.

presence of second sound. D_1 and D_2 can be simplified to

$$D_1 = D_\eta + \gamma D_T, \quad (5.69)$$

$$D_2 = D_T. \quad (5.70)$$

In this regime, D_2 should be considered as the thermal diffusivity governing the diffusion of heat in the fluid. $\chi_{n,n}$ and $\chi_{q,n}$ in the normal phase are

$$\chi_{n,n}(\mathbf{k}, \omega) = \frac{n k^2}{m} \frac{-\omega - i\gamma D_T k^2}{(\omega^2 - c_1^2 k^2 + iD_1 k^2 \omega)(\omega + iD_2 k^2)}, \quad (5.71)$$

$$\chi_{q,n}(\mathbf{k}, \omega) = n T k^2 \frac{\alpha_p D_T k^2 c_1^2}{(\omega^2 - c_1^2 k^2 + iD_1 k^2 \omega)(\omega + iD_2 k^2)}. \quad (5.72)$$

Fig. 5-2 shows a sketch of the response functions in the normal fluid. The heat diffusion mode corresponds to the peaks in $\text{Im}\chi_{n,n}(\mathbf{k}, \omega)/\omega$ and $\text{Im}\chi_{q,n}(\mathbf{k}, \omega)/\omega$ at

$\omega = 0$.

Furthermore, the heat-heat response function $\chi_{q,q}$ can be easily solved by assuming an external temperature modulation, and it has a simple form with a single pole for the heat diffusion

$$\chi_{q,q}(k, \omega) = nc_p T \frac{iD_2 k^2}{\omega + iD_2 k^2}. \quad (5.73)$$

5.2 rf spectroscopy of spin-balanced unitary gases

In order to study the heat transport and compare it with the other transport phenomena in unitary Fermi gases, an independent temperature probe is necessary. rf spectroscopy is able to probe the population of single particle excitations, which depends on the temperature. Therefore, the rf spectroscopy method is a good candidate for local temperature measurement. To study the temperature dependence of rf spectra of spin balanced, unitary Fermi gases, we use the same experimental procedure described in Sec. 4.3. The universal unitary system has only two energy scales: the Fermi energy E_F and thermal energy $k_B T$. The corresponding length scales are the interparticle spacing $\lambda_F = n^{-1/3}$ and the thermal de Broglie wavelength $\lambda_T = h/\sqrt{2\pi m k_B T}$. When the two energy scales are comparable, the system enters a quantum critical regime [141] between Boltzmann gas at high temperatures and the fermionic superfluid at low temperatures. This often leads to the absence of quasiparticles [141, 43, 53].

rf spectra measured at various temperature are shown in Fig. 5-3(a). Across the accessible temperature range $0.1 T_F \lesssim T \lesssim 2.5 T_F$, a single peak is observed for all temperatures from the superfluid regime into the high temperature Boltzmann gas. At high temperatures $T \gtrsim T_F$, there exists both an attractive and a repulsive energy branch, which are symmetric about zero at unitarity [73], and their contributions to the rf spectral shift cancel [44, 195, 51]. As the hot unitary gas is cooled below the Fermi temperature, the peak shift decreases from zero for temperatures $T \gtrsim T_F$, to $E_p \approx -0.8 E_F$ for temperatures below the superfluid transition temperature [see Fig. 5-3(b)]. While the energy shift at low temperatures can be attributed to the

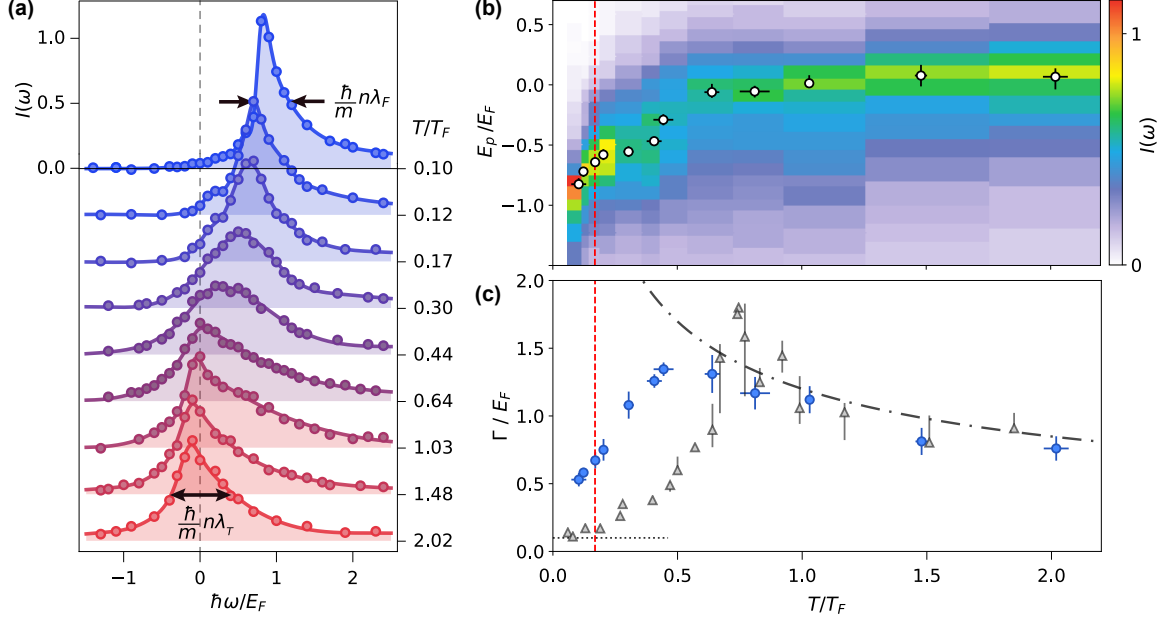


Figure 5-3: (a) Thermal evolution of rf spectra. The Rabi frequency is $\Omega_R = 2\pi \times 0.5$ kHz and the pulse duration is $T_{\text{Pulse}} = 1$ ms. The solid lines are guides to the eye. (b) Frequency of the peak ($E_p = -\hbar\omega$) of the rf spectra as a function of temperature shown as white dots on an intensity plot of the rf response. (c) The full width at half maximum Γ of the rf peak as a function of T/T_F . The black dot-dashed line $\Gamma/E_F = 1.2\sqrt{T_F/T}$ shows the temperature dependence of the width due to scattering in the high-temperature gas (see Sec. 4.2.1 and Ref. [44, 195]). The grey triangles are the corresponding width measurements of a highly spin-imbalanced gas (see Sec. 4.3.1 and Ref. [211]). The horizontal black dotted line represents the Fourier broadening of $0.1 E_F$. The vertical dashed red line in both (b) and (c) marks the superfluid transition [101]. This figure is taken from Ref. [130].

fermion pairing, the thermal fluctuations suppress the onset of coherent pair condensation and superfluidity above $T_c = 0.17(1) T_F$ [142, 101, 162, 217].

The full width at half maximum Γ of the rf spectra provides additional insights into unitary Fermi gases [see Fig. 5-3(c)]. For temperatures much higher than T_F , the system is a Boltzmann gas of atoms scattering with a unitarity limited cross section $\sigma \sim \lambda_T^2 \sim 1/T$, and a mean relative speed $v_{\text{rel}} \sim \hbar/(m\lambda_T) \sim T^{1/2}$ (see Sec. 4.2.1). The width of the rf spectra in this regime corresponds to the scattering rate $\Gamma = n\sigma v_{\text{rel}} \sim \hbar n \lambda_T / m \sim T^{-1/2}$ [43]. At temperatures $T \gtrsim T_{F\uparrow}$, the spectral width of the spin-balanced gas is identical to that of a highly spin-imbalanced gas, as a result of classical gas being insensitive to the spin composition of the system. As the system is cooled from the Boltzmann regime, the width gradually increases, and

attains a maximum of $\Gamma = 1.35(5) E_F$ near $T = 0.44(4) T_F$.

As the cloud is cooled below $T \approx 0.5 T_F$, the width decreases linearly with temperature to $\Gamma \sim 0.52 E_F/\hbar$ in the coldest gases measured ($T = 0.10(1) T_F$). For temperatures below T_c , we expect the gas to consist of fermion pairs of size ξ . The rf spectrum will be broadened by the distribution of momenta $\sim \hbar/\xi$ inside each pair, leading to a spread of possible final kinetic energies $\hbar^2 k^2/m \sim \hbar^2/m\xi^2$ and a corresponding spectral width $\hbar/m\xi^2$. At unitarity and at $T = 0$, the pair size is set by the interparticle spacing λ_F [217, 92, 178]. Thus the rf width at low temperatures is on the order of Fermi energy $\Gamma \sim \hbar n \lambda_F/m \sim E_F/\hbar$.

For temperatures above T_c , it has been suggested that the normal fluid can be described as a Fermi liquid [134, 137]. This would imply a quadratic relation between the peak width and the temperature [155], as observed in the widths of the rf spectra of Fermi polarons at unitarity (see Ch. 4). However, the measured spectral width of the spin-balanced Fermi gas changes linearly in temperature, implying non-Fermi liquid behavior in the normal fluid. In addition, the spectral width is larger than the Fermi energy $\Gamma > E_F/\hbar$ for $0.3 \lesssim T/T_F \lesssim 1.2$, indicating a breakdown of well-defined quasiparticles over a large range of temperatures near the quantum critical regime [141, 43, 53].

The high frequency tail of the rf spectra provides a measurement on the short range contact C , same to the highly spin-imbalanced case discussed in Sec. 4.3.2. The temperature dependence of the measured contact is shown in Fig. 5-4(a). In the spin-balanced case, as the temperature is cooled, the contact shows a gradual increase before entering the superfluid phase. A sudden rise of the contact happens when the system enters the superfluid phase, accompanied by the emergence of the pair condensation observed after a rapid ramp experiment [see Fig. 5-4(b)]. Our contact result here shows a good agreement with the Bragg spectroscopy measurements by the CQOS group [21, 79]. A more detailed discussion of the contact in spin-balanced unitary Fermi gases can be found in Appendix. C.

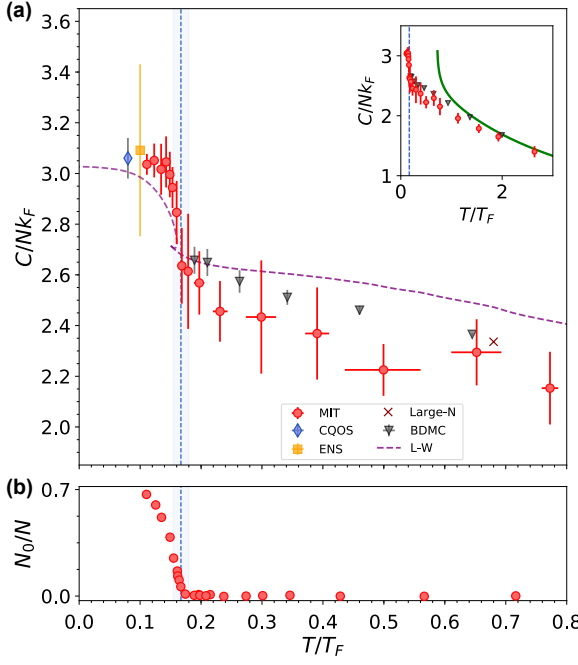


Figure 5-4: The dimensionless contact C/Nk_F (a) and condensate fraction N_0/N (b) of the unitary Fermi gas as a function of the reduced temperature T/T_F . Our measurements of the contact (red points) are consistent with several theory works: Bold-Diagrammatic Monte Carlo (BDMC) [168], Luttinger-Ward (L-W) [44], Large-N [43], and third order Virial Expansion at high temperatures [112] (green line in the inset of (a)), as well as experimental results from loss rate measurements by the ENS group [107] and Bragg spectroscopy by the CQOS group [79]. The vertical blue dotted line indicates the superfluid transition temperature [101]. This figure is taken from Ref. [130].

5.3 Second sound in the superfluid phase

Second sound is a wavelike entropy propagation mode unique to the superfluid and certain solid state materials. In the superfluid, the second sound mode arises from an out-of-phase oscillation between the superfluid and normal component. When the phonons in a crystal experience predominately a elastic scattering (e.g. in graphite [82]), they will form a hydrodynamic gas of quasiparticles, and second sound will emerge as a density wave in the thermal excitation cloud. Here we will focus on the experimental observation of second sound in the superfluid phase of a unitary Fermi gas, as well as the transition from second sound to heat diffusion when the temperature is raised above T_c .

Here we use a temperature-dependent spectral response as a local thermometer to directly observe heat transport. The initial temperature variation is generated by an oscillating gradient potential resonant to the normal modes of second sound, or fast decaying phonons as a local heating source. while the former method is valid when there is a well-defined second sound mode, the latter can be used in both the superfluid and normal phase, allowing the observation of the transition from wavelike to diffusive heat propagation. The frequency dependence of temperature and density

responses of the system yields the response functions of the system [77, 89]. While the speed of second sound c_2 is a direct measure of the superfluid fraction ρ_S/ρ_N , the attenuation of this entropy wave is governed by its diffusivity D_2 , which is a linear combination of thermal conductivity, shear viscosity, and a bulk viscosity related to interconversion of normal and superfluid currents (see Eq. 5.64). The second sound diffusivity displays a peak at the phase transition temperature, resembling the critical behavior found in liquid ^4He .

5.3.1 rf spectroscopic thermometry

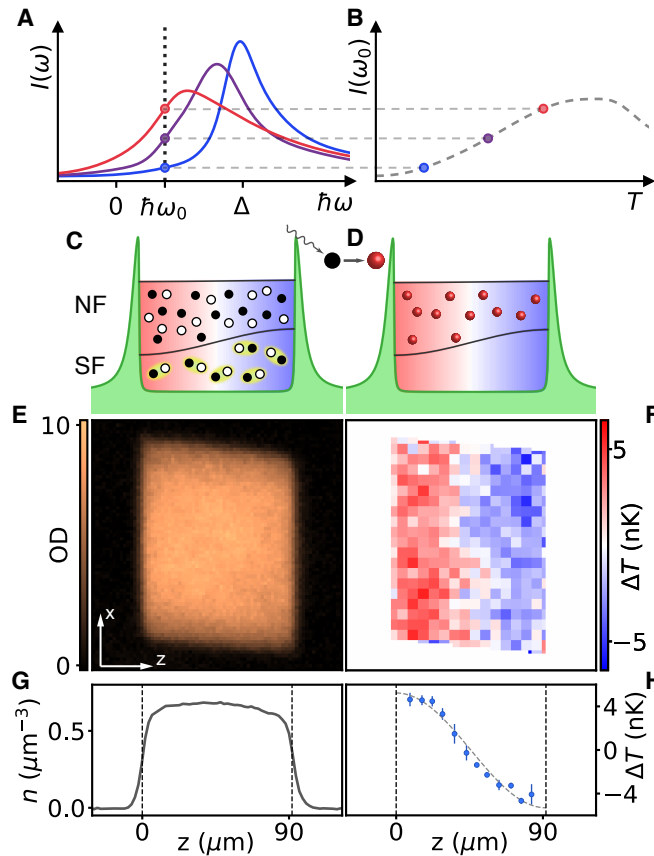


Figure 5-5: (A) A sketch of the rf spectra at various temperatures for unitary Fermi gases (see Sec. 5.2). The blue, purple, and red line corresponds to the rf transfer rate $I(\omega)$ at increasing temperatures. (B) The rf transfer rate on the flank of a peak (black dotted line) is temperature sensitive. (C) In fermionic superfluids, the superfluid component (SF) consists of coherent Fermion pairs, while the normal component (NF) contains broken pairs. (D) The unpaired atoms are transferred to a weakly interacting state by an rf pulse. After creating a resonant second sound using an oscillating axial gradient potential, the density (E) and temperature (F) can be measured by imaging the atoms in state $|3\rangle$ and $|2\rangle$. The axial density (G) and temperature variation (H) is acquired by averaging through the uniform radial axis. The vertical dotted line is the edge of box potential.

Spectroscopic measurement can be used as a local temperature probe. A well known application of this principle is that the temperature of a radiating body, like a glowing iron bar or a distant star, can be determined from the spectrum of its radiation

according to Planck's law. In Sec. 5.2, I have discussed the temperature dependence of the rf spectroscopy of the unitary Fermi gas, which can be used as a local thermometer. In a simple picture, the absorption peak is shifted by the pairing energy Δ from the bare atomic transition at zero temperature, while the increasing temperature creates pair-breaking excitations and shifts the peak toward lower frequency (Fig.5-5A). At a detuning ω_0 on the flank of the peak, the rf response is sensitive to the temperature (Fig.5-5B), allowing a direct measurement of the local temperature from a single image of transferred atoms. The rf probe provides an independent thermometer and enables direct comparison of transport phenomena in heat, momentum [1, 149], and spin [187, 6, 120] in strongly interacting systems. This new method also allows measurement of the complete heat and density response of a system under external perturbation, which contains full hydrodynamic information [89, 77] (see Sec. 5.1.4).

Similar to the experimental setup described in Sec. 4.3, we use the three lowest hyperfine states of ${}^6\text{Li}$, denoted $|1\rangle = |m_J = -1/2, m_I = 1\rangle$, $|2\rangle = |-1/2, 0\rangle$ and $|3\rangle = |-1/2, -1\rangle$ at a magnetic field of 690 G. Here we begin with an equal mixture of resonantly interacting $|1\rangle$ and $|3\rangle$ confined in a uniform potential. The Fermi energy is $E_F = 10.5 \text{ } h \cdot \text{kHz}$ corresponding to a density of $n_0 = 0.75 \text{ } \mu\text{m}^{-3}$ per spin state and a Fermi temperature of $T_F \simeq 500 \text{ nK}$. For spatial temperature detection, a 0.5 ms rf pulse with a Rabi frequency of $\Omega_R = 2\pi \cdot 1.9 \text{ kHz}$ is used to transfer atoms in state $|1\rangle$ to the weakly-interacting final state $|f\rangle = |2\rangle$. An rf detuning of 5 kHz from the bare atomic transition is used for all measurement done with a temperature below $0.15 T_F = 0.9 T_C$, while a range of detunings from 2 to 5 kHz is used at higher temperatures to improve the temperature sensitivity. Following the rf pulse, absorption images of both transferred atoms in $|2\rangle$ and unaffected atoms in $|3\rangle$ are taken to determine the transferred atoms density $n_f(\mathbf{r})$ and the original density $n(\mathbf{r})$ (Fig.5-5E and G). The spatial temperature deviation (as shown in Fig5-5.F and H) from thermal equilibrium can be determined with the calibration of the change in

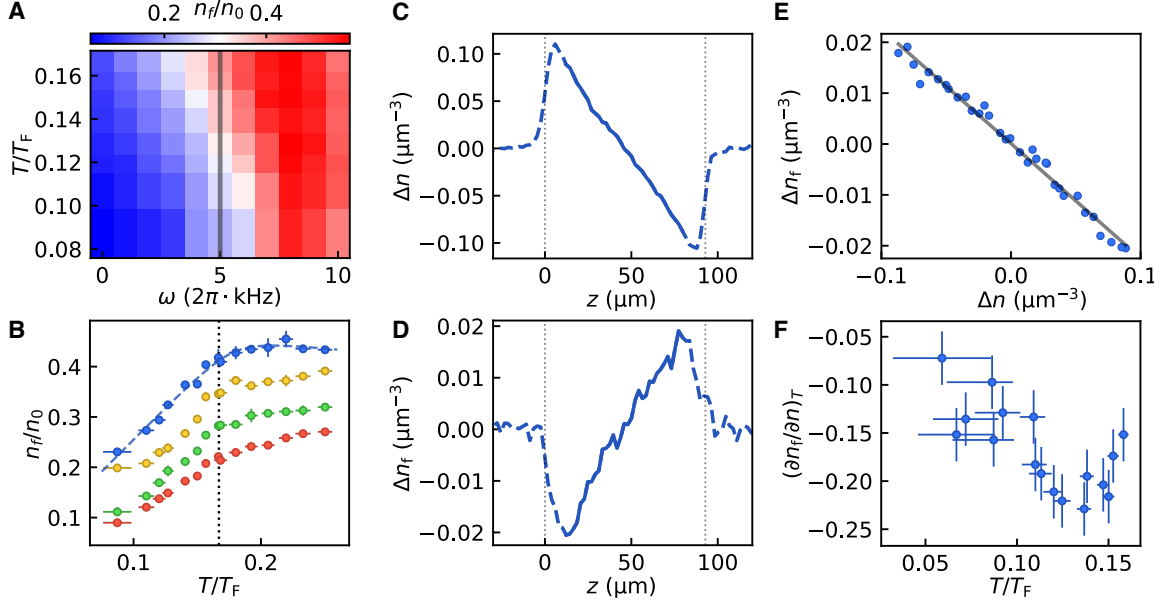


Figure 5-6: (A) rf transfer rate at various temperatures and detuning in the superfluid phase. A maximum linear gradient along the temperature axis exists at a detuning of 5 kHz, marked by the gray vertical line. (B) The temperature dependence of the rf transfer rate across the superfluid transition (vertical dotted line). The blue (yellow, green, and red) circles are the measured rf transfer rate at a detuning of 5 kHz (4, 3, and 2 kHz). The blue dashed line is a hyperbola fit to the rf transfer rate at 5 kHz detuning. (C and D) Density change along the axial direction in the unaffected state $|3\rangle$ (C) and the final state $|f\rangle$ (D) after an adiabatic gradient ramp and the rf pulse. Only the data measured away from the edges of the cloud (marked by the vertical dotted lines) are used for the calibration (solid blue line). (E) The linear response of rf transfer rate to the density change (blue circles). $\left.\frac{\partial n_f}{\partial n}\right|_T$ is determined by a linear fit (solid black line). (F) $\left.\frac{\partial n_f}{\partial n}\right|_T$ measured at various temperatures below T_c , the error bars are estimated by the scattering of individual measures.

rf transfer rate over both temperature $\left.\frac{\partial n_f}{\partial T}\right|_n$, and density $\left.\frac{\partial n_f}{\partial n}\right|_T$:

$$\Delta T(\mathbf{r}, t) = \left. \frac{\partial T}{\partial n_f} \right|_n \left[\Delta n_f(\mathbf{r}, t) - \left. \frac{\partial n_f}{\partial n} \right|_T \Delta n(\mathbf{r}, t) \right]. \quad (5.74)$$

To calibrate the rf transfer rate versus temperature, we kept atomic density constant and measured rf transfer rate at various temperature and detuning, as shown in Fig.5-6A. For temperature below $T_c = 0.16 T_F$, we found an optimal detuning of $\omega = 2\pi \cdot 5$ kHz, where temperature dependence of the transferred fraction n_f/n_0

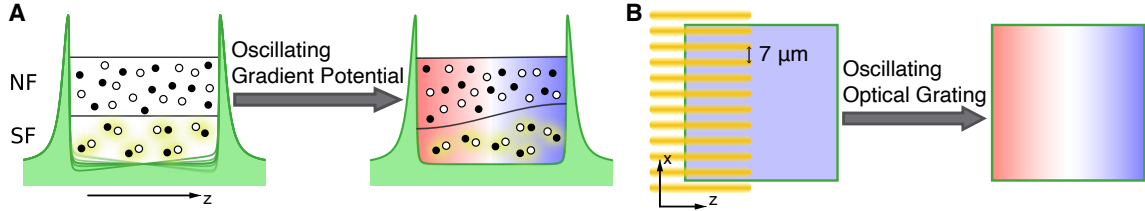


Figure 5-7: Creation of second sound and temperature variation. (A) Creating second sound using an oscillating gradient potential. (B) Creating temperature disparity using an oscillating optical grating. The grating spacing of the potential is $7 \mu\text{m}$. The blue to red color gradient represents a temperature variation from cold to hot.

is almost linear (Fig.5-6B). Above the transition temperature, the rf transfer rate saturates with increasing temperature. A hyperbola function is used to fit the rf-temperature response at 5 kHz and extract the local slope. To calibrate the rf-density response, we ramp up a linear gradient potential along the axial (z) direction and measure the change in both $n(z)$ and $n_f(z)$, as shown in Fig.5-6C and D. The potential ramp is kept slow, so the temperature stays constant across the cloud. Noticeably, the transferred atom number decreases with increasing initial density, as local T/T_F is reduced. A linear fit to the $n_f(\Delta n)$ curve gives the rf-density response (Fig.5-6E). Fig.5-6F shows the temperature dependence of the rf-density response $\left. \frac{\partial n_f}{\partial n} \right|_T$.

5.3.2 Creation and observation of the second sound

To excite the second sound or temperature disparity in the quantum gas, we use an oscillating gradient potential or an intensity-modulated optical grating, as illustrated in Fig.5-7. The gradient potential is generated magnetically by adding a bias current on one of the Feshbach coils. Despite the weak coupling between density and temperature perturbations [200], a standing wave of second sound can be excited by an oscillatory force with a resonant frequency (Fig.5-7A). During gradient potential oscillation, the change in the local magnetic field is less than 0.02 G and the modulation of atomic interaction is negligible. While the gradient oscillation method works well in the regime where a long-lived resonant mode of second sound exists, this method cannot create local temperature variation when the heat propagation is overdamped near or above superfluid transition temperature T_c . Instead, heat can

be injected by exciting high-frequency phonons with a decay length comparable to its wavelength [149, 102]. As the high-frequency phonons rapidly decay into thermal excitations, they create a local hot spot in the cloud. A modulated optical grating potential projected onto half of the atomic cloud is used to excite an entropy propagation mode with good overlap with the lowest axial mode (Fig.5-7B). A 589 nm laser light is used to project the optical grating. The grating spacing on the atomic cloud is $7 \mu\text{m}$. A 2 kHz modulation frequency is used for grating modulation to match the phonon resonance. The amplitude of grating modulation is kept at a low level so that so that density change and first sound wave caused by the optical potential is small.

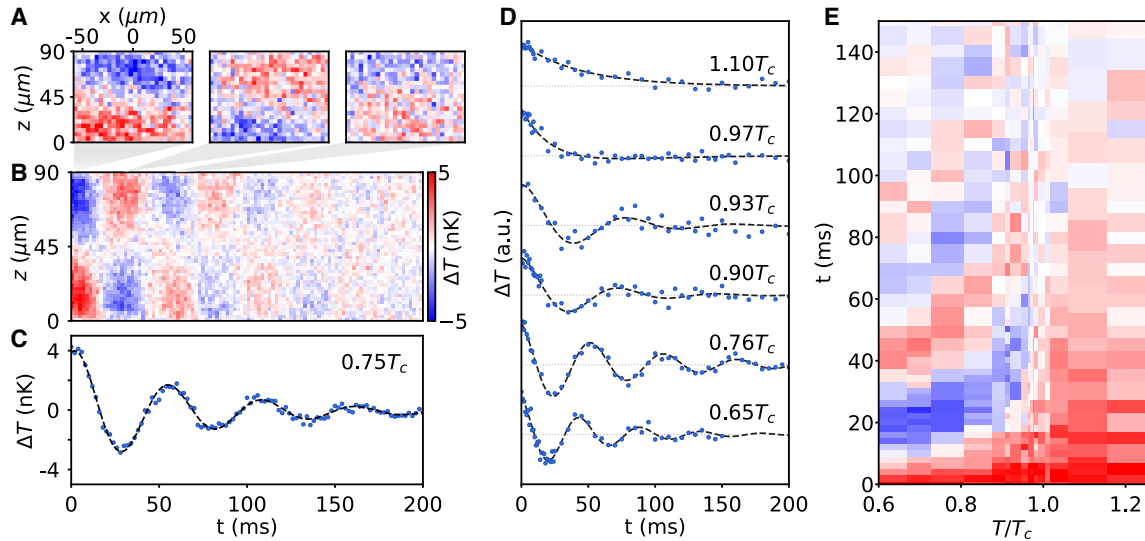


Figure 5-8: Heat propagation in the unitary Fermi gas. (A) in-situ measurement of heat propagation after exciting a second sound wave using rf transfer, at time $t=0$, 26, and 54ms. (B) Time evolution of the local change in temperature along the axial direction. (C) The amplitude of the 1st spatial Fourier mode of temperature profile $\Delta T(k_1, t)$ (blue circles). A fit to the temperature evolution (dashed line) provides the speed and decay rate of second sound. The temperature of the cloud shown in (A),(B) and (C) is $T = 63 \text{ nK}$ or $0.75 T_c$, the oscillation frequency is 19.8 Hz and the amplitude of gradient oscillation is $g = h \cdot 3.18 \text{ Hz}/\mu\text{m}$. (D) The measured amplitude of the 1st spatial Fourier mode of the rf response (solid circles) and fitted curves (dashed lines) at various temperatures across the superfluid transition temperature. (E) 2D plot of the 1st mode temperature evolution across the superfluid transition.

The thermal evolution after a resonant gradient shaking is shown in Fig. 5-8(A-C). Fig.5-8A shows the snapshots of the rf response $\Delta n_f(\mathbf{r}, t)$ at $t = 0$, 26, and 54 ms. Fig.5-8B demonstrates the time evolution of the temperature profile $\Delta T(z, t)$ in a ho-

mogeneous system after the creation of a second sound standing wave. The oscillating temperature profile provides striking evidence for a wave-like heat propagation in a superfluid. As discussed in Sec. 5.1.4, the free evolution of the hydrodynamic system at a given wavenumber k is a damped sinusoidal wave, in analogy to a harmonic oscillator. The frequency of oscillation $\omega = c \cdot k$ yields the speed of sound c , while the damping rate $\Gamma = D \cdot k^2$ measures the diffusivity D . A spatial Fourier transform provides a quantitative measure of the second sound amplitude at wavenumber $k_m = \frac{m\pi}{L}$ in a uniform system, where m is a positive integer and L is length of the cloud:

$$\Delta T(k) = \frac{2}{L} \int_0^L dz \Delta T(z) \cos(kz). \quad (5.75)$$

The linear gradient potential oscillation predominantly excites the resonant mode with $m = 1$. The time evolution of $\Delta T(k_1, t)$ is shown in Fig. 5-8C. Fitting the measured $\Delta T(k_1, t)$ with a damped sinusoidal function gives a speed of second sound $c_2 = \frac{\omega}{k} = 3.57(2)\mu\text{m}/\text{ms}$, and a diffusivity of second sound $D_2 = \Gamma/k^2 = 2.44(11)\frac{\hbar}{m}$. Remarkably, the measured value of second sound diffusivity is close to the universal Heisenberg limit \hbar/m , which has also been observed in the transport of spin [187, 6, 120], momentum [1], and first sound [149] in strongly interacting Fermi gases. A similar diffusivity is also measured for second sound in strongly interacting bosonic superfluid ${}^4\text{He}$ [71, 126], while a much higher value of $D_2 \gtrsim 500\hbar/m$ is measured for second sound in weakly interacting fermionic ${}^3\text{He}$ [34, 119].

The heat propagation across the superfluid transition can be observed with the local heating method (Fig. 5-8 D and E). The signals shown here are the Fourier amplitude of the change in temperature $\Delta T(k_1, t)$. At temperatures well below T_c , a damped oscillation corresponding to second sound is observed. The second sound mode becomes increasingly damped as the temperature is raised to T_c . At temperatures above T_c , the entropy evolution becomes a diffusive exponential decay. The shift in heat propagation from the second sound mode into the purely diffusive mode is a clear signature of the superfluid phase transition.

5.3.3 Response functions

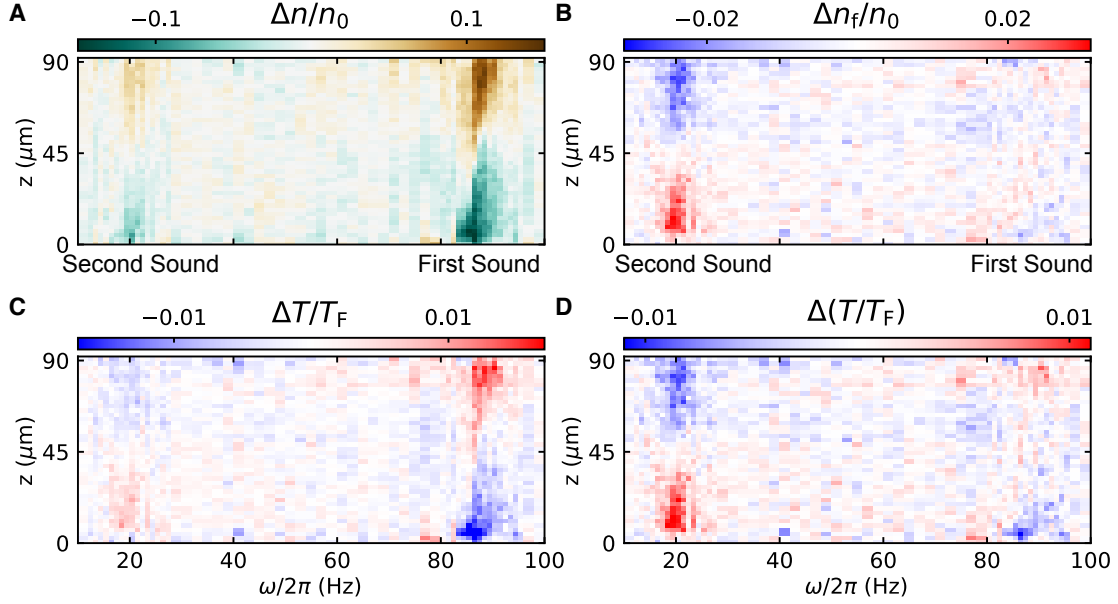


Figure 5-9: Steady state response of density Δn (**A**), rf transfer Δn_f (**B**), temperature ΔT (**C**), and reduced temperature $\Delta(T/T_F)$ (**D**). The steady-state responses are measured after modulating the axial gradient potential for integer cycles. For oscillation frequencies below 50 Hz, the oscillation amplitude is $g = h \cdot 2.12 \text{ Hz}/\mu\text{m}$ and number of oscillation cycles is 5; for oscillation frequencies above 50 Hz, the oscillation amplitude is $g = h \cdot 0.85 \text{ Hz}/\mu\text{m}$ and number of oscillation cycles is 20. The measurements shown here are done at a temperature of $T/T_F = 0.125$.

For a precision measurement of the response functions (see Sec. 5.1.4), we now turn to the steady-state temperature and density response under a continuous gradient potential oscillation. The steady-state temperature $\Delta T(k_1, \omega)$ and density responses $\Delta n(k_1, \omega)$ measured after an integer number of oscillation cycles yield the imaginary part of response functions [77]. Other than Δn and ΔT , another crucial thermodynamic quantity we can get from our measurement is the change in reduced temperature T/T_F :

$$\Delta \frac{T}{T_F}(\mathbf{r}, t) = \frac{\Delta T(\mathbf{r}, t)}{T_F} - \frac{2T}{3T_F} \frac{\Delta n(\mathbf{r}, t)}{n_0}. \quad (5.76)$$

In a scale invariant unitary Fermi gas, the quantity T/T_F dictates the state of the system [73], and $\Delta(T/T_F)$ corresponds directly to the entropy per particle $s = S/N$

by $\Delta s = \frac{c_V}{T/T_F} \Delta(T/T_F)$ or the local heat density q by $\Delta q = n c_V T_F \Delta(T/T_F)$, here c_V is the specific heat per particle at constant density. Measurement of local change in reduced temperature under a continuous potential oscillation gives the normalized-temperature-density response function $\chi_{\tilde{T},n}$, which can be directly linked to the heat-density reponse function $\chi_{q,n}$ by

$$\chi_{\tilde{T},n}(k, \omega) = \frac{\chi_{q,n}(k, \omega)}{n c_V T_F} \quad (5.77)$$

The measured change in density, rf transfer rate, temperature, and reduced temperature after continuous oscillation of axial gradient at a temperature of $T = 0.75 T_c$ is shown in Fig.5-9. Here we find that both first and second sound create change in temperature, while only the second sound mode results in a significant change in reduced temperature. Therefore, the second sound is an entropy wave rather than a temperature wave in a superfluid unitary Fermi gas, while the first sound is an isentropic density wave. This is similar to the case in superfluid helium-4 [93] but drastically different from the case in 2D and 3D Bose gases where both modes are strongly coupled with the density [190, 127, 30, 156]. Interestingly, here in our experiments the rf transfer rate provides an approximate direct measurement of the local reduced temperature.

In Fig. 5-10, we show the thermal evolution of the reduced temperature and density responses in the first spatial Fourier mode, which serve as a direct measurement of the heat-density $\chi_{\tilde{T},n}(k_1, \omega)$ and density-density $\chi_{n,n}(k_1, \omega)$ response functions. For measurements above 50 Hz, the oscillation amplitude is reduced by a factor of 2.5 to avoid saturating the first sound response. The directly measured reduced temperature and density response is shown in Fig. 5-10 A and B, while the response functions $\chi_{\tilde{T},n}$ and $\chi_{n,n}$, which are normalized by the shaking amplitude, are shown in Fig. 5-10 C and D. Complete information about the two-fluid hydrodynamics of the system can is found by fitting the measured data with the solution of hydrodynamic equations. While the speeds and diffusivities of both first and second sound fix the position and width of the peaks in the response functions, the relative weights of the peaks are

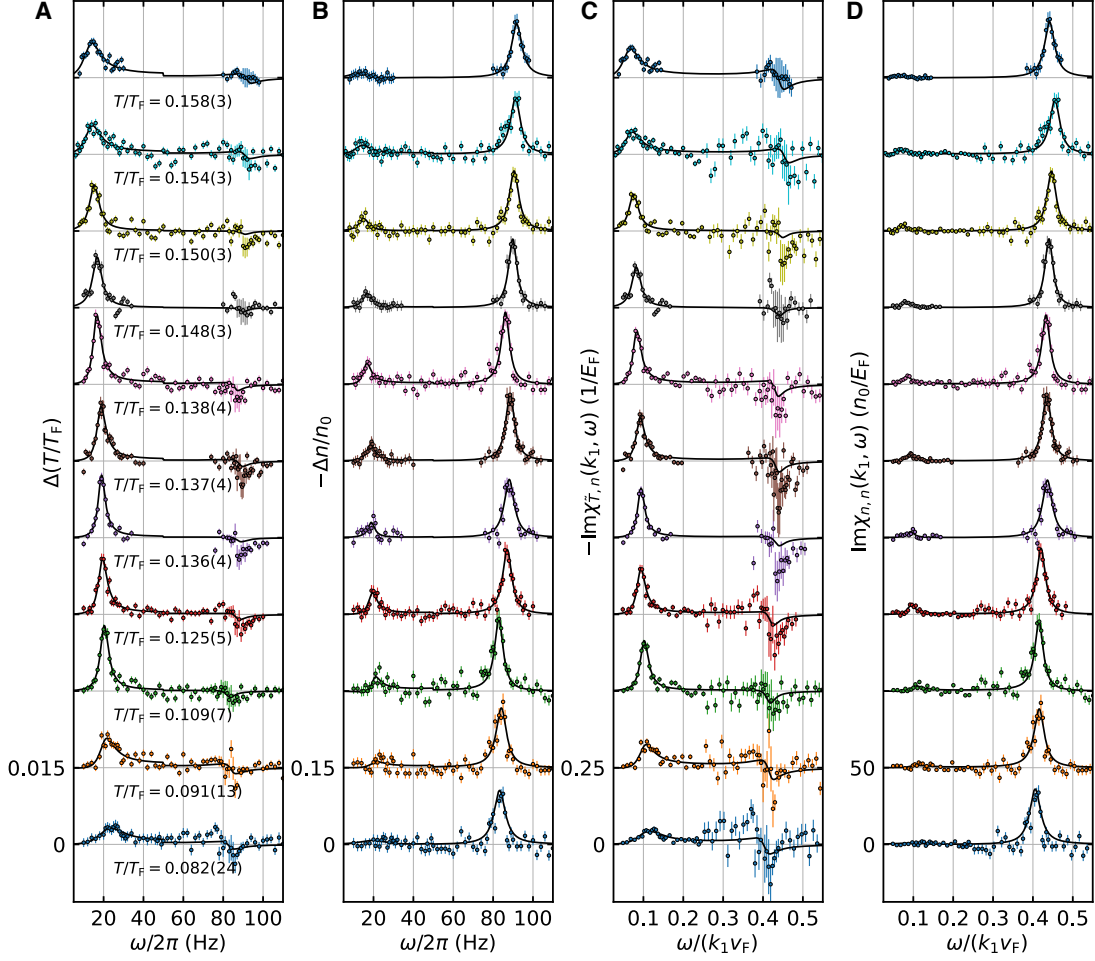


Figure 5-10: Steady state responses under a continuous gradient potential oscillation. **(A and B)** The normalized temperature (A) and density (B) response amplitude is calculated at wavenumber $k_1 = \pi/L$. An oscillation amplitude of $g = h \cdot 2.12$ (0.85) Hz/ μm and 5 (20) shaking cycles are used for oscillation frequencies below (above) 50 Hz. **(C and D)** Calculated normalized-temperature-density $\text{Im}\chi_{T,n}(k_1, \omega)$ (C) and density-density $\text{Im}\chi_{n,n}(k_1, \omega)$ (D) response functions. The solid black lines are fits using the response functions from Sec. 5.1.4.

determined by the isoentropic expansion coefficient γ and thermal expansivity α_P (Fig. 5-11). Though in principle the thermal conductivity κ , shear viscosity η , and bulk viscosity ζ_3 can be acquired from the specific shape of the measured response function, our experimental uncertainty yields errors for these quantities larger than the fitted value.

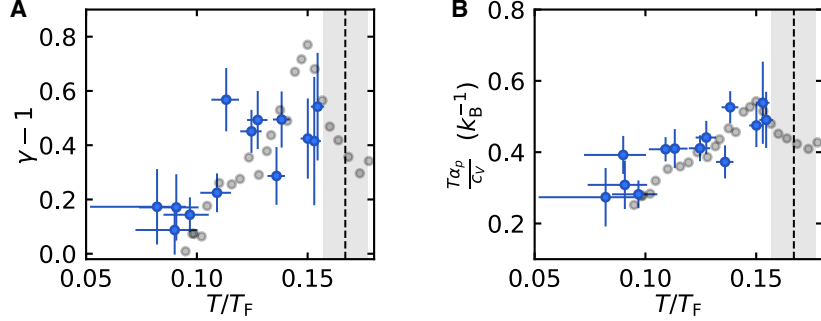


Figure 5-11: Thermodynamic quantities extracted from the response function fit. **(A)** The isentropic expansion coefficient γ acquired from the measured density response (blue circles). **(B)** The fitted amplitude of the reduced temperature response (blue circles). The gray circles in (A) and (B) are the values calculated using the previously measured equation of state [101]. The vertical dashed line and shade area indicates the phase transition temperature and its uncertainty.

5.3.4 Speed and diffusivity of the second sound

The speed of second sound measured by the methods described in Sec. 5.3.2 and 5.3.3 are shown in Fig.5-12A. The superfluid fraction can be extracted from the measured speed of second sound combined with the equation of state of the unitary Fermi gas [101], as shown in Fig.5-12B. Great consistency is shown between the frequency of the free evolution and the peak position in the response functions. The measured speed of second sound shows a qualitative agreement with a previous calculation [200] (the dot-dashed line) and our simple "phonon+pair-breaking" model (see Sec. 5.1.1). Our superfluid fraction result agrees well with the reconstructed homogeneous result from 1D second sound measurement by the Innsbruck group [184]. With the local heating method (red diamonds), we are able to observe the continuous evolution of c_2 and ρ_s from a finite value in the superfluid phase to zero in the normal phase. The phase transition point shown in the out-of-equilibrium heat transport measurement is consistent with the in-equilibrium thermodynamic measurement [101] (the vertical dashed line) and the onset of pair condensation (Fig.5-12C). A quantitative difference between the superfluid fraction and pair condensate fraction is observed in our experiment: the superfluid fraction saturates to a value of unity for temperature $T \lesssim 0.1T_F$, and the condensate fraction remains at ~ 0.75 . The superfluid density ρ_s is the part of the system that carries zero entropy and can travel through a thin capillary without

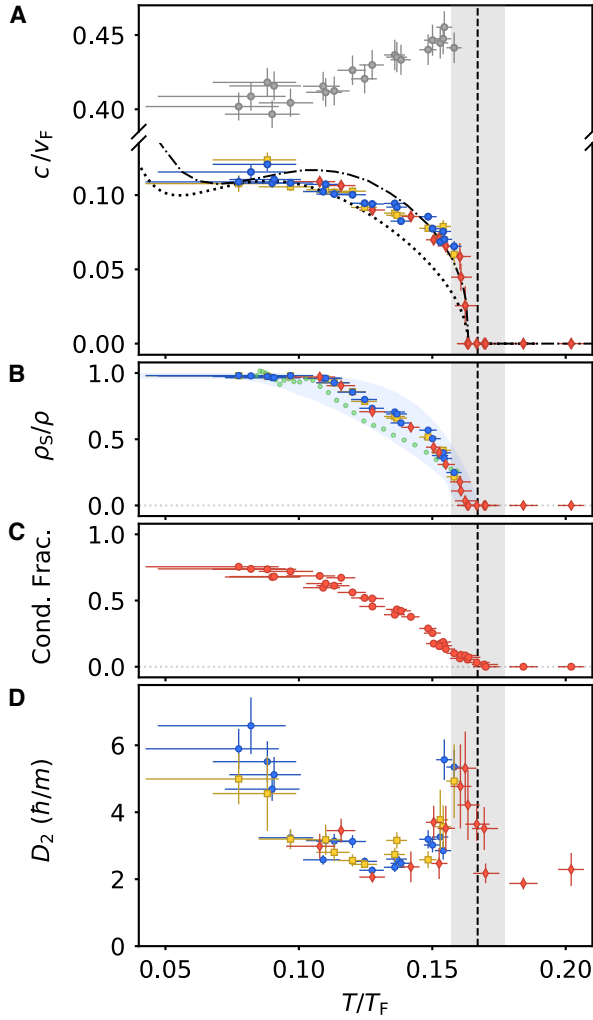


Figure 5-12: (A) The normalized speed of second sound as a function of temperature, determined by fitting the steady state response functions (blue circles) and free evolution of second sound excited by resonant gradient oscillation (yellow squares) or local heating (red diamonds). The first sound speed measured by response function fitting (gray circles) is also shown here. The dot-dashed line is a theoretical result of the second sound speed for a unitary Fermi gas [200]. The dotted line is calculated from the "phonon+pair-breaking" model discussed in Sec 5.1.1. (B) The superfluid fraction extracted from the speed of second sound with respective methods. The blue shaded area indicates the uncertainty from the equation of state. The solid green circles are superfluid fraction measured by the Innsbruck group [184]. (C) The pair condensate fraction measured by a momentum-space mapping of the pair wavefunction (see Sec. 3.1.4). (D) The second sound diffusivity measured with various methods. The vertical dashed line and the gray area indicate the critical temperature of the superfluid phase transition [101] and its uncertainty

friction, while the condensate fraction measures the occupation number of fermion pairs with zero momentum. In the zero-temperature limit, the entire system is superfluid as entropy equals zero, but not all the atoms are in the pair condensate due to quantum depletion caused by Pauli blocking and strong interaction.

The measured second sound diffusivity D_2 is shown in Fig.5-12D. In the temperature regime of $0.1 < T/T_F < 0.15$, second sound has a low diffusivity $D_2 \simeq 2.5\hbar/m$, comparable to the quantum limit \hbar/m . The second sound diffusivity grows substantially at lower temperature $T < 0.1T_F$, as well as at temperature close to T_c . The non-monotonic temperature dependence of D_2 in unitary Fermi gas draws similarity

to the results in liquid ^4He [214, 152, 126, 61]. At low temperatures, the diverging mean free path of phonons results in the growth of diffusivity. Close to the transition temperature T_c , the measured diffusivity peak resembles the $D_2 \propto |T_c - T|^{-1/3}$ critical behavior observed in ^4He [61, 69, 46, 90], as the superfluid phase transition in both strongly interacting Fermi gas and liquid helium belongs to the same 3D XY universality class. Other critical behaviors inferred by the same universality class are $c_2 \propto (T_c - T)^{1/3}$ and $\rho_s \propto (T_c - T)^{2/3}$, which are qualitatively consistent with the steep slope we observed close to T_c . In contrast, the diffusivity of first sound does not show substantial variation across the superfluid phase transition [149], since it is insensitive to the fluctuation of superfluid order parameter [47, 70], unlike the case of second sound. Our measurement of D_2 is the first time a critical phenomenon is observed close to the transition temperature in a transport coefficient for quantum gases. However, the residual inhomogeneity of cloud and finite temperature amplitude will produce a smearing effect of $\Delta(T/T_F) \sim 5 \times 10^{-3}$ on global reduced temperature, preventing a quantitative analysis of the critical behavior. Above the transition temperature, the diffusivity of the remnant heat diffusion mode is still on the order of \hbar/m , as the strong inter-atomic interaction is independent of the phase of matter. The non-monotonic behavior of diffusivity in heat transport has not been observed in spin, momentum, or first sound transport measurement in a unitary Fermi gas, though the same Heisenberg-limited diffusivity scale \hbar/m is shared.

5.4 Thermal diffusion in the normal phase

Using the local heating method, we are able to observe the heat diffusion governed by the thermal conductivity κ in the normal fluid phase, as shown in Fig. 5-8. Measurement on the thermal conductivity in this regime provides a benchmark for theories on the nature of unitary Fermi gases. For example, if the unitary Fermi gas is a Fermi liquid in the normal phase, it will have the characteristic $1/T$ temperature dependence of thermal conductivity. Due to the reduced rf-temperature response, we directly measure the density variation caused by the thermal expansion during a

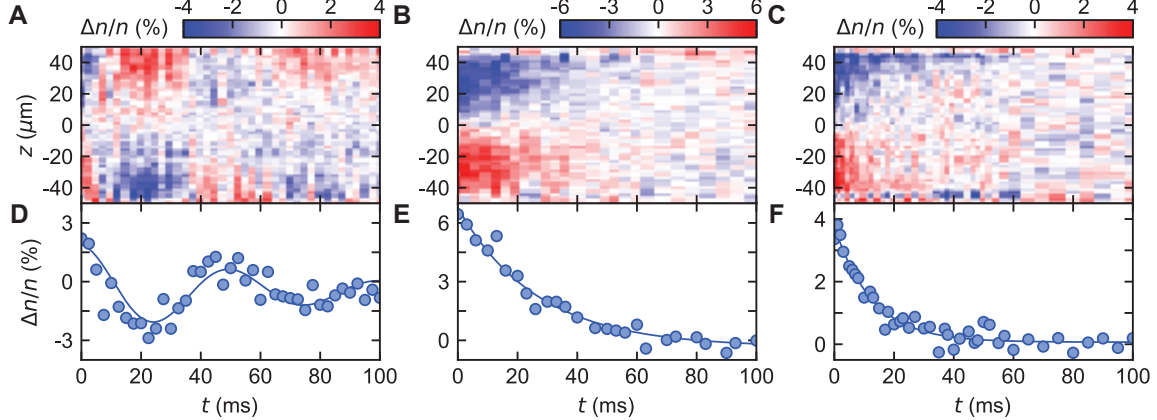


Figure 5-13: Density evolution during heat transport. (A-C) Evolution of axial density profiles $\Delta n(z, t)$ at $T = 0.10 T_F = 0.60 T_c$ (A), $0.25 T_F = 1.50 T_c$ (B), and $0.69 T_F = 4.13 T_c$ (C). (D-E) The corresponding Fourier amplitudes of the axial density profile at $k = \pi/L$.

thermal expansion, as shown in Fig. 5-13. Typical temperature variations ΔT used in this regime are $20 - 50$ nK, which are much higher than the temperature perturbations we used to observe second sound in the superfluid phase.

5.4.1 Thermal conductivity measured from thermal diffusion

The Fourier amplitude of an entropy variation at wavenumber k experiences an exponential decay with a decay rate $\Gamma = D_T k^2$. Here $D_T = \frac{\kappa}{nc_p}$ is the thermal diffusivity, with atomic density n and specific heat specific heat per particle at constant pressure [89]. If we consider the normal phase as a special case of superfluid where the superfluid component vanishes $\rho_s \rightarrow 0$, the thermal diffusivity is a remnant of the second sound diffusivity: $D_T \equiv D_2(\rho_s = 0)$. Indeed, it was predicted that D_2 and D_T shares the same $|T_c - T|^{-1/3}$ critical behavior on the two sides of the superfluid phase transition [46]. Fig. 5-14 shows the complete temperature dependence of D_2 (D_T) in the temperature range $0.08 T_F \lesssim T \lesssim 1.0 T_F$. Combining D_T in the normal phase with the specific heat c_p measured in Ref. [101] yields the thermal conductivity (Fig 5-15). At temperatures above T_C , the monotonic increasing of κ with temperature is a clear deviation from the $1/T$ Fermi liquid behavior. This result complements the non-Fermi-liquid behavior in the width of rf spectra discussed in Sec. 5.2.

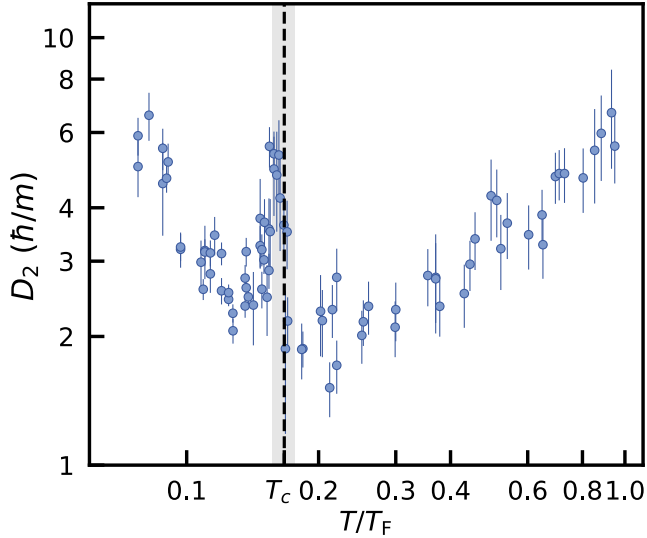


Figure 5-14: Second Sound and thermal diffusivity across the superfluid transition. The vertical dashed line and shaded area are the position and uncertainty of the superfluid transition temperature from Ref. [101].

5.4.2 Viscosity measured from thermal and sound diffusivity

In the normal phase of unitary Fermi gas, the damping of first sound comes from spatial gradients of both density and temperature, hence the diffusivity of first sound depends on both thermal conductivity κ and shear viscosity η :

$$D_1 = \frac{4\eta}{3\rho} + \frac{\kappa}{ncv}. \quad (5.78)$$

Using the thermal conductivity measured from heat diffusion and the diffusivity of first sound (see Appendix. D), we can solve the shear viscosity in Eq. (5.78), as shown in Fig. 5-15B.

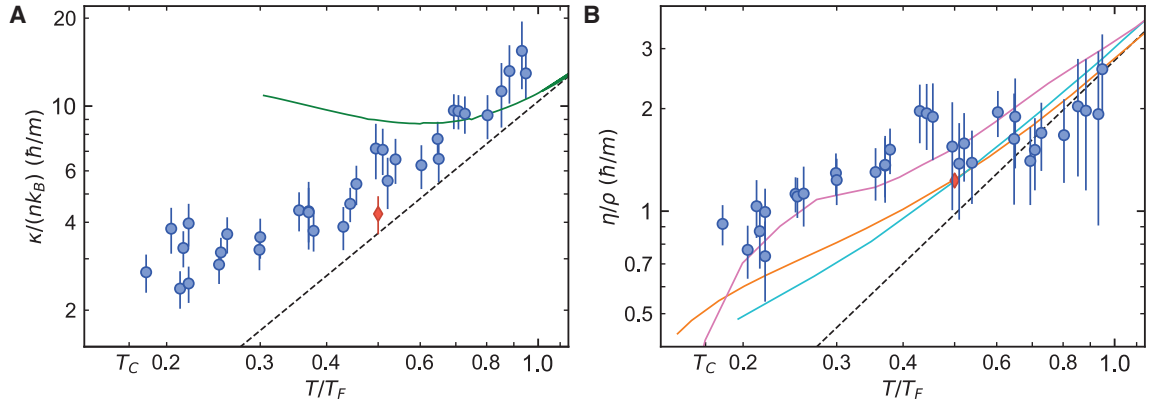


Figure 5-15: Temperature dependence of (**A**) thermal conductivity κ and (**B**) shear viscosity η . The dashed black lines are the $T^{3/2}$ scaling for both quantities at high temperature limit [16]. The thermal conductivity is compared with hydrodynamic response measurement from Ref. [4] (red diamond) and theoretical calculation from Ref. [54] (green line). The measured viscosity is compared with results from hydrodynamic expansion in Ref. [88] (pink line) and [88] (cyan line), and theoretical prediction from Ref. [44] (orange line).

Chapter 6

Conclusions and outlooks

This thesis has presented our team’s work on expanding the toolbox for quantum simulation and improving the understanding of strongly interacting Fermi systems. The realization of uniform Fermi gases promises further insight into phases and states of matter that have eluded observation or quantitative understanding. We have demonstrated that the homogeneous Fermi gas is an ideal platform for spectroscopic study at various temperatures and spin polarizations. The radio-frequency (rf) spectroscopy on a highly spin-imbalanced system reveals a transition from a polaronic Fermi liquid at low temperatures to a classical Boltzmann gas at high temperatures in the peak position and width of the spectra. For a spin-balanced system, we observe a sharp jump of the two-body contact at the superfluid transition, while the peak shift and width of the rf spectra show no singularity. In turn, the knowledge of the temperature dependence of rf spectra yields a local thermometry method for direct observation of heat transport. With this method, we can measure diffusivities of second sound in superfluid and heat diffusion in normal phase for the first time, which display a peak at the phase transition temperature. These new experimental methods pave the way for many promising directions for future research, which I will discuss next.

One of the major motivations for the development of a uniform potential for strongly interacting Fermi gas is the prospect of realizing the Fulde-Ferrell-Larkin-Ovchinnikov (FFLO) state [106, 55, 146, 161, 66] in a 3D bulk system. The FFLO state is a supersolid state in a spin-imbalanced Fermi gas. The mismatch between

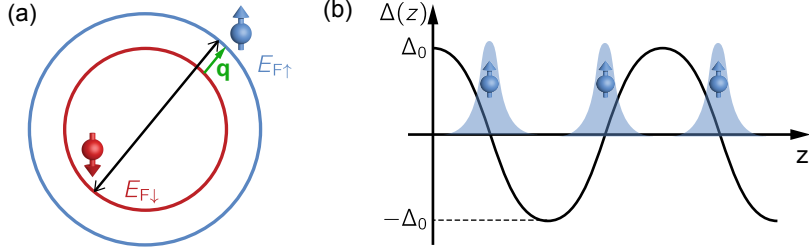


Figure 6-1: Schematic of an FFLO state. (a) Mismatch of Fermi surfaces and pairing at finite total momentum \mathbf{q} . (b) The pairing gap (order parameter) $\Delta(z)$ in an FFLO state (black curve), where the excessive spin majorities concentrate at the nodes of $\Delta(z)$.

the two spin components leads to an energetically favored fermion pair with a finite total momentum \mathbf{q} [Fig. 6-1(a)]. On the many-body level, Larkin and Ovchinnikov considered pair condensations in momentum $\pm\mathbf{q}$ [106], thus an order parameter $\Delta(z) \sim \cos qz$. The energy cost of a spatially modulated order parameter will be offset by putting excessive spin majorities around the nodes of $\Delta(z)$ [Fig. 6-1(b)], as the energy of an unpaired atom on the Fermi surface is given by the local pairing gap $|\Delta|$. Therefore, the ground state of the system has a spatially modulating spin polarization.

Though indirect evidence of the FFLO type phases has been observed in one dimensional Fermi gas [110], the direct observation of the FFLO state in 3D systems is still elusive. Fig. 6-2 illustrates the phase diagram of a spin-imbalanced Fermi gas on the Bardeen–Cooper–Schrieffer (BCS) side of the Feshbach resonance with $1/k_F a = -1$ [146], and the FFLO state is predicted to occur in a narrow range of parameters. Such a state is challenging to observe in a harmonic trap, as it will only reside in a thin shell of the system. A homogeneous Fermi gas occupying a single point on the phase diagram can serve as a potential remedy to this problem. In addition, the phase-contrast imaging method described in Sec. 3.3 provides a sensitive probe to the polarization oscillation in the FFLO state.

Besides the FFLO state, there are a number of other interesting experiment ideas about spin-imbalanced Fermi gases. For a harmonically trapped gas in the phase separation regime, the trap drives the separation of normal and superfluid phases

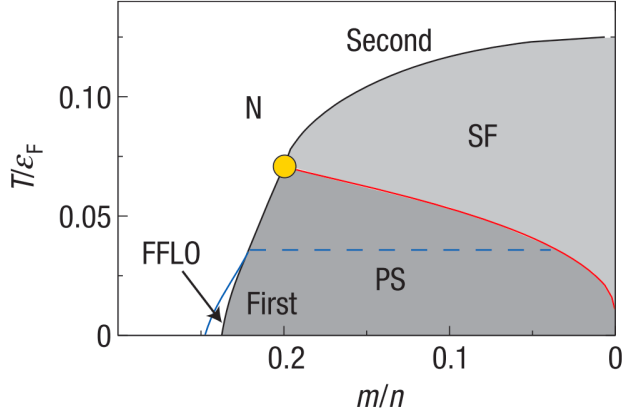


Figure 6-2: Phase diagram for the spin-imbalanced BCS solution at finite temperature and $1/k_Fa = -1$. The FFLO phase resides in a thin strip between the normal phase (N) and phase separation (PS) regime. Here $n = n_\uparrow + n_\downarrow$ is the total density and $m = n_\uparrow - n_\downarrow$ is the spin imbalance. This figure is taken from [146].

into a shell structure [135, 138, 222, 147, 180, 182]. In a homogeneous gas, this phase separation should occur spontaneously and possibly lead to the formation of domain walls. By measuring the dependence of typical domain size on the speed of polarization tuning, we will be able to explore the Kibble-Zurek physics [94, 215] in a strongly interacting system. RF spectroscopy provides another experimental probe to study the phase transition from a polaronic Fermi liquid to a superfluid when the spin polarization is reduced. It will be able to determine if polaronic quasiparticles still exist in the vicinity of the phase. In a spin-imbalanced superfluid, the excessive spin majorities will act as quasiparticle excitations and become part of the normal component. Thus the second sound in such a system will be a combination of spin and entropy wave, like the case in ${}^3\text{He}-A1$ phase [34].

Twenty years have passed since the science community first started the study on strongly interacting Fermi gases, and we are still making significant progress in developing new experimental methods and observing new phenomena. I have high hopes of more intriguing future results in the field of Fermi gases.

Appendix A

Homogeneous Atomic Fermi Gases

This appendix contains a reprint of Ref. [131]: Mukherjee, B., Yan, Z., Patel, P. B., Hadzibabic, Z., Yefsah, T., Struck, J., & Zwierlein, M. W. (2017). Homogeneous Atomic Fermi Gases. *Phys. Rev. Lett.*, 118(12), 123401.



Homogeneous Atomic Fermi Gases

Biswaroop Mukherjee,¹ Zhenjie Yan,¹ Parth B. Patel,¹ Zoran Hadzibabic,^{1,2} Tarik Yefsah,^{1,3} Julian Struck,¹ and Martin W. Zwierlein¹

¹*MIT-Harvard Center for Ultracold Atoms, Research Laboratory of Electronics, and Department of Physics, Massachusetts Institute of Technology, Cambridge, Massachusetts 02139, USA*

²*Cavendish Laboratory, University of Cambridge, J. J. Thomson Avenue, Cambridge CB3 0HE, United Kingdom*

³*Laboratoire Kastler Brossel, CNRS, ENS-PSL Research University, UPMC-Sorbonne Universités and Collège de France, Paris 75005, France*

(Received 31 October 2016; published 23 March 2017)

We report on the creation of homogeneous Fermi gases of ultracold atoms in a uniform potential. In the momentum distribution of a spin-polarized gas, we observe the emergence of the Fermi surface and the saturated occupation of one particle per momentum state: the striking consequence of Pauli blocking in momentum space for a degenerate gas. Cooling a spin-balanced Fermi gas at unitarity, we create homogeneous superfluids and observe spatially uniform pair condensates. For thermodynamic measurements, we introduce a hybrid potential that is harmonic in one dimension and uniform in the other two. The spatially resolved compressibility reveals the superfluid transition in a spin-balanced Fermi gas, saturation in a fully polarized Fermi gas, and strong attraction in the polaronic regime of a partially polarized Fermi gas.

DOI: 10.1103/PhysRevLett.118.123401

Ninety years ago, Fermi derived the thermodynamics of a gas of particles obeying the Pauli exclusion principle [1]. The Fermi gas quickly became a ubiquitous paradigm in many-body physics; yet even today, Fermi gases in the presence of strong interactions pose severe challenges to our understanding. Ultracold atomic Fermi gases have emerged as a flexible platform for studying such strongly correlated fermionic systems [2–6]. In contrast to traditional solid state systems, quantum gases feature tunable spin polarization, dimensionality, and interaction strength. This enables the separation of quantum statistical effects from interaction-driven effects, and invites the exploration of rich phase diagrams, for example bulk Fermi gases in the BEC-BCS crossover [3–10] and Fermi-Hubbard models in optical lattices [11–20].

So far, Fermi gas experiments have been performed in inhomogeneous traps, where the nonuniform density leads to spatially varying energy and length scales. This poses a fundamental problem for studies of critical phenomena for which the correlation length diverges. Furthermore, in a gas with spatially varying density, a large region of the phase diagram is traversed, potentially obscuring exotic phases that are predicted to occur in a narrow range of parameters. This is most severe for supersolid states, such as the elusive FFLO state [21–23], where the emergent spatial period is well defined only in a homogeneous setting. A natural solution to these problems is the use of uniform potentials, which have recently proved to be advantageous for thermodynamic and coherence measurements with Bose gases [24–27].

Here, we realize homogeneous Fermi gases in a versatile uniform potential. For spin-polarized gases, we observe both the formation of the Fermi surface and the saturation at

one fermion per momentum state, due to Pauli blocking. Spatially uniform pair condensates are observed for spin-balanced gases, offering strong prospects for the exploration of long-range coherence, critical fluctuations, and supersolidity.

In cases where the local density approximation (LDA) is valid, the spatially varying local chemical potential in an inhomogeneous trap can be utilized for thermodynamic [28–31] and spectroscopic [7,32,33] measurements. However, reconstructing the local density from line-of-sight integrated density profiles typically increases noise, while spatially selecting a central region of the gas reduces signal. A potential that is uniform along the line-of-sight is the natural solution. Combining the desirable features of homogeneous and spatially varying potentials, we introduce a hybrid potential that is uniform in two dimensions and harmonic in the third. The line-of-sight integration is now turned into an advantage: instead of averaging over a wide region of the phase diagram, the integration yields a higher signal-to-noise measurement of the local density. Using this geometry, we observe the characteristic saturation of isothermal compressibility in a spin-polarized gas, while a strongly interacting spin-balanced gas features a peak in the compressibility near the superfluid transition [31].

In our experiment, we prepare atoms in the two lowest hyperfine states of ${}^6\text{Li}$ near a Feshbach resonance, and load them into the uniform potential of the optical box trap depicted in Fig. 1(a), after evaporative precooling in a crossed dipole trap. We typically achieve densities and Fermi energies of up to $n \approx 10^{12} \text{ cm}^{-3}$ and $E_F \approx \hbar \times 13 \text{ kHz}$, corresponding to $\sim 10^6$ atoms per spin state in the box. The lifetime of the

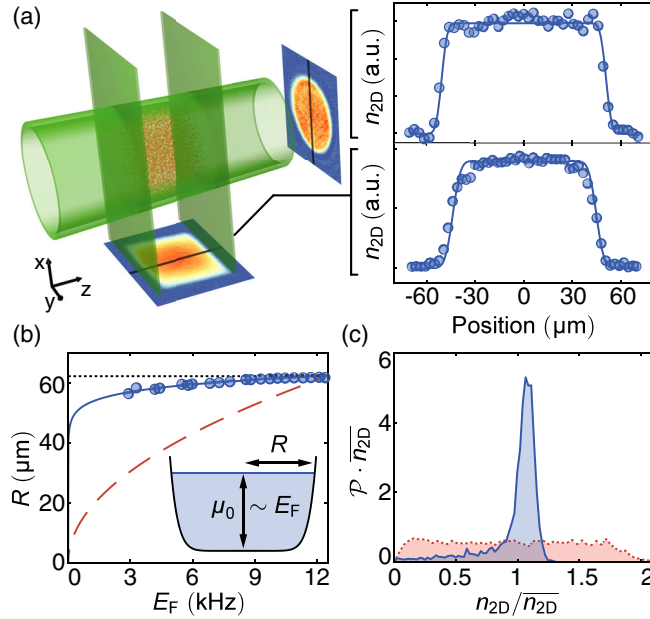


FIG. 1. Homogeneous Fermi gas. (a) Schematic of the box trap and cuts through the column-integrated density profiles along the axial and radial directions. (b) Radius of the cloud as a function of the Fermi energy. The dotted black and dashed red lines correspond to a perfect box potential and a harmonic potential, respectively, and are scaled to converge at the highest E_F . The blue solid line corresponds to a power law potential $V(r) \sim r^{16}$. (c) Measured radial probability density $P(n_{2D})$ for the column-integrated density n_{2D} , averaging about 20 in-trap images. The blue solid and red dashed lines correspond to the uniform and Gaussian traps, respectively.

Fermi gas in the box trap is several tens of seconds. The uniform potential is tailored using blue-detuned laser light for the confining walls. The sharp radial trap barrier is provided by a ring beam generated by an axicon [34,35], while two light sheets act as end caps for the axial trapping [36]. Furthermore, the atoms are levitated against gravity by a magnetic saddle potential [3]. The residual radial anticonfining curvature of the magnetic potential is compensated optically, while an axial curvature results in a weak harmonic potential described by a trapping frequency of $\omega_z = 2\pi \times 23.9$ Hz. This typically results in a variation of the potential along the axial direction that is less than 5% of the Fermi energy. Note that the magnetic moments of the two spin states of ${}^6\text{Li}$ differ by less than 0.1% at unitarity, resulting in a negligible difference in trapping potentials. We characterize the steepness of the trap walls by measuring the radial extent R of the cloud as a function of Fermi energy [see Fig. 1(b)]. Modeling the trap walls with a power law potential, we obtain $V(r) \sim r^{16.2 \pm 1.6}$ [36].

A stringent measure of the homogeneity of the gas is the probability distribution $P(n)$ for the atomic density n . Imaging along the z and x directions yields the radial and axial probability distribution $P(n_{2D})$ for the column density n_{2D} (see Fig. 1(c) and Ref. [36]). The distribution for the

homogeneous gas is sharply peaked near the trap average density \bar{n}_{2D} . For comparison, we also show $P(n_{2D})$ for an optical Gaussian trap, which is spread over a large range of densities.

Fermions at low temperatures are characterized by Pauli blocking [1]. Consequences of Pauli blocking have been observed in ultracold gases, for example, in nondegenerate samples, the reduction of collisions in spin-polarized gases below the p -wave threshold [2,37] and, upon entering degeneracy, Pauli pressure [38,39], reduced collisions [40,41], antibunching in noise correlations [42], and the reduction of density fluctuations [43,44]. In optical lattices under microscopes, Pauli blocking has been observed in real space through observations of band insulating states [16,17,45] and of the Pauli hole in pair correlations [20]. Typically obscured in the time of flight expansion of an inhomogeneous atomic gas, the Fermi surface has been observed by probing only the central region of a harmonically trapped gas [46]. Now, the uniform box potential enables us to directly observe the consequence of Pauli blocking in momentum space for degenerate gases: the Fermi-Dirac momentum distribution, featuring the emergence of a Fermi surface near the Fermi wave vector k_F and the saturated occupation of momentum states below k_F to one particle per momentum cell.

To measure the momentum distribution $f(\mathbf{k})$, we release a highly spin-imbalanced gas ($n_\downarrow/n_\uparrow < 0.05$, where n_\uparrow and n_\downarrow are the densities of the majority and minority spin components, respectively) from the uniform potential into the small residual axial harmonic potential (along the z axis). To ensure the ballistic expansion of the gas, the minority component is optically pumped into a weakly interacting state within 5 μs [36]. After a quarter period of expansion in the harmonic trap, the axial momenta k_z are mapped into real space via $z = \hbar k_z / m\omega_z$ [47–50]. In contrast to conventional time of flight measurements, this method is unaffected by the in-trap size of the gas. The measured integrated density profile $n_{1D}(z) = \int dx dy n(x, y, z)$ reflects the integrated momentum distribution $f_{1D}(k_z) = (2\pi)^{-2} \int dk_x dk_y f(k_x, k_y, k_z)$ via

$$f_{1D}(k_z) = \frac{2\pi\hbar}{Vm\omega_z} n_{1D}(z). \quad (1)$$

Here, V is the volume of the uniform trap. Figure 2(a) shows the integrated momentum distribution for different temperatures. Assuming a spherically symmetric momentum distribution, $f_k \equiv f(\mathbf{k}) = f(k)$. Noting that $\int dk_x dk_y f(\sqrt{k_x^2 + k_y^2 + k_z^2}) = \pi \int_{k_z^2}^{\infty} d(k^2) f(k)$, the three-dimensional momentum distribution can be obtained from the integrated momentum distribution by differentiation:

$$f_k = -4\pi \frac{df_{1D}(k_z)}{dk_z^2}. \quad (2)$$

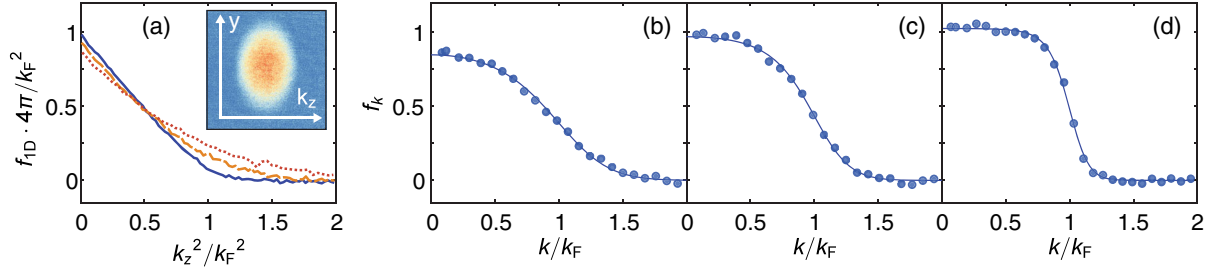


FIG. 2. Momentum distribution of the homogeneous spin-polarized Fermi gas. (a) Doubly integrated momentum distribution f_{ID} for different temperatures in the uniform trap. In order of decreasing temperature: red dotted line, orange dashed line, and blue solid line. Each line corresponds to averages over seven images. The optical density after momentum space mapping along z is shown in the inset. (b),(c),(d) Momentum distribution $f_k = -4\pi df_{ID}/dk^2$, showing Pauli blocking and Fermi surface formation. Fermi-Dirac fits (solid line) give (b) $T/T_F = 0.49(2)$, (c) $T/T_F = 0.32(1)$, and (d) $T/T_F = 0.16(1)$, with k_F ranging between $2.8 \mu\text{m}^{-1}$ and $3.7 \mu\text{m}^{-1}$. The estimated systematic error in the measurement of f_k is 15%.

As the temperature is lowered, the momentum distribution develops a Fermi surface, and we observe a momentum state occupation of 1.04(15) at low momenta [see Figs. 2(b)–2(d)], where the error in f_k is dominated by the systematic uncertainties in the box volume and the imaging magnification [36]. This is the direct consequence of Pauli blocking and confirms saturation at one fermion per momentum state.

An important motivation for the realization of a homogeneous Fermi gas is the prospect of observing exotic strongly correlated states predicted to exist in narrow parts of the phase diagram, such as the FFLO state [21,22]. In a harmonic trap, such states would be confined to thin isopotential shells of the cloud, making them challenging to observe. We observe pair condensation in a uniformly trapped strongly interacting spin-balanced Fermi gas through a rapid ramp of the magnetic field during time of flight [3,51,52], as shown in Figs. 3(a)–3(c). The pair condensate at the end of the ramp barely expands in time of

flight. As a result, the in-trap homogeneity is reflected in a flat top profile of the condensate [see Fig. 3(f)].

Although a fully uniform potential is ideal for measurements that require translational symmetry, a spatially varying potential can access a large region of the phase diagram in a single experimental run. To harness the advantages of both potentials, we introduce a hybrid geometry that combines the radially uniform cylinder trap with an axially harmonic magnetic trap along the z direction [see Fig. 4(a)]. As a benchmark for the hybrid trap, we perform a thermodynamic study of both a strongly spin-imbalanced and a spin-balanced unitary gas. Figures 4(c)–4(e) display for both cases the y -axis averaged local density, temperature, and compressibility. The data shown in Fig. 4 are extracted from an average of just six images per spin component. For comparison, precision measurements of the equation of state at unitarity, performed in conventional harmonic traps, required averaging of over 100 absorption images [31]. The temperature is obtained from fits to the known equations of state of the noninteracting and spin-balanced unitary Fermi gas, respectively. From the local density in the hybrid trap, we determine the normalized isothermal compressibility $\tilde{\kappa} = \kappa/\kappa_0 = -\partial E_F/\partial U|_T$ for the spin-imbalanced and the spin-balanced gas. Here, U is the external potential, and $\kappa_0 = \frac{3}{2}(1/nE_F)$ is the compressibility of the noninteracting Fermi gas at zero temperature [31].

The strongly spin-imbalanced cloud features two distinct regions in the trap. The center of the cloud is a partially polarized region in which $(n_\uparrow - n_\downarrow)/(n_\uparrow + n_\downarrow) > 0.64$, well above the Clogston-Chandrasekhar limit of superfluidity [53–55]. Surrounding the center is a fully polarized region, where the compressibility is seen to saturate: the real space consequence of the Pauli blocking in momentum space demonstrated in Fig. 2.

The majority spin component in the partially polarized region is affected by the presence of the minority spin component. We measure the compressibility $\tilde{\kappa}_\uparrow = -\partial E_{F\uparrow}/\partial U$ in the partially polarized region, and observe an increase compared to the fully polarized gas. This is expected as

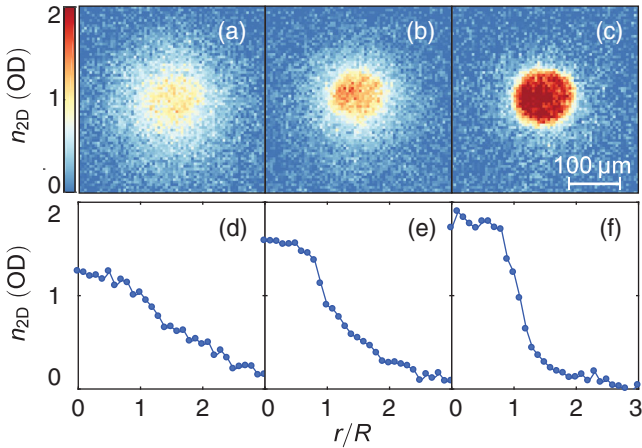


FIG. 3. Pair condensation in the uniform trap. (a), (b), and (c) Absorption images after a rapid ramp of the magnetic field and 10 ms of time of flight. The temperature of the gas is lowered (left to right) by evaporation in the uniform trap. The onset of a bimodal distribution signals the formation of a pair condensate. (d), (e), and (f) show cuts through the images in the top row.

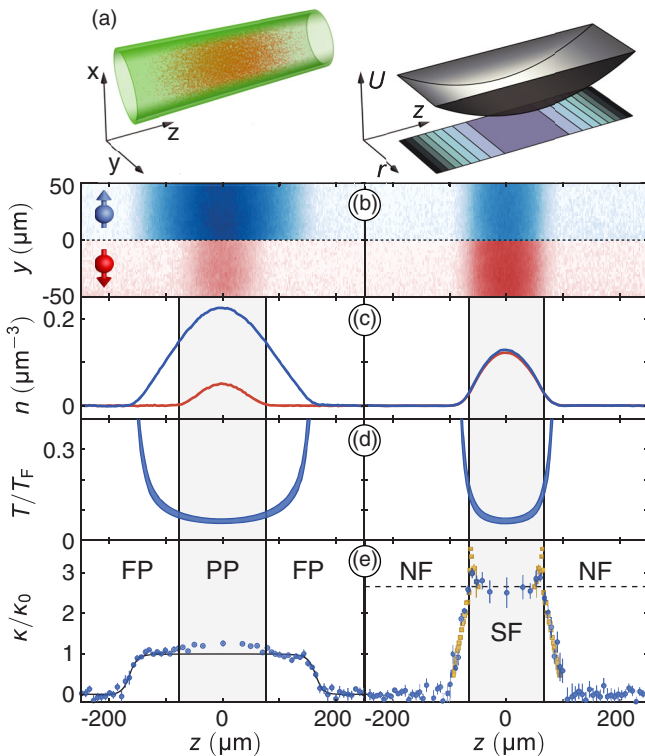


FIG. 4. Unitary Fermi gases in the hybrid trap. (a) Schematic and potential of the trap. The cloud is imaged along an equipotential direction (x axis). Left panels of (b)–(e) show a spin-imbalanced gas above the Clogston-Chandrasekhar limit, whereas the right side corresponds to a spin-balanced gas. The data are averaged over six images. (b) Local density for both spin components, obtained by dividing the column density by the column length. (c) Average density for each x - y equipotential slice. The blue (red) line shows the spin-up (-down) component. (d) Spatially resolved temperature of the gas. The blue shaded region represents the error in the temperature determination. (e) Compressibility of the gas. The solid line in the left panel is the compressibility for an ideal Fermi gas. The crossover from the fully polarized (FP) region to the partially polarized (PP) region is accompanied by an increase in $\tilde{\kappa}$. The yellow squares in the right panel correspond to a precision measurement of the balanced unitary equation of state in the harmonic trap [31]. The peaks in the compressibility signal the phase transition from normal (N) to superfluid (SF). The horizontal dashed line shows the zero-temperature equation of state $\kappa/\kappa_0 = 1/\xi$.

the minority atoms in the center of the trap attract majority atoms and form polarons [7,8]. The effect is indeed predicted by the polaron equation of state [29,30,56]. The observation of this subtle effect highlights the sensitivity of the hybrid potential for thermodynamic measurements.

In the spin-balanced case, κ/κ_0 is significantly larger than for the ideal Fermi gas due to strong interactions. The two prominent peaks in the reduced compressibility signal the superfluid transition at the two boundary surfaces between the superfluid core and the surrounding normal fluid. Near the center of the trap, the reduced compressibility agrees with the $T = 0$ equation of state $\kappa/\kappa_0 = 1/\xi = 2.65(4)$,

where ξ is the Bertsch parameter. The shaded region in the right column of Fig. 4 shows the superfluid part of the gas, where the temperature is below the critical temperature for superfluidity $T_c = 0.17T_F$ [31].

The realization of uniform Fermi gases promises further insight into phases and states of matter that have eluded observation or quantitative understanding. This includes the observation of the quasiparticle jump [57] in the momentum distribution of a Fermi liquid, critical fluctuations in the BEC-BCS crossover, and long-lived solitons [58]. Of particular interest are spin imbalanced mixtures that have been studied extensively in harmonic traps [29,30,55,59–62], where the trap drives the separation of normal and superfluid phases into a shell structure. This phase separation should occur spontaneously in a uniform spin-imbalanced gas, possibly forming domains of superfluid and eventually ordering into an FFLO state. In addition, the hybrid potential is a valuable tool for precision measurements that rely on an in-trap density variation. For example, spatially resolved rf spectroscopy [32] in the hybrid potential would measure the homogenous response of the system over a large range of normalized temperatures T/T_F in a single experimental run.

We thank R. Fletcher for a critical reading of the manuscript, and E. A. Cornell and C. Altamiras for helpful discussions. This work was supported by the NSF, the ARO MURI on Atomtronics, AFOSR PECASE and MURI on Exotic Phases, and the David and Lucile Packard Foundation. Z. H. acknowledges support from EPSRC (Grant No. EP/N011759/1).

- [1] E. Fermi, *Rend. Fis. Acc. Lincei* **3**, 145 (1926).
- [2] B. DeMarco and D. S. Jin, *Science* **285**, 1703 (1999).
- [3] *Ultra-cold Fermi Gases, Proceedings of the International School of Physics Enrico Fermi, Course CLXIV, Varenna 2006*, edited by M. Inguscio, W. Ketterle, and C. Salomon (IOS Press, Amsterdam, 2008).
- [4] S. Giorgini, L. P. Pitaevskii, and S. Stringari, *Rev. Mod. Phys.* **80**, 1215 (2008).
- [5] *The BCS-BEC Crossover and the Unitary Fermi Gas*, edited by W. Zwerger, Lecture Notes in Physics Vol. 836 (Springer-Verlag Berlin Heidelberg, Berlin, Heidelberg, 2012).
- [6] M. W. Zwierlein, in *Novel Superfluids* (Oxford University Press, New York, 2014), pp. 269–422.
- [7] A. Schirotzek, C.-H. Wu, A. Sommer, and M. W. Zwierlein, *Phys. Rev. Lett.* **102**, 230402 (2009).
- [8] S. Nascimbène, N. Navon, K. J. Jiang, L. Tarruell, M. Teichmann, J. McKeever, F. Chevy, and C. Salomon, *Phys. Rev. Lett.* **103**, 170402 (2009).
- [9] M. Koschorreck, D. Pertot, E. Vogt, B. Fröhlich, M. Feld, and M. Köhl, *Nature (London)* **485**, 619 (2012).
- [10] C. Kohstall, M. Zaccanti, M. Jag, A. Trenkwalder, P. Massignan, G. M. Bruun, F. Schreck, and R. Grimm, *Nature (London)* **485**, 615 (2012).
- [11] R. Jördens, N. Strohmaier, K. Günter, H. Moritz, and T. Esslinger, *Nature (London)* **455**, 204 (2008).

- [12] U. Schneider, L. Hackermüller, S. Will, T. Best, I. Bloch, T. A. Costi, R. W. Helmes, D. Rasch, and A. Rosch, *Science* **322**, 1520 (2008).
- [13] T. Esslinger, *Annu. Rev. Condens. Matter Phys.* **1**, 129 (2010).
- [14] I. Bloch, J. Dalibard, and S. Nascimbène, *Nat. Phys.* **8**, 267 (2012).
- [15] R. A. Hart, P. M. Duarte, T.-L. Yang, X. Liu, T. Paiva, E. Khatami, R. T. Scalettar, N. Trivedi, D. A. Huse, and R. G. Hulet, *Nature (London)* **519**, 211 (2015).
- [16] D. Greif, M. F. Parsons, A. Mazurenko, C. S. Chiu, S. Blatt, F. Huber, G. Ji, and M. Greiner, *Science* **351**, 953 (2016).
- [17] L. W. Cheuk, M. A. Nichols, K. R. Lawrence, M. Okan, H. Zhang, and M. W. Zwierlein, *Phys. Rev. Lett.* **116**, 235301 (2016).
- [18] M. F. Parsons, A. Mazurenko, C. S. Chiu, G. Ji, D. Greif, and M. Greiner, *Science* **353**, 1253 (2016).
- [19] M. Boll, T. A. Hilker, G. Salomon, A. Omran, J. Nespolo, L. Pollet, I. Bloch, and C. Gross, *Science* **353**, 1257 (2016).
- [20] L. W. Cheuk, M. A. Nichols, K. R. Lawrence, M. Okan, H. Zhang, E. Khatami, N. Trivedi, T. Paiva, M. Rigol, and M. W. Zwierlein, *Science* **353**, 1260 (2016).
- [21] A. J. Larkin and Y. N. Ovchinnikov, *Zh. Eksp. Teor. Fiz.* **47**, 1136 (1964).
- [22] P. Fulde and R. A. Ferrell, *Phys. Rev.* **135**, A550 (1964).
- [23] L. Radzihovsky and D. E. Sheehy, *Rep. Prog. Phys.* **73**, 076501 (2010).
- [24] A. L. Gaunt, T. F. Schmidutz, I. Gotlibovich, R. P. Smith, and Z. Hadzibabic, *Phys. Rev. Lett.* **110**, 200406 (2013).
- [25] T. F. Schmidutz, I. Gotlibovich, A. L. Gaunt, R. P. Smith, N. Navon, and Z. Hadzibabic, *Phys. Rev. Lett.* **112**, 040403 (2014).
- [26] N. Navon, A. L. Gaunt, R. P. Smith, and Z. Hadzibabic, *Science* **347**, 167 (2015).
- [27] L. Chomaz, L. Corman, T. Bienaimé, R. Desbuquois, C. Weitenberg, S. Nascimbène, J. Beugnon, and J. Dalibard, *Nat. Commun.* **6**, 6162 (2015).
- [28] T.-L. Ho and Q. Zhou, *Nat. Phys.* **6**, 131 (2009).
- [29] S. Nascimbène, N. Navon, K. J. Jiang, F. Chevy, and C. Salomon, *Nature (London)* **463**, 1057 (2010).
- [30] N. Navon, S. Nascimbene, F. Chevy, and C. Salomon, *Science* **328**, 729 (2010).
- [31] M. J. H. Ku, A. T. Sommer, L. W. Cheuk, and M. W. Zwierlein, *Science* **335**, 563 (2012).
- [32] Y.-I. Shin, C. H. Schunck, A. Schirotzek, and W. Ketterle, *Phys. Rev. Lett.* **99**, 090403 (2007).
- [33] A. Schirotzek, Y.-I. Shin, C. H. Schunck, and W. Ketterle, *Phys. Rev. Lett.* **101**, 140403 (2008).
- [34] J. H. McLeod, *J. Opt. Soc. Am.* **44**, 592 (1954).
- [35] I. Manek, Y. Ovchinnikov, and R. Grimm, *Opt. Commun.* **147**, 67 (1998).
- [36] See Supplemental Material at <http://link.aps.org/supplemental/10.1103/PhysRevLett.118.123401> for further information on making and characterizing the uniform trap, optical pumping for the momentum-space mapping, and calibrating the absorption imaging.
- [37] R. Thomas, K. O. Roberts, E. Tiesinga, A. C. J. Wade, P. B. Blakie, A. B. Deb, and N. Kjærgaard, *Nat. Commun.* **7**, 12069 (2016).
- [38] A. G. Truscott, K. E. Strecker, W. I. McAlexander, G. B. Partridge, and R. G. Hulet, *Science* **291**, 2570 (2001).
- [39] F. Schreck, L. Khaykovich, K. L. Corwin, G. Ferrari, T. Bourdel, J. Cubizolles, and C. Salomon, *Phys. Rev. Lett.* **87**, 080403 (2001).
- [40] B. DeMarco, S. B. Papp, and D. S. Jin, *Phys. Rev. Lett.* **86**, 5409 (2001).
- [41] A. Sommer, M. Ku, and M. W. Zwierlein, *New J. Phys.* **13**, 055009 (2011).
- [42] T. Rom, T. Best, D. van Oosten, U. Schneider, S. Fölling, B. Paredes, and I. Bloch, *Nature (London)* **444**, 733 (2006).
- [43] T. Müller, B. Zimmermann, J. Meineke, J.-P. Brantut, T. Esslinger, and H. Moritz, *Phys. Rev. Lett.* **105**, 040401 (2010).
- [44] C. Sanner, E. J. Su, A. Keshet, R. Gommers, Y.-I. Shin, W. Huang, and W. Ketterle, *Phys. Rev. Lett.* **105**, 040402 (2010).
- [45] A. Omran, M. Boll, T. A. Hilker, K. Kleinlein, G. Salomon, I. Bloch, and C. Gross, *Phys. Rev. Lett.* **115**, 263001 (2015).
- [46] T. E. Drake, Y. Sagi, R. Paudel, J. T. Stewart, J. P. Gaebler, and D. S. Jin, *Phys. Rev. A* **86**, 031601 (2012).
- [47] I. Shvarchuck, C. Buggle, D. S. Petrov, K. Dieckmann, M. Zielonkovski, M. Kemmann, T. G. Tiecke, W. von Klitzing, G. V. Shlyapnikov, and J. T. M. Walraven, *Phys. Rev. Lett.* **89**, 270404 (2002).
- [48] A. H. van Amerongen, J. J. P. van Es, P. Wicke, K. V. Kheruntsyan, and N. J. van Druten, *Phys. Rev. Lett.* **100**, 090402 (2008).
- [49] S. Tung, G. Lamporesi, D. Lobser, L. Xia, and E. A. Cornell, *Phys. Rev. Lett.* **105**, 230408 (2010).
- [50] P. A. Murthy, D. Kedar, T. Lompe, M. Neidig, M. G. Ries, A. N. Wenz, G. Zürn, and S. Jochim, *Phys. Rev. A* **90**, 043611 (2014).
- [51] C. A. Regal, M. Greiner, and D. S. Jin, *Phys. Rev. Lett.* **92**, 040403 (2004).
- [52] M. W. Zwierlein, C. A. Stan, C. H. Schunck, S. M. F. Raupach, A. J. Kerman, and W. Ketterle, *Phys. Rev. Lett.* **92**, 120403 (2004).
- [53] B. S. Chandrasekhar, *Appl. Phys. Lett.* **1**, 7 (1962).
- [54] A. M. Clogston, *Phys. Rev. Lett.* **9**, 266 (1962).
- [55] M. W. Zwierlein, A. Schirotzek, C. H. Schunck, and W. Ketterle, *Science* **311**, 492 (2006).
- [56] Y.-I. Shin, *Phys. Rev. A* **77**, 041603 (2008).
- [57] G. D. Mahan, *Many-Particle Physics* (Springer, Boston, MA, 2000).
- [58] M. J. H. Ku, B. Mukherjee, T. Yefsah, and M. W. Zwierlein, *Phys. Rev. Lett.* **116**, 045304 (2016).
- [59] G. B. Partridge, W. Li, R. I. Kamar, Y.-A. Liao, and R. G. Hulet, *Science* **311**, 503 (2006).
- [60] Y.-I. Shin, M. W. Zwierlein, C. H. Schunck, A. Schirotzek, and W. Ketterle, *Phys. Rev. Lett.* **97**, 030401 (2006).
- [61] Y.-I. Shin, C. H. Schunck, A. Schirotzek, and W. Ketterle, *Nature (London)* **451**, 689 (2008).
- [62] Y.-A. Liao, A. S. C. Rittner, T. Paprotta, W. Li, G. B. Partridge, R. G. Hulet, S. K. Baur, and E. J. Mueller, *Nature (London)* **467**, 567 (2010).

Supplemental Material: Homogeneous Atomic Fermi Gases

Biswaroop Mukherjee,¹ Zhenjie Yan,¹ Parth B. Patel,¹
Zoran Hadzibabic,^{1,2} Tarik Yefsah,^{1,3} Julian Struck,¹ and Martin W. Zwierlein¹

¹*MIT-Harvard Center for Ultracold Atoms, Research Laboratory of Electronics, and Department of Physics, Massachusetts Institute of Technology, Cambridge, Massachusetts 02139, USA*

²*Cavendish Laboratory, University of Cambridge, J. J. Thomson Avenue, Cambridge CB3 0HE, United Kingdom*

³*Laboratoire Kastler Brossel, CNRS, ENS-PSL Research University, UPMC-Sorbonne Universités and Collège de France, Paris, France*

CYLINDER-SHAPED TRAP

For the repulsive optical potential, we use laser light that is blue detuned with respect to the D-lines of ${}^6\text{Li}$ at 671 nm. The laser source is a multi-mode 10W laser at 532 nm. Figure S1 shows the optical setup that is used to shape the beam into a hollow core cylinder. A collimated gaussian beam propagates through an axicon and a microscope objective, generating a hollow cylindrical beam in the Fourier plane [S2, S3]. An opaque circular silver mask is placed in the focal plane to block the residual light inside the ring and provide a sharper inner edge. The resulting intensity distribution at the focal plane is imaged onto the atoms along the z-axis. This confines the atoms into a cylinder oriented along the axial direction (z-axis).

In addition to the radial cylinder-shaped trap, the uniform trap requires sharp end cap walls that confine the atoms along the axial direction. For the endcaps, we use second 532 nm beam from the same laser source and detuned it by 160 MHz to avoid interference between the beams. The end cap beam is split into two elliptically shaped beams with opposite polarizations, which are fo-

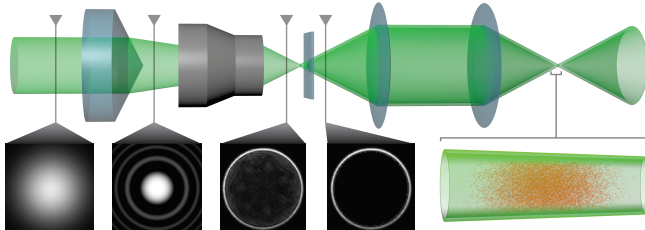


FIG. S1. Optical setup for cylinder-shaped trap. From left to right: A gaussian beam propagates through an axicon resulting in a Bessel beam in the near field. Subsequently the Bessel beam is focused through a microscope objective. In the focal plane, the resulting intensity pattern is a ring with gaussian rim. A matched circular opaque mask is used to block out residual light in the center of the ring. Finally the mask is projected through an imaging system onto the atoms, creating the cylinder-shaped trap for the atoms. A small variation of cylinder radius is unavoidable when using a single axicon [S1].

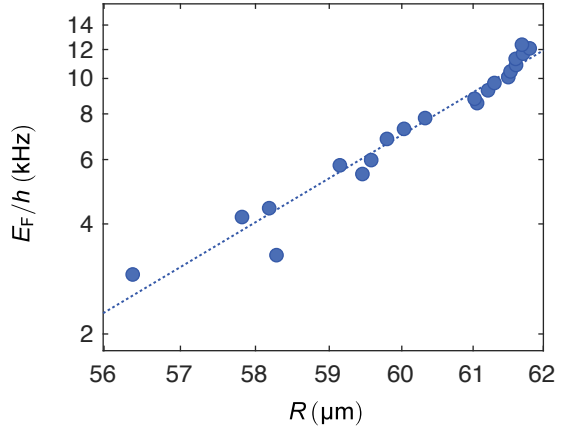


FIG. S2. Determination of the power law exponent of the radial wall potential. Log-log plot of the data shown in Fig. 1(b). The blue dotted line is a linear fit, with a slope of $m = 16.2 \pm 1.6$ for the power law exponent.

cused onto the edges of a rectangular opaque mask. The intensity distribution at the mask is projected onto the atoms and provides two sharp confining walls.

TRAP CHARACTERIZATION

Radial Trap Wall: Power Law Potential

To describe the radial extent of the gas as a function of the Fermi energy, we model our radial potential with a power law $U(r) = \alpha r^m$. Within the local density approximation, the local chemical potential is then determined by $\mu(r) = \mu_0 - \alpha r^m$, where $\mu_0 = \mu(r = 0)$. The radius measurements have been performed with a spin-balanced superfluid. Assuming $T = 0$, the cloud has a well defined Thomas-Fermi radius R , where the density drops to zero:

$$\mu_0 = \xi E_F = \alpha R^m, \quad (\text{S1})$$

with the Bertsch parameter ξ . Fitting the data shown in Fig. S2 with a power-law gives $m = 16.2 \pm 1.6$.

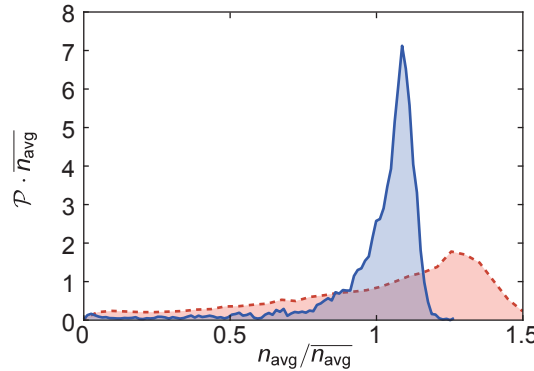


FIG. S3. Axial probability distribution. The blue solid line (red dashed line) shows $\mathcal{P}(n_{\text{avg}})$ for the uniform (hybrid) trap. Absorption images are taken along x-axis. The line of sight averaged local density n_{avg} is calculated assuming a uniform cylindrical trap.

Probability Distribution for the Atomic Density

The density distribution $\mathcal{P}(n)$ describes the probability $\mathcal{P}(n)dn$ to find an atom at a density between n and $n + dn$, and is normalized to unity. We evaluate the probability distribution from absorption images by binning the measured column integrated density n_{2D} , and weighting each bin by the number of atoms representing the bin.

To extract information about the axial homogeneity of the gas, we image the atoms along the x-axis. We obtain the line-of-sight averaged local density n_{avg} from the column density by dividing by the local column length. Figure S3 shows the probability distribution $\mathcal{P}(n_{\text{avg}})$ for the line-of-sight averaged density of the uniform and hybrid trap. The axial probability distribution shows a narrow peak similar to the one observed for the radial distribution. The probability distribution for the hybrid trap is broadened due to the harmonic trapping along the z direction.

OPTICAL PUMPING OF THE MINORITY ATOMS FOR MOMENTUM-SPACE MAPPING

The measurement of the momentum distribution relies on ballistic expansion of the gas immediately after release from the trap. However, the expansion of the atoms is strongly influenced by a small minority fraction ($< 5\%$) of strongly interacting atoms admixed to ensure the thermalization of the gas. To eliminate the interactions between the two spin states during the expansion, the minority atoms are optically pumped into the hyperfine state $|m_J = +1/2, m_I = 0\rangle$ that is weakly interacting with the majority cloud. The $5\ \mu\text{s}$ pumping pulse is applied right before the release of the atoms into the harmonic trap. On average, 1.5 photons are required

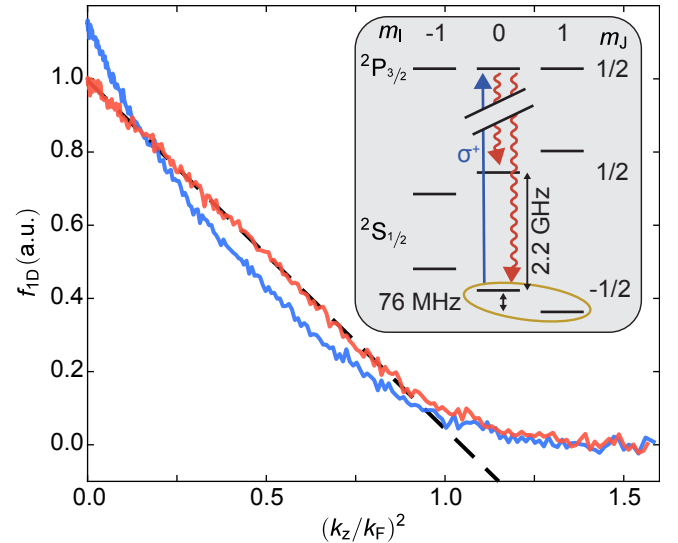


FIG. S4. Influence of the minority atoms on the expansion of the majority cloud. The blue (red) line corresponds to the observed integrated momentum distribution without (with) optical pumping of the minority atoms. The dashed line is a guide to the eye. The inset displays the level scheme for the optical pumping at a magnetic field of $B = 832\text{G}$. The yellow ellipse marks the two strongly interacting spin states, where the minority is in $|m_J = -1/2, m_I = 0\rangle$. The pumping transition is shown as the blue line and the spontaneous decay channels with red curvy lines.

to pump an atom into the weakly interacting hyperfine state. The transitions involved in this pumping scheme are shown in the inset of Fig. S4. Figure S4 shows the integrated momentum distribution of the gas obtained using momentum-space mapping with and without pumping of minority atoms. Note that without the optical pumping of the minority atoms, f_{1D} is distorted from the triangular shape expected for a low temperature Fermi gas.

DENSITY MEASUREMENT WITH ABSORPTION IMAGING

For heavy atoms, such as Rb and Cs, and imaging intensities that are small compared to the saturation intensity (I_{sat}), the column density $n_{\text{col}} = -(1/\sigma_0) \log(I_f/I_i)$ is determined by the Beer-Lambert law. Here, I_i and I_f are the intensities of the imaging beam before and after the atoms, respectively, and σ_0 is the absorption cross-section. However, for light atoms such as Li, the Doppler effect plays a dominant role in realistic experimental scenarios, where a low imaging intensity and short exposure time is in conflict with a high signal to noise ratio. For our experiment, depending on the column density of the sample, preferred values for the imaging intensities are $0.1 - 0.5 I_{\text{sat}}$ at an exposure time of $4 - 10\ \mu\text{s}$.

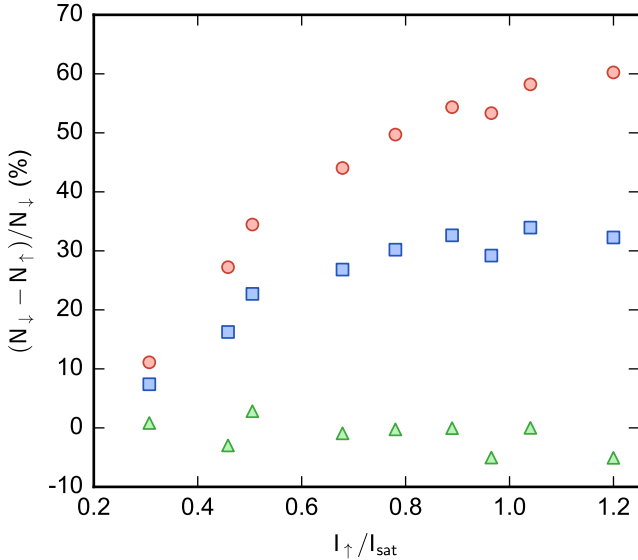


FIG. S5. Apparent atom count for the spin up component (N_{\uparrow}) measured at different imaging intensities (I_{\uparrow}). A reference atom count (N_{\downarrow}) is obtained by subsequently imaging a second spin component at a fixed imaging intensity ($I_{\downarrow} = 0.23I_{\text{sat}}$). Red circles, blue squares, and green triangles are obtained using Beer-Lambert, saturated Beer-Lambert, and Doppler Beer-Lambert, respectively. Spin balanced clouds are used for these measurements.

Under these conditions, each ${}^6\text{Li}$ atom scatters up to 35 photons. The corresponding photon recoil results in a Doppler shift of up to 6 MHz, which is comparable to the natural linewidth of ${}^6\text{Li}$.

In order to account for the Doppler and saturation effects, we numerically solve two coupled differential equations for the local, time-dependent saturation parameter $s(z, t) = I(z, t)/I_{\text{sat}}$ and velocity $v(z, t)$:

$$\frac{\partial s}{\partial z} = -n\sigma_0 \frac{s}{1 + s + (2kv/\Gamma)^2}. \quad (\text{S2a})$$

$$\frac{\partial v}{\partial t} = \frac{\hbar k \Gamma}{2m} \frac{s}{1 + s + (2kv/\Gamma)^2}. \quad (\text{S2b})$$

Here, σ_0 , k , m and Γ are the bare scattering cross-section, photon wave vector, atomic mass and natural linewidth.

In the limit where the Doppler effect is negligible ($v = 0$), the analytical solution of Eq. S2 is $n_{\text{col}}\sigma_0 = -\log(s_f/s_i) - (s_f - s_i)$. Here, s_i and s_f are reduced imaging intensities before and after the atoms, respectively. This is the modified version of the Beer-Lambert law that includes saturation of the atomic transition. For the general case, we numerically solve Eq. S2 to find the Doppler-corrected relation between I_i and I_f (which we call the “Doppler Beer-Lambert” law).

We compare these aforementioned methods by subsequently imaging the two spin states of a spin-balanced gas with a fast SCMOS camera. The first image is taken with fixed saturation intensity of $s_{\downarrow} = 0.23$ and serves as the density reference. The second absorption image for the other spin component, with a variable s_{\uparrow} , is obtained 15 μs after the first image. Figure S5 shows the differences in the measured total atom numbers between two spin components for various s_{\uparrow} calculated using the Beer-Lambert law (red circles), the saturated Beer-Lambert law (blue squares) and Doppler Beer-Lambert (green triangles). For the atom number differences calculated using the Doppler Beer-Lambert law, the mean deviation from the reference density is only 3% compared to 27% and 46% for the saturated Beer-Lambert and the basic Beer-Lambert law, respectively.

-
- [S1] A. L. Gaunt, *Degenerate Bose Gases : Tuning Interactions & Geometry*, PhD, University of Cambridge (2014).
 - [S2] J. H. McLeod, Journal of the Optical Society of America **44**, 592 (1954).
 - [S3] I. Manek, Y. Ovchinnikov, and R. Grimm, Optics Communications **147**, 67 (1998).

Appendix B

Boiling a Unitary Fermi Liquid

This appendix contains a reprint of Ref. [211]: Yan, Z., Patel, P. B., Mukherjee, B., Fletcher, R. J., Struck, J., & Zwierlein, M. W. (2019). Boiling a Unitary Fermi Liquid. *Phys. Rev. Lett.*, 122(9), 093401.

Boiling a Unitary Fermi Liquid

Zhenjie Yan,¹ Parth B. Patel,¹ Biswaroop Mukherjee,¹ Richard J. Fletcher,¹ Julian Struck,^{1,2} and Martin W. Zwierlein¹

¹MIT-Harvard Center for Ultracold Atoms, Department of Physics, and Research Laboratory of Electronics, Massachusetts Institute of Technology, Cambridge, Massachusetts 02139, USA

²Département de Physique, Ecole Normale Supérieure/PSL Research University, CNRS, 24 rue Lhomond, 75005 Paris, France



(Received 1 November 2018; published 6 March 2019)

We study the thermal evolution of a highly spin-imbalanced, homogeneous Fermi gas with unitarity limited interactions, from a Fermi liquid of polarons at low temperatures to a classical Boltzmann gas at high temperatures. Radio-frequency spectroscopy gives access to the energy, lifetime, and short-range correlations of Fermi polarons at low temperatures T . In this regime, we observe a characteristic T^2 dependence of the spectral width, corresponding to the quasiparticle decay rate expected for a Fermi liquid. At high T , the spectral width decreases again towards the scattering rate of the classical, unitary Boltzmann gas, $\propto T^{-1/2}$. In the transition region between the quantum degenerate and classical regime, the spectral width attains its maximum, on the scale of the Fermi energy, indicating the breakdown of a quasiparticle description. Density measurements in a harmonic trap directly reveal the majority dressing cloud surrounding the minority spins and yield the compressibility along with the effective mass of Fermi polarons.

DOI: 10.1103/PhysRevLett.122.093401

Landau's Fermi liquid theory provides a quasiparticle description of the low-temperature behavior for a large class of unordered fermionic states of matter, including most normal metals, atomic nuclei, and liquid helium-3 [1]. Strongly interacting Fermi gases with highly imbalanced spin populations have been identified as belonging to the same class [2–14]. The quasiparticles in spin-imbalanced Fermi gases are Fermi polarons: spin impurities dressed by an excess cloud of majority fermions. The stability of quasiparticles in a Fermi liquid is a consequence of the restricted phase space for collisions due to Pauli blocking. With increasing temperature T , the accessible phase space increases, and the lifetime of quasiparticles shortens, leading to the breakdown of Fermi liquid theory. In this intermediate temperature regime, the gas is neither a Fermi liquid nor a classical Boltzmann gas. For strong interactions, this regime is void of well-defined quasiparticles and controlled by the quantum critical point of the unitary spin-balanced gas at zero chemical potential and temperature [15–17].

Ultracold Fermi gases offer a unique opportunity to study the crossover from a low-temperature Fermi liquid to a classical Boltzmann gas, due to the large accessible temperature range. In spin-imbalanced Fermi gases, the two inequivalent Fermi surfaces provide additional richness. As the temperature is lowered from the classical regime, the Fermi surface of the majority forms first, giving minority spins the quasiparticle character of polarons. At even lower temperatures, the polarons themselves become quantum degenerate and form a Fermi surface.

In this Letter, we access the entire crossover from degenerate polarons to the classical Boltzmann gas through

the quantum critical region. The internal properties of the polaronic quasiparticles are measured via radio-frequency (rf) spectroscopy [10,18–20] on a homogeneous Fermi gas [21,22]. At low temperatures, the peak position and width of the rf spectra reflect energy and decay rate of the polarons. Note that the decay rate of a quasiparticle can be viewed as the rate of momentum relaxation in a transport measurement (see, e.g., [7]). The wings of the rf spectra yield information about the short-range correlations and the contact [23–27], controlling the change in the polaron energy with interaction strength. Further thermodynamic properties of the polaron gas are directly obtained from *in situ* density profiles in the presence of a harmonic potential [6,12,13,28–30], revealing the number of atoms in the majority dressing cloud of a polaron. The compressibility of the impurity gas at low temperature yields the effective mass of Fermi polarons.

For the spectroscopic studies we employ rf *ejection* spectroscopy, where the many-body state is first prepared and then probed by transferring a small fraction of one spin component into a weakly or noninteracting final state. Radio-frequency ejection spectroscopy has been used to, e.g., measure interactions, correlations, pairing phenomena in Fermi gases [31,32], and more specifically, the binding energy of the attractive Fermi polaron at low temperatures [10,19]. A prerequisite for our measurements is a spatially uniform box potential. This avoids the spectral broadening caused by an inhomogeneous density and impurity concentration [21,33]. The three energetically lowest hyperfine states of ⁶Li (labeled |1⟩, |2⟩, |3⟩) are utilized to create and probe the strongly interacting spin mixture. The minority

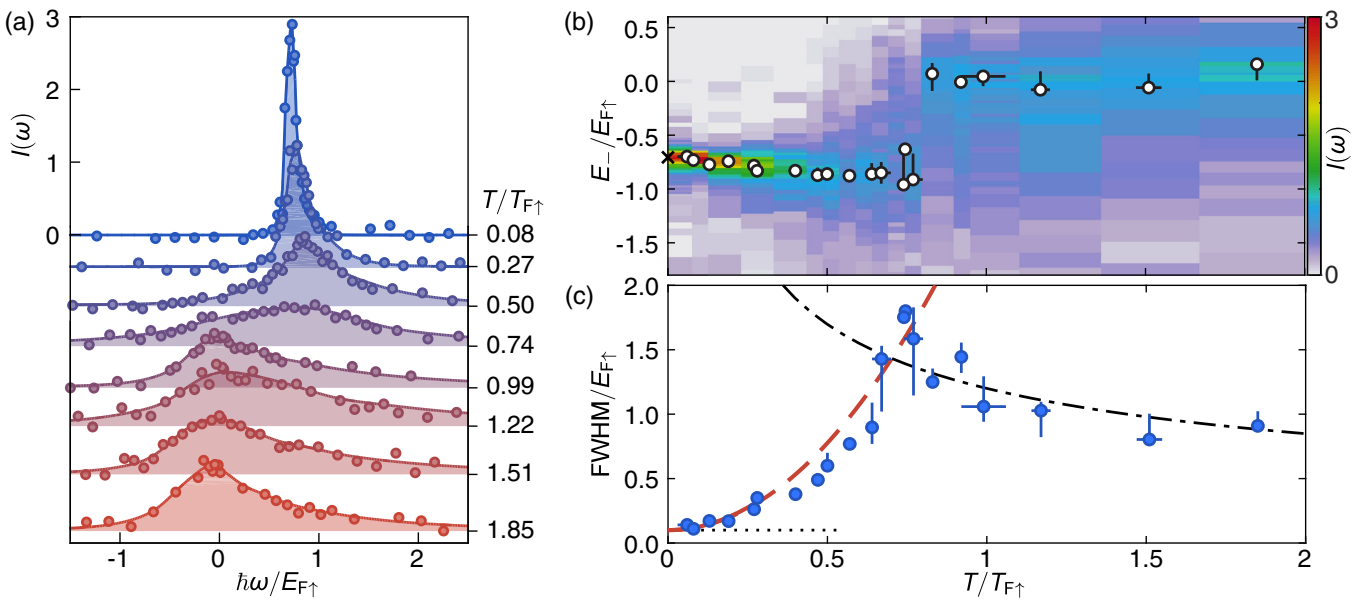


FIG. 1. (a) Thermal evolution of the minority rf spectra. The impurity concentration is $n_\downarrow/n_\uparrow = 0.10 \pm 0.03$, the Rabi frequency $\Omega_R = 2\pi \times 0.5$ kHz, and the pulse duration $T_{\text{pulse}} = 1$ ms. (b) 2D plot of the minority spectra with maxima highlighted by white points. To reflect the energy of the initial many-body state, the spectra are shown with the inverse frequency $E_-/E_{F\uparrow}$, where $E_- = -\hbar\omega$. The cross corresponds to the theoretical zero temperature result for the polaron energy, including a correction for final state interactions [3–5,8,38]. (c) FWHM of the rf spectra. (Dotted line) Fourier resolution limit; (dashed red line) single-polaron decay rate $\Gamma/E_{F\uparrow} = 2.71(T/T_{F\uparrow})^2$ [7], offset by the Fourier limit; (dash-dotted black line) FWHM of the rf spectrum in the high-temperature limit $\Gamma/E_{F\uparrow} = 1.2\sqrt{T_{F\uparrow}/T}$ [40,41], reflecting the scattering rate in the classical, unitary Boltzmann gas. [For the errors in (b) and (c), see the Supplemental Material [33].]

(impurity) and majority components are prepared in $|\downarrow\rangle = |1\rangle$ and $|\uparrow\rangle = |3\rangle$ and transferred via the rf drive into the final state $|f\rangle = |2\rangle$ [33,37]. All measurements have been performed at a magnetic field of 690 G, where the interactions between minority and majority atoms are unitarity limited. Final state interactions are weakly repulsive with $k_{F\uparrow}a_{\uparrow f} \lesssim 0.2$ ($a_{\uparrow f} = 62$ nm). The impurity concentration (minority to majority density ratio n_\downarrow/n_\uparrow) is controllably varied between 10% and 30%.

The rf response is linked to the probability that a hole of energy E and momentum \mathbf{p} is excited by ejecting a particle from the many-body state, as described by the occupied spectral function $\mathcal{A}_{-\downarrow}(\mathbf{p}, E)$ [10,32,38,39]. Detecting a free particle of momentum \mathbf{p} after rf transfer implies a momentum \mathbf{p} and energy $E_p = \mathbf{p}^2/2m - \mu_\downarrow - \hbar\omega$ of the leftover hole, where μ_\downarrow is the minority chemical potential and $\hbar\omega$ is the energy of the rf photon with respect to the non-interacting transition. The number of transferred minority atoms $N_f(\omega)$ is proportional to the momentum integral of the occupied spectral function $\mathcal{A}_{-\downarrow}(\mathbf{p}, E_p)$. Fermi liquids feature a spectral function that is sharply peaked around $\epsilon_0 + \mathbf{p}^2/2m^* - \mu_\downarrow$, with the effective mass m^* and dressed energy ϵ_0 of the quasiparticles. The width of the peak is determined by the quasiparticle decay rate $\Gamma(p, T)$. For low temperatures and impurity concentrations, only low-momentum states are populated and the peak position

of the rf spectrum corresponds to the polaron binding energy [10].

Figure 1(a) shows the evolution with temperature of the rf spectra. Here, we have defined the normalized transfer $I(\omega) = [N_f(\omega)/N_\downarrow](E_{F\uparrow}/\hbar\Omega_R^2 T_{\text{pulse}})$, with the number of particles in the final (initial) state N_f (N_\downarrow), the pulse duration T_{pulse} , and the single particle Rabi frequency Ω_R . The term $\Omega_R^2 T_{\text{pulse}}$ originates from the linear response to the rf pulse. The factor $E_{F\uparrow}/\hbar$ in I is owed to the scale invariance of the unitary Fermi gas, which implies that its spectral features, such as the peak position, amplitude, and width directly scale with the Fermi energy [31,32]. The normalized transfer only depends on the dimensionless parameters $T/T_{F\uparrow}$, n_\downarrow/n_\uparrow , and $\hbar\omega/E_{F\uparrow}$, apart from small corrections due to final state interactions and Fourier broadening that break the scale invariance of the system. The energy of the gas is measured by an isoenergetic release from the uniform to a harmonic trap. After thermalization, the in-trap size reveals the energy, from which we obtain the temperature via the equation of state (see Supplemental Material [33]).

In the deeply degenerate limit ($T/T_{F\uparrow} < 0.1$), we observe a sharply defined resonance [Fig. 1(a)] signaling the stable long-lived Fermi polaron [10]. Its width, defined by the full width at half maximum (FWHM), is limited by the Fourier resolution. From the position of the spectral

peak at low temperature [Fig. 1(b)] and correction for weak final state interactions as in [10], we obtain a zero temperature polaron binding energy $A \equiv \epsilon_0/E_{F\uparrow} = -0.60 \pm 0.05$, with a linear extrapolation of the peak positions below $T/T_{F\uparrow} = 0.3$.

With increasing temperature, the spectral peak initially shifts to higher frequencies and broadens significantly [Figs. 1(b) and 1(c)]. A rise in the polaron binding energy with temperature is expected, given the increased scattering phase space of the majority spins, and is found theoretically [42,43]. However, note that the position of the maximum at finite temperature and impurity concentration is influenced by the density of states, the difference in the effective mass between initial and final state [20], and the thermal population of momentum states. At a temperature near $T/T_{F\uparrow} \approx 0.75$, a sharp jump in the position of the global maximum to $\omega \approx 0$ is observed [Figs. 1(a) and 1(b)] [44]. In this regime, the width of the spectra reaches its maximum [Fig. 1(c)], on the order of the Fermi energy. Beyond this temperature, the position of the maximum remains constant at $\omega \approx 0$, as expected theoretically [40,41]. It reflects a merging of attractive and repulsive branches, symmetric about zero on resonance [45], as the temperature exceeds their splitting.

The spectral function of a Fermi liquid is a single Lorentzian peak with a width given by the decay rate of the quasiparticles [1]. The width of the rf spectra is dominated by this decay rate at low temperatures. We observe a quadratic scaling of the width at low temperatures, a hallmark of Fermi liquid theory, in agreement with a theoretical calculation [Fig. 1(c)] [7]. In the quantum critical regime around $T \approx T_{F\uparrow}$, the lifetime of the polarons drops below the Fermi time ($\hbar/E_{F\uparrow}$), signaling a breakdown of quasiparticles [15–17]. The decrease in width at temperatures beyond the Fermi temperature is expected for a classical Boltzmann gas with unitarity limited interactions. The thermal scattering rate in the dilute impurity limit is given by $\Gamma_{\text{th}} = n_\uparrow \sigma_{\text{th}} v_{\text{th}} \sim 1/\sqrt{T}$, with the thermal velocity $v_{\text{th}} \sim \sqrt{T}$ and the unitarity limited scattering cross section $\sigma_{\text{th}} \sim \lambda^2 \sim 1/T$.

Apart from energies and lifetimes, rf spectra also directly yield the strength of short-range correlations, quantified by contact C [Fig. 2(a)] [24–27,31,46,47]. The contact is a central quantity in a set of universal relations, linking microscopic properties to thermodynamics, which apply to all many-body systems with contact interactions [23]. It governs the tail of the momentum distribution, short-range pair correlations, and the change in energy with interaction strength [27,31,32]. As the contact is a measure of pair correlations, the tails of the rf spectrum of the minority and majority components are identical. For unitarity limited interactions, the fraction of transferred atoms in the high-frequency limit is given by [27]

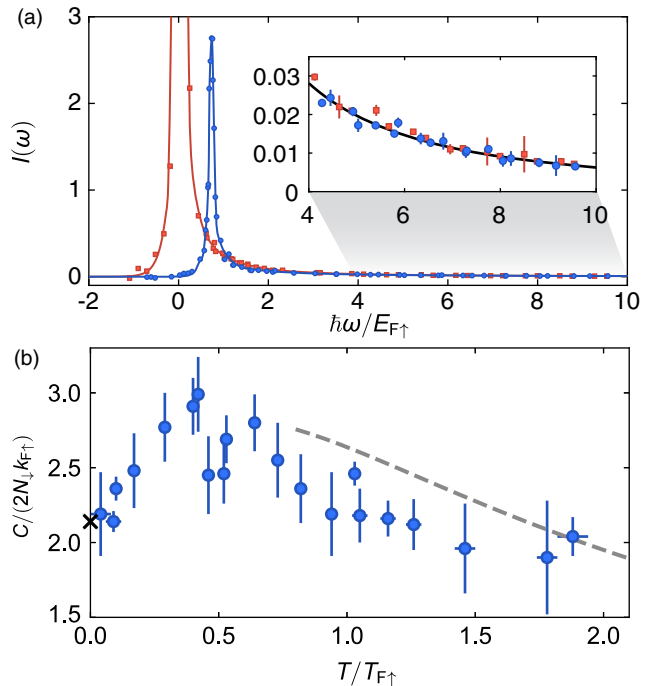


FIG. 2. Contact of the spin-imbalanced Fermi gas. (a) Typical rf spectra of the spin minority (blue circles) and majority (red squares). The impurity concentration is 10%. (Inset) High-frequency tails of the minority and majority spectra together with a fit of Eq. (1). (b) Contact as a function of temperature, obtained by measuring the transferred fraction of atoms as a function of rf pulse duration for frequencies $\hbar\omega/E_{F\uparrow} > 5.5$ and use of Eq. (1). The gray dashed line shows the third-order viral expansion [48] and the cross shows the result from the Chevy ansatz [3,49].

$$I(\omega) \underset{\omega \rightarrow \infty}{=} \frac{C}{2N_\downarrow k_{F\uparrow}} \frac{1}{2\sqrt{2}\pi(1 + \hbar\omega/E_b)} \left(\frac{E_{F\uparrow}}{\hbar\omega} \right)^{3/2}, \quad (1)$$

where $E_b = \hbar^2/m a_{\uparrow f}^2 \approx \hbar \times 433$ kHz. The inset of Fig. 2(a) shows the corresponding fit of the tails with Eq. (1), leaving only the contact as a free parameter.

The temperature dependence of the contact displays a nonmonotonic behavior with a maximum located around $T \approx 0.4T_{F\uparrow}$ [Fig. 2(b)]. The observed initial rise in temperature is partially expected from the increase in scattering phase space and has also been found theoretically in a spin-imbalanced few-body calculation of the contact [50]. In the high-temperature limit, the contact is proportional to the scattering cross section and vanishes as $1/T$.

The contact quantifies short-range correlations. However, the polaron is an extended object with pair correlations extending out over distances even beyond the majority interparticle spacing [51]. We thus set out to probe the entire cloud of excess majority atoms surrounding the impurity spin of density $\Delta n_\uparrow = n_\uparrow(\mu_\uparrow, \mu_\downarrow, T) - n_0(\mu_\uparrow, T)$ by *in situ* density measurements [Fig. 3(a)]. Here, $n_\uparrow(\mu_\uparrow, \mu_\downarrow, T)$ is the actual measured density of the interacting majority

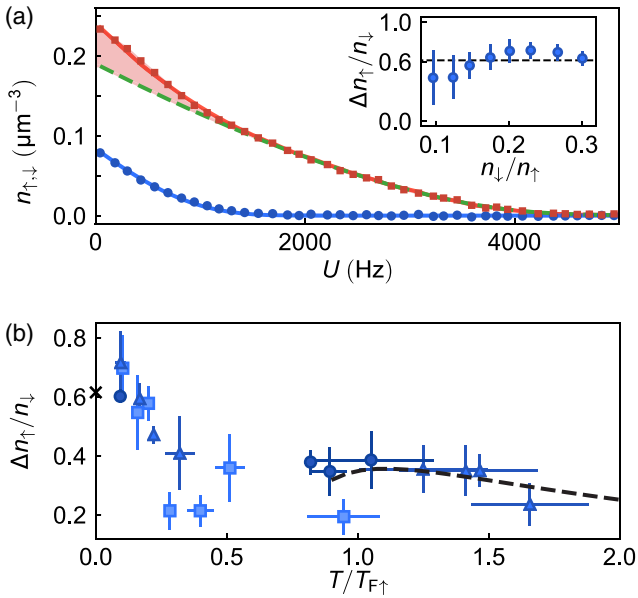


FIG. 3. Observation of the majority excess cloud. (a) Density profiles in a harmonically varying external potential U . Blue (red) data points indicate the profiles of the minority (majority) spin component. The normalized temperature of the gas is $T/T_{F\uparrow} = 0.07$ in the trap center ($U = 0$). The green dashed line represents the equation of state of the ideal Fermi gas, the red (blue) solid line is the Fermi liquid ansatz [Eq. (3)] for the majority (minority) component. The red shaded area displays the excess majority density Δn_{\uparrow} . (Inset) Dependence of the excess majority to minority ratio on the impurity concentration. (b) Temperature dependence of the majority excess cloud. Data points show the excess majority density Δn_{\uparrow} for an impurity concentration of $n_{\downarrow}/n_{\uparrow} = 0.1$ (squares), $n_{\downarrow}/n_{\uparrow} = 0.2$ (triangles), and $n_{\downarrow}/n_{\uparrow} = 0.3$ (circles). The cross indicates the low-temperature prediction of the Fermi liquid ansatz $\Delta n_{\uparrow}/n_{\downarrow} = -A = 0.615$ [8] and the dashed line shows the third-order virial expansion.

component and $n_0(\mu_{\uparrow}, T)$ corresponds to the density of a noninteracting gas with the same temperature and majority chemical potential. For this measurement, we use a hybrid trapping potential that is harmonic along one direction and uniform along the other two axes [21]. This trapping geometry gives direct access to the density of each spin component as a function of the trapping potential U [Fig. 3(a)]. Under the local density approximation, the knowledge of $n_{\uparrow,\downarrow}(U)$ can be used to extract a variety of thermodynamic quantities [12,13,30,33]. The majority chemical potential and temperature are obtained from the low-fugacity wings of the gas. In the case of a partially spin polarized wing, we use the third-order virial expansion [48], whereas for a fully spin polarized wing, we use the ideal equation of state. For the lowest temperatures, the excess majority density per minority atom is $\Delta n_{\uparrow}/n_{\downarrow} = 0.63(5)$ [Fig. 3(b)]. For increasing temperature, the excess density drops until it reaches the value predicted by the virial expansion for the density. $\Delta n_{\uparrow}/n_{\downarrow}$ displays no dependency

on the minority concentration within our error up to $n_{\downarrow}/n_{\uparrow} = 0.3$.

To elucidate the origin of the excess density from thermodynamics, we model the total pressure of the system as

$$P(\mu_{\uparrow}, \mu_{\downarrow}, T) = P_0(\mu_{\uparrow}, T) + \left(\frac{m^*}{m}\right)^{\frac{3}{2}} P_0(\mu_{\downarrow} - A\mu_{\uparrow}, T). \quad (2)$$

Here, $P_0(\mu, T)$ is the pressure of the noninteracting Fermi gas. The ansatz describes the total pressure of the system as the sum of the partial pressure of the noninteracting majority component and the partial pressure of an ensemble of polarons with an effective chemical potential of $\mu_{\downarrow} - A\mu_{\uparrow}$ and an effective mass m^* [12,13]. It contains weak interactions among the polarons that amount to a few percent of the total energy of the system [52]. From this pressure ansatz, the density can be calculated with the Gibbs-Duhem equation at constant temperature and scattering length ($dP = n_{\uparrow} d\mu_{\uparrow} + n_{\downarrow} d\mu_{\downarrow}$),

$$\begin{aligned} n_{\uparrow}(\mu_{\uparrow}, \mu_{\downarrow}, T) &= n_0(\mu_{\uparrow}, T) - A n_{\downarrow}(\mu_{\uparrow}, \mu_{\downarrow}, T), \\ n_{\downarrow}(\mu_{\uparrow}, \mu_{\downarrow}, T) &= (m^*/m)^{\frac{3}{2}} n_0(\mu_{\downarrow} - A\mu_{\uparrow}, T), \end{aligned} \quad (3)$$

where $n_0(\mu, T) \equiv \partial P_0 / \partial \mu$ is the density of the noninteracting gas. Each minority is accumulating on average $|A| = 0.6$ excess majority atoms over the noninteracting limit, in agreement with our measured value [Fig. 3(b)].

Since the Fermi liquid ansatz describes the thermodynamics accurately in the low-temperature regime $T/T_{F\uparrow} < 0.2$, we now focus on this temperature regime and utilize the ansatz to determine the effective mass of the polarons from a measurement of the minority compressibility. In analogy to the total compressibility of the gas, the normalized isothermal minority compressibility is defined as $\tilde{\kappa}_{\downarrow} \equiv -dE_{F\downarrow}/dU_{\text{eff}}$ [30]. Here, $U_{\text{eff}} = (1 - A)U$ is the effective potential of the minority component generated by the interaction with the majority component [4,11]. Using Eq. (3) for the minority density, one finds

$$\tilde{\kappa}_{\downarrow}(T/T_{F\downarrow}) = \frac{m^* \kappa_0(T, T_{F\downarrow} m^*/m)}{m \kappa_0(0, T_{F\downarrow} m^*/m)}, \quad (4)$$

where $\kappa_0(T, T_{F\downarrow}) \equiv n_0^{-2} (\partial n_0 / \partial \mu)_T$ is the compressibility of the noninteracting Fermi gas at fixed density. Figure 4 shows the measured isothermal compressibility of the minority component. A fit of Eq. (4) fixing $A = -0.615$ [8] results in an effective mass of $m^*/m = 1.25(5)$, which is in agreement with results obtained from diagrammatic Monte Carlo simulations [8], a variational ansatz [5], and previous low-temperature experiments [11–13]. The saturation of the minority compressibility at low temperatures signals the formation of a degenerate Fermi sea of polarons.

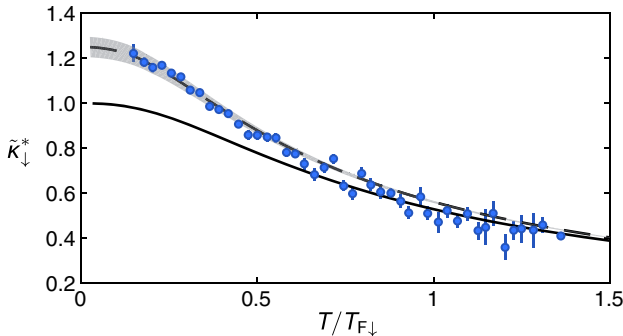


FIG. 4. Isothermal minority compressibility. The solid line is the Fermi liquid ansatz for $m^*/m = 1$, while the dashed line corresponds to a fit with an effective mass of $m^*/m = 1.25(5)$ assuming $A = -0.615$ [8]. The gray shaded area represents the standard deviation of the fit. For the entire range of temperatures displayed, the majority component is degenerate ($T/T_{F\uparrow} < 0.2$).

In conclusion, we have studied the temperature dependence of a highly spin-imbalanced unitary Fermi gas with rf spectroscopy and in-trap density profiles. When the majority component is degenerate ($T/T_{F\uparrow} \ll 1$), long-lived quasiparticles emerge. In the spirit of Fermi liquid theory, these polarons behave like a weakly interacting Fermi gas forming a sharp Fermi sea for $T/T_{F\downarrow} \ll 1$. The weakly interacting character of the quasiparticles is also reflected in the independence of the majority dressing cloud on the impurity concentration. In the opposing high-temperature regime, the gas is accurately described as a classical Boltzmann gas. At intermediate temperatures ($T \approx T_{F\uparrow}$) the quasiparticle description breaks down. The spectral features of the attractive polarons dissolve, merging with excited branches, such as dressed dimerons [8,49,53] and repulsive polarons [18–20,38,53,54].

We thank Richard Schmidt and Felix Werner for helpful discussions. This work was supported by the National Science Foundation (Center for Ultracold Atoms Awards No. PHY-1734011 and No. PHY-1506019), Air Force Office of Scientific Research (FA9550-16-1-0324 and MURI Quantum Phases of Matter FA9550-14-1-0035), Office of Naval Research (N00014-17-1-2257) and the David and Lucile Packard Foundation. J. S. was supported by LabEX ENS-ICFP: ANR-10-LABX-0010/ANR-10-IDEX-0001-02 PSL*.

- [1] P. Nozières and D. Pines, *The Theory of Quantum Liquids, Vol. I: Normal Fermi Liquids*, 1st ed. (W.A. Benjamin, New York, 1966).
- [2] M. W. Zwierlein, A. Schirotzek, C. H. Schunck, and W. Ketterle, *Science* **311**, 492 (2006).
- [3] F. Chevy, *Phys. Rev. A* **74**, 063628 (2006).
- [4] C. Lobo, A. Recati, S. Giorgini, and S. Stringari, *Phys. Rev. Lett.* **97**, 200403 (2006).
- [5] R. Combescot, A. Recati, C. Lobo, and F. Chevy, *Phys. Rev. Lett.* **98**, 180402 (2007).
- [6] Y.-I. Shin, C. H. Schunck, A. Schirotzek, and W. Ketterle, *Nature (London)* **451**, 689 (2008).
- [7] G. M. Bruun, A. Recati, C. J. Pethick, H. Smith, and S. Stringari, *Phys. Rev. Lett.* **100**, 240406 (2008).
- [8] N. Prokof'ev and B. Svistunov, *Phys. Rev. B* **77**, 020408 (2008).
- [9] M. Veillette, E. G. Moon, A. Lamacraft, L. Radzhovsky, S. Sachdev, and D. E. Sheehy, *Phys. Rev. A* **78**, 033614 (2008).
- [10] A. Schirotzek, C.-H. Wu, A. Sommer, and M. W. Zwierlein, *Phys. Rev. Lett.* **102**, 230402 (2009).
- [11] S. Nascimbène, N. Navon, K. J. Jiang, L. Tarruell, M. Teichmann, J. McKeever, F. Chevy, and C. Salomon, *Phys. Rev. Lett.* **103**, 170402 (2009).
- [12] S. Nascimbène, N. Navon, K. J. Jiang, F. Chevy, and C. Salomon, *Nature (London)* **463**, 1057 (2010).
- [13] N. Navon, S. Nascimbène, F. Chevy, and C. Salomon, *Science* **328**, 729 (2010).
- [14] A. Sommer, M. Ku, and M. W. Zwierlein, *New J. Phys.* **13**, 055009 (2011).
- [15] P. Nikolić and S. Sachdev, *Phys. Rev. A* **75**, 033608 (2007).
- [16] T. Enss, *Phys. Rev. A* **86**, 013616 (2012).
- [17] B. Frank, J. Lang, and W. Zwerger, *ZhETF* **154**, 953 (2018) [*J. Exp. Theor. Phys.* **127**, 812 (2018)].
- [18] C. Kohstall, M. Zaccanti, M. Jag, A. Trenkwalder, P. Massignan, G. M. Bruun, F. Schreck, and R. Grimm, *Nature (London)* **485**, 615 (2012).
- [19] M. Koschorreck, D. Pertot, E. Vogt, B. Fröhlich, M. Feld, and M. Köhl, *Nature (London)* **485**, 619 (2012).
- [20] F. Scazza, G. Valtolina, P. Massignan, A. Recati, A. Amico, A. Burchianti, C. Fort, M. Inguscio, M. Zaccanti, and G. Roati, *Phys. Rev. Lett.* **118**, 083602 (2017).
- [21] B. Mukherjee, Z. Yan, P. B. Patel, Z. Hadzibabic, T. Yefsah, J. Struck, and M. W. Zwierlein, *Phys. Rev. Lett.* **118**, 123401 (2017).
- [22] K. Hueck, N. Luick, L. Sobirey, J. Siegl, T. Lompe, and H. Moritz, *Phys. Rev. Lett.* **120**, 060402 (2018).
- [23] S. Tan, *Ann. Phys. (Amsterdam)* **323**, 2971 (2008).
- [24] G. Baym, C. J. Pethick, Z. Yu, and M. W. Zwierlein, *Phys. Rev. Lett.* **99**, 190407 (2007).
- [25] M. Punk and W. Zwerger, *Phys. Rev. Lett.* **99**, 170404 (2007).
- [26] W. Schneider, V. B. Shenoy, and M. Randeria, *arXiv: 0903.3006*.
- [27] E. Braaten, D. Kang, and L. Platter, *Phys. Rev. Lett.* **104**, 223004 (2010).
- [28] Y.-I. Shin, *Phys. Rev. A* **77**, 041603 (2008).
- [29] M. Horikoshi, S. Nakajima, M. Ueda, and T. Mukaiyama, *Science* **327**, 442 (2010).
- [30] M. J. H. Ku, A. T. Sommer, L. W. Cheuk, and M. W. Zwierlein, *Science* **335**, 563 (2012).
- [31] M. W. Zwierlein, in *Novel Superfluids*, edited by K.-H. Bennemann and J. B. Ketterson, 1st ed. (Oxford University Press, New York, 2014), Vol. 2, Chap. 18, pp. 269–422.
- [32] W. Zwerger, in *Quantum Matter at Ultralow Temperatures, Proceedings of the International School of Physics “Enrico Fermi,” Course CXCI*, edited by M. Inguscio, W. Ketterle,

- S. Stringari, and G. Roati (IOS Press, Amsterdam, 2016), Chap. 2, pp. 63–142.
- [33] See Supplemental Material at <http://link.aps.org/supplemental/10.1103/PhysRevLett.122.093401> for more information regarding the homogeneity of the gas, state preparation, thermometry, and rf spectroscopy, which includes Refs. [34–36].
- [34] J. E. Thomas, J. Kinast, and A. Turlapov, *Phys. Rev. Lett.* **95**, 120402 (2005).
- [35] T. L. Ho, *Phys. Rev. Lett.* **92**, 090402 (2004).
- [36] S. Nascimbène, N. Navon, S. Pilati, F. Chevy, S. Giorgini, A. Georges, and C. Salomon, *Phys. Rev. Lett.* **106**, 215303 (2011).
- [37] C. H. Schunck, Y.-I. Shin, A. Schirotzek, and W. Ketterle, *Nature (London)* **454**, 739 (2008).
- [38] P. Massignan, M. Zaccanti, and G. M. Bruun, *Rep. Prog. Phys.* **77**, 034401 (2014).
- [39] P. Törmä, *Phys. Scr.* **91**, 043006 (2016).
- [40] T. Enss, R. Haussmann, and W. Zwerger, *Ann. Phys. (Amsterdam)* **326**, 770 (2011).
- [41] M. Sun and X. Leyronas, *Phys. Rev. A* **92**, 053611 (2015).
- [42] H. Tajima and S. Uchino, *New J. Phys.* **20**, 073048 (2018).
- [43] B. C. Mulkerin, X.-J. Liu, and H. Hu, [arXiv:1808.07671](https://arxiv.org/abs/1808.07671).
- [44] Recently, a preprint appeared in which the authors, motivated by our work, found similar sudden shifts of the peak rf transfer. See H. Tajima and S. Uchino, [arXiv:1812.05889](https://arxiv.org/abs/1812.05889).
- [45] T. L. Ho and E. J. Mueller, *Phys. Rev. Lett.* **92**, 160404 (2004).
- [46] P. Pieri, A. Perali, and G. C. Strinati, *Nat. Phys.* **5**, 736 (2009).
- [47] J. T. Stewart, J. P. Gaebler, T. E. Drake, and D. S. Jin, *Phys. Rev. Lett.* **104**, 235301 (2010).
- [48] X.-J. Liu and H. Hu, *Phys. Rev. A* **82**, 043626 (2010).
- [49] M. Punk, P. T. Dumitrescu, and W. Zwerger, *Phys. Rev. A* **80**, 053605 (2009).
- [50] Y. Yan and D. Blume, *Phys. Rev. A* **88**, 023616 (2013).
- [51] C. Trefzger and Y. Castin, *Europhys. Lett.* **101**, 30006 (2013).
- [52] C. Mora and F. Chevy, *Phys. Rev. Lett.* **104**, 230402 (2010).
- [53] R. Schmidt and T. Enss, *Phys. Rev. A* **83**, 063620 (2011).
- [54] R. Schmidt, M. Knap, D. A. Ivanov, J.-S. You, M. Cetina, and E. Demler, *Rep. Prog. Phys.* **81**, 024401 (2018).

Supplemental Material: Boiling a Unitary Fermi Liquid

Zhenjie Yan,¹ Parth B. Patel,¹ Biswaroop Mukherjee,¹ Richard J. Fletcher,¹ Julian Struck,^{1,2} and Martin W. Zwierlein¹

¹*MIT-Harvard Center for Ultracold Atoms, Research Laboratory of Electronics, and Department of Physics, Massachusetts Institute of Technology, Cambridge, Massachusetts 02139, USA*

²*Département de Physique, Ecole Normale Supérieure / PSL Research University, CNRS, 24 rue Lhomond, 75005 Paris, France*

STATE PREPARATION

The three hyperfine states $|\downarrow\rangle = |1\rangle$, $|f\rangle = |2\rangle$ and $|\uparrow\rangle = |3\rangle$ are adiabatically connected to the respective states $|F = \frac{1}{2}, m_F = \frac{1}{2}\rangle$, $|\frac{1}{2}, -\frac{1}{2}\rangle$ and $|\frac{3}{2}, -\frac{3}{2}\rangle$ at vanishing magnetic field. As in previous works at MIT [S1], we start from a degenerate and fully spin-polarized gas in state $|1\rangle$ in an optical dipole trap, and prepare the spin-imbalanced mixture through two consecutive Landau-Zener sweeps at a magnetic field of $B = 569$ G, where the interactions between all three states are weak. The magnetic field is then ramped up within 1 ms to the $|1\rangle$ - $|3\rangle$ Feshbach resonance at $B = 690$ G, where the gas is loaded into the uniform potential and cooled through forced evaporation over 2 seconds [S2].

UNIFORM CYLINDER TRAP

Uniform trapping potentials offer a crucial advantage for non-local rf spectroscopy. For non-uniform traps, the Fermi energy and the impurity concentration vary spa-

tially, leading to an artificial broadening of the rf spectra.

For the rf measurements we load the gas into a cylinder-shaped uniform optical trap [S2] [Fig.S1 (a) and (b)]. Forced evaporation in this trap leads to temperatures of $T \simeq 0.05 T_{F\uparrow}$ and majority Fermi energies of $E_{F\uparrow}/h \sim 10$ kHz. Instead of adjusting the temperature of the gas by evaporation, we introduce an additional heating step by periodically modulating the cylindrical trapping potential by 20% at 1 kHz up to 4.5 s. We have found that this additional step reduces the spread in Fermi energies for different temperatures compared to a control through the evaporation.

We directly probe the variation in impurity concentration in the cloud from in-situ measurements of the cloud profiles [Fig.S1 (c) and (d)]. We find that the ratio of the effective volume of the minority component and the majority component is $V_\downarrow/V_\uparrow > 0.8$. More significantly for our purposes, well over 90% of the minority cloud is in a region of constant majority density at all temperatures. The radius $R_{\uparrow,\downarrow}$ and length $L_{\uparrow,\downarrow}$ of the gas have been determined by fitting the column integrated density profiles of the minority and majority component. The fitting functions along the radial (x) and the axial (z) direction are given by:

$$n_{\text{col}}(x) = \bar{n}_{\text{col}} \sqrt{R^2 - x^2}, \quad (\text{S1})$$

$$n_{\text{col}}(z) = \bar{n}_{\text{col}} \left(\text{erf} \left(\frac{L/2 + z}{\sqrt{2}\sigma_1} \right) + \text{erf} \left(\frac{L/2 - z}{\sqrt{2}\sigma_2} \right) \right) / 2. \quad (\text{S2})$$

Here, $\text{erf}(z)$ denotes the error function and $\sigma_{1,2}$ the effective widths of the potentials walls along the axial direction.

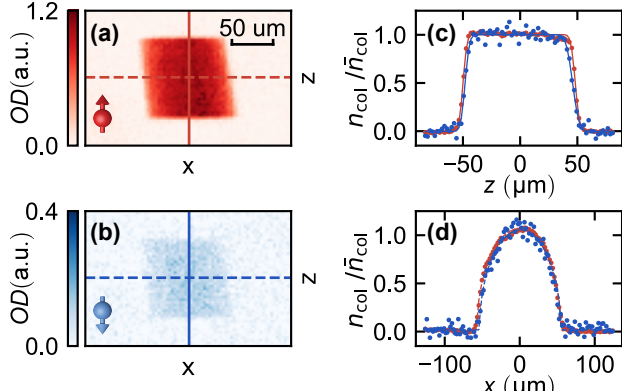


FIG. S1. Spin-imbalanced Fermi gas in the cylinder-shaped optical trap. Here, $E_{F\uparrow}/h = 10.3 \pm 0.1$ kHz, $T/T_{F\uparrow} = 0.74 \pm 0.01$ and $n_\downarrow/n_\uparrow = 0.1$. *In situ* absorption images of the majority (a) and minority (b) component along the radial direction of the cylinder. The column density along the axial (c) and radial (d) direction. The red (blue) points correspond to the majority (minority) component. The solid lines indicate the fits with Eqs. (S1) and (S2).

THERMOMETRY OF THE HOMOGENEOUS UNITARY FERMI GAS

Standard thermometry methods for ultracold atoms rely on the low-fugacity tails in non-uniform traps. In addition, for weakly or non-interacting gases the momentum distribution, measured in time-of-flight, can be used to infer the temperature. However, in the case of strongly interacting homogeneous gases none of these methods is

directly applicable. Here we describe our thermometry method to obtain the temperature of the unitary Fermi gas in a uniform trap. First, we determine the energy of the gas in the uniform box potential. This energy then yields the temperature using the equation of state of the imbalanced gas.

Energy Measurement

The total energy of the homogeneous gas is measured by an isoenergetic expansion into a hybrid cylindrical trap that features a harmonic potential along the axial direction ($\omega_z = 2\pi \cdot 23$ Hz) and is uniform in the radial direction [S2]. Figure S2 shows the isoenergetic transfer between the two trapping potentials. For the transfer the two endcaps of the cylindrical trap are instantaneously removed and therefore no work is performed on the atoms. Subsequently the gas expands isoenergetically along the axial direction. Note that the underlying harmonic potential along the axial direction is always present, even for the experiments in the uniform trap. However, the potential variation due to the harmonic potential is only a few percent of the Fermi energy [S2]. After the removal of the endcaps we wait for 2 s to equilibrate the gas. The total energy of the gas in the hybrid cylindrical trap can be determined from the *in situ* density profiles using a one-dimensional version of the virial theorem [S3].

The total energy of the system is given by sum of the internal and potential energy

$$E = \int d^3r (\epsilon(r) + n(r) U(r)), \quad (S3)$$

with the internal energy density $\epsilon(r)$, the total density $n(r) = n_{\downarrow}(r) + n_{\uparrow}(r)$ and the potential energy $U(r)$. The hybrid trap is uniform along the radial direction and we can express Eq. (S3) with the cylindrical cross-section A_{cyl} as

$$E = A_{\text{cyl}} \int dz (\epsilon(z) + n(z) U(z)), \quad (S4)$$

where we have defined $\epsilon(z) \equiv \epsilon(x = 0, y = 0, z)$, $n(z) \equiv n(x = 0, y = 0, z)$ and $U(z) \equiv U(x = 0, y = 0, z)$. For the unitary Fermi gas the internal energy is directly related to the pressure $\epsilon(z) = 3/2 P(z)$ [S4]. Combined with a partial integration of the first term in Eq. (S4) this leads to

$$E = -\frac{3}{2} A_{\text{cyl}} \int z \frac{\partial P(z)}{\partial z} dz + A_{\text{cyl}} \int n(z) U(z) dz, \quad (S5)$$

where we have assumed that the pressure $P(z)$ is an even function of z . With the equation for hydrostatic equilibrium (Gibbs-Duhem equation at constant scattering length and temperature) $dP = n d\mu$ and the local

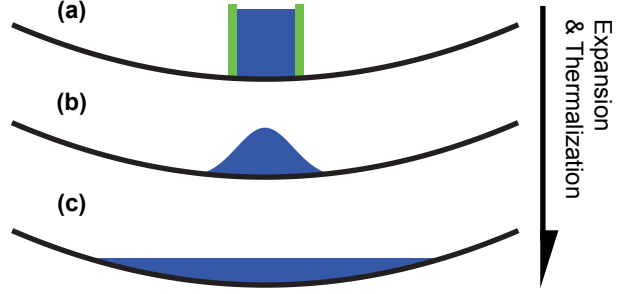


FIG. S2. Isoenergetic expansion from the uniform to harmonic trap. (a) Initially the gas is trapped in a quasi-uniform potential, (b) then the end caps of the trap are instantaneously removed, allowing the gas to expand into a harmonic trapping potential along the axial direction. (c) After a 2 s hold time the gas is in thermal equilibrium and the energy is determined using a one-dimensional virial theorem.

density approximation $d\mu = -dU$, we obtain the one-dimensional virial theorem

$$\begin{aligned} E &= \frac{3}{2} A_{\text{cyl}} \int z n(z) \frac{\partial U(z)}{\partial z} dz + A_{\text{cyl}} \int n(z) U(z) dz, \\ &= 2 A_{\text{cyl}} m \omega_z^2 \int n(z) z^2 dz. \end{aligned} \quad (S6)$$

In the second step of Eq. (S6) we have used the explicit expression for the harmonic potential $U(z) = m \omega_z^2 z^2 / 2$, with the trapping frequency ω_z and mass m .

Equation of State of the Spin-Imbalanced Unitary Fermi Gas

The conversion of the total energy into the corresponding temperature requires knowledge of the finite-temperature equation of state of the system. For this purpose, we have measured the finite temperature pressure equation of state of the spin-imbalanced unitary Fermi gas. As mentioned previously, at unitarity pressure and energy are directly related through $E = 3/2 PV$, with V as the volume [S4]. The zero-temperature equation of state of the spin-imbalanced Fermi gas has been measured previously, confirming Fermi-Liquid behaviour beyond the Chandrasekhar-Clogston limit in the normal fluid phase [S5–S9]. We determine the pressure of the gas from *in situ* density profiles in the hybrid trap [S2] and a precise knowledge of the harmonic trapping potential U along the axial direction of the trap [Fig. S3(a)]. From the equation for hydrostatic equilibrium and the local density approximation follows for the pressure $P(U) = \int_U^\infty n(U) dU$ [S10] [Fig. S3(b)]. The impurity concentration is varying in this non-uniform trapping potential [Fig. S3(c)]. To fill the three-dimensional parameter space $P(n, n_{\downarrow}/n_{\uparrow}, T)$, we measure density profiles for varying initial evaporation parameters. The temperature

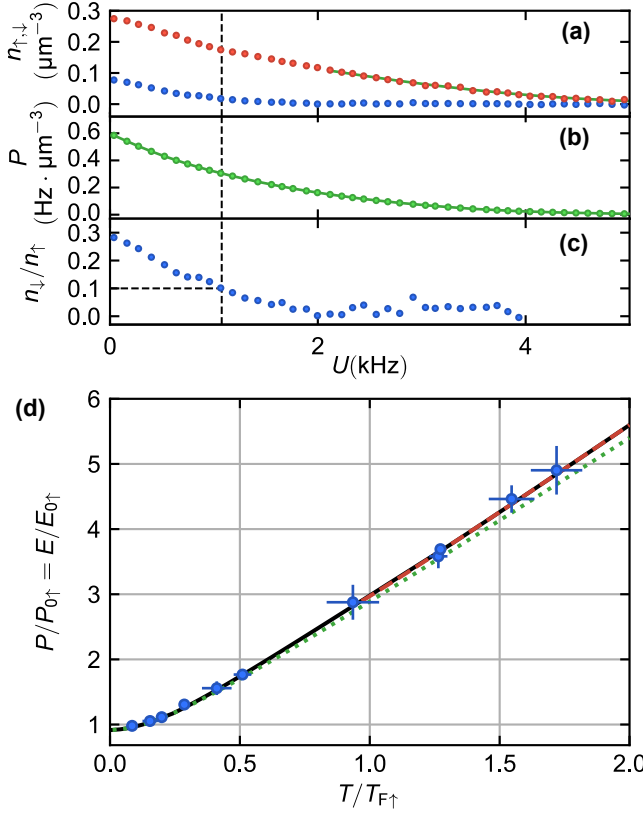


FIG. S3. Pressure of the spin-imbalanced unitary Fermi gas. (a) An example of *in situ* density profiles of the majority (red) and minority (blue) component in the hybrid trap. The temperature of $T = 31 \pm 2$ nK is determined from a fit of the spin-polarized tail of the majority component with the equation of state of the non-interacting Fermi gas (green solid line). The majority Fermi energy in the center of the trap ($U = 0$) is $E_{F\uparrow}/\hbar = 5.4 \pm 0.2$ kHz. (b) The local pressure of the gas, obtained from integrating the density profiles. (c) The local minority concentration. The relevant values for a minority concentration of $n_\downarrow/n_\uparrow = 0.1$ are indicated with the dashed line. (d) The equation of state of the gas at fixed impurity concentration of $n_\downarrow/n_\uparrow = 0.1$. Our measurement is compared with the Fermi liquid ansatz (green dotted line) and 3rd order Virial expansion (red dashed line). An interpolation function (black solid line) is used to connect the Fermi liquid ansatz and Virial expansion.

is obtained from third order virial expansion fits [S11] to the low-fugacity tails of the gas or fits with the equation of state of the non-interacting Fermi gas, in case of spin-polarized tails.

Figure S3(d) shows the equation of state at a fixed impurity concentration of $n_\downarrow/n_\uparrow = 0.1$. For the unitary Fermi gas, the normalized pressure and energy are identical: $P/P_{0\uparrow} = E/E_{0\uparrow}$, with the ground state energy $E_{0\uparrow} = 3/5 N_\uparrow E_{F\uparrow}$ and pressure $P_{0\uparrow} = 2/5 n_\uparrow E_{F\uparrow}$ of the majority atoms. At low temperatures, the normalized pressure is in agreement with the Fermi liquid pressure ansatz [Eq. (3)], while at higher temperatures it

is in agreement with the virial expansion. We use an interpolation function that connects the high and low temperature regime to be able to determine the temperature for arbitrary pressure (energy) values [Fig. S3(d)].

RF SPECTROSCOPY

In this section, we discuss the detection scheme used for rf spectroscopy, the determination of the transfer rate in the linear response regime and the definition of the error bars in Fig. 1 (b) and (c).

Detection

For the measurement of the normalized transfer $I(\omega)$, the atom numbers in all three spin states $|1\rangle$, $|2\rangle$ and $|3\rangle$ after the rf pulse need to be determined. For this purpose we have implemented a triple absorption imaging scheme that allows us to detect all three spin components in a single experimental run. The amount of transferred atoms N_f is determined from an absorption image along the axial direction of the cylinder trap recorded on an EMCCD camera. After 3 ms, the spin components $|1\rangle$ and $|3\rangle$ are subsequently imaged along the radial direction of the cylinder trap and recorded on a fast SCMOS camera with a time delay of $10 \mu\text{s}$ between the two states.

Linear Response

Linear response is an essential requirement for the applicability of Eqs. (1) and (2), linking the rf spectra to the spectral function and the contact. The linear transfer rate can be determined by measuring the transfer fraction N_f/N_\downarrow as a function of the rf pulse duration [Fig. S4]. For the contact data we fit the transfer rate with the exponential function $N_f/N_\downarrow = \Gamma\tau(1 - \exp(-t/\tau))$ to account for saturation effects (time scale τ) and use the initial slope at short times to derive the linear transfer rate Γ [Fig. S4].

Error Bars in Figure 1

Figure 1 shows the peak position and full width at half maximum (FWHM) at different temperatures. To determine the experimental uncertainty for these observables, we use the standard error of the measured transferred fraction without any rf pulse (see $T_{\text{Pulse}} = 0$ in Fig. S4). The errors for the peak position and FWHM are then inferred from the frequency range of data points that lie within the standard error of the amplitude of the maximum and half maxima respectively.

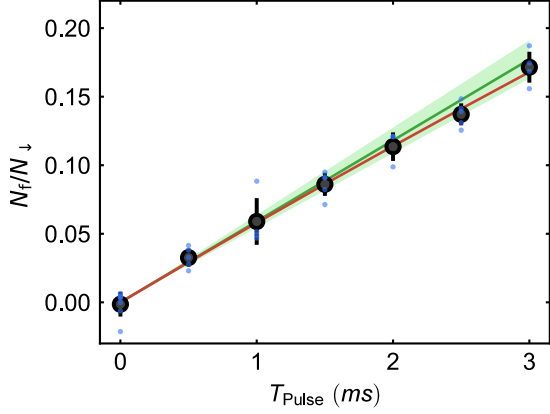


FIG. S4. Time resolved rf response of the minority component. Here, the majority Fermi energy is $E_{F\uparrow}/h = 9.9 \pm 0.2, the impurity concentration $n_\downarrow/n_\uparrow = 0.11 \pm 0.02$, the rf detuning $\omega = 2\pi \times 60 and the temperature $T/T_{F\uparrow} = 0.73 \pm 0.02$. The blue datapoints correspond to the measured rf transfer for several experimental runs and the black circles are the averaged data points. The transferred fraction is fitted with an exponential function (red solid line). The green solid line (shaded area) shows the initial linear slope Γ (standard error) of the fit.$$

- [S1] C. H. Schunck, Y.-I. Shin, A. Schirotzek, and W. Ketterle, *Nature* **454**, 739 (2008).
- [S2] B. Mukherjee, Z. Yan, P. B. Patel, Z. Hadzibabic, T. Yefsah, J. Struck, and M. W. Zwierlein, *Phys. Rev. Lett.* **118**, 123401 (2017).
- [S3] J. E. Thomas, J. Kinast, and A. Turlapov, *Phys. Rev. Lett.* **95**, 120402 (2005).
- [S4] T.-L. Ho, *Phys. Rev. Lett.* **92**, 090402 (2004).
- [S5] Y.-I. Shin, C. H. Schunck, A. Schirotzek, and W. Ketterle, *Nature* **451**, 689 (2008).
- [S6] Y.-I. Shin, *Phys. Rev. A* **77**, 041603 (2008).
- [S7] S. Nascimbène, N. Navon, K. J. Jiang, F. Chevy, and C. Salomon, *Nature* **463**, 1057 (2010).
- [S8] N. Navon, S. Nascimbène, F. Chevy, and C. Salomon, *Science* **328**, 729 (2010).
- [S9] S. Nascimbène, N. Navon, S. Pilati, F. Chevy, S. Giorgini, A. Georges, and C. Salomon, *Phys. Rev. Lett.* **106**, 215303 (2011).
- [S10] M. J. H. Ku, A. T. Sommer, L. W. Cheuk, and M. W. Zwierlein, *Science* **335**, 563 (2012).
- [S11] X.-J. Liu and H. Hu, *Phys. Rev. A* **82**, 043626 (2010).

Appendix C

Spectral Response and Contact of the Unitary Fermi gas

This appendix contains a reprint of Ref. [130]: Mukherjee, B., Patel, P. B., Yan, Z., Fletcher, R. J., Struck, J., & Zwierlein, M. W. (2019). Spectral Response and Contact of the Unitary Fermi Gas. *Phys. Rev. Lett.*, 122(20), 203402.

Spectral Response and Contact of the Unitary Fermi Gas

Biswaroop Mukherjee,¹ Parth B. Patel,¹ Zhenjie Yan,¹ Richard J. Fletcher,¹
Julian Struck,^{1,2} and Martin W. Zwierlein¹

¹MIT-Harvard Center for Ultracold Atoms, Research Laboratory of Electronics, and Department of Physics,
Massachusetts Institute of Technology, Cambridge, Massachusetts 02139, USA

²Département de Physique, Ecole Normale Supérieure / PSL Research University, CNRS, 24 rue Lhomond, 75005 Paris, France



(Received 21 February 2019; published 23 May 2019)

We measure radio frequency (rf) spectra of the homogeneous unitary Fermi gas at temperatures ranging from the Boltzmann regime through quantum degeneracy and across the superfluid transition. For all temperatures, a single spectral peak is observed. Its position smoothly evolves from the bare atomic resonance in the Boltzmann regime to a frequency corresponding to nearly one Fermi energy at the lowest temperatures. At high temperatures, the peak width reflects the scattering rate of the atoms, while at low temperatures, the width is set by the size of fermion pairs. Above the superfluid transition, and approaching the quantum critical regime, the width increases linearly with temperature, indicating non-Fermi-liquid behavior. From the wings of the rf spectra, we obtain the contact, quantifying the strength of short-range pair correlations. We find that the contact rapidly increases as the gas is cooled below the superfluid transition.

DOI: 10.1103/PhysRevLett.122.203402

Understanding fermion pairing and pair correlations is of central relevance to strongly interacting Fermi systems such as nuclei [1,2], ultracold gases [3–6], liquid ^3He [7], high temperature superconductors [8], and neutron stars [9]. Strong interactions on the order of the Fermi energy challenge theoretical approaches, especially methods that predict dynamic properties such as transport or the spectral response at finite temperature [10]. Atomic Fermi gases at Feshbach resonances realize a paradigmatic system where the gas becomes as strongly interacting as allowed by unitarity [3–6,11]. Here, the system becomes universal, requiring only two energy scales: the Fermi energy E_F and thermal energy $k_B T$, where k_B is the Boltzmann constant and T is the temperature. The corresponding length scales are the interparticle spacing $\lambda_F = n^{-1/3}$ and the thermal de Broglie wavelength $\lambda_T = h/\sqrt{2\pi m k_B T}$, where m and n are the mass and number density of the atoms, respectively. When the two energy scales are comparable, the system enters a quantum critical regime separating the high temperature Boltzmann gas from the fermionic superfluid [12]. Quantum criticality is often associated with the absence of quasiparticles [10,12,13], spurring a debate on the applicability of Fermi liquid theory to the degenerate normal fluid below the Fermi temperature $T_F = E_F/k_B$ but above the superfluid transition temperature $T_c \approx 0.167T_F$ [14–16]. It has been conjectured that preformed pairs exist above T_c , up to a pairing temperature T^* [3,5,11,17–21].

Radio frequency (rf) spectroscopy measures the momentum integrated, occupied spectral function, providing a powerful tool for studying interactions and correlations in Fermi gases [22–27]. Here, a particle is ejected from the

interacting many-body state and transferred into a weakly interacting final state. Shifts in rf spectra indicate attractive or repulsive interactions in the gas. At high temperatures, the width of the rf spectrum reflects the scattering rate in the gas, while at low temperatures, the width has been used to infer the pair size of superfluid fermion pairs [26].

The high frequency tails of the rf spectra are sensitive to the spectral function at high momenta and, therefore, are governed by short range correlations quantified by the contact, which also determines the change of the energy with respect to the interaction strength [28–30]. From the momentum distribution within nuclei [1,2] to the frequency dependence of the shear viscosity in ultracold fermionic superfluids [31,32], the contact is central to Fermi gases dominated by short-range interactions. Since the contact is proposed to be sensitive to the superfluid pairing gap, it could signal a pseudogap regime above T_c [32–35]. Although the temperature dependence of the contact near T_c has been the subject of many theoretical predictions, a consensus has not been reached [32,36–38].

Initial studies of unitary Fermi gases using rf spectroscopy were affected by inhomogeneous densities in harmonic traps, yielding doubly peaked spectra that were interpreted as observations of the pairing gap [25,39], and from the influence of interactions in the final state, which caused significantly narrower spectra and smaller shifts than expected [22,39–41]. Measurements of the contact, made using both rf [42,43] and Bragg [44–46] spectroscopy, were also broadened by inhomogeneous potentials. To avoid trap broadening, tomographic techniques have been used to measure local rf spectra, yielding measurements of the superfluid gap [47], the spectral function [17,18], and the

contact [48]. A recent advance has been the creation of uniform box potentials [49–51]. These are ideal for rf spectroscopy and precision measurements of the contact: since the entire cloud is at a constant density, global probes such as rf address all atoms, and benefit from a stronger signal.

In this Letter, we report on rf spectroscopy of the homogeneous unitary Fermi gas in a box potential. A single peak is observed for all temperatures from the superfluid regime into the high temperature Boltzmann gas. The tails of the rf spectra reveal the contact, which shows a rapid rise as the temperature is reduced below T_c .

We prepare ${}^6\text{Li}$ atoms in two of the three lowest hyperfine states $|\downarrow\rangle = |1\rangle$ and $|\uparrow\rangle = |3\rangle$ at a magnetic field of 690 G, where interspin interactions are resonant. A uniform optical box potential with cylindrical symmetry is loaded with $N \sim 10^6$ atoms per spin state (with Fermi energies $E_F \sim h \times 10$ kHz), creating spin-balanced homogeneous gases at temperatures ranging from $T/T_F = 0.10$ to 3.0 [50]. A square rf pulse transfers atoms from state $|\downarrow\rangle$ into state $|f\rangle = |2\rangle$. Final state interactions between atoms in state $|f\rangle$ and atoms in states $|\uparrow\rangle$ and $|\downarrow\rangle$ are small ($k_F a_f \lesssim 0.2$, where a_f is the scattering length characterizing collisions between atoms in the final and initial states, and $\hbar k_F = \sqrt{2mE_F}$ is the Fermi momentum)

[26]. After the rf pulse, we measure the atom numbers N_\downarrow and N_f in the initial and final states. Within linear response, according to Fermi's golden rule, N_f is proportional to the pulse time T_{Pulse} , the square of the single-particle Rabi frequency Ω_R , and an energy density of states. Thus, we define a normalized, dimensionless rf spectrum as $I(\omega) = [N_f(\omega)/N_\downarrow](E_F/\hbar\Omega_R^2 T_{\text{Pulse}})$ [52,57]. Because of the scale invariance of the balanced unitary Fermi gas, this dimensionless function can only depend on T/T_F and $\hbar\omega/E_F$.

For thermometry, we release the cloud from the uniform potential into a harmonic trap along one direction [57]. Since the cloud expands isoenergetically, the resulting spatial profile after thermalization provides the energy per particle, which can be related to the reduced temperature, T/T_F , using a virial relation and the measured equation of state [14]. To clearly identify the superfluid transition, we measure the pair momentum distribution by a rapid ramp of the magnetic field to the molecular side of the Feshbach resonance before releasing the gas into a harmonic trap for a quarter period [50,52].

Initially, we focus on changes in the line shape for rf frequencies within $\sim E_F/\hbar$ of the bare (single-particle) resonance [see Fig. 1(a)], and follow the changes in

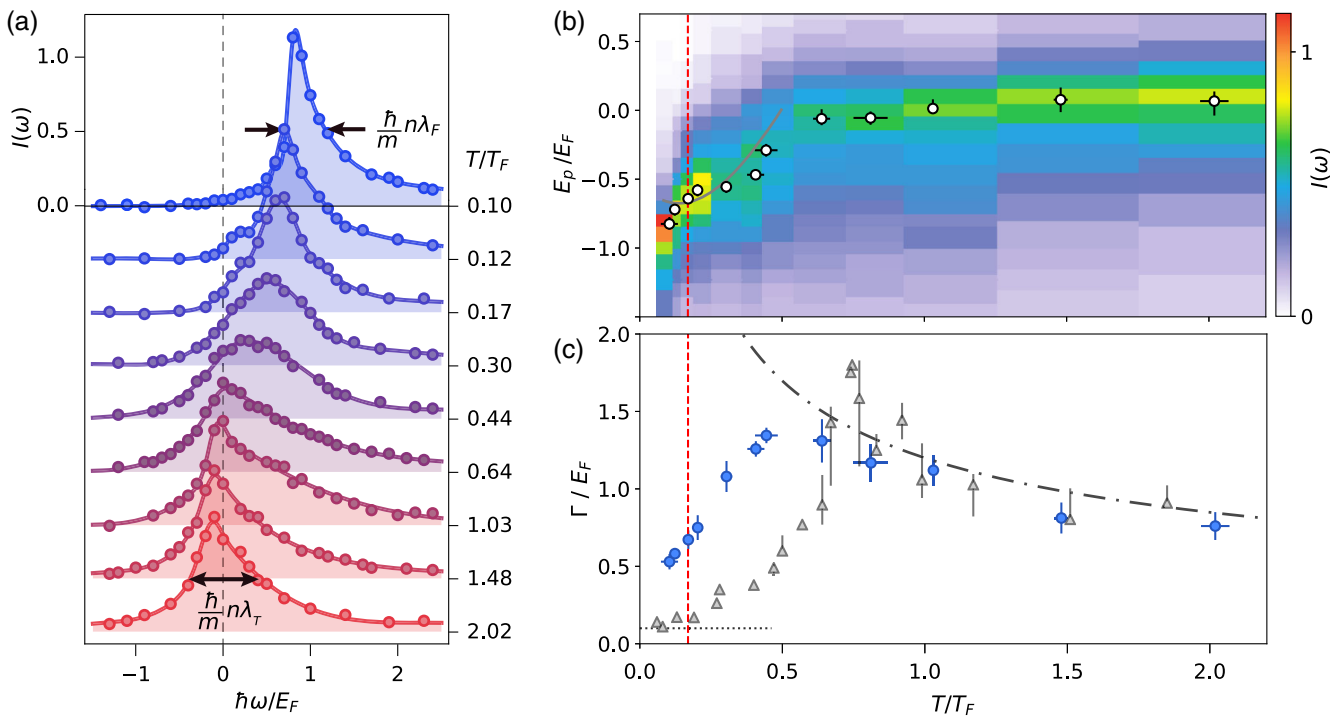


FIG. 1. (a) Thermal evolution of rf spectra. The Rabi frequency is $\Omega_R = 2\pi \times 0.5$ kHz and the pulse duration is $T_{\text{Pulse}} = 1$ ms. The solid lines are guides to the eye. (b) Frequency of the peak ($E_p = -\hbar\omega$) of the rf spectra as a function of temperature shown as white dots on an intensity plot of the rf response. The grey solid line is a solution to the Cooper problem at nonzero temperature [52]. (c) The full width at half maximum Γ of the rf peak as a function of T/T_F . The black dotted-dashed line $\Gamma/E_F = 1.2\sqrt{T_F/T}$ shows the temperature dependence of the width due to scattering in the high-temperature gas [32,60]. The grey triangles are the corresponding width measurements of a highly spin-imbalanced gas [57]. The horizontal black dotted line represents the Fourier broadening of $0.1E_F$ [52]. The vertical dashed red line in both (b) and (c) marks the superfluid transition [14].

the peak position E_p [shown in Fig. 1(b)]. As the hot spin-balanced Fermi gas is cooled below the Fermi temperature, the peak shift decreases from roughly zero for temperatures $T \gtrsim T_F$, to $E_p \approx -0.8E_F$ for temperatures below the superfluid transition temperature [see Fig. 1(b)]. At high temperatures, one might naïvely expect a shift on the order of $E_p \sim \hbar n \lambda_T / m$ due to unitarity-limited interactions in the gas. However, there exists both an attractive and a repulsive energy branch, which are symmetric about zero at unitarity [58], and when $T \gg T_F$, their contributions to the shift cancel [32,59,60]. As to the interpretation of the peak shift at degenerate temperatures, a solution to the Cooper problem in the presence of a $T > 0$ Fermi sea shows that it is energetically favorable to form pairs when $T \lesssim 0.5T_F$ [52], and the resulting pair energy agrees qualitatively with the observed shifts [grey line in Fig. 1(b)]. However, it is known that fluctuations suppress the onset of pair condensation and superfluidity to $0.167(13)T_F$ [5,11,14,61]. In a zero-temperature superfluid, BCS theory would predict a peak shift given by the pair binding energy $E_B = \Delta^2/2E_F$, where Δ is the pairing gap [3]. Including Hartree terms is found to result in an additional shift of the peak [27,47].

Now, we turn to the widths, Γ , defined as the full width at half maximum of the rf spectra [see Fig. 1(c)]. As the gas is cooled from the Boltzmann regime, the width gradually increases, and attains a maximum of $\Gamma = 1.35(5)E_F$ near $T = 0.44(4)T_F$. For temperatures much higher than T_F , the system is a Boltzmann gas of atoms scattering with a unitarity limited cross section $\sigma \sim \lambda_T^2$. Transport properties and short-range pair correlations are governed by the scattering rate $\Gamma = n_{\downarrow} \sigma \langle v_{\text{rel}} \rangle \sim \hbar n_{\downarrow} \lambda_T / m$ and a mean-free path $l = (n_{\downarrow} \sigma)^{-1} \sim (n_{\downarrow} \lambda_T^2)^{-1}$, where n_{\downarrow} is the density of atoms in $|\downarrow\rangle$, and $\langle v_{\text{rel}} \rangle \sim \hbar / m \lambda_T$ is the thermally averaged relative velocity. This leads to a width that scales as $\Gamma \propto 1/\sqrt{T}$, shown as the dotted-dashed line in Fig. 1(c) [32].

As the cloud is cooled below $T \approx 0.5T_F$, the width decreases linearly with temperature to $\Gamma \sim 0.52E_F/\hbar$ in the coldest gases measured [$T = 0.10(1)T_F$]. For temperatures below T_c , we expect the gas to consist of pairs of size ξ . The rf spectrum will be broadened by the distribution of momenta $\sim \hbar/\xi$ inside each pair, leading to a spread of possible final kinetic energies $\hbar^2 k^2 / m \sim \hbar^2 / m \xi^2$ and a corresponding spectral width $\hbar/m\xi^2$. At unitarity and at $T = 0$, the pair size is set by the interparticle spacing λ_F [3,5,26]. Thus, the rf width at low temperatures is $\Gamma \sim \hbar n \lambda_F / m$.

For temperatures above T_c , it has been suggested that the normal fluid can be described as a Fermi liquid [15,62]. This would imply a quadratic relation between the peak width and the temperature [63], as observed in the widths of the rf spectra of Fermi polarons at unitarity [57]. However, the measured width of the spin-balanced Fermi gas changes linearly in temperature, implying non-Fermi

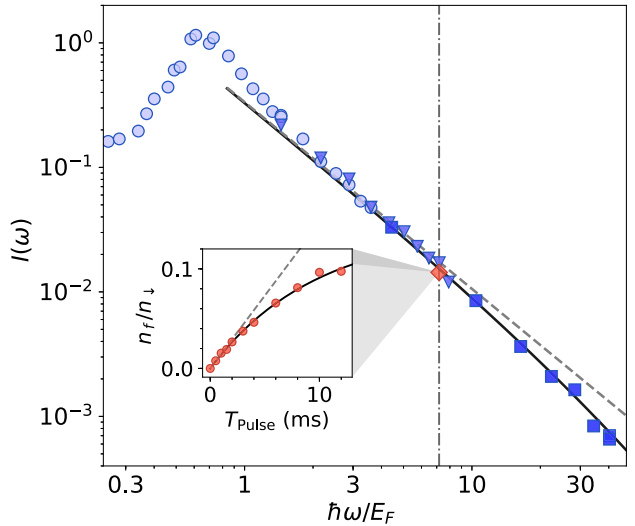


FIG. 2. Rf spectrum at high frequencies. Here, the temperature of the gas is $T/T_F = 0.10(1)$, the pulse duration is $T_{\text{Pulse}} = 1$ ms, and the Rabi frequencies are $2\pi \times 536$ Hz (light blue circles), $2\pi \times 1.20$ kHz (medium blue triangles), and $2\pi \times 3.04$ kHz (dark blue squares). The black solid line shows a fit of Eq. (1) to the data, while the grey dashed line shows the fit neglecting final state interactions. The contact can be directly obtained from the transfer rate at a fixed detuning of 60 kHz ($\hbar\omega/E_F \sim 7.1$) (dotted-dashed vertical line). Inset: we vary the pulse time at this fixed detuning, and extract the initial slope (dashed line) of the exponential saturating fit (solid line). The rf transfer rate obtained from the initial linear slope is shown as the red diamond in the main plot. Here, $\Omega_R = 2\pi \times 1.18$ kHz.

liquid behavior in the normal fluid. In addition, $\Gamma > E_F/\hbar$ for $0.3 \lesssim T/T_F \lesssim 1.2$, indicating a breakdown of well-defined quasiparticles over a large range of temperatures near the quantum critical regime [10,12,13].

We now consider the rf spectrum at frequencies much larger than E_F/\hbar , where the rf-coupled high-momentum tails reveal information about the short-range pair correlations between atoms. In a gas with contact interactions, the pair correlation function at short distances is $\lim_{r \rightarrow 0} \langle n_{\uparrow}(\mathbf{r}_0 + \mathbf{r}/2) n_{\downarrow}(\mathbf{r}_0 - \mathbf{r}/2) \rangle = C/(4\pi r)^2$. The contact C connects a number of fundamental relations, independent of the details of the short-range interaction potential [28]. In particular, the contact governs the momentum distribution at large momenta: $\lim_{k \rightarrow \infty} n(k) = C/k^4$. For rf spectroscopy, the density of final states scales as $\sqrt{\omega}$, and the energy cost to flip a spin at high momenta is $\lim_{k \rightarrow \infty} \hbar\omega = \hbar^2 k^2 / m$. Thus, the number of atoms transferred by the rf pulse at high frequencies in linear response is $\propto C/\omega^{3/2}$ [5,27]. Including final state interactions, the general expression for the rf transfer rate in a gas with unitarity-limited initial state interactions is [64]

$$\lim_{\omega \rightarrow \infty} I(\omega) = \left(\frac{C}{Nk_F} \right) \frac{1}{2\sqrt{2\pi}(1 + \hbar\omega/E_b)} \left(\frac{E_F}{\hbar\omega} \right)^{3/2}, \quad (1)$$

where $N = N_\uparrow + N_\downarrow$ is the total number of atoms, and the final state molecular binding energy is $E_b = \hbar^2/m a_f^2 \approx \hbar \times 433 \text{ kHz} \approx 40 E_F$. Figure 2 shows a typical rf spectrum at $T/T_F = 0.10$, with a fit of Eq. (1) to data with detunings $\hbar\omega > 3E_F$, using the dimensionless contact $\tilde{C} = C/Nk_F$ as the only free parameter. At detunings larger than about $10 E_F$, the data deviate from a typical $\omega^{-3/2}$ tail, and are better described by the full expression Eq. (1) including final state interactions. Here, the Rabi frequency was varied across the plot to ensure small transfers near the peak and a high signal-to-noise ratio at detunings up to $\hbar\omega/E_F = 31$. The fit of Eq. (1) to the data gives a low-temperature contact of $\tilde{C} = 3.07(6)$, consistent with a quantum Monte Carlo result $\tilde{C} = 2.95(10)$ [65], the Luttinger-Ward (LW) calculation $\tilde{C} = 3.02$ [27], as well as previous measurements using losses $\tilde{C} = 3.1(3)$ [66] and Bragg spectroscopy $\tilde{C} = 3.06(8)$ [46].

For a more efficient measurement of the contact across a range of temperatures, we vary the pulse time at a fixed detuning of 60 kHz ($\hbar\omega/E_F \gtrsim 6$) that is large compared to the Fermi energy and temperature. [52]. Deviations from linear response are observed for transfers as small as 5% (see inset of Fig. 2). We fit the transfers to an exponentially saturating function $A[1 - \exp(-T_{\text{Pulse}}/\tau)]$, and find the initial linear slope A/τ in order to extract the contact for each temperature using Eq. (1). This ensures that every measurement is taken in the linear response regime.

In Fig. 3(a), we show the temperature dependence of the contact. As the gas is cooled, the contact shows a gradual increase down to the superfluid transition T_c . Entering the superfluid transition, the contact rapidly rises by approximately 15%. The changes in the contact reveal the temperature dependence of short-range pair correlations in the spin-balanced Fermi gas. At temperatures far above T_F , the contact reflects the inverse mean free path in the gas $1/l \sim 1/T$. At lower temperatures, the behavior of the contact is better described by a third-order virial expansion [see inset of 3(a)] [36]. Near T_c , predictions of the contact vary considerably. In the quantum critical regime, a leading-order $1/N$ calculation (equivalent to a Gaussian pair fluctuation or Nozières-Schmitt-Rink method) results in a prediction $\tilde{C}(\mu = 0, T \approx 0.68T_F) = 2.34$ [10], which is consistent with our measurement of $\tilde{C}[T = 0.65(4)T_F] = 2.29(13)$. For temperatures above the superfluid transition, our data agree well with both a bold diagrammatic Monte Carlo calculation [38], and, especially near T_c , the LW calculation [32]. The contact rises as the temperature is decreased below T_c , a feature captured by the LW formalism, in which the contact is directly sensitive to pairing: $\tilde{C} \sim (\Delta/E_F)^2$ [27,33]. While short-range pair correlations do not necessarily signify pairing [35], the rapid rise of the contact below T_c is strongly indicative of an additional contribution from fermion pairs, as predicted

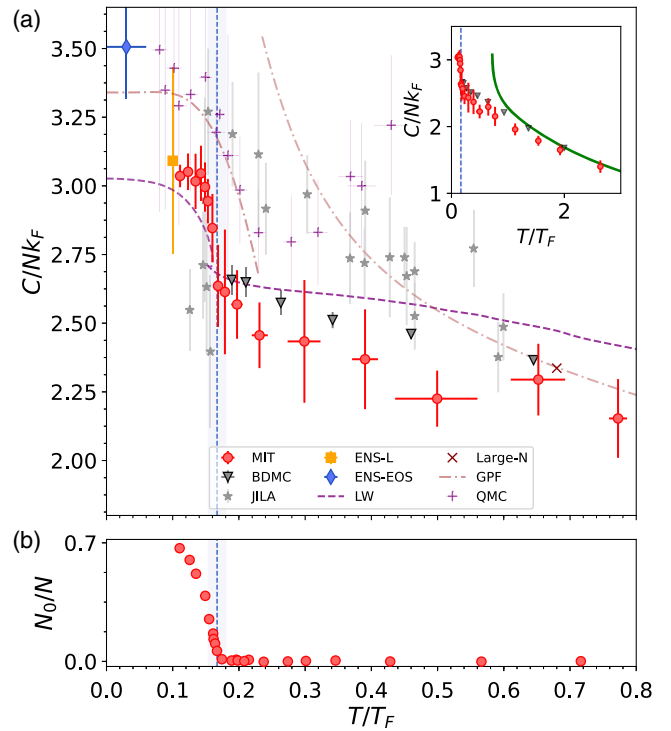


FIG. 3. The dimensionless contact C/Nk_F (a) and condensate fraction N_0/N (b) of the unitary Fermi gas as a function of the reduced temperature T/T_F . Our measurements of the contact (red points) are compared with a number of theoretical estimates: bold-diagrammatic Monte Carlo (BDMC) [38], quantum Monte Carlo (QMC) [37], Luttinger-Ward (LW) [32], large N [10], and Gaussian pair fluctuations (GPF) [36]. Also shown is the homogeneous contact obtained from the equation of state at the École normale supérieure (ENS-EOS) [62], from loss rate measurements (ENS-L) [66], and from rf spectroscopy by the JILA group [18] across a range of temperatures. The vertical blue dotted lines and light blue shaded vertical regions mark $T_c/T_F = 0.167(13)$ [14]. The inset of (a) shows the contact over a wider range of temperatures and marks the high-temperature agreement with the third order virial expansion. The error bars account for the statistical uncertainties in the data.

by LW. At temperatures $T \ll T_c$, below the reach of our experiment, phonons are likely the only remaining excitations in the unitary Fermi gas, and are expected to contribute to the contact by an amount that scales as T^4 [67].

In conclusion, rf spectroscopy of the homogeneous unitary Fermi gas reveals strong attractive interactions, the non-Fermi-liquid nature of excitations in the gas across the quantum critical regime, and a rapid increase in short-range pair correlations upon entering the superfluid regime. The strong variation with temperature of the position of the spectral peak may serve as a local thermometer in future studies of heat transport in ultracold Fermi gases. Furthermore, these measurements of the contact provide a benchmark for many-body theories of the unitary Fermi gas. The uniform trap enables direct access to homogeneous measurements of thermodynamic quantities,

and increases sensitivity to abrupt changes of those quantities near phase transitions. This could be particularly useful in the limit of high spin imbalance, where the nature of impurities suddenly transitions from Fermi polarons to molecules. [68,69].

We note that measurements of the temperature dependence of the contact were simultaneously performed at Swinburne using Bragg spectroscopy [70]. Their data are in excellent agreement with the present results.

We thank C. J. Vale, F. Werner, and W. Zwerger for helpful discussions. This work was supported by the National Science Foundation (Center for Ultracold Atoms Awards No. PHY-1734011 and No. PHY-1506019), Air Force Office of Scientific Research (FA9550-16-1-0324 and MURI Quantum Phases of Matter FA9550-14-1-0035), Office of Naval Research (N00014-17-1-2257) and the David and Lucile Packard Foundation. J. S. was supported by LabEX ENS-ICFP; ANR-10-LABX-0010/ANR-10-IDEX-0001-02 PSL*.

- [1] O. Hen *et al.*, *Science* **346**, 614 (2014).
- [2] R. Weiss, B. Bazak, and N. Barnea, *Phys. Rev. Lett.* **114**, 012501 (2015).
- [3] W. Ketterle and M. W. Zwierlein, in “Ultra-Cold Fermi Gases,” *Proceedings of the International School of Physics “Enrico Fermi,” Course CLXIV*, edited by M. Inguscio, W. Ketterle, and C. Salomon (IOS Press, Amsterdam, 2008), pp. 247–422.
- [4] S. Giorgini, L. P. Pitaevskii, and S. Stringari, *Rev. Mod. Phys.* **80**, 1215 (2008).
- [5] W. Zwerger, in “Quantum Matter at Ultralow Temperatures,” *Proceedings of the International School of Physics “Enrico Fermi” Course CLXCI*, edited by M. Inguscio, W. Ketterle, S. Stringari, and G. Roati (IOS Press, Amsterdam, 2016), pp. 63–142.
- [6] M. W. Zwierlein, in *Novel Superfluids* (Oxford University Press, Oxford, 2014), pp. 269–422.
- [7] A. J. Leggett, *Phys. Rev. Lett.* **29**, 1227 (1972).
- [8] P. A. Lee, N. Nagaosa, and X.-G. Wen, *Rev. Mod. Phys.* **78**, 17 (2006).
- [9] G. Baym, C. Pethick, and D. Pines, *Nature (London)* **224**, 673 (1969).
- [10] T. Enss, *Phys. Rev. A* **86**, 013616 (2012).
- [11] M. Randeria and E. Taylor, *Annu. Rev. Condens. Matter Phys.* **5**, 209 (2014).
- [12] P. Nikolic and S. Sachdev, *Phys. Rev. A* **75**, 033608 (2007).
- [13] B. Frank, J. Lang, and W. Zwerger, *J. Exp. Theor. Phys.* **127**, 812 (2018).
- [14] M. J. H. Ku, A. T. Sommer, L. W. Cheuk, and M. W. Zwierlein, *Science* **335**, 563 (2012).
- [15] S. Nascimbène, N. Navon, S. Pilati, F. Chevy, S. Giorgini, A. Georges, and C. Salomon, *Phys. Rev. Lett.* **106**, 215303 (2011).
- [16] I. Z. Rothstein and P. Shrivastava, *Phys. Rev. B* **99**, 035101 (2019).

- [17] J. P. Gaebler, J. T. Stewart, T. E. Drake, D. S. Jin, A. Perali, P. Pieri, and G. C. Strinati, *Nat. Phys.* **6**, 569 (2010).
- [18] Y. Sagi, T. E. Drake, R. Paudel, R. Chapurin, and D. S. Jin, *Phys. Rev. Lett.* **114**, 075301 (2015).
- [19] A. Perali, P. Pieri, G. C. Strinati, and C. Castellani, *Phys. Rev. B* **66**, 024510 (2002).
- [20] H. Hu, X. J. Liu, P. D. Drummond, and H. Dong, *Phys. Rev. Lett.* **104**, 240407 (2010).
- [21] P. Magierski, G. Włazłowski, and A. Bulgac, *Phys. Rev. Lett.* **107**, 145304 (2011).
- [22] S. Gupta, Z. Hadzibabic, M. W. Zwierlein, C. A. Stan, K. Dieckmann, C. H. Schunck, E. G. Van Kempen, B. J. Verhaar, and W. Ketterle, *Science* **300**, 1723 (2003).
- [23] C. A. Regal and D. S. Jin, *Phys. Rev. Lett.* **90**, 230404 (2003).
- [24] C. A. Regal, C. Ticknor, J. L. Bohn, and D. S. Jin, *Nature (London)* **424**, 47 (2003).
- [25] C. Chin, M. Bartenstein, A. Altmeyer, S. Riedl, S. Jochim, J. Denschlag, and R. Grimm, *Science* **305**, 1128 (2004).
- [26] C. H. Schunck, Y.-I. Shin, A. Schirotzek, and W. Ketterle, *Nature (London)* **454**, 739 (2008).
- [27] R. Haussmann, M. Punk, and W. Zwerger, *Phys. Rev. A* **80**, 063612 (2009).
- [28] S. Tan, *Ann. Phys. (Amsterdam)* **323**, 2971 (2008).
- [29] S. Tan, *Ann. Phys. (Amsterdam)* **323**, 2952 (2008).
- [30] S. Tan, *Ann. Phys. (Amsterdam)* **323**, 2987 (2008).
- [31] E. Taylor and M. Randeria, *Phys. Rev. A* **81**, 053610 (2010).
- [32] T. Enss, R. Haussmann, and W. Zwerger, *Ann. Phys. (Amsterdam)* **326**, 770 (2011).
- [33] P. Pieri, A. Perali, and G. C. Strinati, *Nat. Phys.* **5**, 736 (2009).
- [34] F. Palestini, A. Perali, P. Pieri, and G. C. Strinati, *Phys. Rev. A* **82**, 021605(R) (2010).
- [35] E. J. Mueller, *Rep. Prog. Phys.* **80**, 104401 (2017).
- [36] H. Hu, X. J. Liu, and P. D. Drummond, *New J. Phys.* **13**, 035007 (2011).
- [37] O. Goulko and M. Wingate, *Phys. Rev. A* **93**, 053604 (2016).
- [38] R. Rossi, T. Ohgoe, E. Kozik, N. Prokof’ev, B. Svistunov, K. Van Houcke, and F. Werner, *Phys. Rev. Lett.* **121**, 130406 (2018).
- [39] C. H. Schunck, Y. Shin, A. Schirotzek, M. W. Zwierlein, and W. Ketterle, *Science* **316**, 867 (2007).
- [40] G. Baym, C. J. Pethick, Z. Yu, and M. W. Zwierlein, *Phys. Rev. Lett.* **99**, 190407 (2007).
- [41] M. Punk and W. Zwerger, *Phys. Rev. Lett.* **99**, 170404 (2007).
- [42] J. T. Stewart, J. P. Gaebler, T. E. Drake, and D. S. Jin, *Phys. Rev. Lett.* **104**, 235301 (2010).
- [43] C. Shkedrov, Y. Florshaim, G. Ness, A. Gandman, and Y. Sagi, *Phys. Rev. Lett.* **121**, 093402 (2018).
- [44] E. D. Kuhnle, H. Hu, X. J. Liu, P. Dyke, M. Mark, P. D. Drummond, P. Hannaford, and C. J. Vale, *Phys. Rev. Lett.* **105**, 070402 (2010).
- [45] E. D. Kuhnle, S. Hoinka, P. Dyke, H. Hu, P. Hannaford, and C. J. Vale, *Phys. Rev. Lett.* **106**, 170402 (2011).
- [46] S. Hoinka, M. Lingham, K. Fenech, H. Hu, C. J. Vale, J. E. Drut, and S. Gandolfi, *Phys. Rev. Lett.* **110**, 055305 (2013).
- [47] A. Schirotzek, Y.-I. Shin, C. H. Schunck, and W. Ketterle, *Phys. Rev. Lett.* **101**, 140403 (2008).

- [48] Y. Sagi, T. E. Drake, R. Paudel, and D. S. Jin, *Phys. Rev. Lett.* **109**, 220402 (2012).
- [49] A. L. Gaunt, T. F. Schmidutz, I. Gotlibovych, R. P. Smith, and Z. Hadzibabic, *Phys. Rev. Lett.* **110**, 200406 (2013).
- [50] B. Mukherjee, Z. Yan, P. B. Patel, Z. Hadzibabic, T. Yefsah, J. Struck, and M. W. Zwierlein, *Phys. Rev. Lett.* **118**, 123401 (2017).
- [51] K. Hueck, N. Luick, L. Sobirey, J. Siegl, T. Lompe, and H. Moritz, *Phys. Rev. Lett.* **120**, 060402 (2018).
- [52] See Supplemental Material at <http://link.aps.org/supplemental/10.1103/PhysRevLett.122.203402> for further information, which includes Refs. [53–56].
- [53] L. N. Cooper, *Phys. Rev.* **104**, 1189 (1956).
- [54] M. Y. Veillette, D. E. Sheehy, and L. Radzhivsky, *Phys. Rev. A* **75**, 043614 (2007).
- [55] L. Pisani, P. Pieri, and G. C. Strinati, *Phys. Rev. B* **98**, 104507 (2018).
- [56] M. Naraschewski and D. M. Stamper-Kurn, *Phys. Rev. A* **58**, 2423 (1998).
- [57] Z. Yan, P. B. Patel, B. Mukherjee, R. J. Fletcher, J. Struck, and M. W. Zwierlein, *Phys. Rev. Lett.* **122**, 093401 (2019).
- [58] T.-L. Ho and E. J. Mueller, *Phys. Rev. Lett.* **92**, 160404 (2004).
- [59] R. J. Fletcher, R. Lopes, J. Man, N. Navon, R. P. Smith, M. W. Zwierlein, and Z. Hadzibabic, *Science* **355**, 377 (2017).
- [60] M. Sun and X. Leyronas, *Phys. Rev. A* **92**, 053611 (2015).
- [61] P. Nozières and S. Schmitt-Rink, *J. Low Temp. Phys.* **59**, 195 (1985).
- [62] S. Nascimbène, N. Navon, K. J. Jiang, F. Chevy, and C. Salomon, *Nature (London)* **463**, 1057 (2010).
- [63] P. Nozieres and D. Pines, *The Theory of Quantum Liquids, Vol I: Normal Fermi Liquids*, 1st ed. (W.A. Benjamin, New York, 1966).
- [64] E. Braaten, D. Kang, and L. Platter, *Phys. Rev. Lett.* **104**, 223004 (2010).
- [65] J. E. Drut, T. A. Lähde, and T. Ten, *Phys. Rev. Lett.* **106**, 205302 (2011).
- [66] S. Laurent, M. Pierce, M. Delehaye, T. Yefsah, F. Chevy, and C. Salomon, *Phys. Rev. Lett.* **118**, 103403 (2017).
- [67] Z. Yu, G. M. Bruun, and G. Baym, *Phys. Rev. A* **80**, 023615 (2009).
- [68] M. Punk, P. T. Dumitrescu, and W. Zwerger, *Phys. Rev. A* **80**, 053605 (2009).
- [69] A. Schirotzek, C.-H. Wu, A. Sommer, and M. W. Zwierlein, *Phys. Rev. Lett.* **102**, 230402 (2009).
- [70] C. Carcy, S. Hoinka, M. G. Lingham, P. Dyke, C. C. N. Kuhn, H. Hu, and C. J. Vale, preceding Letter, *Phys. Rev. Lett.* **122**, 203401 (2019).

Supplemental Material: Spectral response and contact of the unitary Fermi gas

Biswaroop Mukherjee,¹ Parth B. Patel,¹ Zhenjie Yan,¹

Richard J. Fletcher,¹ Julian Struck,^{1,2} and Martin W. Zwierlein¹

¹MIT-Harvard Center for Ultracold Atoms, Research Laboratory of Electronics, and Department of Physics, Massachusetts Institute of Technology, Cambridge, Massachusetts 02139, USA

²Département de Physique, Ecole Normale Supérieure / PSL Research University, CNRS, 24 rue Lhomond, 75005 Paris, France

DENSITY CALIBRATION IN THE HOMOGENEOUS TRAP

The density of atoms in the homogeneous trap is measured using *in situ* absorption imaging [S1]. The absolute atom numbers are calibrated by loading a spin-imbalanced gas into a hybrid trap that is axially harmonic and radially homogeneous [S2]. In Fig. S1, we plot the 1D density profile given by the integrated profile along the two homogeneous directions and the isothermal compressibility $\kappa/\kappa_0 = -\partial E_{F\uparrow}/\partial U$ of the majority component, where $\kappa_0 = \frac{3}{2n_\uparrow E_F}$ is the compressibility of an ideal Fermi gas at density n_\uparrow . The compressibility in the spin-polarized region provides the calibration of our measurement of density.

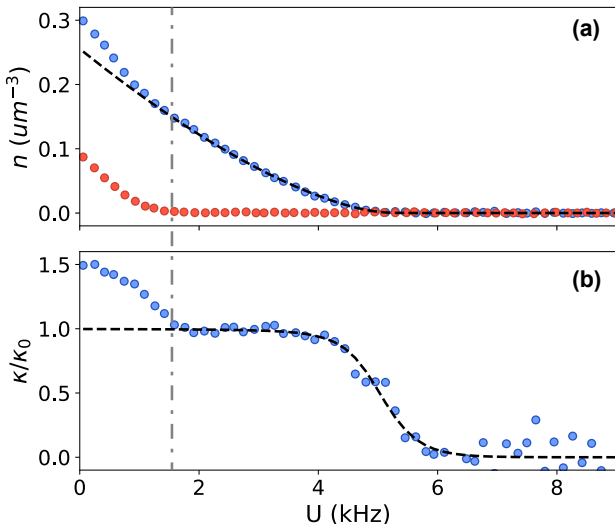


FIG. S1. Density calibration using the spin-imbalanced Fermi gas in the axially harmonic, radially homogeneous trap. Here, the majority Fermi energy is $E_{F\uparrow}/\hbar = 5.7(1)$ kHz, $T/T_{F\uparrow} = 0.05(1)$ and the imbalance is $N_\downarrow/N_\uparrow = 0.18$. (a) Majority (minority) density profiles in blue (red) data points. The dashed line is a fit to the ideal equation of state for the spin-polarized Fermi gas, restricted to the polarized wings of the cloud (outside the minority component edge, marked with the dot-dashed line). (b) The isothermal compressibility of the majority component as a function of position.

RF SPECTROSCOPY MEASUREMENTS

For rf spectroscopy measurements, two images are taken within several μs of each other. The first image records the transferred cloud in state $|f\rangle = |2\rrangle$, while the second image allows for counting the number of atoms in the initial state $|\downarrow\rangle = |1\rangle$. For measurements of the full spectrum, the pulse time is set to $T_{\text{Pulse}} = 1$ ms, giving a Fourier-limited spectral resolution of 1 kHz. For measurements of the contact, we select a detuning that is large compared to both the Fermi energy and the temperature of the cloud. This ensures that atoms are transferred from the high-momentum tails, and the transfer rate accurately measures the contact. For detunings between $\hbar\omega \approx 5E_F$ and $\hbar\omega \approx 13E_F$, we verified that the measured value of \tilde{C} is constant within statistical errors. The Rabi frequencies are adjusted between $\Omega_R = 2\pi \times 500$ Hz and $\Omega_R = 2\pi \times 1$ kHz to maintain a high signal to noise ratio.

COOPER PROBLEM AT FINITE TEMPERATURE

In the Cooper problem [S3] one searches for the binding energy of two opposite-spin fermions on top of the filled Fermi sea. The Fermi sea is treated as “inert”, its only role being to block momentum states that would otherwise be available to the scattering pair. This constraint alone already leads to pairing in three dimensions. Cooper’s solution can be extended to non-zero temperature, in the search of a bound state on top of a finite temperature Fermi gas. A standard approach [S4] yields an equation for the bound state energy E_c for Cooper pairs:

$$-\frac{m}{4\pi\hbar^2 a} = \int \frac{d^3 p}{(2\pi)^3} \left(\frac{(1 - n_F(\xi_p))^2}{2\xi_p - E_c} - \frac{1}{2\epsilon_p} \right), \quad (\text{S1})$$

where $n_F(\epsilon) = (1 + \exp(\epsilon/T))^{-1}$ is the Fermi function, $\xi_p = \frac{p^2}{2m} - \mu$, and μ the chemical potential of the non-interacting Fermi gas at temperature T . The factor $(1 - n_F(\xi_p))^2$ represents Pauli blocking of momentum states already occupied in the spin up and the spin down Fermi sea. Without it, there would be no pairing of two

particles, as is well known in three dimensions. This simplest approach to pairing in a Fermi gas predicts a Cooper pair energy at resonance ($1/a = 0$) of $E_c = -0.61E_F$ at zero temperature, and an onset of pairing ($E_c < 0$) at $T^*/T_F = 0.41E_F$. To look for binding in the full many-body framework, one searches for poles of the pair propagator. In the lowest-order T-matrix calculation or equivalently to lowest order in a $1/N$ expansion [S5, S6] (where $2N$ is the number of spin components of the Fermi gas), one finds an equation for this pole that is nearly identical to the above:

$$-\frac{m}{4\pi\hbar^2 a} = \int \frac{d^3 p}{(2\pi)^3} \left(\frac{(1 - n_F(\xi_p))^2 - n_F(\xi_p)^2}{2\xi_p - E_c} - \frac{1}{2\epsilon_p} \right). \quad (\text{S2})$$

Compared to the simple Cooper problem, the many-body approach yields an additional contribution to the integral from occupied momentum states $\propto -n_F(\xi_p)^2$ as fermions within the Fermi sea now also profit from pairing. This does not change the prediction for the $T = 0$ binding energy $E_c = -0.61E_F$, but it yields stronger binding at finite temperature, and predicts an onset of pairing at $T^*/T_F = 0.5$. In the main text, we show E_c from this lowest-order many-body approach. As is well-known, fluctuations reduce the onset of superfluidity to lower T_c . The next order in the $1/N$ expansion yields [S5] $T_c/T_F = 0.14$, and the self-consistent T-matrix approach [S7] yields $T_c/T_F = 0.16$, in agreement with the experimental value $T_c/T_F = 0.167(13)$ [S8]. However, T^* is often interpreted as the crossover temperature scale for pair formation [S9], and the region between T_c and T^* is the putative “pseudogap” regime. For a recent analysis of pair correlations see [S10].

CONDENSATE FRACTION

The condensate fraction is measured by performing a momentum space mapping of the pair wavefunction. The atoms are released from the optical box potential into a magnetic harmonic trap with a confining trapping frequency $\omega_z = 2\pi \times 23$ Hz along the z-direction. Simultaneously, the bias field is rapidly ramped from the Feshbach resonance to a value near a zero crossing of the scattering length, which associates existing fermion pairs into bosonic molecules, and preserves the center of mass momentum. Assuming the resulting molecules are non-interacting, the density profile of the cloud after a quarter-period oscillation in the harmonic trap provides the pair center of mass momentum distribution [S2]. The measured integrated profiles $n_{1D}(z)$ are functions of the momentum $k_z = m\omega_z z/\hbar$ along the z direction (see Fig. S2). We fit the wings with the momentum distribution for a thermal gas of non-interacting bosons [S11]:

$$n_{1D}(k_z) = \frac{1}{(2\pi k_B T)^{3/2}} g_{3/2} \left(e^{-|\hbar^2 k_z^2/2m - \mu|/k_B T} \right) \quad (\text{S3})$$

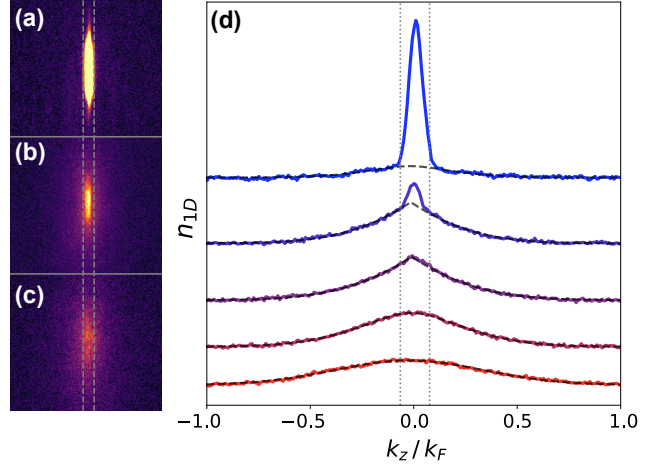


FIG. S2. Momentum space mapping of the box pair wavefunction. (a)-(c) Images of the cloud at $T/T_F = 0.13$ in (a), 0.16 in (b), and 0.18 in (c), after a quarter-period release along the horizontal direction. (d) From top to bottom, $T/T_F = 0.13, 0.16, 0.18, 0.21, 0.43$. Here, n_{1D} is the two-axis integrated pair center of mass momentum distribution, and the dashed black lines are polylogarithm fits to the thermal wings. The dashed vertical lines in (a)-(c) and the dotted vertical lines in (d) mark the condensate region excluded from the fit ($\approx \pm 0.07k_F$). Here, k_F is the Fermi wavevector in the uniform trap.

As the gas is cooled, the profiles display an increased occupation near zero momentum, and at T_c , a clear condensate peak emerges. We define the condensate fraction N_0/N as the difference in area between the observed profile and the fit to the thermal wings.

- [S1] Z. Yan, P. B. Patel, B. Mukherjee, R. J. Fletcher, J. Struck, and M. W. Zwierlein, (2018).
- [S2] B. Mukherjee, Z. Yan, P. B. Patel, Z. Hadzibabic, T. Yefsah, J. Struck, and M. W. Zwierlein, Phys. Rev. Lett. **118**, 123401 (2017).
- [S3] L. N. Cooper, Phys. Rev. **104**, 1189 (1956).
- [S4] W. Ketterle and M. W. Zwierlein, *Ultra-cold Fermi Gases, Proceedings of the International School of Physics Enrico Fermi, Course CLXIV, Varenna 2006*, edited by M. Inguscio, W. Ketterle, and C. Salomon (IOS Press, Amsterdam, 2008) pp. 247–422.
- [S5] P. Nikolic and S. Sachdev, Phys. Rev. A **75**, 033608 (2007).
- [S6] M. Y. Veillette, D. E. Sheehy, and L. Radzihovsky, Phys. Rev. A **75**, 043614 (2007).
- [S7] W. Zwerger, *Proceedings of the International School of Physics “Enrico Fermi” - Course 191 “Quantum Matter at Ultralow Temperatures”*, edited by M. Inguscio, W. Ketterle, S. Stringari, and G. Roati (IOS Press, Amsterdam; SIF Bologna, 2016) pp. 63–142.
- [S8] M. J. H. Ku, A. T. Sommer, L. W. Cheuk, and M. W. Zwierlein, Science **335**, 563 (2012).

- [S9] M. Randeria and E. Taylor, Annual Review of Condensed Matter Physics **5**, 209 (2014).
- [S10] L. Pisani, P. Pieri, and G. C. Strinati, Phys. Rev. B **98**, 104507 (2018).
- [S11] M. Naraschewski and D. M. Stamper-Kurn, Phys. Rev. A **58**, 2423 (1998).

Appendix D

Universal sound diffusion in a strongly interacting Fermi gas

This appendix contains a reprint of Ref. [149]: Patel, P. B., Yan, Z., Mukherjee, B., Fletcher, R. J., Struck, J., & Zwierlein, M. W. (2020). Universal sound diffusion in a strongly interacting Fermi gas. *Science*, 370(6521), 1222–1226.

QUANTUM GASES

Universal sound diffusion in a strongly interacting Fermi gas

Parth B. Patel^{1,2,3}, Zhenjie Yan^{1,2,3}, Biswaroop Mukherjee^{1,2,3}, Richard J. Fletcher^{1,2,3}, Julian Struck^{1,2,3,4}, Martin W. Zwierlein^{1,2,3*}

Transport of strongly interacting fermions is crucial for the properties of modern materials, nuclear fission, the merging of neutron stars, and the expansion of the early Universe. Here, we observe a universal quantum limit of diffusivity in a homogeneous, strongly interacting atomic Fermi gas by studying sound propagation and its attenuation through the coupled transport of momentum and heat. In the normal state, the sound diffusivity D monotonically decreases upon lowering the temperature, in contrast to the diverging behavior of weakly interacting Fermi liquids. Below the superfluid transition temperature, D attains a universal value set by the ratio of Planck's constant and the particle mass. Our findings inform theories of fermion transport, with relevance for hydrodynamic flow of electrons, neutrons, and quarks.

Transport in fermionic quantum matter lies at the heart of phenomena as varied as superconductivity in cuprates (1) and bilayer graphene (2), inspirals of neutron star binaries (3), and perfect fluidity of the early universe (4). For hydrodynamic flow, transport is governed by diffusion, which facilitates the decay of spatial variations in globally conserved quantities—such as momentum, energy, charge, or spin—at a rate set by the corresponding diffusivity. A ubiquitous example is the attenuation of sound in fluids, where the modulation in current density and temperature causes diffusion of momentum and heat, leading to attenuation of sound at a rate set by the sound diffusivity D . The magnitude and temperature dependence of sound diffusivity reveal many of the characteristic features of the underlying substance.

Kinetic theory yields an estimate of $D \approx v l$, where v is the average velocity of the particles and l is their mean free path, which can vary over many orders of magnitude across substances. However, for strongly interacting quantum liquids and gases, a certain universality of diffusion coefficients may be expected. Here, the mean free path becomes on the order of the interparticle spacing, and the velocity takes on the Heisenberg-limited value $v \sim \hbar/m$, where \hbar is the reduced Planck's constant and m is the particle mass. This leads to a limiting value of $D \sim \hbar/m$, with a numerical prefactor of order unity determined by the specific microscopic interactions. Such Heisenberg-limited values were observed for the spin diffusivity in a unitary Fermi gas (5–7), as well as the momentum

diffusivity (the shear viscosity) in both the quark-gluon plasma of the early Universe and the unitary Fermi gas (4). Notably, the quantum liquids of bosonic ^4He and fermionic ^3He display similar sound diffusivities of $D \sim \hbar/m$ around 4 K (8, 9). However, upon lowering the temperature into the deeply degenerate regime, these two quantum liquids display markedly different behaviors in the damping of sound. Down to about 1 K, the sound attenuation in ^4He does not vary strongly with temperature, decreasing only by a factor of two across the superfluid transition, with a minimum of $D \approx 0.5\hbar/m$ (8, 10). By contrast, ^3He features a diverging diffusivity ($\propto 1/T^2$), characteristic of a Fermi liquid, growing to $\sim 50,000\hbar/m$ around 2 mK, followed by a steep drop at the superfluid transition and settling to a value of $\sim 5000\hbar/m$ (9). A priori, it is unclear whether the temperature dependence of sound attenuation in a strongly interacting, fermionic gas—of atoms, electrons, or neutrons—should resemble that of a quantum liquid, and if so, whether it corresponds more closely to the strongly interacting, but bosonic, liquid ^4He or to the fermionic, but weakly interacting, liquid ^3He .

Ultracold atomic Fermi gases at unitarity are a prototypical strongly interacting quantum fluid for transport experiments (11–15). Featuring a mean free path as short as one interparticle spacing, these systems display the most robust form of fermionic superfluidity and near-perfect hydrodynamic flow even in the normal state (16–18). The presence of scale invariance leads to universality in physics properties (13–15, 19–21), including transport (5, 22–24). The universality directly connects this system to a host of other strongly interacting Fermi systems across all energy and length scales from nuclear matter to neutron stars. For the unitary Fermi gas, scale invariance implies that sound diffusivity must remain the same upon changing all length scales by the same

factor. The diffusivity is thus \hbar/m times a universal function of T/T_F , where the temperature T is normalized by the Fermi temperature T_F that only depends on the particle density n (25). At nondegenerate temperatures $T \gg T_F$, we expect a unitary Boltzmann gas, where the thermal wavelength $\lambda = \sqrt{2\pi\hbar^2/(mk_B T)}$ (k_B , Boltzmann constant) sets both the mean free path and the typical velocity of excitations, $l \sim 1/(n\lambda^2)$ and $v \sim \hbar/(m\lambda)$, implying $D \sim (\hbar/m)(T/T_F)^{3/2}$. In the quantum critical regime of the unitary gas (26, 27), at $T \sim T_F$, the interaction and thermal energies are comparable and even the nature of the equilibrium state is a subject of debate (28, 29). At low temperatures $T \ll T_F$, it remains unknown whether the sound diffusivity diverges as $1/T^2$ (30), as in the Fermi liquid ^3He (31, 32), and whether any sudden drop in the sound diffusion occurs upon entering the superfluid regime. Calculation of such transport parameters is very difficult; for example, predictions for the shear viscosity vary from zero (33), as suggested by experiments on expanding inhomogeneous gases (22, 24), to infinity if phonon damping dominates (23, 34–36).

Transport experiments on Fermi gases have thus far used harmonic traps (15) or terminal configurations (37, 38) and have been used to probe collective oscillations (39–41), spin transport (5, 7, 42), viscosity (22), conductivity (37), and Josephson oscillations (38). However, obtaining transport coefficients of homogeneous matter from inhomogeneous samples in atom traps requires sophisticated analysis and assumptions on the spatial flow profile (5, 22, 43). With the recent advent of optical box traps (44–47), it is now possible to directly probe the transport properties of homogeneous quantum gases (47–50). The gas is then in the same state throughout, and transport properties are identical across the system.

Measurements of transport properties involve the response of a system to an external drive. In linear response, an applied potential change δV couples to perturbations in the fluid density $\delta n = -\chi\delta V$ by the density response function χ . Sound corresponds to a resonant response, that is, a pole in χ at a frequency $\omega = ck$, set by the speed of sound c and wave number k , in the vicinity of which $\chi(\omega, k) \sim 1/(\omega^2 - c^2k^2 + i\Gamma\omega)$ (51, 52). Here, i is the unit imaginary number and Γ is the damping rate of sound, given by $\Gamma = Dk^2$ (53) for hydrodynamic systems. Measurements of χ and Γ thus directly provide the sound diffusivity. Experiments involving liquid helium have used a number of techniques to measure χ , from free decay of resonant modes in a cylindrical resonator (8, 9) to Brillouin scattering off of sound waves (54).

In our homogeneous quantum gas, the constant background density enables an ideal realization of a density response measurement

¹Department of Physics, Massachusetts Institute of Technology, Cambridge, MA 02139, USA. ²MIT-Harvard Center for Ultracold Atoms, Cambridge, MA 02139, USA. ³Research Laboratory of Electronics, Massachusetts Institute of Technology, Cambridge, MA 02139, USA. ⁴Département de Physique, Ecole Normale Supérieure/PSL Research University, CNRS, 24 rue Lhomond, 75005 Paris, France.

*Corresponding author. Email: zwierlein@mit.edu

(Fig. 1A). We use an equal two-state mixture of ${}^6\text{Li}$ atoms with resonant interstate interactions, confined to a cylindrical optical box potential composed of three repulsive laser beams: a hollow cylindrical beam providing the radial confinement (radius 60 μm) and two sheets of light serving as endcaps (length $L \sim 100 \mu\text{m}$) (45). The number $N \sim 10^6$ of atoms per spin state yields a Fermi energy of $E_F = \hbar^2 k_F^2 / (2m) \sim \hbar \times 10 \text{ kHz}$. To inject sound waves, we sinusoidally modulate the intensity of one endcap beam, which drives the gas at a well-defined frequency ω , and a wide range of spatial wave numbers, Fourier limited by the width $\sim 4 \mu\text{m}$ of the endcap potential's edge (55). At the given driving frequency, the resonant sound response of the gas is dominated by a specific wave number $k = \omega/c$, resulting in a traveling wave of sound. An in situ absorption image is taken after an evolution time sufficiently short such that no reflections occur, and the resonant wave number k is directly measured (Fig. 1B, ii to iv). By repeating this protocol for different drive frequencies, we obtain the dispersion relation $\omega(k)$ for wave numbers $k < 0.14k_F$ (Fig. 1C). It is linear within our measurement error, corresponding to a constant speed of sound $c = \omega/k$ as a function of wave number. We note that at wavelengths approaching the interparticle spacing, and thus at momenta $\hbar k$ approaching the Fermi momentum ($k \sim k_F$), deviations from linear sound dispersion are expected for the unitary Fermi gas (56).

The precise measurement of the speed of sound allows a sensitive test of scale invariance of the unitary Fermi gas. In general, the speed of isentropic sound propagation c is directly tied to the equation of state by the hydrodynamic relation $mc^2 = (\partial P/\partial n)_S = (V^2/N)(\partial^2 E/\partial V^2)|_S$. Here, E is the energy, S is the entropy, V is the volume, and $P = -(\partial E/\partial V)|_S$ is the pressure of the gas. A notable property of all nonrelativistic scale invariant systems in three dimensions is that their total energy scales as $E \propto V^{-2/3}$; this follows from the scaling behavior $E \rightarrow E/\lambda^2$ under dilation of space by a factor λ . This directly yields $mc^2 = (10/9)E/N$, independent of temperature or the phase of matter. In Fig. 1D, we show the measured speed of sound as a function of the energy per particle E/N , obtained from an isoenergetic expansion of the gas from the box into a harmonic trap (57). For both superfluid and normal samples (blue and red, respectively), the scale invariant prediction (solid black line) captures the data well with no free parameters. This demonstrates the universality of the speed of sound and scale invariance in the unitary Fermi gas in the explored window of temperature.

The attenuation of sound is already apparent in the spatial decay of the traveling waves shown in Fig. 1. For a precision measurement

of the sound diffusivity, we now turn to the steady-state response of the system to a continuous drive, which directly reveals the density response function χ . The intensity of one of the endcaps is modulated for a sufficiently long time such that the density evolution has reached a steady state. After an integer number of driving cycles, the spatial Fourier transform of the density yields the out-of-phase response of the system, or $\text{Im}[\chi(\omega, k)]$ (55). This quantity also gives the average power absorbed by the system for a drive at frequency ω and spatial frequency k , and thus directly reveals the poles of χ as resonances.

The measurements are summarized in Fig. 2. Each row of pixels in Fig. 2B shows the fractional density modulation at a particular drive frequency after integration along the radial axis. This “sonogram” reveals discrete normal modes, the first five of which are shown in Fig. 2A. The spatial Fourier transform, giving the out-of-phase response function, is shown in Fig. 2C. For each normal mode in the box, it features a peak at $\omega = ck$. The sound attenuation rate can be seen to increase with k , revealed in both a broadened frequency response as well as a reduced peak height.

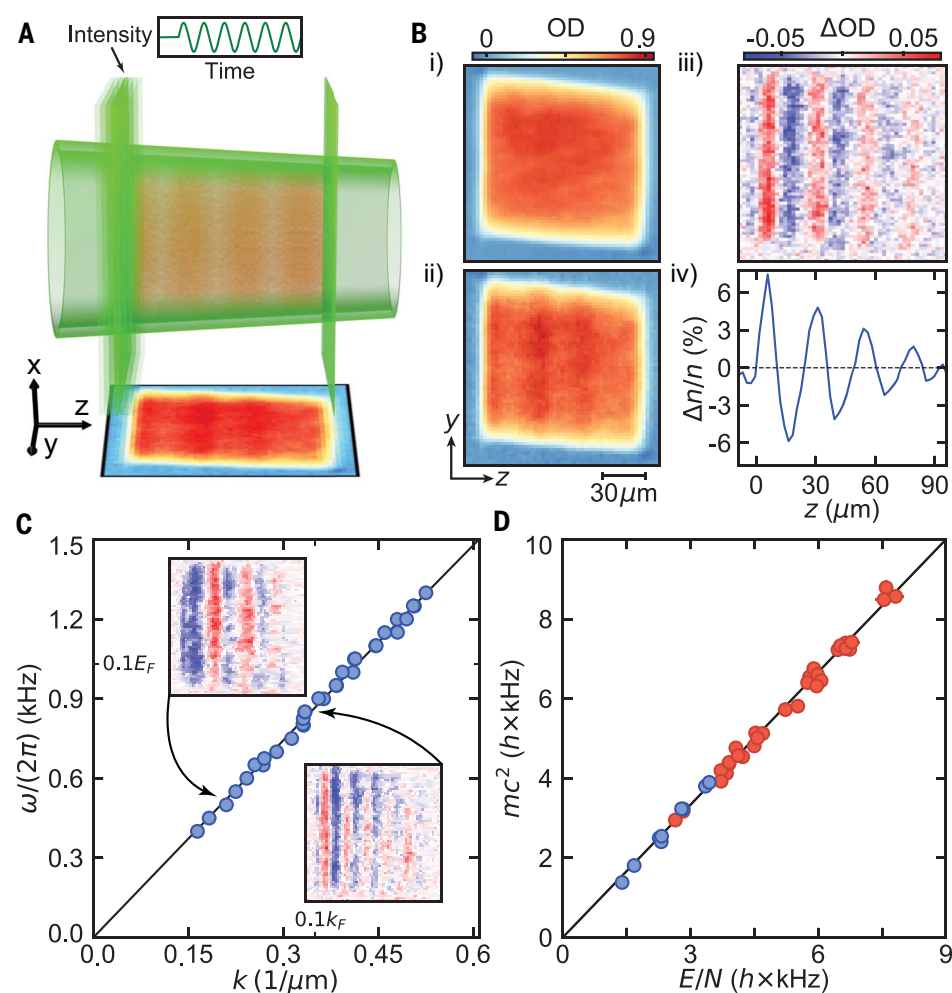


Fig. 1. Sound waves in a homogeneous unitary Fermi gas. (A) Fermionic ${}^6\text{Li}$ atoms are trapped in a three-dimensional cylindrical box made from green laser beams. Sound is excited by modulating the intensity of one of the laser walls. (B) The resulting density wave is observed via an in situ absorption image, shown as optical density (OD) for both an unperturbed (i) and modulated (ii) sample. Here, the modulation frequency is $2\pi \times 600 \text{ Hz}$. Taking their difference (iii) and integrating along the homogeneous radial trap axis reveals (iv) a perturbation in the fractional density difference $\Delta n/n$, propagating along the axial direction z and exhibiting a well-defined wave number k corresponding to the applied modulation frequency ω . (C) Dispersion of sound $\omega(k)$. The fitted slope (black line) provides the speed of sound. The insets display sound waves observed at $\omega = 2\pi \times 600 \text{ Hz}$ and $\omega = 2\pi \times 850 \text{ Hz}$. Errors in the measured k are smaller than the point size. (D) Measurement of the universal relation between the measured speed of sound and the energy-per-particle E/N (see text). The black solid line shows the predicted linear dependence for any nonrelativistic scale invariant system in three dimensions; $mc^2 = \frac{10}{9}E/N$. Data are shown for both the normal (red) and the superfluid (blue) phase.

The density response $\text{Im}[\chi(\omega, k_j)]$ at the wave number $k_j = j\pi/L$ of the j^{th} normal mode of the box is shown in Fig. 3A, along with Lorentzian fits (solid lines). The full-width at half-maximum yields the damping rate of sound Γ , which is shown as a function of k in Fig. 3B, for gases both above (red and green) and below (blue) the superfluid transition. At temperatures above the superfluid transition temperature $T_C = 0.17T_F$ (20), we observe $\Gamma(k)$ to increase quadratically with k for all explored wave numbers ($k \lesssim 0.3 mc/\hbar$). This establishes diffusive damping of sound in the normal regime, as expected in the collisionally hydrodynamic regime (16, 58).

Below the superfluid transition temperature, $T < T_C$, we observe a crossover from quadratic scaling of $\Gamma(k)$ at wave numbers $k \lesssim 0.2mc/\hbar$ to linear behavior, indicating a departure from purely hydrodynamic transport at high wave numbers. This is expected when the modulation frequency becomes comparable to the damping rate of thermal phonons Γ_{ph} (36, 59). Collisionless or Landau damping of sound is caused by nonlinearities resulting from the kinetic energy density carried by sound and the density dependence of the speed of sound. Fermi's golden rule yields a rate $\Gamma_{\text{ph}} \propto k$ (36, 51) proportional to the energy $\hbar ck$ carried by a phonon. Including a nonzero damping rate of phonons Γ_{ph} yields a crossover from hydro-

dynamic to collisionless damping as the sound frequency ck exceeds Γ_{ph} (59). The relation $\Gamma = Dk^2 f(ck/\Gamma_{\text{ph}})$ with $f(x) = \tan^{-1}(x)/x$ (59) shows a good agreement with the data (solid line). The scale of the fitted relaxation rate $\Gamma_{\text{ph}} = 0.27(8)k_B T/\hbar$ is on the order of the gas temperature, hinting toward quantum critical damping (27). We note that the observation of quadratic scaling of Γ with k at low wave numbers implies that sound is primarily attenuated in the bulk, and that edge effects are negligible (53, 60).

As the main result of this work, we present in Fig. 4 the sound diffusivity D of the unitary Fermi gas. This is obtained as $D = \Gamma/k^2$ using the $j = 2$ normal mode, for which ck/Γ_{ph} is always less than 0.25, ensuring that it is well described by a hydrodynamic framework. The measured values are shown in units of \hbar/m and, at low temperatures, exhibit a numerical prefactor ~ 1 . This demonstrates universal sound diffusion, with no dependence on microscopic parameters of the gas.

Generally, the sound diffusivity contains contributions from both the bulk and shear viscosity, ζ and η , respectively (which damp momentum gradients), and the thermal conductivity κ (which damps temperature gradients) (53). However, for a scale-invariant fluid, the bulk viscosity vanishes (61) and $D = D_\eta + D_\kappa$ only, with $D_\eta = 4\eta/(3mn)$ and

$D_\kappa = 4\kappa T/(15P)$ (55). We note that our measurements of D therefore constrain the relationship between the viscosity and thermal conductivity, which is usually quantified by the Prandtl number $\text{Pr} = c_p\eta/\kappa$ (53), where c_p is the specific heat at constant pressure (55).

The solid black line in Fig. 4 shows a prediction $D = 6.46 (\hbar/m)(T/T_F)^{3/2}$, which uses the high-temperature results for viscosity (23, 62) and thermal conductivity (23, 25), along with the ideal gas equation of state. This simple model captures the high-temperature behavior well without any free parameters. However, it is expected to underestimate D when $T/T_F \lesssim 1$ because it neglects the suppression of scattering arising from Pauli blocking.

As the temperature is reduced, D smoothly drops to a value $\sim \hbar/m$, consistent with Heisenberg-limited diffusivity. Notably, at intermediate temperatures, we observe neither the $D \sim 1/T^2$ scaling typical of a Fermi liquid nor any sudden change at the superfluid transition. This is further demonstrated by the inset of Fig. 4, where we show a magnified plot of D (blue points) in the vicinity of the superfluid transition (vertical red line) (20). Also shown is the pair condensate fraction (red points) obtained from the measured pair center-of-mass momentum distribution (63), which

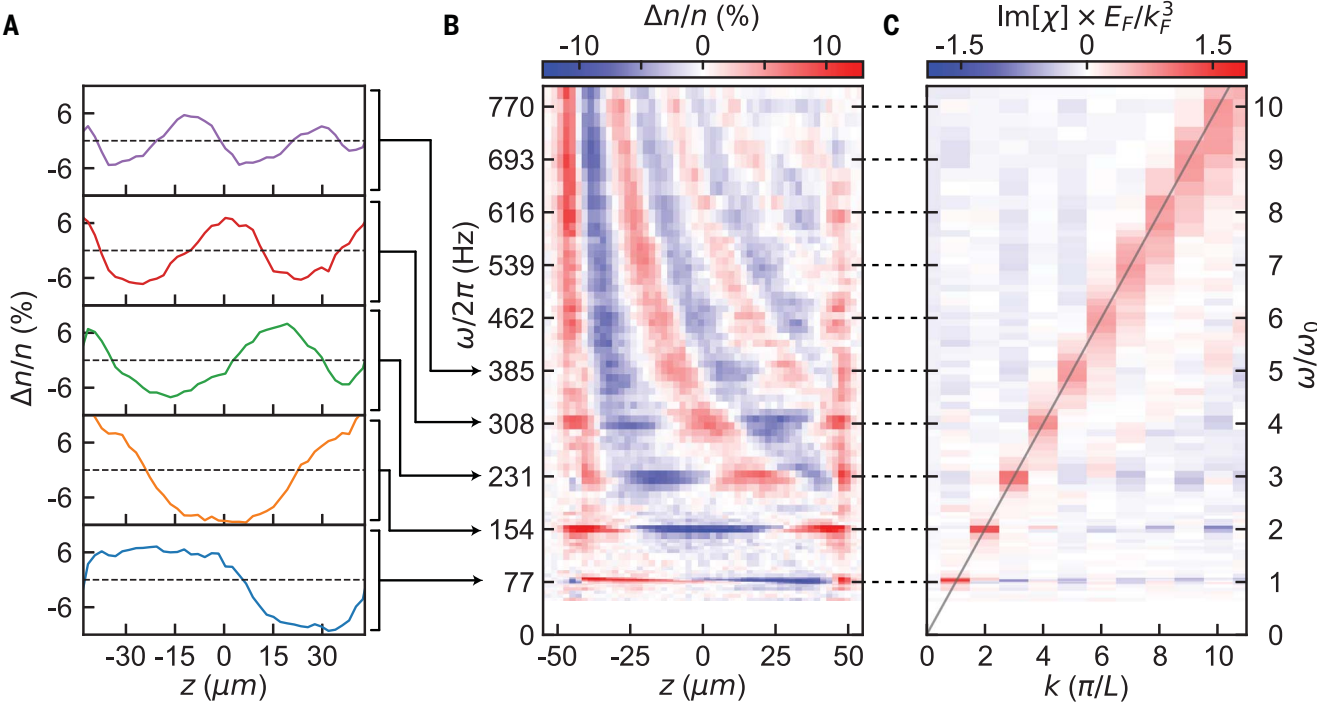


Fig. 2. Normal modes of the cylindrical box trap. (A and B) The steady-state density response of the gas is obtained by modulating the container walls at frequency ω for 30 cycles of the drive. Standing waves of sound corresponding to the normal modes in the box are observed at frequencies $\omega_j = j\pi c/L \approx 2\pi j \times 77\text{Hz}$ (where $j \in \mathbb{Z}$), the first five of which are shown in (A). The full sonogram is shown in (B). Here, each row of pixels corresponds to a particular realization of the experiment at a given frequency. (C) The spatial Fourier transform directly yields the density response function $\text{Im}[\chi(k, \omega)]$. It reveals well-defined resonance peaks exhibiting both the linear dispersion of sound and increasing widths in frequency at higher wave numbers, corresponding to increased rates of sound attenuation.

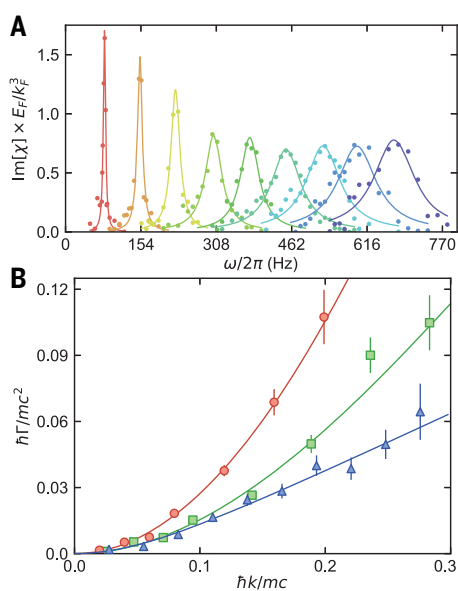


Fig. 3. Spectral response of sound and its attenuation rate. (A) The imaginary part of the density response function at each normal mode wave number k_j displays a well-defined peak in frequency, whose full-width at half-maximum yields the mode damping rate Γ . This is obtained from a Lorentzian fit, shown by solid lines. (B) Damping rate $\Gamma(k)$ for gas temperatures $T/T_F = 0.36(5)$ (red circles), $T/T_F = 0.21(3)$ (green squares), and $T/T_F = 0.13(2)$ (blue triangles). For all temperatures, $\Gamma(k)$ displays a quadratic scaling at low momenta characteristic of diffusive damping. For our coldest samples, as k increases, we observe a deviation from this behavior, revealed by a crossover to linear scaling. At all temperatures and wave numbers, our data are well captured by the model of (59) (solid lines), which accounts for the finite relaxation rate of the fluid. Error bars represent 1σ statistical uncertainty.

serves as both an indicator of superfluidity and a robust thermometer in the superfluid phase (15). Despite the definitive onset of pair condensation, we observe no measurable sharp feature in the diffusivity, which remains approximately constant as the temperature is reduced. Our nonvanishing diffusivity therefore contrasts previous measurements of a vanishing viscosity in the low-temperature limit (24).

This behavior can qualitatively be understood as follows. In the superfluid phase, viscosity arises entirely from the normal component, giving a diffusivity $D \sim (n_n/n)lv$ where $l = 1/(n_n\sigma)$ is the mean free path of a typical excitation with scattering cross section σ , velocity v , and density n_n (30, 64). The dependence on the (strongly temperature-dependent) n_n therefore cancels, giving $D \sim v/(\sigma n)$. At the temperatures studied here, the normal component is dominated by broken pairs (15), whose velocity and cross section are only weakly

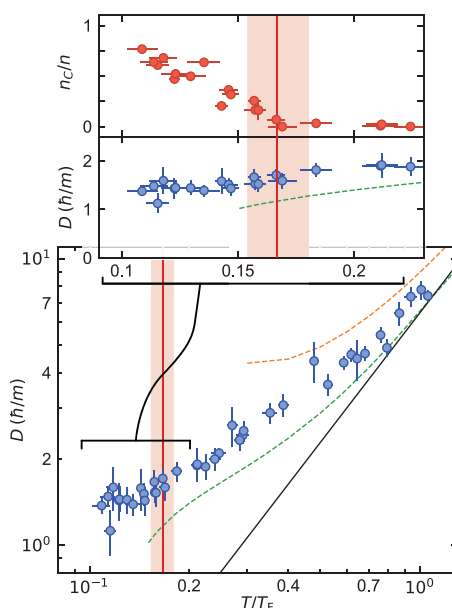


Fig. 4. Temperature dependence of the sound diffusivity. For temperatures comparable to the Fermi temperature, the sound diffusivity (D , normalized by \hbar/m ; blue circles) approaches the expected high-temperature scaling of $T^{3/2}$ (solid black line). As the temperature is lowered, D decreases monotonically and attains a quantum-limited value close to \hbar/m . Below the superfluid transition [vertical red line, from (20)], D is observed to be almost independent of temperature and condensate fraction (n_c/n , red circles in inset). From the transition temperature ($n_c/n = 0$) to the coldest temperatures ($n_c/n \sim 0.8$), the changes in D are within the standard error of the measurements. Theoretical predictions for D are as follows: The dashed orange line is from the sound attenuation length calculated in the framework of kinetic theory (25), and the dashed green line is from a calculation of shear viscosity (23), assuming a Prandtl number of 2/3. Bars denote statistical error arising from the uncertainty in Γ . Additionally, the dominant systematic uncertainty in D is an error of 13% arising from the nonzero width of the endcaps. The red shaded regions represent the uncertainty in the superfluid transition temperature (20).

temperature-dependent. Broken pairs are primarily formed at the Fermi surface, which is broadened by the pairing gap Δ . This results in a typical velocity $v \sim \hbar k_F/m$ and cross section $\sigma \sim k_F^{-2}(\Delta/E_F)^2$, where the $(\Delta/E_F)^2$ accounts for the restriction of phase space available for scattering arising from Pauli blocking. In the unitary Fermi gas, $\Delta \sim 0.4E_F$ (41, 65), giving a diffusivity $D \sim \hbar/m$, consistent with our observations. By contrast, the pairing gap in ${}^3\text{He}$ is $\Delta \sim 10^{-3}E_F$, leading to a much larger value of $D \sim 5000\hbar/m$ (60, 66).

We have measured the sound diffusivity of the unitary Fermi gas. The diffusivity ap-

proaches a Heisenberg-limited value of \hbar/m at low temperatures, similar to the strongly interacting, bosonic quantum fluid ${}^4\text{He}$. In contrast to Fermi liquid behavior seen in weakly interacting fermionic systems, the diffusivity monotonically increases with increasing temperatures and eventually follows the high-temperature behavior $D \sim \hbar/m(T/T_F)^{3/2}$. The measured sound diffusivity constrains the shear viscosity and thermal conductivity of the unitary Fermi gas. In particular, combined with the calculated shear viscosity in (23), we find a Prandtl number strictly lower than unity for all explored temperatures (55). This excludes the existence of a relativistic conformal gravity dual of the unitary Fermi gas (67), because this would require $\text{Pr} = 1$. Thanks to the scale invariance of the unitary Fermi gas, the results obtained here apply broadly to other strongly interacting forms of fermionic matter, from hydrodynamic electron flow to nuclei and neutron matter.

REFERENCES AND NOTES

- P. A. Lee, N. Nagaosa, X.-G. Wen, *Rev. Mod. Phys.* **78**, 17–85 (2006).
- Y. Cao et al., *Nature* **556**, 43–50 (2018).
- M. G. Alford, L. Bovard, M. Hanuske, L. Rezzolla, K. Schwenzer, *Phys. Rev. Lett.* **120**, 041101 (2018).
- A. Adams, L. D. Carr, T. Schäfer, P. Steinberg, J. E. Thomas, *New J. Phys.* **14**, 115009 (2012).
- A. Sommer, M. Ku, G. Roati, M. W. Zwierlein, *Nature* **472**, 201–204 (2011).
- A. B. Bardon et al., *Science* **344**, 722–724 (2014).
- C. Luciuk et al., *Phys. Rev. Lett.* **118**, 130405 (2017).
- K. H. Bennemann, J. B. Ketterson, *The Physics of Liquid and Solid Helium* (Wiley, 1976).
- D. Vollhardt, P. Wölfle, *The Superfluid Phases of Helium 3* (Dover Publications, Inc., 2013).
- V. S. L'vov, L. Skrbek, K. R. Sreenivasan, *Phys. Fluids* **26**, 041703 (2014).
- W. Ketterle, M. W. Zwierlein, in *Ultra-cold Fermi Gases*, vol. 164 of *Proceedings of the International School of Physics "Enrico Fermi"*, M. Inguscio, W. Ketterle, C. Salomon, Eds. (IOS Press, 2007), pp. 95–287.
- I. Bloch, J. Dalibard, W. Zwerger, *Rev. Mod. Phys.* **80**, 885–964 (2008).
- S. Giorgini, L. P. Pitaevskii, S. Stringari, *Rev. Mod. Phys.* **80**, 1215–1274 (2008).
- W. Zwerger, Ed., *The BCS-BEC Crossover and the Unitary Fermi Gas* (Springer, 2012).
- M. W. Zwierlein, *Novel Superfluids* (Oxford Univ. Press, 2014), pp. 269–422.
- K. M. O'Hara, S. L. Hemmer, M. E. Gehm, S. R. Granade, J. E. Thomas, *Science* **298**, 2179–2182 (2002).
- A. Altmeier et al., *Phys. Rev. Lett.* **98**, 040401 (2007).
- M. K. Tey et al., *Phys. Rev. Lett.* **110**, 055303 (2013).
- T.-L. Ho, *Phys. Rev. Lett.* **92**, 090402 (2004).
- M. J. H. Ku, A. T. Sommer, L. W. Cheuk, M. W. Zwierlein, *Science* **335**, 563–567 (2012).
- M. Randeria, E. Taylor, *Annu. Rev. Condens. Matter Phys.* **5**, 209–232 (2014).
- C. Cao et al., *Science* **331**, 58–61 (2011).
- T. Enss, R. Haussmann, W. Zwerger, *Ann. Phys.* **326**, 770–796 (2011).
- J. A. Joseph, E. Elliott, J. E. Thomas, *Phys. Rev. Lett.* **115**, 020401 (2015).
- M. Braby, J. Chao, T. Schäfer, *Phys. Rev. A* **82**, 033619 (2010).
- P. Nikolić, S. Sachdev, *Phys. Rev. A* **75**, 033608 (2007).
- T. Enss, *Phys. Rev. A* **86**, 013616 (2012).
- S. Nascimbène et al., *Phys. Rev. Lett.* **106**, 215303 (2011).
- I. Z. Rothstein, P. Shrivastava, *Phys. Rev. B* **99**, 035101 (2019).

30. H. Smith, H. H. Jensen, *Transport Phenomena* (Clarendon, 1989).
31. M. A. Black, H. E. Hall, K. Thompson, *J. Phys. C Solid State Phys.* **4**, 129–142 (1971).
32. C. N. Archie, T. A. Alvesalo, J. D. Reppy, R. C. Richardson, *J. Low Temp. Phys.* **42**, 295–332 (1981).
33. H. Guo, D. Wu, C.-C. Chien, K. Levin, *New J. Phys.* **13**, 075011 (2011).
34. G. Rupak, T. Schäfer, *Phys. Rev. A* **76**, 053607 (2007).
35. M. Mannarelli, C. Manuel, L. Tolos, *Ann. Phys.* **336**, 12–35 (2013).
36. H. Kurkjian, Y. Castin, A. Sinatra, *Ann. Phys.* **529**, 1600352 (2017).
37. S. Krinner, T. Esslinger, J.-P. Brantut, *J. Phys. Condens. Matter* **29**, 343003 (2017).
38. G. Valtolina et al., *Science* **350**, 1505–1508 (2015).
39. M. Bartenstein et al., *Phys. Rev. Lett.* **92**, 203201 (2004).
40. J. Kinast, S. L. Hemmer, M. E. Gehm, A. Turlapov, J. E. Thomas, *Phys. Rev. Lett.* **92**, 150402 (2004).
41. S. Hoinka et al., *Nat. Phys.* **13**, 943–946 (2017).
42. M. Koschorreck, D. Pertot, E. Vogt, M. Köhl, *Nat. Phys.* **9**, 405–409 (2013).
43. M. Bluhm, J. Hou, T. Schäfer, *Phys. Rev. Lett.* **119**, 065302 (2017).
44. A. L. Gaunt, T. F. Schmidutz, I. Gotlibovich, R. P. Smith, Z. Hadzibabic, *Phys. Rev. Lett.* **110**, 200406 (2013).
45. B. Mukherjee et al., *Phys. Rev. Lett.* **118**, 123401 (2017).
46. K. Hueck et al., *Phys. Rev. Lett.* **120**, 060402 (2018).
47. L. Baird, X. Wang, S. Roof, J. E. Thomas, *Phys. Rev. Lett.* **123**, 160402 (2019).
48. N. Navon, A. L. Gaunt, R. P. Smith, Z. Hadzibabic, *Nature* **539**, 72–75 (2016).
49. J. L. Ville et al., *Phys. Rev. Lett.* **121**, 145301 (2018).
50. S. J. Garratt et al., *Phys. Rev. A (Coll. Park)* **99**, 021601 (2019).
51. P. C. Hohenberg, P. C. Martin, *Ann. Phys.* **34**, 291–359 (1965).
52. P. C. Hohenberg, *J. Low Temp. Phys.* **11**, 745–750 (1973).
53. L. D. Landau, E. M. Lifshitz, *Fluid Mechanics* (Elsevier, 1959).
54. J. A. Tarvin, F. Vidal, T. J. Greytak, *Phys. Rev. B* **15**, 4193–4210 (1977).
55. See supplementary materials.
56. H. Kurkjian, Y. Castin, A. Sinatra, *Phys. Rev. A* **93**, 013623 (2016).
57. Z. Yan et al., *Phys. Rev. Lett.* **122**, 093401 (2019).
58. M. J. Wright et al., *Phys. Rev. Lett.* **99**, 150403 (2007).
59. C. J. Pethick, D. Ter Haar, *Physica* **32**, 1905–1920 (1966).
60. G. Eska et al., *Phys. Rev. Lett.* **44**, 1337–1340 (1980).
61. D. T. Son, *Phys. Rev. Lett.* **98**, 020604 (2007).
62. G. M. Bruun, H. Smith, *Phys. Rev. A* **72**, 043605 (2005).
63. B. Mukherjee et al., *Phys. Rev. Lett.* **122**, 203402 (2019).
64. C. J. Pethick, H. Smith, P. Bhattacharyya, *Phys. Rev. B* **15**, 3384–3400 (1977).
65. A. Schirotzek, Y. I. Shin, C. H. Schunck, W. Ketterle, *Phys. Rev. Lett.* **101**, 140403 (2008).
66. Y. A. Ono, J. Hara, K. Nagai, *J. Low Temp. Phys.* **48**, 167–188 (1982).
67. M. Rangamani, S. F. Ross, D. Son, E. G. Thompson, *J. High Energy Phys.* **2009**, 075 (2009).
68. P. B. Patel et al., Replication data for: Universal sound diffusion in a strongly interacting Fermi gas. Harvard Dataverse (2020); <https://doi.org/10.7910/DVN/UVM2KN>.

ACKNOWLEDGMENTS

We thank Y. Castin, T. Enss, T. Schäfer, C. J. Vale, and W. Zwerger for helpful discussions. **Funding:** This work was supported by the National Science Foundation (Center for Ultracold Atoms award nos. PHY-1734011 and PHY- 1506019), U.S. Air Force Office of Scientific Research (FA9550-16-1-0324 and MURI Quantum Phases of Matter FA9550-14-1-0035), U.S. Office of Naval Research (N00014-17-1-2257), and the David and Lucile Packard Foundation. J.S. was supported by LabEX ENS-ICFP: ANR-10-LABX-0010/ANR-10-IDEX-0001-02 PSL*. **Author contributions:** P.B.P., Z.Y., and J.S. performed the experimental measurements and data analysis. All authors contributed to the interpretation of the data and the preparation of the manuscript. **Competing interests:** The authors declare no competing interests. **Data and materials availability:** All data shown in this work can be found at Harvard Dataverse (68).

SUPPLEMENTARY MATERIALS

science.sciencemag.org/content/370/1222/suppl/DC1
Materials and Methods
Supplementary Text
Figs. S1 and S2
References (69–73)

20 September 2019; accepted 24 October 2020
10.1126/science.aaz5756

Supplementary Materials for **Universal sound diffusion in a strongly interacting Fermi gas**

Parth B. Patel, Zhenjie Yan, Biswaroop Mukherjee, Richard J. Fletcher,
Julian Struck, Martin W. Zwierlein*

*Corresponding author. Email: zwierlei@mit.edu

Published 4 December 2020, *Science* **370**, 1222 (2020)
DOI: 10.1126/science.aaz5756

This PDF file includes:

Materials and Methods
Supplementary Text
Figs. S1 and S2
References

Materials and Methods

The strongly interacting unitary Fermi gas was realized using an equal mixture of the first and third lowest hyperfine states of ${}^6\text{Li}$, $|1\rangle = |m_J = -\frac{1}{2}, m_I = 1\rangle$ and $|3\rangle = |-\frac{1}{2}, -1\rangle$ respectively, with magnetic fields tuned to an interstate Feshbach resonance centered at ~ 690 G (69, 70). The temperature and density were calibrated using the measured equation of state (20).

Sound waves were generated by sinusoidally modulating the intensity of one of the endcap laser sheets with sharpness $\sim 4 \mu\text{m}$ (45). This drives the gas at a wide range of wavenumbers ($k \lesssim 0.5 \mu\text{m}^{-1}$ or $k/k_F \lesssim 0.15$) simultaneously. The sound wave amplitude $\Delta n/n$ was deliberately kept below 10% to ensure that the response is in the linear regime and the local velocity $v = (\Delta n/n) c$ is smaller than the critical velocity.

Supplementary Text

Thermal conductivity and Prandtl number.

Within hydrodynamics, the change in the energy of a sound wave is given by $\dot{E} = -Dk^2 E$ with $D = 4\eta/(3\rho) + \alpha^2 c^2 \kappa T / (\rho c_P^2)$ (53). Here $\alpha = (1/V)(\partial V / \partial T)|_P$ is the thermal expansivity and $\rho = mn$ is the mass density. The scale invariance of the unitary Fermi gas implies $c^2 = 5P/(3\rho)$ and $c_P = 5P\alpha/(2\rho)$ (15), which simplifies the sound diffusivity to $D = 4\eta/(3\rho) + 4\kappa T/(15P)$, valid at all temperatures above T_c . Below T_c , coupling to the second sound increases the contribution from viscosity by $\sim 30\%$ for the unitary Fermi gas (51).

Our measurements of the sound diffusivity constrain the value of the viscosity and thermal conductivity according to $D = D_\eta + D_\kappa$, where $D_\eta = 4\eta/(3\rho)$ and $D_\kappa = 4\kappa T/(15P)$. For example, the thermal conductivity $\kappa = (D - D_\eta)(15P)/(4T)$ can be calculated from the sound diffusivity D if the equation of state and viscosity are known. We calculate the thermal con-

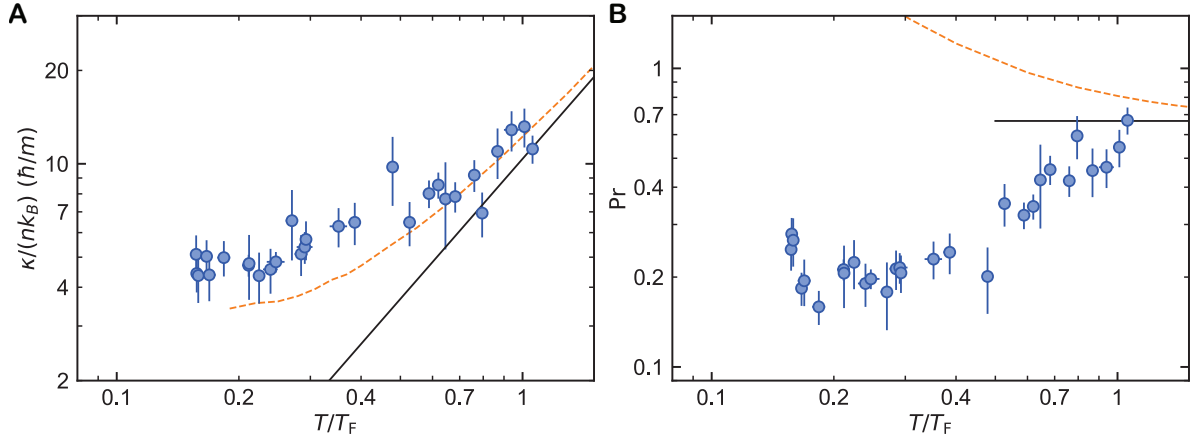


Figure S1: Thermal conductivity and Prandtl number. For temperatures comparable to the Fermi temperature ($T \sim T_F$), the thermal conductivity (**A**; $\kappa/(nk_B)$, normalized by \hbar/m ; blue circles) approaches the expected high temperature scaling $T^{3/2}$ (solid black line) as the Prandtl number (**B**; Pr ; blue circles) approaches the predicted high temperature value of $2/3$ (solid black line). The orange dashed line in both **A** and **B** are theoretical predictions calculated in the framework of kinetic theory (25).

ductivity κ (Fig. S1A) and Prandtl number $\text{Pr} = c_P\eta/\kappa$ (Fig. S1B) using the measured sound diffusivity, the experimental equation of state (20), and a theoretical calculation for the shear viscosity η above T_c (23), performed within the same framework that gave excellent agreement with the experimental equation of state (20). Similar to the sound diffusivity and viscosity, the thermal conductivity increases with temperature as $T^{3/2}$ for $T \gg T_F$. The solid black line in Fig. S1A shows the limiting behavior $\kappa/(nk_B) = 10.38 (\hbar/m) (T/T_F)^{3/2}$ for the thermal conductivity at high temperatures (25), which captures our data well without any free parameters.

The Prandtl number, Pr , quantifies the relative importance of viscosity and thermal conductivity for the attenuation of sound in fluids. For compressible fluids such as air, both the viscosity and the thermal conductivity play an important role in the diffusion of sound, resulting in Pr being close to unity. In contrast, for incompressible fluids such as water, thermal gradients associated with sound waves are minimal, resulting in a $\text{Pr} \gg 1$. The unitary Fermi gas is a compressible fluid, whose Pr is predicted to reach the classical limit of $2/3$ at high

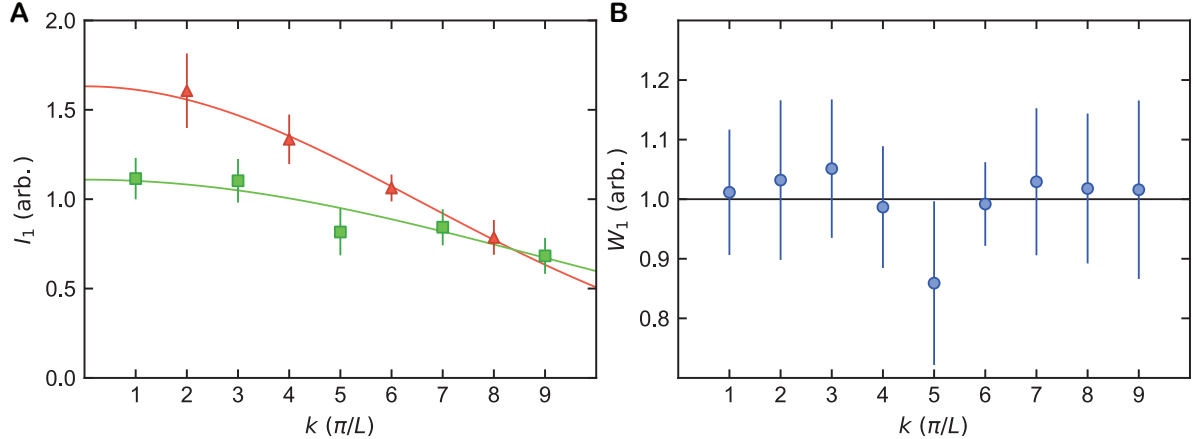


Figure S2: Weight of the first-sound mode in χ . (A) Integral over the density response $I_1(k) = \int d\omega \delta n(\omega, k)/\omega$ for even (red triangles) and odd (green square) modes. They are fit with a Gaussian function (solid lines) which models the drive $V_0(k)$. (B) The weight of the first sound in the density response function $W_1(k) = \int d\omega \text{Im}[\chi(\omega, k)]/\omega$ calculated from the measured I_1 and the modelled drive potential, $W_1(k) = I_1(k)/V_0(k)$.

temperatures (25). Our data indeed approach this value at high temperatures. We find the P_r to be significantly below 1 at all temperatures, excluding the existence of a relativistic conformal gravity dual of the unitary Fermi gas (67).

The response function χ and its normalization

The response function χ relates the perturbations in a fluid's number density to the applied external potential, $\delta n(\omega, k) = \chi(\omega, k)V(\omega, k)$ (51). With knowledge of χ , the density response of a fluid to an arbitrary external perturbation can be calculated via a Fourier transform, $\delta n(t, x) = \int \frac{d\omega'}{2\pi} e^{-i\omega' t} \int \frac{dk}{2\pi} e^{-ikx} \chi(\omega', k)V(\omega', k)$. For example, the density response to a sinusoidal drive $V(\omega', k) = -i\pi V_0(k)(\delta(\omega' + \omega) - \delta(\omega' - \omega))$, with frequency ω and amplitude $V_0(k)$, is

$$\delta n(t, k) = V_0(k) \sin(\omega t) \text{Re}[\chi(\omega, k)] - V_0(k) \cos(\omega t) \text{Im}[\chi(\omega, k)].$$

Similar to a classical harmonic oscillator, the in-phase and out-of-phase density responses are proportional to $\text{Re}[\chi]$ and $\text{Im}[\chi]$ respectively, providing an experimentally convenient tool to

measure the density response function. Data shown in Fig. 2 were taken after 30 complete cycles of the $\sin(\omega t)$ drive, which was found to be sufficiently long to reach a steady state of the density evolution at all frequencies and temperatures explored. During this drive, the energy injected by the external potential is less than 4% of the energy of the system.

In the vicinity of a sound mode ($\omega \sim ck$), the response of the fluid can be well modeled by a damped driven harmonic oscillator with a resonance frequency $\omega_0 = ck$ and damping rate Γ (51). The equation of motion of a harmonic oscillator implies a response function $\chi \sim 1/(\omega^2 - \omega_0^2 + i\Gamma\omega)$ whose imaginary part, $\text{Im}[\chi] \sim 1/((\omega - \omega_0)^2 + \Gamma^2)$, has a Lorentzian peak with full-width-at-half-maximum Γ centered at $\omega = \omega_0$.

In general, the response function χ for a unitary Fermi gas is given by two-fluid hydrodynamics, as discussed in Refs. (51, 52, 71). Fixing k , the function $\text{Im}(\chi(\omega, k))/\omega$ contains in general two peaks: one is centered at the first-sound resonance, corresponding to predominantly density waves. The second peak is present when thermal gradients can cause density gradients, which occurs for non-zero expansivity α or equivalently for a specific heat ratio $c_P/c_V \neq 1$. In the normal state, the second peak occurs at zero frequency, corresponding to purely diffusive heat transport coupled to density. In the superfluid regime, this peak moves to finite frequency, corresponding to the emergence of second sound. It is predominantly (for c_P/c_V not far from 1) a temperature wave that propagates ballistically (72, 73).

An exact sum rule relates the integral of $\text{Im}(\omega, k)/\omega$ to the isothermal compressibility (51, 71). The integral $W_1 = \int d\omega \text{Im}[\chi(\omega, k)]/\omega$ over only the first-sound peak is $n\pi/(2mc^2)$, related to the speed of sound and thus the isentropic compressibility, independent of the wavenumber. We verify this ‘first sound sum-rule’ in Fig. S2 and utilize it to calibrate the amplitude $V_0(k)$ of the drive. The measured out-of-phase density response (Fig. 2C and Fig. 3A) is given by $\delta n(\omega, k) = \text{Im}[\chi(\omega, k)]V_0(k)$. The weight of the first-sound mode is calculated from the density response, $W_1 = [\int d\omega \delta n(\omega, k)/\omega]/V_0(k) \equiv I_1/V_0(k)$, where I_1 is the integral over

the δn (Fig. S2A). We model the shape of the potential wall $V_0(x)$ by a Gaussian function with a width σ such that $V_0(k) \sim \exp[-k^2\sigma^2/2]$. To account for the slight asymmetry between the two endcap potentials, we use $\sigma = 4.4(1)\mu\text{m}$ and $3.2\mu\text{m}$ for the even and odd modes, respectively, acquired from Gaussian fits to I_1 . The calculated weight $W_1(k)$ (Fig 6B) is independent of the wavenumber to within the standard error of the measurements. By requiring the average value of $W_1(k)$ to be $n\pi/(2mc^2)$, we calibrate the amplitude of $V_0(k)$ and normalize $\text{Im}[\chi]$ shown in Fig. 3A.

References and Notes

1. P. A. Lee, N. Nagaosa, X.-G. Wen, Doping a Mott insulator: Physics of high-temperature superconductivity. *Rev. Mod. Phys.* **78**, 17–85 (2006). [doi:10.1103/RevModPhys.78.17](https://doi.org/10.1103/RevModPhys.78.17)
2. Y. Cao, V. Fatemi, S. Fang, K. Watanabe, T. Taniguchi, E. Kaxiras, P. Jarillo-Herrero, Unconventional superconductivity in magic-angle graphene superlattices. *Nature* **556**, 43–50 (2018). [doi:10.1038/nature26160](https://doi.org/10.1038/nature26160) Medline
3. M. G. Alford, L. Bovard, M. Hanuske, L. Rezzolla, K. Schwenzer, Viscous dissipation and heat conduction in binary neutron-star mergers. *Phys. Rev. Lett.* **120**, 041101 (2018). [doi:10.1103/PhysRevLett.120.041101](https://doi.org/10.1103/PhysRevLett.120.041101) Medline
4. A. Adams, L. D. Carr, T. Schäfer, P. Steinberg, J. E. Thomas, Strongly correlated quantum fluids: Ultracold quantum gases, quantum chromodynamic plasmas and holographic duality. *New J. Phys.* **14**, 115009 (2012). [doi:10.1088/1367-2630/14/11/115009](https://doi.org/10.1088/1367-2630/14/11/115009)
5. A. Sommer, M. Ku, G. Roati, M. W. Zwierlein, Universal spin transport in a strongly interacting Fermi gas. *Nature* **472**, 201–204 (2011). [doi:10.1038/nature09989](https://doi.org/10.1038/nature09989) Medline
6. A. B. Bardon, S. Beattie, C. Luciuk, W. Cairncross, D. Fine, N. S. Cheng, G. J. A. Edge, E. Taylor, S. Zhang, S. Trotzky, J. H. Thywissen, Transverse demagnetization dynamics of a unitary Fermi gas. *Science* **344**, 722–724 (2014). [doi:10.1126/science.1247425](https://doi.org/10.1126/science.1247425) Medline
7. C. Luciuk, S. Smale, F. Böttcher, H. Sharum, B. A. Olsen, S. Trotzky, T. Enss, J. H. Thywissen, Observation of quantum-limited spin transport in strongly interacting two-dimensional Fermi gases. *Phys. Rev. Lett.* **118**, 130405 (2017). [doi:10.1103/PhysRevLett.118.130405](https://doi.org/10.1103/PhysRevLett.118.130405) Medline
8. K. H. Bennemann, J. B. Ketterson, *The Physics of Liquid and Solid Helium* (Wiley, 1976).
9. D. Vollhardt, P. Wölfle, *The Superfluid Phases of Helium 3* (Dover Publications, Inc., 2013).
10. V. S. L'vov, L. Skrbek, K. R. Sreenivasan, Viscosity of liquid ^4He and quantum of circulation: Are they related? *Phys. Fluids* **26**, 041703 (2014). [doi:10.1063/1.4871291](https://doi.org/10.1063/1.4871291)
11. W. Ketterle, M. W. Zwierlein, in *Ultra-cold Fermi Gases*, vol. 164 of *Proceedings of the International School of Physics “Enrico Fermi”*, M. Inguscio, W. Ketterle, C. Salomon, Eds. (IOS Press, 2007), pp. 95–287.
12. I. Bloch, J. Dalibard, W. Zwerger, Many-body physics with ultracold gases. *Rev. Mod. Phys.* **80**, 885–964 (2008). [doi:10.1103/RevModPhys.80.885](https://doi.org/10.1103/RevModPhys.80.885)
13. S. Giorgini, L. P. Pitaevskii, S. Stringari, Theory of ultracold atomic Fermi gases. *Rev. Mod. Phys.* **80**, 1215–1274 (2008). [doi:10.1103/RevModPhys.80.1215](https://doi.org/10.1103/RevModPhys.80.1215)
14. W. Zwerger, Ed., *The BCS-BEC Crossover and the Unitary Fermi Gas* (Springer, 2012).
15. M. W. Zwierlein, *Novel Superfluids* (Oxford Univ. Press, 2014), pp. 269–422.
16. K. M. O'Hara, S. L. Hemmer, M. E. Gehm, S. R. Granade, J. E. Thomas, Observation of a strongly interacting degenerate Fermi gas of atoms. *Science* **298**, 2179–2182 (2002). [doi:10.1126/science.1079107](https://doi.org/10.1126/science.1079107) Medline

17. A. Altmeyer, S. Riedl, C. Kohstall, M. J. Wright, R. Geursen, M. Bartenstein, C. Chin, J. H. Denschlag, R. Grimm, Precision measurements of collective oscillations in the BEC-BCS crossover. *Phys. Rev. Lett.* **98**, 040401 (2007). [doi:10.1103/PhysRevLett.98.040401](https://doi.org/10.1103/PhysRevLett.98.040401) [Medline](#)
18. M. K. Tey, L. A. Sidorenkov, E. R. S. Guajardo, R. Grimm, M. J. H. Ku, M. W. Zwierlein, Y.-H. Hou, L. Pitaevskii, S. Stringari, Collective modes in a unitary Fermi gas across the superfluid phase transition. *Phys. Rev. Lett.* **110**, 055303 (2013). [doi:10.1103/PhysRevLett.110.055303](https://doi.org/10.1103/PhysRevLett.110.055303) [Medline](#)
19. T.-L. Ho, Universal thermodynamics of degenerate quantum gases in the unitarity limit. *Phys. Rev. Lett.* **92**, 090402 (2004). [doi:10.1103/PhysRevLett.92.090402](https://doi.org/10.1103/PhysRevLett.92.090402) [Medline](#)
20. M. J. H. Ku, A. T. Sommer, L. W. Cheuk, M. W. Zwierlein, Revealing the superfluid lambda transition in the universal thermodynamics of a unitary Fermi gas. *Science* **335**, 563–567 (2012). [doi:10.1126/science.1214987](https://doi.org/10.1126/science.1214987) [Medline](#)
21. M. Randeria, E. Taylor, Crossover from Bardeen-Cooper-Schrieffer to Bose-Einstein condensation and the unitary Fermi gas. *Annu. Rev. Condens. Matter Phys.* **5**, 209–232 (2014). [doi:10.1146/annurev-conmatphys-031113-133829](https://doi.org/10.1146/annurev-conmatphys-031113-133829)
22. C. Cao, E. Elliott, J. Joseph, H. Wu, J. Petricka, T. Schäfer, J. E. Thomas, Universal quantum viscosity in a unitary Fermi gas. *Science* **331**, 58–61 (2011). [doi:10.1126/science.1195219](https://doi.org/10.1126/science.1195219) [Medline](#)
23. T. Enss, R. Haussmann, W. Zwerger, Viscosity and scale invariance in the unitary Fermi gas. *Ann. Phys.* **326**, 770–796 (2011). [doi:10.1016/j.aop.2010.10.002](https://doi.org/10.1016/j.aop.2010.10.002)
24. J. A. Joseph, E. Elliott, J. E. Thomas, Shear viscosity of a unitary Fermi gas near the superfluid phase transition. *Phys. Rev. Lett.* **115**, 020401 (2015). [doi:10.1103/PhysRevLett.115.020401](https://doi.org/10.1103/PhysRevLett.115.020401) [Medline](#)
25. M. Braby, J. Chao, T. Schäfer, Thermal conductivity and sound attenuation in dilute atomic Fermi gases. *Phys. Rev. A* **82**, 033619 (2010). [doi:10.1103/PhysRevA.82.033619](https://doi.org/10.1103/PhysRevA.82.033619)
26. P. Nikolić, S. Sachdev, Renormalization-group fixed points, universal phase diagram, and $1/N$ expansion for quantum liquids with interactions near the unitarity limit. *Phys. Rev. A* **75**, 033608 (2007). [doi:10.1103/PhysRevA.75.033608](https://doi.org/10.1103/PhysRevA.75.033608)
27. T. Enss, Quantum critical transport in the unitary Fermi gas. *Phys. Rev. A* **86**, 013616 (2012). [doi:10.1103/PhysRevA.86.013616](https://doi.org/10.1103/PhysRevA.86.013616)
28. S. Nascimbène, N. Navon, S. Pilati, F. Chevy, S. Giorgini, A. Georges, C. Salomon, Fermi-liquid behavior of the normal phase of a strongly interacting gas of cold atoms. *Phys. Rev. Lett.* **106**, 215303 (2011). [doi:10.1103/PhysRevLett.106.215303](https://doi.org/10.1103/PhysRevLett.106.215303) [Medline](#)
29. I. Z. Rothstein, P. Shrivastava, Symmetry obstruction to Fermi liquid behavior in the unitary limit. *Phys. Rev. B* **99**, 035101 (2019). [doi:10.1103/PhysRevB.99.035101](https://doi.org/10.1103/PhysRevB.99.035101)
30. H. Smith, H. H. Jensen, *Transport Phenomena* (Clarendon, 1989).
31. M. A. Black, H. E. Hall, K. Thompson, The viscosity of liquid helium 3. *J. Phys. C Solid State Phys.* **4**, 129–142 (1971). [doi:10.1088/0022-3719/4/2/001](https://doi.org/10.1088/0022-3719/4/2/001)

32. C. N. Archie, T. A. Alvesalo, J. D. Reppy, R. C. Richardson, Viscosity measurements in superfluid ^3He -B from 2 to 29 bar. *J. Low Temp. Phys.* **42**, 295–332 (1981). [doi:10.1007/BF00120208](https://doi.org/10.1007/BF00120208)
33. H. Guo, D. Wulin, C.-C. Chien, K. Levin, Perfect fluids and bad metals: Insights from ultracold Fermi gases. *New J. Phys.* **13**, 075011 (2011). [doi:10.1088/1367-2630/13/7/075011](https://doi.org/10.1088/1367-2630/13/7/075011)
34. G. Rupak, T. Schäfer, Shear viscosity of a superfluid Fermi gas in the unitarity limit. *Phys. Rev. A* **76**, 053607 (2007). [doi:10.1103/PhysRevA.76.053607](https://doi.org/10.1103/PhysRevA.76.053607)
35. M. Mannarelli, C. Manuel, L. Tolos, Phonon contribution to the shear viscosity of a superfluid Fermi gas in the unitarity limit. *Ann. Phys.* **336**, 12–35 (2013). [doi:10.1016/j.aop.2013.05.015](https://doi.org/10.1016/j.aop.2013.05.015)
36. H. Kurkjian, Y. Castin, A. Sinatra, Three-phonon and four-phonon interaction processes in a pair-condensed Fermi gas. *Ann. Phys.* **529**, 1600352 (2017). [doi:10.1002/andp.201600352](https://doi.org/10.1002/andp.201600352)
37. S. Krinner, T. Esslinger, J.-P. Brantut, Two-terminal transport measurements with cold atoms. *J. Phys. Condens. Matter* **29**, 343003 (2017). [doi:10.1088/1361-648X/aa74a1](https://doi.org/10.1088/1361-648X/aa74a1) [Medline](#)
38. G. Valtolina, A. Burchianti, A. Amico, E. Neri, K. Xhani, J. A. Seman, A. Trombettoni, A. Smerzi, M. Zaccanti, M. Inguscio, G. Roati, Josephson effect in fermionic superfluids across the BEC-BCS crossover. *Science* **350**, 1505–1508 (2015). [doi:10.1126/science.aac9725](https://doi.org/10.1126/science.aac9725) [Medline](#)
39. M. Bartenstein, A. Altmeyer, S. Riedl, S. Jochim, C. Chin, J. H. Denschlag, R. Grimm, Collective excitations of a degenerate gas at the BEC-BCS crossover. *Phys. Rev. Lett.* **92**, 203201 (2004). [doi:10.1103/PhysRevLett.92.203201](https://doi.org/10.1103/PhysRevLett.92.203201) [Medline](#)
40. J. Kinast, S. L. Hemmer, M. E. Gehm, A. Turlapov, J. E. Thomas, Evidence for superfluidity in a resonantly interacting Fermi gas. *Phys. Rev. Lett.* **92**, 150402 (2004). [doi:10.1103/PhysRevLett.92.150402](https://doi.org/10.1103/PhysRevLett.92.150402) [Medline](#)
41. S. Hoinka, P. Dyke, M. G. Lingham, J. J. Kinnunen, G. M. Bruun, C. J. Vale, Goldstone mode and pair-breaking excitations in atomic Fermi superfluids. *Nat. Phys.* **13**, 943–946 (2017). [doi:10.1038/nphys4187](https://doi.org/10.1038/nphys4187)
42. M. Koschorreck, D. Pertot, E. Vogt, M. Köhl, Universal spin dynamics in two-dimensional Fermi gases. *Nat. Phys.* **9**, 405–409 (2013). [doi:10.1038/nphys2637](https://doi.org/10.1038/nphys2637)
43. M. Bluhm, J. Hou, T. Schäfer, Determination of the density and temperature dependence of the shear viscosity of a unitary Fermi gas based on hydrodynamic flow. *Phys. Rev. Lett.* **119**, 065302 (2017). [doi:10.1103/PhysRevLett.119.065302](https://doi.org/10.1103/PhysRevLett.119.065302) [Medline](#)
44. A. L. Gaunt, T. F. Schmidutz, I. Gotlibovich, R. P. Smith, Z. Hadzibabic, Bose-Einstein condensation of atoms in a uniform potential. *Phys. Rev. Lett.* **110**, 200406 (2013). [doi:10.1103/PhysRevLett.110.200406](https://doi.org/10.1103/PhysRevLett.110.200406) [Medline](#)
45. B. Mukherjee, Z. Yan, P. B. Patel, Z. Hadzibabic, T. Yefsah, J. Struck, M. W. Zwierlein, Homogeneous atomic Fermi gases. *Phys. Rev. Lett.* **118**, 123401 (2017). [doi:10.1103/PhysRevLett.118.123401](https://doi.org/10.1103/PhysRevLett.118.123401) [Medline](#)

46. K. Hueck, N. Luick, L. Sobirey, J. Siegl, T. Lompe, H. Moritz, Two-dimensional homogeneous Fermi gases. *Phys. Rev. Lett.* **120**, 060402 (2018).
[doi:10.1103/PhysRevLett.120.060402](https://doi.org/10.1103/PhysRevLett.120.060402) [Medline](#)
47. L. Baird, X. Wang, S. Roof, J. E. Thomas, Measuring the hydrodynamic linear response of a unitary Fermi gas. *Phys. Rev. Lett.* **123**, 160402 (2019).
[doi:10.1103/PhysRevLett.123.160402](https://doi.org/10.1103/PhysRevLett.123.160402) [Medline](#)
48. N. Navon, A. L. Gaunt, R. P. Smith, Z. Hadzibabic, Emergence of a turbulent cascade in a quantum gas. *Nature* **539**, 72–75 (2016). [doi:10.1038/nature20114](https://doi.org/10.1038/nature20114) [Medline](#)
49. J. L. Ville, R. Saint-Jalm, É. Le Cerf, M. Aidelsburger, S. Nascimbène, J. Dalibard, J. Beugnon, Sound propagation in a uniform superfluid two-dimensional Bose gas. *Phys. Rev. Lett.* **121**, 145301 (2018). [doi:10.1103/PhysRevLett.121.145301](https://doi.org/10.1103/PhysRevLett.121.145301) [Medline](#)
50. S. J. Garratt, C. Eigen, J. Zhang, P. Turzák, R. Lopes, R. P. Smith, Z. Hadzibabic, N. Navon, From single-particle excitations to sound waves in a box-trapped atomic Bose-Einstein condensate. *Phys. Rev. A (Coll. Park)* **99**, 021601 (2019).
[doi:10.1103/PhysRevA.99.021601](https://doi.org/10.1103/PhysRevA.99.021601)
51. P. C. Hohenberg, P. C. Martin, Microscopic theory of superfluid helium. *Ann. Phys.* **34**, 291–359 (1965). [doi:10.1016/0003-4916\(65\)90280-0](https://doi.org/10.1016/0003-4916(65)90280-0)
52. P. C. Hohenberg, Density correlation function in superfluid helium near T ? *J. Low Temp. Phys.* **11**, 745–750 (1973). [doi:10.1007/BF00654455](https://doi.org/10.1007/BF00654455)
53. L. D. Landau, E. M. Lifshitz, *Fluid Mechanics* (Elsevier, 1959).
54. J. A. Tarvin, F. Vidal, T. J. Greytak, Measurements of the dynamic structure factor near the lambda temperature in liquid helium. *Phys. Rev. B* **15**, 4193–4210 (1977).
[doi:10.1103/PhysRevB.15.4193](https://doi.org/10.1103/PhysRevB.15.4193)
55. See supplementary materials.
56. H. Kurkjian, Y. Castin, A. Sinatra, Concavity of the collective excitation branch of a Fermi gas in the BEC-BCS crossover. *Phys. Rev. A* **93**, 013623 (2016).
[doi:10.1103/PhysRevA.93.013623](https://doi.org/10.1103/PhysRevA.93.013623)
57. Z. Yan, P. B. Patel, B. Mukherjee, R. J. Fletcher, J. Struck, M. W. Zwierlein, Boiling a unitary Fermi liquid. *Phys. Rev. Lett.* **122**, 093401 (2019).
[doi:10.1103/PhysRevLett.122.093401](https://doi.org/10.1103/PhysRevLett.122.093401) [Medline](#)
58. M. J. Wright, S. Riedl, A. Altmeyer, C. Kohstall, E. R. S. Guajardo, J. H. Denschlag, R. Grimm, Finite-temperature collective dynamics of a Fermi gas in the BEC-BCS crossover. *Phys. Rev. Lett.* **99**, 150403 (2007). [doi:10.1103/PhysRevLett.99.150403](https://doi.org/10.1103/PhysRevLett.99.150403) [Medline](#)
59. C. J. Pethick, D. Ter Haar, On the attenuation of sound in liquid helium. *Physica* **32**, 1905–1920 (1966). [doi:10.1016/0031-8914\(66\)90157-1](https://doi.org/10.1016/0031-8914(66)90157-1)
60. G. Eska, K. Neumaier, W. Schoepe, K. Uhlig, W. Wiedemann, P. Wölfle, First-sound attenuation and viscosity of superfluid $^3\text{He-B}$. *Phys. Rev. Lett.* **44**, 1337–1340 (1980).
[doi:10.1103/PhysRevLett.44.1337](https://doi.org/10.1103/PhysRevLett.44.1337)

61. D. T. Son, Vanishing bulk viscosities and conformal invariance of the unitary Fermi gas. *Phys. Rev. Lett.* **98**, 020604 (2007). [doi:10.1103/PhysRevLett.98.020604](https://doi.org/10.1103/PhysRevLett.98.020604) [Medline](#)
62. G. M. Bruun, H. Smith, Viscosity and thermal relaxation for a resonantly interacting Fermi gas. *Phys. Rev. A* **72**, 043605 (2005). [doi:10.1103/PhysRevA.72.043605](https://doi.org/10.1103/PhysRevA.72.043605)
63. B. Mukherjee, P. B. Patel, Z. Yan, R. J. Fletcher, J. Struck, M. W. Zwierlein, Spectral response and contact of the unitary Fermi gas. *Phys. Rev. Lett.* **122**, 203402 (2019). [doi:10.1103/PhysRevLett.122.203402](https://doi.org/10.1103/PhysRevLett.122.203402) [Medline](#)
64. C. J. Pethick, H. Smith, P. Bhattacharyya, Transport processes in superfluid ^3He -B at low temperatures. *Phys. Rev. B* **15**, 3384–3400 (1977). [doi:10.1103/PhysRevB.15.3384](https://doi.org/10.1103/PhysRevB.15.3384)
65. A. Schirotzek, Y. I. Shin, C. H. Schunck, W. Ketterle, Determination of the superfluid gap in atomic Fermi gases by quasiparticle spectroscopy. *Phys. Rev. Lett.* **101**, 140403 (2008). [doi:10.1103/PhysRevLett.101.140403](https://doi.org/10.1103/PhysRevLett.101.140403) [Medline](#)
66. Y. A. Ono, J. Hara, K. Nagai, Shear viscosity of the B phase of superfluid ^3He . III. *J. Low Temp. Phys.* **48**, 167–188 (1982). [doi:10.1007/BF00681569](https://doi.org/10.1007/BF00681569)
67. M. Rangamani, S. F. Ross, D. Son, E. G. Thompson, Conformal non-relativistic hydrodynamics from gravity. *J. High Energy Phys.* **2009**, 075 (2009). [doi:10.1088/1126-6708/2009/01/075](https://doi.org/10.1088/1126-6708/2009/01/075)
68. P. B. Patel, Z. Yan, B. Mukherjee, R. J. Fletcher, J. Struck, M. W. Zwierlein, Replication data for: Universal sound diffusion in a strongly interacting Fermi gas. Harvard Dataverse (2020); <https://doi.org/10.7910/DVN/UVM2KN>.
69. C. Chin, R. Grimm, P. Julienne, E. Tiesinga, Feshbach resonances in ultracold gases. *Rev. Mod. Phys.* **82**, 1225–1286 (2010). [doi:10.1103/RevModPhys.82.1225](https://doi.org/10.1103/RevModPhys.82.1225)
70. G. Zürn, T. Lompe, A. N. Wenz, S. Jochim, P. S. Julienne, J. M. Hutson, Precise characterization of ^6Li Feshbach resonances using trap-sideband-resolved RF spectroscopy of weakly bound molecules. *Phys. Rev. Lett.* **110**, 135301 (2013). [doi:10.1103/PhysRevLett.110.135301](https://doi.org/10.1103/PhysRevLett.110.135301) [Medline](#)
71. H. Hu, P. Zou, X.-J. Liu, Low-momentum dynamic structure factor of a strongly interacting Fermi gas at finite temperature: A two-fluid hydrodynamic description. *Phys. Rev. A (Coll. Park)* **97**, 023615 (2018). [doi:10.1103/PhysRevA.97.023615](https://doi.org/10.1103/PhysRevA.97.023615)
72. G. Bertaina, L. Pitaevskii, S. Stringari, First and second sound in cylindrically trapped gases. *Phys. Rev. Lett.* **105**, 150402 (2010). [doi:10.1103/PhysRevLett.105.150402](https://doi.org/10.1103/PhysRevLett.105.150402) [Medline](#)
73. L. A. Sidorenkov, M. K. Tey, R. Grimm, Y.-H. Hou, L. Pitaevskii, S. Stringari, Second sound and the superfluid fraction in a Fermi gas with resonant interactions. *Nature* **498**, 78–81 (2013). [doi:10.1038/nature12136](https://doi.org/10.1038/nature12136) [Medline](#)

Appendix E

Correlation functions and response functions

In this appendix, I will describe the connection between the response functions of a system under external perturbation and the correlation functions in thermal equilibrium. Here we consider the evolution of the system under an external perturbation described by $H_{\text{ext}}(t)$, while the unperturbed Hamiltonian is H_0 .

$$H = H_0 + H_{\text{ext}}(t) \quad (\text{E.1})$$

The perturbation Hamiltonian has the form

$$H_{\text{ext}}(t) = \int d\mathbf{r} \sum_j \hat{A}_j(\mathbf{r}, t) a_j(\mathbf{r}, t). \quad (\text{E.2})$$

Here $\hat{A}_j(\mathbf{r}, t)$ is the quantum operator of an observable quantity, and $a_j(\mathbf{r}, t)$ is the generalized external force. Some examples of the observable quantities in many-body systems and their corresponding generalized force are listed in Tab. E.1.

In the interaction picture, the evolution of the density matrix ρ of the system is governed by

$$i\hbar \frac{\partial \rho}{\partial t} = [H_{\text{ext}}, \rho], \quad (\text{E.3})$$

Observable operators \hat{A}_j	Generalized external forces a_j
Density $\hat{n}(\mathbf{r}, t)$	External potential $\delta V(\mathbf{r}, t)$
Spin polarization $\hat{\mathbf{M}}(\mathbf{r}, t)$	External magnetic field $\mathbf{H}(\mathbf{r}, t)$
Charge density $\hat{\rho}_e(\mathbf{r}, t)$	Electric scalar potential $\phi(\mathbf{r}, t)$
Current density $\hat{\mathbf{j}}(\mathbf{r}, t)$	Magnetic vector potential $\mathbf{A}(\mathbf{r}, t)$

Table E.1: Examples of observable quantities and generalized external forces.

where $[,]$ is the quantum commutator. Here we assume the system was at thermal equilibrium at $t = -\infty$. Time dependent perturbation theory yields the deviation of density matrix $\delta\rho$ from its value ρ_0 at equilibrium to the first order

$$\begin{aligned}\delta\rho(t) &= \frac{1}{i\hbar} \int_{-\infty}^t [H_{\text{ext}}, \rho_0] dt' \\ &= \frac{1}{i\hbar} \int_{-\infty}^t dt' \int d^3\mathbf{r}' \left[\sum_j \hat{A}_j(\mathbf{r}', t') a_j(\mathbf{r}', t'), \rho_0 \right].\end{aligned}\quad (\text{E.4})$$

The expectation value of physical observable $A_i(\mathbf{r}, t)$ is the matrix trace of the product of operator \hat{A}_i and the density matrix ρ . Therefore, the perturbed quantity $\delta A_i(\mathbf{r}, t)$ can be expressed as

$$\begin{aligned}\delta A_i(\mathbf{r}, t) &= \text{Tr}(\hat{A}_i(\mathbf{r}, t) \delta\rho(t)) \\ &= \frac{1}{i\hbar} \text{Tr} \left(\hat{A}_i(\mathbf{r}, t) \int_{-\infty}^t dt' \int d^3\mathbf{r}' \left[\sum_j \hat{A}_j(\mathbf{r}', t') a_j(\mathbf{r}', t'), \rho_0 \right] \right) \\ &= \frac{1}{i\hbar} \int_{-\infty}^t dt' \int d^3\mathbf{r}' \sum_j a_j(\mathbf{r}', t') \langle [\hat{A}_i(\mathbf{r}, t), \hat{A}_j(\mathbf{r}', t')] \rangle,\end{aligned}\quad (\text{E.5})$$

where $\langle \rangle$ denotes an average over the equilibrium thermal ensemble $\langle A \rangle = \text{Tr}(\hat{A} \rho_0)$. Eq. E.5 connects the transport properties (such as the electric conductivity) to the correlation functions in equilibrium χ_{ij}

$$\tilde{\chi}_{ij}(\mathbf{r}, \mathbf{r}'; t - t') = \frac{1}{i\hbar} \eta(t - t') \langle [\hat{A}_i(\mathbf{r}, t), \hat{A}_j(\mathbf{r}', t')] \rangle. \quad (\text{E.6})$$

$\eta(t - t')$ is a step function, and can be expressed as a Fourier transform:

$$\begin{aligned}\eta(t - t') &= \lim_{\epsilon \rightarrow 0^+} i \int \frac{d\omega}{2\pi} \frac{e^{-i\omega(t-t')}}{\omega + i\epsilon} = 0 \text{ for } t < t', \\ &= 1 \text{ for } t > t'.\end{aligned}\quad (\text{E.7})$$

The correlation function $\tilde{\chi}_{ij}$ serves as a response function of observable A_i over external perturbation a_j :

$$\delta A_i(\mathbf{r}, t) = \sum_j \int_{-\infty}^{+\infty} dt' \int d^3\mathbf{r}' \tilde{\chi}_{ij}(\mathbf{r}, \mathbf{r}'; t - t') a_j(\mathbf{r}', t'). \quad (\text{E.8})$$

In a system with space and time translational symmetry, we can express the correlation functions χ_{ij} , generalized force a_j , and response of physical quantities δA_i in the Fourier space

$$\chi_{ij}(\mathbf{k}, \omega) = \int dt \int d^3\mathbf{r} \chi_{ij}(\mathbf{r}, 0; t) e^{-i\mathbf{k}\cdot\mathbf{r} + i\omega t}, \quad (\text{E.9})$$

$$\tilde{a}_j(\mathbf{k}, \omega) = \int dt \int d^3\mathbf{r} a_j(\mathbf{r}, t) e^{-i\mathbf{k}\cdot\mathbf{r} + i\omega t}, \quad (\text{E.10})$$

$$\tilde{A}_i(\mathbf{k}, \omega) = \int dt \int d^3\mathbf{r} \delta A_i(\mathbf{r}, t) e^{-i\mathbf{k}\cdot\mathbf{r} + i\omega t}. \quad (\text{E.11})$$

In the Fourier space, Eq. (E.8) can be rewritten as

$$\tilde{A}_i(\mathbf{k}, \omega) = \sum_j \chi_{ij}(\mathbf{k}, \omega) \tilde{a}_j(\mathbf{k}, \omega). \quad (\text{E.12})$$

We can define the "absorptive" part of response function in Fourier space $\chi''_{ij}(\mathbf{k}, \omega)$ and in real space $\tilde{\chi}''_{ij}(\mathbf{r}, \mathbf{r}', t - t')$ as:

$$\chi''_{ij}(\mathbf{k}, \omega) = - \int dt \int d^3\mathbf{r} \frac{1}{2\hbar} \langle [\hat{A}_i(\mathbf{r}, t), \hat{A}_j(0, 0)] \rangle e^{-i\mathbf{k}\cdot\mathbf{r} + i\omega t}, \quad (\text{E.13})$$

$$\tilde{\chi}''_{ij}(\mathbf{r}, \mathbf{r}', t - t') = - \frac{1}{2\hbar} \langle [\hat{A}_i(\mathbf{r}, t), \hat{A}_j(0, 0)] \rangle \quad (\text{E.14})$$

The evolution of observable δA_i can be rewritten from Eq. (E.5):

$$\begin{aligned}
\delta A_i(\mathbf{r}, t) &= \sum_j \frac{1}{i\hbar} \int_{-\infty}^{+\infty} dt' \int d^3\mathbf{r}' \eta(t - t') \langle [\hat{A}_i(\mathbf{r}, t), \hat{A}_j(\mathbf{r}', t')] \rangle a_j(\mathbf{r}', t') \\
&= - \int_{-\infty}^{+\infty} dt' \int \frac{d^3\mathbf{k}}{2\pi} e^{i\mathbf{k}\cdot\mathbf{r}} \lim_{\epsilon \rightarrow 0^+} \int \frac{d\omega_1}{2\pi} \frac{1}{\omega_1 + i\epsilon} \int \frac{d\omega_2}{\pi} \chi''_{ij}(\mathbf{k}, \omega_2) \int \frac{d\omega_3}{2\pi} \tilde{a}_j(\mathbf{k}, \omega_3) \\
&\quad \cdot e^{i(\omega_1 + \omega_2 - \omega_3)t'} \cdot e^{-i(\omega_1 + \omega_2)t} \\
&= \int \frac{d^3\mathbf{k}}{2\pi} e^{i\mathbf{k}\cdot\mathbf{r}} \int \frac{d\omega_3}{2\pi} \lim_{\epsilon \rightarrow 0^+} \int \frac{d\omega_2}{\pi} \frac{\chi''_{ij}(\mathbf{k}, \omega_2)}{\omega_2 - \omega_3 - i\epsilon} \tilde{a}_j(\mathbf{k}, \omega_3) e^{-i\omega_3 t} \tag{E.15}
\end{aligned}$$

By comparing Eq. (E.15) and Eq. (E.12), we can find the connection between $\chi''_{ij}(\mathbf{k}, \omega)$ and $\chi_{ij}(\mathbf{k}, \omega)$

$$\begin{aligned}
\chi_{ij}(\mathbf{k}, \omega) &= \lim_{\epsilon \rightarrow 0^+} \int \frac{d\omega_2}{\pi} \frac{\chi''_{ij}(\mathbf{k}, \omega')}{\omega' - \omega - i\epsilon} \\
&= \int \frac{d\omega_2}{\pi} \chi''_{ij}(\mathbf{k}, \omega') \left[\mathcal{P} \frac{1}{\omega' - \omega} + i\pi\delta(\omega' - \omega) \right]. \tag{E.16}
\end{aligned}$$

Next, I will discuss the general symmetry properties of $\chi''_{ij}(\mathbf{k}, \omega)$ and $\tilde{\chi}_{ij}''(\mathbf{r}, \mathbf{r}'; t - t')$. Since $\tilde{\chi}_{ij}''(\mathbf{r}, \mathbf{r}'; t - t')$ is a commutator, it is antisymmetric under interchange of \mathbf{r} with \mathbf{r}' , i with j , and t with t' .

$$\tilde{\chi}_{ij}''(\mathbf{r}, \mathbf{r}'; t - t') = -\tilde{\chi}_{ji}''(\mathbf{r}', \mathbf{r}; t' - t) \tag{E.17}$$

$$\chi''_{ij}(\mathbf{k}, \omega) = -\chi''_{ji}(-\mathbf{k}, -\omega) \tag{E.18}$$

$\langle [\hat{A}_i(\mathbf{r}, t), \hat{A}_j(0, 0)] \rangle$ is purely imaginary due to \hat{A}_i and \hat{A}_j being Hermitian operators. Therefore, we have

$$[\tilde{\chi}_{ij}''(\mathbf{r}, \mathbf{r}'; t - t')]^* = -\tilde{\chi}_{ij}''(\mathbf{r}, \mathbf{r}'; t - t'), \tag{E.19}$$

$$\chi''_{ij}(\mathbf{k}, \omega) = -\chi''_{ij}^*(-\mathbf{k}, -\omega) = \chi''_{ji}^*(-\mathbf{k}, -\omega). \tag{E.20}$$

Under time reversal, physical quantities might get a sign change

$$TA_i(r, t) = \epsilon_i A_i(r, -t). \tag{E.21}$$

Physical variables that do not change sign upon time reversal include density, energy, electromagnetic scalar potential, and acceleration, while other variables include velocity, time, angular momentum, and electromagnetic vector potential, will change sign upon time reversal. When the Hamiltonian is invariant under time reversal, we have

$$\tilde{\chi}_{ij}''(\mathbf{r}, \mathbf{r}'; t - t') = \epsilon_i \epsilon_j \tilde{\chi}_{ji}''(\mathbf{r}', \mathbf{r}; t - t'), \quad (\text{E.22})$$

$$\chi_{ij}''(\mathbf{k}, \omega) = \epsilon_i \epsilon_j \chi_{ji}''(-\mathbf{k}, \omega). \quad (\text{E.23})$$

If A_i and A_j have the same sign under time reversal, $\chi_{ij}''(\mathbf{k}, \omega)$ is odd in ω , and is a real function. In contrast, when $\epsilon_i \epsilon_j = -1$, $\chi_{ij}''(\mathbf{k}, \omega)$ is an imaginary even function of ω . When $\chi_{ij}''(\mathbf{k}, \omega)$ is a real function, we can rewrite Eq. (E.16) using Kramers–Kronig relation:

$$\chi_{ij}(\mathbf{k}, \omega) = \chi'_{ij}(\mathbf{k}, \omega) + i\chi''_{ij}(\mathbf{k}, \omega), \quad (\text{E.24})$$

where both χ'_{ij} and χ''_{ij} are both real functions, and corresponds to the real and imaginary part of response function, respectively. Hence $\chi''_{ij}(\mathbf{k}, \omega)$ describes the out-of-phase response of the system, corresponding to energy absorption process.

Appendix F

Magnetic coils making

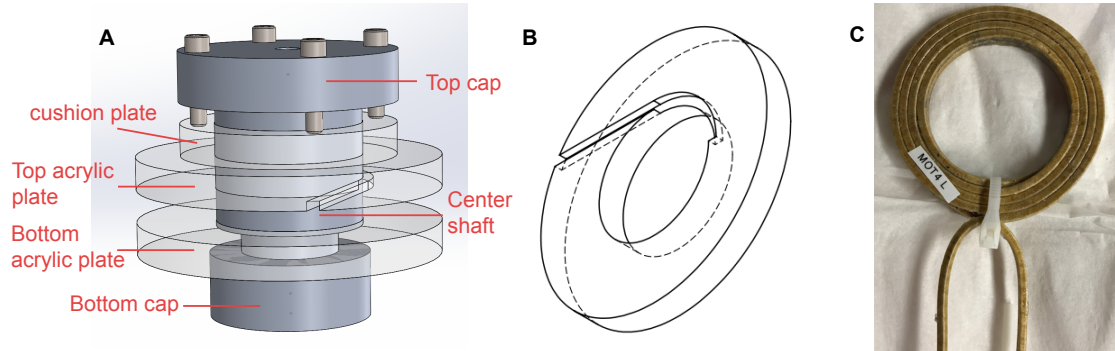


Figure F-1: (A) The assembled coil winding mold. (B) The top acrylic plate with a notch for the wire to come out. (C) A two-layer coil we made.

In this appendix, I will detail the methods for making magnetic coils. Fig. F-1 illustrates the mold for coil winding. An aluminum center shaft defines the inner diameter of the coils. The diameter of the shaft is reduced in the bottom to allow easy removal of the coil after winding. A very thin layer of Kapton tape is wrapped around the shaft during coil winding to avoid bonding between the coil and the shaft. Two acrylic plates, which will not bond with epoxy, are used to define the flat top and bottom surface of the coils. The acrylic plates are fixed in place by the aluminum top and bottom caps which are attached to the center shaft with screws. The top acrylic is pushed onto the top surface of the coil by screws on the top aluminum cap, and a cushion plate is used to avoid damaging the flat surface of the top acrylic plate. A notch on the top plate allows a lead of the coil to come out from the center when we

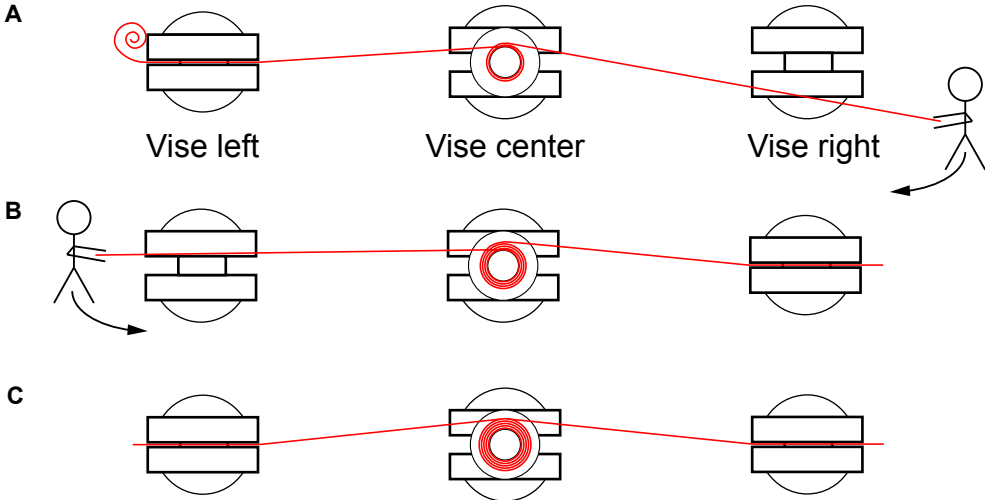


Figure F-2: Winding method for two-layer magnetic coils. We perform coil winding on a table with three vises. The coil mold is mounted on the center vise. (A) We first clamp the lead on the second layer on the left vise and use the other lead to wind the first layer. (B) After finishing the first layer, we clamp the lead on the right vise and wind the second layer with the lead previously clamped on the left vise. (C) After winding both layers, we clamp both leads on the side vises and wait for the epoxy to be cured. A second person applying epoxy on the wire and helping to pass the moving wire below the fixed wire is not shown in the figure.

wind the first layer. This mold can be used for both the hollow core square wire and the flat solid wire. The depth and width of the notch on the top acrylic plate need to be adjusted to fit the size of the wire.

All the magnetic coils we used in Fermi3 are two-layer coils or a combination of them (Fig. F-1C). The two-layer setup allows both leads to come out from the outer rim of the coil. This saves the space in the center for optics elements. Fig. F-2 illustrates the making process of the magnetic coils. We make the coils with three vises mounted on a table. The mold is initially mounted on the center vise without the top acrylic plate. We start the coil winding by making an α shape knot with the wire. We use a hammer and a small metal piece to knock the wire to make sure it is tightly wrapped around the center shaft. Then we put on the top acrylic plate and let the top lead of the wire come out from the notch. This lead is fixed on one of the side vises. Using the screws on the top cap, we limit the spacing between the top and bottom acrylic plates to be the height of the wire and start to wind the first layer using the free lead (Fig. F-2A). Every time the free wire passes through the fixed

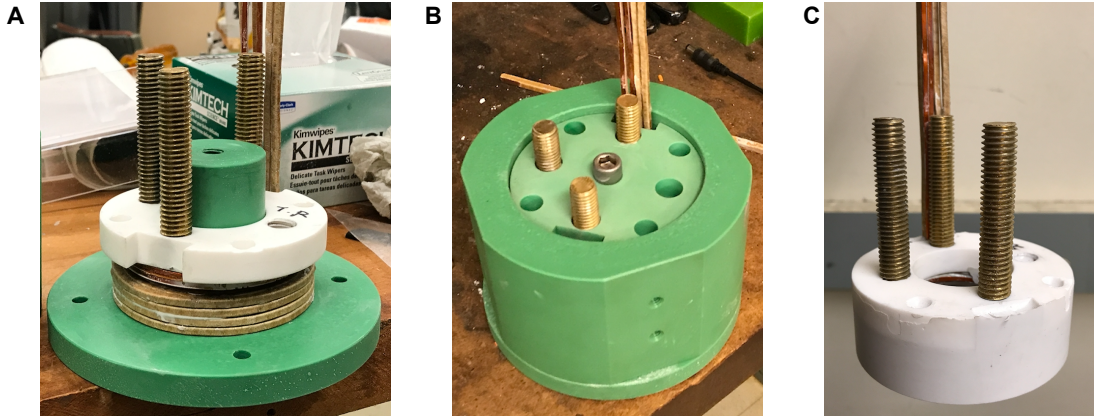


Figure F-3: Casting of the MOT chamber coil set. (A) The coils are stacked together on a center nylon shaft (green). A threaded macor plate with long brass set screw attached is put on top of the coil. (B) The coil set is put into a nylon bucket. The bucket is then filled with epoxy. (C) The MOT coil set casted in epoxy.

lead, it needs to go under it. Epoxy is put on the wire as we wind the coil. After finishing the first layer, we fix the lead on the other side vise, remove the top acrylic plate, inspect the coil, and knock the coil with a hammer to remove any spacing between the wire and bottom acrylic plate. Next, we flip the top acrylic plate and put it back, letting the flat surface face the wire. Finally, we use the other lead to wind the second layer (Fig. F-2B) and clamp it on the vise again after finishing the second layer (Fig. F-2C).

The epoxy we use is non-magnetic Cotronics Duralco NM25. After winding each coils, we wait for 24 hours before removing the coil from the mold to let the epoxy cure. Copper tubes with 1/4' outer diameter is silver soldered to the hollow core wire by MIT central machine shop to allow water cooling of the coils.

We cast the MOT chamber coil set, which includes the MOT coils, the MOT bias coils, and a macor (machinable glass ceramic) mounting plate using epoxy, as shown in Fig. F-3. long brass set screws on the macor plate are used to mount the coils. The coils and mounting plates are stacked on a nylon center shaft and putted into a nylon bucket. A top cap is attached to the center shaft with a screw to tightly push the coils and mounting plate together. We fill the nylon bucket with epoxy through the holes on the top cap. Mold release spray is applied on the nylon surfaces before casting to ensure easy removal after epoxy curing. A screw can be inserted

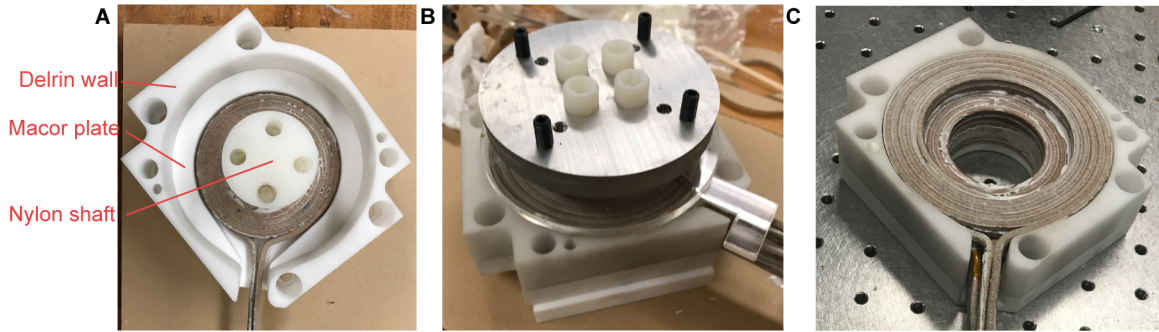


Figure F-4: Casting of the science cell coil set. (A) The coils are stacked together on a macor mounting plate (only the curvature coil is shown here). The center hole is plugged by a nylon shaft. (B) A top cap is used to push the coils and macor plate together. (C) The finished science cell coil set.

into a threaded hole to push apart the bucket wall and the center shaft. Similarly, the science cell coil set, which includes the Feshbach, gradient, and curvature coils, is also casted in epoxy with a macor mounting plate, as shown in Fig. F-4. A Delrin wall is mounted on the macor to hold the coils and epoxy resin. The science cell coil set is directly mounted on the copper support structure by brass screws.

Fig. F-5 shows the copper support structure on which the coils are mounted. The structure is directly mounted on the optics table with two 1.5" posts. An $0.02\mu\text{m}$ layer gold is coated on the surface of the support structure to avoid oxidation. The magnetic transport coils are directly attached to the copper support plate with epoxy. Copper tubes with 0.5" outer diameter (not shown in the figure) are welded to the trenches on the copper plates to provide water cooling for the transport coils.

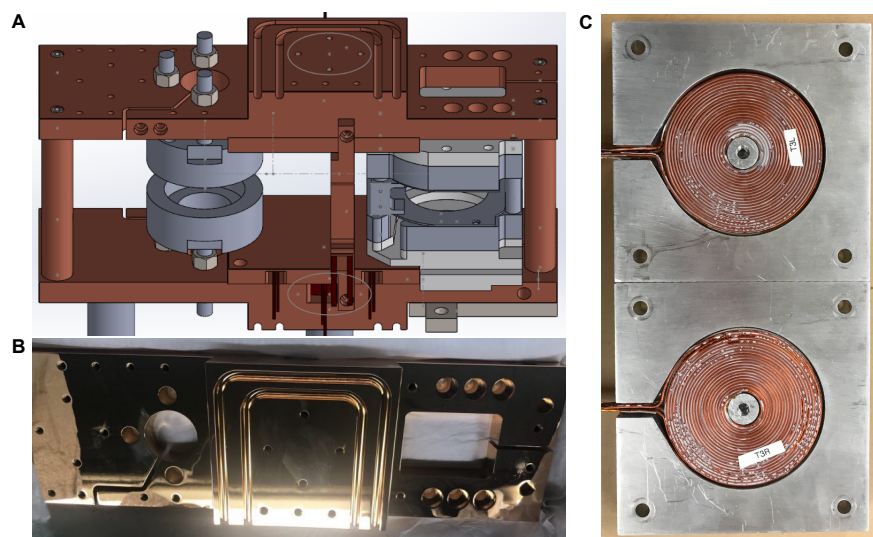


Figure F-5: Coil support structure and transport coils. (A) CAD drawing of the coil support structure with the MOT (left) and science cell (right) coil sets. The magnetic transport coils are directly attached to the support structure. (B) One side of the copper supporting plate. (C) Magnetic transport coils on test mounts.

Bibliography

- [1] Allan Adams, Lincoln D. Carr, Thomas Schäfer, Peter Steinberg, and John E. Thomas. Strongly correlated quantum fluids: ultracold quantum gases, quantum chromodynamic plasmas and holographic duality. *New J. Phys.*, 14(11):115009, Nov 2012.
- [2] K. Aikawa, A. Frisch, M. Mark, S. Baier, A. Rietzler, R. Grimm, and F. Ferlaino. Bose-Einstein Condensation of Erbium. *Phys. Rev. Lett.*, 108(21):210401, may 2012.
- [3] M. R. Andrews, C. G. Townsend, H. J. Miesner, D. S. Durfee, D. M. Kurn, and W. Ketterle. Observation of interference between two bose condensates. *Science*, 275(5300):637–641, 1997.
- [4] Lorin Baird, Xin Wang, Stetson Roof, and J. E. Thomas. Measuring the Hydrodynamic Linear Response of a Unitary Fermi Gas. *Phys. Rev. Lett.*, 123(16):160402, 2019.
- [5] Waseem S. Bakr, Jonathon I. Gillen, Amy Peng, Simon Fölling, and Markus Greiner. A quantum gas microscope for detecting single atoms in a Hubbard-regime optical lattice. *Nature*, 462(7269):74–77, 2009.
- [6] A. B. Bardon, S. Beattie, C. Luciuk, W. Cairncross, D. Fine, N. S. Cheng, G. J. A. Edge, E. Taylor, S. Zhang, S. Trotzky, and J. H. Thywissen. Transverse Demagnetization Dynamics of a Unitary Fermi Gas. *Science*, 344(6185):722–724, May 2014.
- [7] M. Bartenstein, A. Altmeyer, S. Riedl, S. Jochim, C. Chin, J. Hecker Denschlag, and R. Grimm. Crossover from a Molecular Bose-Einstein Condensate to a Degenerate Fermi Gas. *Phys. Rev. Lett.*, 92(12):120401, mar 2004.
- [8] Gordon Baym, C. J. Pethick, Zhenhua Yu, and Martin W. Zwierlein. Coherence and Clock Shifts in Ultracold Fermi Gases with Resonant Interactions. *Phys. Rev. Lett.*, 99(19):190407, Nov 2007.
- [9] Hannes Bernien, Sylvain Schwartz, Alexander Keesling, Harry Levine, Ahmed Omran, Hannes Pichler, Soonwon Choi, Alexander S. Zibrov, Manuel Endres, Markus Greiner, Vladan Vuletic, and Mikhail D. Lukin. Probing many-body dynamics on a 51-atom quantum simulator. *Nature*, 551(7682):579–584, 2017.

- [10] Hauke Biss, Lennart Sobirey, Niclas Luick, Markus Bohlen, Jami J. Kinnunen, Georg M. Bruun, Thomas Lompe, and Henning Moritz. Excitation Spectrum and Superfluid Gap of an Ultracold Fermi Gas. *arXiv:2105.09820*, may 2021.
- [11] Immanuel Bloch, Jean Dalibard, and Wilhelm Zwerger. Many-body physics with ultracold gases. *Reviews of Modern Physics*, 80(3):885–964, 2008.
- [12] Markus Bohlen, Lennart Sobirey, Niclas Luick, Hauke Biss, Tilman Enss, Thomas Lompe, and Henning Moritz. Sound Propagation and Quantum-Limited Damping in a Two-Dimensional Fermi Gas. *Phys. Rev. Lett.*, 124(24):240403, 2020.
- [13] Martin Boll, Timon A Hilker, Guillaume Salomon, Ahmed Omran, Jacopo Nespolo, Lode Pollet, Immanuel Bloch, and Christian Gross. Spin- and density-resolved microscopy of antiferromagnetic correlations in Fermi-Hubbard chains. *Science*, 353(6305):1257–1260, 2016.
- [14] T. Bourdel, L. Khaykovich, J. Cubizolles, J. Zhang, F. Chevy, M. Teichmann, L. Tarruell, S. J. J. M. F. Kokkelmans, and C. Salomon. Experimental Study of the BEC-BCS Crossover Region in Lithium 6. *Phys. Rev. Lett.*, 93(5):050401, Jul 2004.
- [15] Eric Braaten, Daekyoung Kang, and Lucas Platter. Short-Time Operator Product Expansion for rf Spectroscopy of a Strongly Interacting Fermi Gas. *Phys. Rev. Lett.*, 104(22):223004, jun 2010.
- [16] Matt Braby, Jingyi Chao, and Thomas Schäfer. Thermal conductivity and sound attenuation in dilute atomic Fermi gases. *Phys. Rev. A*, 82(3):033619, sep 2010.
- [17] J.-P. Brantut, Charles Grenier, Jakob Meineke, David Stadler, Sebastian Krinner, Corinna Kollath, Tilman Esslinger, and Antoine Georges. A Thermoelectric Heat Engine with Ultracold Atoms. *Science*, 342(6159):713–715, Nov 2013.
- [18] J.-P. Brantut, J. Meineke, D. Stadler, S. Krinner, and T. Esslinger. Conduction of Ultracold Fermions Through a Mesoscopic Channel. *Science*, 337(6098):1069–1071, Aug 2012.
- [19] G. M. Bruun, A. Recati, C. J. Pethick, H. Smith, and S. Stringari. Collisional properties of a polarized fermi gas with resonant interactions. *Phys. Rev. Lett.*, 100(24):3–6, 2008.
- [20] C. Cao, E. Elliott, J. Joseph, H. Wu, J. Petricka, T. Schäfer, and J. E. Thomas. Universal quantum viscosity in a unitary fermi gas. *Science*, 331(6013):58–61, 2011.
- [21] C. Carcy, S. Hoinka, M. G. Lingham, P. Dyke, C. C. N. Kuhn, H. Hu, and C. J. Vale. Contact and Sum Rules in a Near-Uniform Fermi Gas at Unitarity. *Phys. Rev. Lett.*, 122(20):203401, May 2019.

- [22] Yvan Castin. Exact scaling transform for a unitary quantum gas in a time dependent harmonic potential. *Comptes Rendus Phys.*, 5(3):407–410, Apr 2004.
- [23] B. S. Chandrasekhar. A note on the maximum critical field of high-field superconductors. *Appl. Phys. Lett.*, 1(1):7–8, 1962.
- [24] Lawrence W. Cheuk, Matthew A. Nichols, Katherine R. Lawrence, Melih Okan, Hao Zhang, Ehsan Khatami, Nandini Trivedi, Thereza Paiva, Marcos Rigol, and Martin W. Zwierlein. Observation of spatial charge and spin correlations in the 2D Fermi-Hubbard model. *Science*, 353:1260–1264, 2016.
- [25] F. Chevy. Universal phase diagram of a strongly interacting Fermi gas with unbalanced spin populations. *Phys. Rev. A*, 74(6):063628, 2006.
- [26] C Chin, M Bartenstein, A Altmeyer, S Riedl, S Jochim, J Hecker Denschlag, and R Grimm. Observation of the pairing gap in a strongly interacting Fermi gas. *Science*, 305(5687):1128–1130, 2004.
- [27] Cheng Chin. A simple model of Feshbach molecules. *arXiv:0506313v2*, 2005.
- [28] Cheng Chin, Rudolf Grimm, Paul Julienne, and Eite Tiesinga. Feshbach resonances in ultracold gases. *Rev. Mod. Phys.*, 82(2):1225–1286, 2010.
- [29] Lauriane Chomaz, Laura Corman, Tom Bienaimé, Rémi Desbuquois, Christof Weitenberg, Sylvain Nascimbène, Jérôme Beugnon, and Jean Dalibard. Emergence of coherence via transverse condensation in a uniform quasi-two-dimensional Bose gas. *Nat. Commun.*, 6(1):6162, may 2015.
- [30] Panagiotis Christodoulou, Maciej Gałka, Nishant Dogra, Raphael Lopes, Julian Schmitt, and Zoran Hadzibabic. Observation of first and second sound in a Berezinskii-Kosterlitz-Thouless superfluid. *arXiv:2008.06044*, Aug 2020.
- [31] C.J.Foot. *Atomic Physics*. Oxford University Press, 2004.
- [32] A. M. Clogston. Upper Limit for the Critical Field in Hard Superconductors. *Phys. Rev. Lett.*, 9(6):266–267, sep 1962.
- [33] R. Combescot, A. Recati, C. Lobo, and F. Chevy. Normal State of Highly Polarized Fermi Gases: Simple Many-Body Approaches. *Phys. Rev. Lett.*, 98(18):180402, 2007.
- [34] L. R. Corruccini and D. D. Osheroff. Observation of Second Sound in ${}^3\text{He}3\text{-A}_1$. *Phys. Rev. Lett.*, 45(25):2029–2032, Dec 1980.
- [35] R. Côté and A. Dalgarno. Elastic scattering of two Na atoms. *Phys. Rev. A*, 50(6):4827–4835, Dec 1994.
- [36] R. Côté, E. J. Heller, and A. Dalgarno. Quantum suppression of cold atom collisions. *Phys. Rev. A*, 53(1):234–241, Jan 1996.

- [37] J. Cubizolles, T. Bourdel, S. J. J. M. F. Kokkelmans, G. V. Shlyapnikov, and C. Salomon. Production of Long-Lived Ultracold Li₂ Molecules from a Fermi Gas. *Phys. Rev. Lett.*, 91(24):240401, Dec 2003.
- [38] Marion Delehaye, Sébastien Laurent, Igor Ferrier-Barbut, Shuwei Jin, Frédéric Chevy, and Christophe Salomon. Critical Velocity and Dissipation of an Ultracold Bose-Fermi Counterflow. *Phys. Rev. Lett.*, 115(26):1–5, 2015.
- [39] B. DeMarco and D. S. Jin. Onset of Fermi Degeneracy in a Trapped Atomic Gas. *Science*, 285(5434):1703–1706, Sep 1999.
- [40] K. Dieckmann, C. A. Stan, S. Gupta, Z. Hadzibabic, C. H. Schunck, and W. Ketterle. Decay of an Ultracold Fermionic Lithium Gas near a Feshbach Resonance. *Phys. Rev. Lett.*, 89(20):203201, 2002.
- [41] T E Drake, Y Sagi, R Paudel, J T Stewart, J P Gaebler, and D S Jin. Direct observation of the Fermi surface in an ultracold atomic gas. *Phys. Rev. A*, 86(3):31601, Sep 2012.
- [42] S. Eckel, F. Jendrzejewski, A. Kumar, C. J. Lobb, and G. K. Campbell. Interferometric Measurement of the Current-Phase Relationship of a Superfluid Weak Link. *Phys. Rev. X*, 4(3):031052, sep 2014.
- [43] Tilman Enss. Quantum critical transport in the unitary Fermi gas. *Phys. Rev. A*, 86(1):013616, Jul 2012.
- [44] Tilman Enss, Rudolf Haussmann, and Wilhelm Zwerger. Viscosity and scale invariance in the unitary Fermi gas. *Ann. Phys. (N. Y.)*, 326(3):770–796, 2011.
- [45] Richard I. Epstein. Acoustic properties of neutron stars. *Astrophys. J.*, 333(9):880, Oct 1988.
- [46] R. A. Ferrell, N. Menyhárd, H. Schmidt, F. Schwabl, and P. Szépfalusy. Dispersion in second sound and anomalous heat conduction at the lambda point of liquid helium. *Phys. Rev. Lett.*, 18(21):891–894, May 1967.
- [47] R. A. Ferrell, N. Menyhárd, H. Schmidt, F. Schwabl, and P. Szépfalusy. Fluctuations and lambda phase transition in liquid helium. *Ann. Phys. (N. Y.)*, 47(3):565–613, 1968.
- [48] Igor Ferrier-Barbut, Holger Kadau, Matthias Schmitt, Matthias Wenzel, and Tilman Pfau. Observation of Quantum Droplets in a Strongly Dipolar Bose Gas. *Phys. Rev. Lett.*, 116(21):215301, may 2016.
- [49] Richard P. Feynman. Simulating physics with computers. *International Journal of Theoretical Physics*, 21(6-7):467–488, 1982.
- [50] V. V. Flambaum, G. F. Gribakin, and C. Harabati. Analytical calculation of cold-atom scattering. *Phys. Rev. A*, 59(3):1998–2005, mar 1999.

- [51] Richard J. Fletcher, Raphael Lopes, Jay Man, Nir Navon, Robert P. Smith, Martin W Zwierlein, and Zoran Hadzibabic. Two- and three-body contacts in the unitary Bose gas. *Science*, 355(6323):377–380, Jan 2017.
- [52] Richard J. Fletcher, Airlia Shaffer, Cedric C. Wilson, Parth B. Patel, Zhenjie Yan, Valentin Crépel, Biswaroop Mukherjee, and Martin W. Zwierlein. Geometric squeezing into the lowest Landau level. *Science*, 372(6548):1318–1322, Jun 2021.
- [53] Bernhard Frank, Johannes Lang, and Wilhelm Zwerger. Universal Phase Diagram and Scaling Functions of Imbalanced Fermi Gases. *J. Exp. Theor. Phys.*, 127(5):812–825, Nov 2018.
- [54] Bernhard Frank, Wilhelm Zwerger, and Tilman Enss. Quantum critical thermal transport in the unitary Fermi gas. *Phys. Rev. Res.*, 2(2):023301, jun 2020.
- [55] Peter Fulde and Richard A. Ferrell. Superconductivity in a strong spin-exchange field. *Phys. Rev.*, 135(3A):A550, 1964.
- [56] J. P. Gaebler, J. T. Stewart, T. E. Drake, D. S. Jin, A. Perali, P. Pieri, and G. C. Strinati. Observation of pseudogap behaviour in a strongly interacting Fermi gas. *Nat. Phys.*, 6(8):569–573, Aug 2010.
- [57] Bo Gao. Quantum-defect theory of atomic collisions and molecular vibration spectra. *Phys. Rev. A*, 58(5):4222–4225, nov 1998.
- [58] Alexander L Gaunt, Tobias F Schmidutz, Igor Gotlibovych, Robert P Smith, and Zoran Hadzibabic. Bose-Einstein Condensation of Atoms in a Uniform Potential. *Phys. Rev. Lett.*, 110(20):200406, May 2013.
- [59] Alexander Lloyd Gaunt. *Degenerate Bose Gases : Tuning Interactions & Geometry*. Phd, University of Cambridge, 2014.
- [60] Stefano Giorgini, Lev P. Pitaevskii, and Sandro Stringari. Theory of ultracold atomic Fermi gases. *Rev. Mod. Phys.*, 80(4):1215–1274, Oct 2008.
- [61] Lori S. Goldner, Norbert Mulders, and Guenter Ahlers. Second sound very near $T\lambda$. *J. Low Temp. Phys.*, 93(1-2):131–182, 1993.
- [62] S. R. Granade, M. E. Gehm, K. M. O’Hara, and J. E. Thomas. All-Optical Production of a Degenerate Fermi Gas. *Phys. Rev. Lett.*, 88(12):4, 2002.
- [63] Markus Greiner, Immanuel Bloch, Theodor W. Hänsch, and Tilman Esslinger. Magnetic transport of trapped cold atoms over a large distance. *Phys. Rev. A*, 63(3):031401, feb 2001.
- [64] Markus Greiner, Cindy A. Regal, and Deborah S. Jin. Emergence of a molecular Bose-Einstein condensate from a Fermi gas. *Nature*, 426(6966):537–540, 2003.

- [65] Elmer Guardado-Sánchez, Peter T. Brown, Debayan Mitra, Trithep Devakul, David A. Huse, Peter Schauß, and Waseem S. Bakr. Probing the Quench Dynamics of Antiferromagnetic Correlations in a 2D Quantum Ising Spin System. *Phys. Rev. X*, 8(2):021069, 2018.
- [66] Jan Gukelberger, Sebastian Lienert, Evgeny Kozik, Lode Pollet, and Matthias Troyer. Fulde-Ferrell-Larkin-Ovchinnikov pairing as leading instability on the square lattice. *Phys. Rev. B*, 94(7):075157, Aug 2016.
- [67] S. Gupta, Z. Hadzibabic, M. W. Zwierlein, C. A. Stan, K. Dieckmann, C. H. Schunck, E. G.M. Van Kempen, B. J. Verhaar, and W. Ketterle. Radio-frequency spectroscopy of ultracold fermions. *Science*, 300(5626):1723–1726, 2003.
- [68] Z. Hadzibabic, C. A. Stan, K. Dieckmann, S. Gupta, M. W. Zwierlein, A. Görslitz, and W. Ketterle. Two-Species Mixture of Quantum Degenerate Bose and Fermi Gases. *Phys. Rev. Lett.*, 88(16):160401, Apr 2002.
- [69] B. I. Halperin and P. C. Hohenberg. Generalization of Scaling Laws to Dynamical Properties of a System Near its Critical Point. *Phys. Rev. Lett.*, 19(12):700–703, Sep 1967.
- [70] B. I. Halperin and P. C. Hohenberg. Scaling laws for dynamic critical phenomena. *Phys. Rev.*, 177(2):952–971, 1969.
- [71] W. B. Hanson and J. R. Pellam. Second sound attenuation in liquid helium II. *Physical Review*, 95(2):321–327, 1954.
- [72] G. B. Hess and W. M. Fairbank. Measurements of Angular Momentum in Superfluid Helium. *Phys. Rev. Lett.*, 19(5):216–218, Jul 1967.
- [73] Tin Lun Ho. Universal thermodynamics of degenerate quantum gases in the unitarity limit. *Phys. Rev. Lett.*, 92(9):090402–1, 2004.
- [74] Tin-Lun Ho and Erich J. Mueller. High Temperature Expansion Applied to Fermions near Feshbach Resonance. *Phys. Rev. Lett.*, 92(16):160404, Apr 2004.
- [75] Daniel Kai Hoffmann, Vijay Pal Singh, Thomas Paintner, Manuel Jäger, Wolfgang Limmer, Ludwig Mathey, and Johannes Hecker Denschlag. Second sound in the BEC-BCS crossover. *arXiv:2003.06847*, mar 2020.
- [76] P C Hohenberg. Density correlation function in superfluid helium near T_λ . *J. Low Temp. Phys.*, 11(5-6):745–750, Jun 1973.
- [77] P. C. Hohenberg and P. C. Martin. Microscopic theory of superfluid helium. *Ann. Phys. (N. Y.)*, 34(2):291–359, 1965.
- [78] Sascha Hoinka, Paul Dyke, Marcus G. Lingham, Jami J. Kinnunen, Georg M. Bruun, and Chris J. Vale. Goldstone mode and pair-breaking excitations in atomic Fermi superfluids. *Nat. Phys.*, 13(10):943–946, 2017.

- [79] Sascha Hoinka, Marcus Lingham, Kristian Fenech, Hui Hu, Chris J Vale, Joaquín E Drut, and Stefano Gandolfi. Precise Determination of the Structure Factor and Contact in a Unitary Fermi Gas. *Phys. Rev. Lett.*, 110(5):055305, Jan 2013.
- [80] Munekazu Horikoshi, Shuta Nakajima, Masahito Ueda, and Takashi Mukaiyama. Measurement of Universal Thermodynamic Functions for a Unitary Fermi Gas. *Science*, 327(5964):442–445, Jan 2010.
- [81] Kerson Huang. *Statistical Mechanics*. Wiley, NewYork, 2nd edition, 1987.
- [82] Samuel Huberman, Ryan A. Duncan, Ke Chen, Bai Song, Vazrik Chiloyan, Zhiwei Ding, Alexei A. Maznev, Gang Chen, and Keith A. Nelson. Observation of second sound in graphite at temperatures above 100 K. 2019.
- [83] Klaus Hueck, Niclas Luick, Lennart Sobirey, Jonas Siegl, Thomas Lompe, and Henning Moritz. Two-Dimensional Homogeneous Fermi Gases. *Phys. Rev. Lett.*, 120(6):60402, Feb 2018.
- [84] Dominik Husmann, Martin Lebrat, Samuel Häusler, Jean Philippe Brantut, Laura Corman, and Tilman Esslinger. Breakdown of the wiedemann–franz law in a unitary fermi gas. *Proc. Natl. Acad. Sci. U. S. A.*, 115(34):8563–8568, 2018.
- [85] S. Jochim, M. Bartenstein, A. Altmeyer, G. Hendl, C. Chin, J. Hecker Denschlag, and R. Grimm. Pure Gas of Optically Trapped Molecules Created from Fermionic Atoms. *Phys. Rev. Lett.*, 91(24):240402, Dec 2003.
- [86] S. Jochim, M. Bartenstein, A. Altmeyer, G. Hendl, S. Riedl, S. Chin, J. Heck Denschlag, and R. Grimm. Bose-Einstein Condensation of Molecules. *Science*, 302(5653):2101–2103, Dec 2003.
- [87] S. Jochim, M. Bartenstein, G. Hendl, J. Hecker Denschlag, R. Grimm, A. Mosk, and M. Weidemüller. Magnetic Field Control of Elastic Scattering in a Cold Gas of Fermionic Lithium Atoms. *Phys. Rev. Lett.*, 89(27):273202, 2002.
- [88] J. A. Joseph, E. Elliott, and J. E. Thomas. Shear Viscosity of a Unitary Fermi Gas Near the Superfluid Phase Transition. *Phys. Rev. Lett.*, 115(2):020401, Jul 2015.
- [89] Leo P. Kadanoff and Paul C. Martin. Hydrodynamic equations and correlation functions. *Ann. Phys. (N. Y.)*, 24(1-2):419–469, Oct 1963.
- [90] Leo P. Kadanoff and Jack Swift. Transport Coefficients near the Liquid-Gas Critical Point. *Phys. Rev.*, 166(1):89–101, Feb 1968.
- [91] W Ketterle, D. S. Durfee, and D. M. Stamper-Kurn. Making, probing and understanding Bose-Einstein condensates. *arXiv:9904034*, apr 1999.

- [92] Wolfgang Ketterle and Martin W. Zwierlein. Making, probing and understanding ultracold Fermi gases. *Rivista del Nuovo Cimento*, 31(5):247–422, 2008.
- [93] Isaac M. Khalatnikov. *An Introduction to the Theory of Superfluidity*. W. A. Benjamin, 1965.
- [94] T W B Kibble. Topology of cosmic domains and strings. *J. Phys. A. Math. Gen.*, 9(8):1387–1398, Aug 1976.
- [95] J. Kinast, S. L. Hemmer, M. E. Gehm, A. Turlapov, and J. E. Thomas. Evidence for Superfluidity in a Resonantly Interacting Fermi Gas. *Phys. Rev. Lett.*, 92(15):150402, Apr 2004.
- [96] C. Kohstall, M. Zaccanti, M. Jag, A. Trenkwalder, P. Massignan, G. M. Bruun, F. Schreck, and R. Grimm. Metastability and coherence of repulsive polarons in a strongly interacting Fermi mixture. *Nature*, 485(7400):615–618, 2012.
- [97] M Koschorreck, D Pertot, E Vogt, B Fröhlich, M Feld, and M Köhl. Attractive and repulsive Fermi polarons in two dimensions. *Nature*, 485(7400):619–622, 2012.
- [98] Marco Koschorreck, Daniel Pertot, Enrico Vogt, and Michael Köhl. Universal spin dynamics in two-dimensional Fermi gases. *Nat. Phys.*, 9(7):405–409, Jul 2013.
- [99] Sebastian Krinner, Martin Lebrat, Dominik Husmann, Charles Grenier, Jean Philippe Brantut, and Tilman Esslinger. Mapping out spin and particle conductances in a quantum point contact. *Proc. Natl. Acad. Sci. U. S. A.*, 113(29):8144–8149, 2016.
- [100] Mark J. H. Ku, Biswaroop Mukherjee, Tarik Yefsah, and Martin W. Zwierlein. Cascade of Solitonic Excitations in a Superfluid Fermi gas: From Planar Solitons to Vortex Rings and Lines. *Phys. Rev. Lett.*, 116(4):045304, Jan 2016.
- [101] Mark J H Ku, A. T. Sommer, L. W. Cheuk, and M. W. Zwierlein. Revealing the Superfluid Lambda Transition in the Universal Thermodynamics of a Unitary Fermi Gas. *Science*, 335(6068):563–567, 2012.
- [102] C. C.N. Kuhn, S. Hoinka, I. Herrera, P. Dyke, J. J. Kinnunen, G. M. Bruun, and C. J. Vale. High-Frequency Sound in a Unitary Fermi Gas. *Phys. Rev. Lett.*, 124(15):150401, 2020.
- [103] E. D. Kuhnle, H. Hu, X.-J. Liu, P. Dyke, M. Mark, P. D. Drummond, P. Hannaford, and C. J. Vale. Universal Behavior of Pair Correlations in a Strongly Interacting Fermi Gas. *Phys. Rev. Lett.*, 105(7):070402, Aug 2010.
- [104] L. Landau. Theory of the superfluidity of helium II. *Physical Review*, 60(4):356–358, 1941.

- [105] L. D. Landau and E. M. Lifshitz. *Fluid Mechanics*. Elsevier, 1959.
- [106] A. J. Larkin and Y. N. Ovchinnikov. Nonuniform state of superconductors. *Zh. Eksp. Teor. Fiz.*, 47:1136, 1964.
- [107] Sébastien Laurent, Matthieu Pierce, Marion Delehaye, Tarik Yefsah, Frédéric Chevy, and Christophe Salomon. Connecting Few-Body Inelastic Decay to Quantum Correlations in a Many-Body System: A Weakly Coupled Impurity in a Resonant Fermi Gas. *Phys. Rev. Lett.*, 118(10):16–18, 2017.
- [108] Martin Lebrat, Samuel Häusler, Philipp Fabritius, Dominik Husmann, Laura Corman, and Tilman Esslinger. Quantized Conductance through a Spin-Selective Atomic Point Contact. *Phys. Rev. Lett.*, 123(19):193605, 2019.
- [109] Patrick A Lee, Naoto Nagaosa, and Xiao-Gang Wen. Doping a Mott insulator: Physics of high-temperature superconductivity. *Rev. Mod. Phys.*, 78(1):17–85, Jan 2006.
- [110] Yean-an Liao, Ann Sophie C. Rittner, Tobias Paprotta, Wenhui Li, Guthrie B. Partridge, Randall G. Hulet, Stefan K. Baur, and Erich J. Mueller. Spin-imbalance in a one-dimensional Fermi gas. *Nature*, 467(7315):567–569, Sep 2010.
- [111] Weizhe Edward Liu, Zhe Yu Shi, Jesper Levinsen, and Meera M. Parish. Radio-Frequency Response and Contact of Impurities in a Quantum Gas. *Phys. Rev. Lett.*, 125(6):65301, 2020.
- [112] Xia-Ji Liu. Virial expansion for a strongly correlated Fermi system and its application to ultracold atomic Fermi gases. *Phys. Rep.*, 524(2):37–83, Mar 2013.
- [113] Xia Ji Liu and Hui Hu. Virial expansion for a strongly correlated Fermi gas with imbalanced spin populations. *Phys. Rev. A - At. Mol. Opt. Phys.*, 82(4):1–7, 2010.
- [114] Xia-Ji Liu, Hui Hu, and Peter D. Drummond. Three attractively interacting fermions in a harmonic trap: Exact solution, ferromagnetism, and high-temperature thermodynamics. *Phys. Rev. A*, 82(2):023619, Aug 2010.
- [115] C. Lobo, A. Recati, S. Giorgini, and S. Stringari. Normal State of a Polarized Fermi Gas at Unitarity. *Phys. Rev. Lett.*, 97(20):200403, Nov 2006.
- [116] T Loftus, C a Regal, C Ticknor, J L Bohn, and D S Jin. Resonant Control of Elastic Collisions in an Optically Trapped Fermi Gas of Atoms. *Phys. Rev. Lett.*, 88(17):173201, 2002.
- [117] Robert Löw, Hendrik Weimer, Johannes Nipper, Jonathan B. Balewski, Björn Butscher, Hans Peter Büchler, and Tilman Pfau. An experimental and theoretical guide to strongly interacting Rydberg gases. *J. Phys. B At. Mol. Opt. Phys.*, 45:113001, 2012.

- [118] Mingwu Lu, Nathaniel Q. Burdick, Seo Ho Youn, and Benjamin L. Lev. Strongly Dipolar Bose-Einstein Condensate of Dysprosium. *Phys. Rev. Lett.*, 107(19):190401, Oct 2011.
- [119] S. T. Lu and H. Kojima. Observation of Second Sound in Superfluid $^3\text{He-B}$. *Physical Review Letters*, 55(16):1677–1680, Oct 1985.
- [120] C. Luciuk, S. Smale, F. Böttcher, H. Sharum, B. A. Olsen, S. Trotzky, T. Enss, and J. H. Thywissen. Observation of Quantum-Limited Spin Transport in Strongly Interacting Two-Dimensional Fermi Gases. *Phys. Rev. Lett.*, 118(13):130405, Mar 2017.
- [121] Niclas Luick, Lennart Sobirey, Markus Bohlen, Vijay Pal Singh, Ludwig Mathey, Thomas Lompe, and Henning Moritz. An ideal Josephson junction in an ultracold two-dimensional Fermi gas. *Science*, 369(6499):89–91, 2020.
- [122] Niclas Luick, Lennart Sobirey, Markus Bohlen, Vijay Pal Singh, Ludwig Mathey, Thomas Lompe, and Henning Moritz. An ideal Josephson junction in an ultracold two-dimensional Fermi gas. *Science*, 369(6499):89–91, 2020.
- [123] M. Marinescu. Computation of the scattering length and effective range in molecular physics. *Phys. Rev. A*, 50(4):3177–3180, Oct 1994.
- [124] Pietro Massignan, Matteo Zaccanti, and Georg M Bruun. Polarons, dressed molecules and itinerant ferromagnetism in ultracold Fermi gases. *Rep. Prog. Phys.*, 77(3):034401, 2014.
- [125] Anton Mazurenko, Christie S. Chiu, Geoffrey Ji, Maxwell F. Parsons, Márton Kanász-Nagy, Richard Schmidt, Fabian Grusdt, Eugene Demler, Daniel Greif, and Markus Greiner. Experimental realization of a long-range antiferromagnet in the Hubbard model with ultracold atoms. *Nature*, 545(7655):462–466, 2016.
- [126] Raui Mehrotra and Guenter Ahlers. Damping of second sound near the superfluid transition of He4 as a function of pressure. *Physical Review B*, 30(9):5116–5134, Nov 1984.
- [127] R. Meppelink, S. B. Koller, and P. Van Der Straten. Sound propagation in a Bose-Einstein condensate at finite temperatures. *Physical Review A - Atomic, Molecular, and Optical Physics*, 80(4):1–6, 2009.
- [128] D. E. Miller, J. K. Chin, C. A. Stan, Y. Liu, W. Setiawan, C. Sanner, and W. Ketterle. Critical Velocity for Superfluid Flow across the BEC-BCS Crossover. *Phys. Rev. Lett.*, 99(7):070402, aug 2007.
- [129] Christophe Mora and Frédéric Chevy. Normal Phase of an Imbalanced Fermi Gas. *Phys. Rev. Lett.*, 104(23):230402, Jun 2010.

- [130] Biswaroop Mukherjee, Parth B. Patel, Zhenjie Yan, Richard J. Fletcher, Julian Struck, and Martin W. Zwierlein. Spectral Response and Contact of the Unitary Fermi Gas. *Physical Review Letters*, 122(20):203402, 2019.
- [131] Biswaroop Mukherjee, Zhenjie Yan, Parth B. Patel, Zoran Hadzibabic, Tarik Yefsah, Julian Struck, and Martin W. Zwierlein. Homogeneous Atomic Fermi Gases. *Physical Review Letters*, 118(12):123401, 2017.
- [132] Brendan C Mulkerin, Xia-Ji Liu, and Hui Hu. Breakdown of the Fermi polaron description near Fermi degeneracy at unitarity. *Ann. Phys. (N. Y.)*, 407:29–45, Aug 2019.
- [133] P. A. Murthy, D. Kedar, T. Lompe, M. Neidig, M. G. Ries, A. N. Wenz, G. Zürn, and S. Jochim. Matter-wave Fourier optics with a strongly interacting two-dimensional Fermi gas. *Phys. Rev. A*, 90(4):043611, Oct 2014.
- [134] S. Nascimbène, N. Navon, K. J. Jiang, F. Chevy, and C. Salomon. Exploring the thermodynamics of a universal Fermi gas. *Nature*, 463(7284):1057–1060, Feb 2010.
- [135] S. Nascimbene, N. Navon, K. J. Jiang, F. Chevy, and C. Salomon. Exploring the thermodynamics of a universal Fermi gas. *Nature*, 463(7284):1057–1060, 2010.
- [136] S. Nascimbène, N. Navon, K. J. Jiang, L. Tarruell, M. Teichmann, J. McKeever, F. Chevy, and C. Salomon. Collective Oscillations of an Imbalanced Fermi Gas: Axial Compression Modes and Polaron Effective Mass. *Phys. Rev. Lett.*, 103(17):170402, Oct 2009.
- [137] S. Nascimbène, N. Navon, S. Pilati, F. Chevy, S. Giorgini, A. Georges, and C. Salomon. Fermi-Liquid Behavior of the Normal Phase of a Strongly Interacting Gas of Cold Atoms. *Phys. Rev. Lett.*, 106(21):215303, May 2011.
- [138] N. Navon, S. Nascimbene, F. Chevy, and C. Salomon. The Equation of State of a Low-Temperature Fermi Gas with Tunable Interactions. *Science*, 328(5979):729–732, May 2010.
- [139] Nir Navon, Alexander L. Gaun, Robert P. Smith, and Zoran Hadzibabic. Critical dynamics of spontaneous symmetry breaking in a homogeneous Bose gas. *Science*, 347(6218):167–170, Jan 2015.
- [140] Nir Navon, Alexander L. Gaunt, Robert P. Smith, and Zoran Hadzibabic. Emergence of a turbulent cascade in a quantum gas. *Nature*, 539(7627):72–75, Nov 2016.
- [141] Predrag Nikolić and Subir Sachdev. Renormalization-group fixed points, universal phase diagram, and $1/N$ expansion for quantum liquids with interactions near the unitarity limit. *Phys. Rev. A*, 75(3):033608, mar 2007.

- [142] P. Nozieres and S. Schmitt-Rink. Bose condensation in an attractive fermion gas: From weak to strong coupling superconductivity. *J. Low Temp. Phys.*, 59(3-4):195–211, May 1985.
- [143] K. M. O’Hara, S. L. Hemmer, M. E. Gehm, S. R. Granade, and J. E. Thomas. Observation of a Strongly-Interacting Degenerate Fermi Gas of Atoms. *Science*, 298(5601):2179–2182, Dec 2002.
- [144] K. M. O’Hara, S. L. Hemmer, S. R. Granade, M. E. Gehm, J. E. Thomas, V. Venturi, E. Tiesinga, and C. J. Williams. Measurement of the zero crossing in a Feshbach resonance of fermionic ^6Li . *Phys. Rev. A*, 66(4):041401, 2002.
- [145] Lars Onsager. Reciprocal Relations in Irreversible Processes. I. *Phys. Rev.*, 37(4):405–426, Feb 1931.
- [146] M. M. Parish, F. M. Marchetti, A. Lamacraft, and B. D. Simons. Finite-temperature phase diagram of a polarized Fermi condensate. *Nat. Phys.*, 3(2):124–128, Feb 2007.
- [147] G. B. Partridge, Wenhui Li, Ramsey I. Kamar, Yean-an Liao, and Randall G. Hulet. Pairing and Phase Separation in a Polarized Fermi Gas. *Science*, 311(5760):503–505, Jan 2006.
- [148] G. B. Partridge, K. E. Strecker, R. I. Kamar, M. W. Jack, and R. G. Hulet. Molecular Probe of Pairing in the BEC-BCS Crossover. *Phys. Rev. Lett.*, 95(2):020404, Jul 2005.
- [149] Parth B. Patel, Zhenjie Yan, Biswaroop Mukherjee, Richard J. Fletcher, Julian Struck, and Martin W. Zwierlein. Universal sound diffusion in a strongly interacting Fermi gas. *Science*, 370(6521):1222–1226, 2020.
- [150] W. Pauli. The Connection Between Spin and Statistics. *Phys. Rev.*, 58(8):716–722, Oct 1940.
- [151] V. P. Peshkov. “Second sound” in helium II. *J. Phys.*, 8:381, 1944.
- [152] V P Peshkov. Second sound in Helium II. *Jetp*, 11(3):799–805, 1960.
- [153] D. S. Petrov, C. Salomon, and G. V. Shlyapnikov. Weakly Bound Dimers of Fermionic Atoms. *Phys. Rev. Lett.*, 93(9):090404, Aug 2004.
- [154] Pierbiagio Pieri, Andrea Perali, and Giancarlo Calvanese Strinati. Enhanced paraconductivity-like fluctuations in the radiofrequency spectra of ultracold Fermi atoms. *Nat. Phys.*, 5(10):736–740, Oct 2009.
- [155] D. Pines and P Nozieres. *The Theory of Quantum Liquids, Vol. I: Normal Fermi Liquids*. W.A. Benjamin, 1966.
- [156] Lev Pitaevskii and Sandro Stringari. Second sound in ultracold atomic gases. In *Universal Themes of Bose-Einstein Condensation*, pages 322–347. 2017.

- [157] N. V. Prokof'ev and B. V. Svistunov. Bold diagrammatic Monte Carlo: A generic sign-problem tolerant technique for polaron models and possibly interacting many-body problems. *Phys. Rev. B*, 77(12):125101, Mar 2008.
- [158] Nikolay Prokof'ev and Boris Svistunov. Fermi-polaron problem: Diagrammatic Monte Carlo method for divergent sign-alternating series. *Phys. Rev. B - Condens. Matter Mater. Phys.*, 77(2):1–4, 2008.
- [159] M. Punk, P. T. Dumitrescu, and W. Zwerger. Polaron-to-molecule transition in a strongly imbalanced Fermi gas. *Phys. Rev. A - At. Mol. Opt. Phys.*, 80(5):1–10, 2009.
- [160] M. Punk and W. Zwerger. Theory of rf-spectroscopy of strongly interacting fermions. *Phys. Rev. Lett.*, 99(17):1–4, 2007.
- [161] Leo Radzihovsky and Daniel E. Sheehy. Imbalanced Feshbach-resonant Fermi gases. *Reports Prog. Phys.*, 73(7):076501, Jul 2010.
- [162] Mohit Randeria and Edward Taylor. Crossover from Bardeen-Cooper-Schrieffer to Bose-Einstein Condensation and the Unitary Fermi Gas. *Annu. Rev. Condens. Matter Phys.*, 5(1):209–232, Mar 2014.
- [163] C A Regal, M Greiner, and D S Jin. Observation of Resonance Condensation of Fermionic Atom Pairs. *Phys. Rev. Lett.*, 92(4):040403, Jan 2004.
- [164] C. A. Regal and D. S. Jin. Measurement of Positive and Negative Scattering Lengths in a Fermi Gas of Atoms. *Phys. Rev. Lett.*, 90(23):230404, Jun 2003.
- [165] Cindy a Regal, Christopher Ticknor, John L Bohn, and Deborah S Jin. Creation of ultracold molecules from a Fermi gas of atoms. *Nature*, 424(6944):47–50, Jul 2003.
- [166] S. Riedl, E. R. Sánchez Guajardo, C. Kohstall, J. Hecker Denschlag, and R. Grimm. Superfluid quenching of the moment of inertia in a strongly interacting Fermi gas. *New J. Phys.*, 13(3):035003, 2011.
- [167] G. Roati, F. Riboli, G. Modugno, and M. Inguscio. Fermi-Bose Quantum Degenerate ^{40}K - ^{87}Rb Mixture with Attractive Interaction. *Phys. Rev. Lett.*, 89(15):150403, Sep 2002.
- [168] R Rossi, T Ohgoe, E Kozik, N. Prokof'ev, B Svistunov, K. Van Houcke, and F Werner. Contact and Momentum Distribution of the Unitary Fermi Gas. *Phys. Rev. Lett.*, 121(13):130406, Sep 2018.
- [169] Timur M. Rvachov, Hyungmok Son, Ariel T. Sommer, Sepehr Ebadi, Juliana J. Park, Martin W. Zwierlein, Wolfgang Ketterle, and Alan O. Jamison. Long-Lived Ultracold Molecules with Electric and Magnetic Dipole Moments. *Physical Review Letters*, 119(14):143001, 2017.

- [170] F Scazza, G Valtolina, P Massignan, A Recati, A Amico, A Burchianti, C Fort, M Inguscio, M Zaccanti, and G Roati. Repulsive Fermi Polarons in a Resonant Mixture of Ultracold ^6Li Atoms. *Phys. Rev. Lett.*, 118(8):083602, Feb 2017.
- [171] R.A. Schill. General relation for the vector magnetic field of a circular current loop: a closer look. *IEEE Trans. Magn.*, 39(2):961–967, Mar 2003.
- [172] André Schirotzek, Yong-il Shin, Christian H. Schunck, and Wolfgang Ketterle. Determination of the Superfluid Gap in Atomic Fermi Gases by Quasiparticle Spectroscopy. *Phys. Rev. Lett.*, 101(14):140403, Oct 2008.
- [173] André Schirotzek, Cheng-Hsun Wu, Ariel Sommer, and Martin W Zwierlein. Observation of Fermi polarons in a tunable Fermi liquid of ultracold atoms. *Phys. Rev. Lett.*, 102(23):230402, Jun 2009.
- [174] Tobias F. Schmidutz, Igor Gotlibovych, Alexander L. Gaunt, Robert P. Smith, Nir Navon, and Zoran Hadzibabic. Quantum Joule-Thomson Effect in a Saturated Homogeneous Bose Gas. *Phys. Rev. Lett.*, 112(4):040403, Jan 2014.
- [175] William Schneider, Vijay B. Shenoy, and Mohit Randeria. Theory of Radio Frequency Spectroscopy of Polarized Fermi Gases. *ArXiv:0903.3006*, (1):4, 2009.
- [176] F Schreck, L Khaykovich, K L Corwin, G Ferrari, T Bourdel, J Cubizolles, and C Salomon. Quasipure Bose-Einstein Condensate Immersed in a Fermi Sea. *Phys. Rev. Lett.*, 87(8):080403, Aug 2001.
- [177] Christian H Schunck, Y. Shin, André Schirotzek, Martin W Zwierlein, and Wolfgang Ketterle. Pairing Without Superfluidity: The Ground State of an Imbalanced Fermi Mixture. *Science*, 316(5826):867–870, May 2007.
- [178] Christian H Schunck, Yong-Il Shin, André Schirotzek, and Wolfgang Ketterle. Determination of the fermion pair size in a resonantly interacting superfluid. *Nature*, 454(7205):739–743, 2008.
- [179] Y. Shin, C. H. Schunck, a. Schirotzek, and W. Ketterle. Tomographic rf spectroscopy of a trapped fermi gas at unitarity. *Phys. Rev. Lett.*, 99(9):2–5, 2007.
- [180] Y. Shin, M. W. Zwierlein, C. H. Schunck, A. Schirotzek, and W. Ketterle. Observation of phase separation in a strongly interacting imbalanced fermi gas. *Phys. Rev. Lett.*, 97(3), 2006.
- [181] Yong-il Shin. Determination of the equation of state of a polarized Fermi gas at unitarity. *Phys. Rev. A*, 77(4):041603, Apr 2008.
- [182] Yong-Il Shin, Christian H Schunck, André Schirotzek, and Wolfgang Ketterle. Phase diagram of a two-component Fermi gas with resonant interactions. *Nature*, 451(7179):689–693, Feb 2008.

- [183] I Shvarchuck, Ch Buggle, D S Petrov, K Dieckmann, M Zielonkowski, M Kemmann, T G Tiecke, W von Klitzing, G V Shlyapnikov, and J T M Walraven. Bose-Einstein Condensation into Nonequilibrium States Studied by Condensate Focusing. *Phys. Rev. Lett.*, 89(27):270404, Dec 2002.
- [184] Leonid A. Sidorenkov, Meng Khoon Tey, Rudolf Grimm, Yan-Hua Hou, Lev Pitaevskii, and Sandro Stringari. Second sound and the superfluid fraction in a Fermi gas with resonant interactions. *Nature*, 498(7452):78–81, Jun 2013.
- [185] Lennart Sobirey, Niclas Luick, Markus Bohlen, Hauke Biss, Henning Moritz, and Thomas Lompe. Observation of superfluidity in a strongly correlated two-dimensional Fermi gas. *Science*, 372(6544):844–846, May 2021.
- [186] Lennart Sobirey, Niclas Luick, Markus Bohlen, Hauke Biss, Henning Moritz, and Thomas Lompe. Observation of superfluidity in a strongly correlated two-dimensional Fermi gas. *Science*, 372(6544):844–846, 2021.
- [187] Ariel Sommer, Mark Ku, Giacomo Roati, and Martin W. Zwierlein. Universal spin transport in a strongly interacting Fermi gas. *Nature*, 472(7342):201–204, Apr 2011.
- [188] Ariel Sommer, Mark Ku, and Martin W. Zwierlein. Spin transport in polaronic and superfluid Fermi gases. *New J. Phys.*, 13(5):055009, May 2011.
- [189] David Stadler, Sebastian Krinner, Jakob Meineke, Jean-Philippe Brantut, and Tilman Esslinger. Observing the drop of resistance in the flow of a superfluid Fermi gas. *Nature*, 491(7426):736–739, Nov 2012.
- [190] D. M. Stamper-Kurn, H. J. Miesner, S. Inouye, M. R. Andrews, and W. Ketterle. Collisionless and hydrodynamic excitations of a bose-einstein condensate. *Physical Review Letters*, 81(3):500–503, 1998.
- [191] J. T. Stewart, J. P. Gaebler, T. E. Drake, and D. S. Jin. Verification of Universal Relations in a Strongly Interacting Fermi Gas. *Phys. Rev. Lett.*, 104(23):235301, Jun 2010.
- [192] J T Stewart, J P Gaebler, and D S Jin. Using photoemission spectroscopy to probe a strongly interacting Fermi gas. *Nature*, 454(7205):744–747, 2008.
- [193] Horst L. Stormer, Daniel C. Tsui, and Arthur C. Gossard. The fractional quantum Hall effect. *Rev. Mod. Phys.*, 71(2):S298–S305, Mar 1999.
- [194] Kevin E. Strecker, Guthrie B. Partridge, and Randall G. Hulet. Conversion of an Atomic Fermi Gas to a Long-Lived Molecular Bose Gas. *Phys. Rev. Lett.*, 91(8):080406, Aug 2003.
- [195] Mingyuan Sun and Xavier Leyronas. High-temperature expansion for interacting fermions. *Phys. Rev. A*, 92(5):053611, Nov 2015.

- [196] Hiroyuki Tajima and Shun Uchino. Thermal crossover, transition, and coexistence in Fermi polaronic spectroscopies. *Phys. Rev. A*, 99(6):063606, Jun 2019.
- [197] Shina Tan. Energetics of a strongly correlated Fermi gas. *Ann. Phys. (N. Y.)*, 323(12):2952–2970, Dec 2008.
- [198] Shina Tan. Large momentum part of a strongly correlated Fermi gas. *Ann. Phys. (N. Y.)*, 323(12):2971–2986, 2008.
- [199] E. Taylor, H. Hu, X.-J. Liu, and A. Griffin. Variational theory of two-fluid hydrodynamic modes at unitarity. *Phys. Rev. A*, 77(3):033608, Mar 2008.
- [200] E. Taylor, H. Hu, X.-J. Liu, L. P. Pitaevskii, A. Griffin, and S. Stringari. First and second sound in a strongly interacting Fermi gas. *Phys. Rev. A*, 80(5):053601, 2009.
- [201] L. Tisza. Transport Phenomena in Helium II. *Nature*, 141(3577):913–913, May 1938.
- [202] Päivi Törmä. Physics of ultracold Fermi gases revealed by spectroscopies. *Phys. Scr.*, 91(4):043006, Apr 2016.
- [203] Christian Trefzger and Yvan Castin. Polaron residue and spatial structure in a Fermi gas. *EPL (Europhysics Lett.)*, 101(3):30006, Feb 2013.
- [204] Andrew G Truscott, Kevin E Strecker, William I McAlexander, Guthrie B Partridge, and Randall G Hulet. Observation of Fermi Pressure in a Gas of Trapped Atoms. *Science*, 291(5513):2570 – 2572, Mar 2001.
- [205] S Tung, G Lamporesi, D Lobser, L Xia, and E A Cornell. Observation of the Presuperfluid Regime in a Two-Dimensional Bose Gas. *Phys. Rev. Lett.*, 105(23):230408, Dec 2010.
- [206] Giacomo Valtolina, Alessia Burchianti, A. Amico, E. Neri, Klejdja Xhani, Jorge Amin Seman, Andrea Trombettoni, Augusto Smerzi, Matteo Zaccanti, Massimo Inguscio, and Giacomo Roati. Josephson effect in fermionic superfluids across the BEC-BCS crossover. *Science*, 350(6267):1505–1508, Dec 2015.
- [207] A H van Amerongen, J J P van Es, P Wicke, K V Kheruntsyan, and N J van Druten. Yang-Yang Thermodynamics on an Atom Chip. *Phys. Rev. Lett.*, 100(9):090402, Mar 2008.
- [208] G. Veeravalli, E. Kuhnle, P. Dyke, and C. J. Vale. Bragg spectroscopy of a strongly interacting fermi gas. *Phys. Rev. Lett.*, 101(25):2–5, 2008.
- [209] Martin Veillette, Eun Gook Moon, Austen Lamacraft, Leo Radzhovsky, Subir Sachdev, and D. E. Sheehy. Radio-frequency spectroscopy of a strongly imbalanced Feshbach-resonant Fermi gas. *Phys. Rev. A*, 78(3):033614, Sep 2008.

- [210] Bo Yan, Steven A. Moses, Bryce Gadway, Jacob P. Covey, Kaden R.A. Hazard, Ana Maria Rey, Deborah S. Jin, and Jun Ye. Observation of dipolar spin-exchange interactions with lattice-confined polar molecules. *Nature*, 501(7468):521–525, 2013.
- [211] Zhenjie Yan, Parth B. Patel, Biswaroop Mukherjee, Richard J. Fletcher, Julian Struck, and Martin W. Zwierlein. Boiling a Unitary Fermi Liquid. *Physical Review Letters*, 122(9):093401, 2019.
- [212] Zoe Z. Yan, Jee Woo Park, Yiqi Ni, Huanqian Loh, Sebastian Will, Tijs Karman, and Martin Zwierlein. Resonant Dipolar Collisions of Ultracold Molecules Induced by Microwave Dressing. *Phys. Rev. Lett.*, 125(6):63401, 2020.
- [213] Tarik Yefsah, Ariel T. Sommer, Mark J. H. Ku, Lawrence W. Cheuk, Wenjie Ji, Waseem S. Bakr, and Martin W. Zwierlein. Heavy solitons in a fermionic superfluid. *Nature*, 499(7459):426–430, Jul 2013.
- [214] Z. N. Zinov’eva. The coefficient of volume absorption of second sound and the viscosity of the normal component of Helium II down to 0.83 K. *Sov. Phys. JETP*, 4(1):36–40, 1957.
- [215] W H Zurek. Cosmological experiments in superfluid helium? *Nature*, 317(6037):505–508, Oct 1985.
- [216] G. Zürn, T. Lompe, A. N. Wenz, S. Jochim, P. S. Julienne, and J. M. Hutson. Precise Characterization of Li₆ Feshbach Resonances Using Trap-Sideband-Resolved RF Spectroscopy of Weakly Bound Molecules. *Phys. Rev. Lett.*, 110(13):135301, Mar 2013.
- [217] Wilhelm Zwerger. Strongly Interacting Fermi Gases. In M. Inguscio, W. Ketterle, S. Stringari, and G. Roati, editors, *Quantum Matter Ultralow Temp. Proc. of the Int. Sch. of Physics “Enrico Fermi,” Course CXCI*, chapter Chapter 3, pages 63–142. IOS Press, Amsterdam, Aug 2016.
- [218] M W Zwierlein, J R Abo-Shaeer, A Schirotzek, C H Schunck, and W Ketterle. Vortices and superfluidity in a strongly interacting Fermi gas. *Nature*, 435(7045):1047–1051, Jun 2005.
- [219] M. W. Zwierlein, C. A. Stan, C. H. Schunck, S. M. F. Raupach, S. Gupta, Z. Hadzibabic, and W. Ketterle. Observation of Bose-Einstein Condensation of Molecules. *Phys. Rev. Lett.*, 91(25):250401, Dec 2003.
- [220] M W Zwierlein, C A Stan, C H Schunck, S M F Raupach, A J Kerman, and W Ketterle. Condensation of Pairs of Fermionic Atoms near a Feshbach Resonance. *Phys. Rev. Lett.*, 92(12):120403, Mar 2004.
- [221] Martin W. Zwierlein. Superfluidity in ultracold atomic Fermi gases. In K.-H. Bennemann and J. B. Ketterson, editors, *Nov. Superfluids*, pages 269–422. Oxford Univ. Press, 2015.

- [222] Martin W Zwierlein, Andre Schirotzek, Christian H. Schunck, and Wolfgang Ketterle. Fermionic Superfluidity with Imbalanced Spin Populations. *Science*, 311(5760):492–496, Jan 2006.